UNIVERSITY OF SOUTHAMPTON

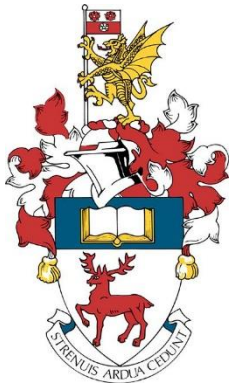

FACULTY OF NATURAL AND ENVIRONMENTAL SCIENCES

School of Ocean and Earth Science

The Effect of Gas Hydrate Saturation and Distribution on the Geophysical Properties of Marine Sediments

by

Sourav Kumar Sahoo

Thesis for the degree of Doctor of Philosophy

March 2018

UNIVERSITY OF SOUTHAMPTON

ABSTRACT

FACULTY OF NATURAL AND ENVIRONMENTAL SCIENCES

Ocean and Earth Science

Thesis for the degree of Doctor of Philosophy

THE EFFECT OF GAS HYDRATE SATURATION AND DISTRIBUTION ON THE GEOPHYSICAL PROPERTIES OF MARINE SEDIMENTS

Sourav Kumar Sahoo

Gas hydrates are ice–like compounds found in marine sediments and permafrosts. A significant fraction of all known hydrocarbons in nature is in the form of hydrate. Gas hydrates are a potential energy resource, with possible roles in seafloor slope stability and climate change. As such, improved geophysical methods are needed to identify and quantify *in situ* natural hydrates to better study their potential impacts. Current estimates of the distribution and volume of gas hydrates vary widely, by orders of magnitude, largely because of uncertainties in geophysical inversion results. The presence of hydrate affects the geophysical properties of the host sediment, creating anomalies that can be detected by seismic or electrical measurements. However, the precise relationships between measured geophysical properties and hydrate content (and distribution) are not fully understood, leading to uncertainties in hydrate estimates. Previous studies have shown that both the hydrate saturation (content) and its distribution (morphology or habit) affect the geophysical properties of the host sediment, and separating these effects presents a challenge to geophysical data interpretation. As this knowledge is generally required to interpret field data, this thesis instead seeks to gain this understanding from controlled laboratory experimental studies.

I studied laboratory hydrate formation and dissociation in Berea sandstone and Leighton Buzzard sand to understand their effect on P- and S-wave velocities and attenuations, and on electrical resistivity. I used high resolution synchrotron radiation X-ray tomography (SRXCT) to visualize the pore-scale evolution of hydrate morphology with saturation. These observations could be

important for seismic data interpretation in terms of hydrate content and sediment strength, which are needed for natural resource and geohazard assessments (also for joint seismic and electromagnetic survey data interpretation). Hence, I was able to observe how hydrate distribution within the pores (morphology or habit) changes with hydrate formation and dissociation, and how these changes affect the P- and S-wave velocities and attenuations. I calculated hydrate saturation continuously from changes in pressure and temperature and independently from electrical resistivity during hydrate formation and dissociation. I applied a new rock physics model to relate P- and S-wave velocities and attenuations with changes in hydrate saturation and morphology.

I found that not all the gas formed hydrate, even when the system was under hydrate stability conditions with excess water. The synchrotron CT results suggest that the dominant mechanism for co-existing gas is the formation of hydrate films on gas bubbles; these bubbles either rupture, releasing trapped gas, or remain trapped within an aggregate of hydrate grains. From a geophysical remote sensing perspective, such co-existing gas could cause errors in hydrate saturation estimates from electrical resistivity as both gas and hydrate are resistive compared to saline pore fluid. I saw that hydrate starts forming in the pore-floating morphology (where hydrate grains are surrounded by brine) and evolves into the pore-bridging morphology (where hydrate connects mineral grains). Eventually, hydrate from adjacent pores joins and forms a pore hydrate framework, interlocking with the sand grain framework and separated by thin water films. I was able to relate these changes in morphology to our elastic wave measurements using the HBES (Hydrate Bearing Effective Sediment) rock physics model. For low hydrate saturations, both P and S wave velocity follows the pore-floating model curve. As hydrate formation continues, the P-wave velocity follows the pore-bridging model curve, similar to other studies. In contrast, the S-wave velocity was lower than the pore-bridging model but higher than the pore-floating model curves. I think that the presence of water films between hydrate and the rock frame inhibited the ability of pore-bridging hydrate to increase the frame shear modulus. The higher S-wave velocity than the pore-floating model predictions is likely due to interlocking rock and pore-bridging hydrate frameworks. The magnitude of relative changes in attenuation is much higher than that of velocity due to changes in hydrate content and distribution. Elastic wave attenuation frequency spectra between 448 and 782 kHz show systematic and repeatable changes during hydrate formation and dissociation. In our experiments, the dominant mechanism of attenuation and velocity changes with an increase in hydrate saturation is (i) a decrease in methane gas bubble radius and (ii) an increase in secondary porosity with hydrate formation. The accurate measurement of both velocity and attenuation at multiple frequencies in the pulse-echo system allow us to constrain the dominant attenuation mechanisms using the HBES rock physics model.

Overall, I conclude that hydrate-sediment systems are complex with interlocking solid hydrate aggregate and host grain frameworks separated by water films, with isolated pockets of gas within the hydrate. Such an interlocking pore hydrate framework and co-existing gas, if widespread in nature, should be considered in hydrate quantification from elastic wave velocities. For more reliable estimates of *in situ* hydrate, multiple geophysical parameter measurements are required (e.g., P and S wave velocities and attenuation, electrical resistivity, and at multiple frequencies), and hydrate estimates from seismic velocities alone could lead to significant errors at low hydrate saturations (< 40%).

Table of Contents

Table of Tables

Table of Figures

Academic Thesis: Declaration of Authorship

I, Sourav Kumar Sahoo declare that this thesis and the work presented in it are my own and has been generated by me as the result of my own original research.

The effect of gas hydrate saturation and distribution on the geophysical properties of marine sediments

I confirm that:

1. This work was done wholly or mainly while in candidature for a research degree at this University;
2. Where any part of this thesis has previously been submitted for a degree or any other qualification at this University or any other institution, this has been clearly stated;
3. Where I have consulted the published work of others, this is always clearly attributed;
4. Where I have quoted from the work of others, the source is always given. With the exception of such quotations, this thesis is entirely my own work;
5. I have acknowledged all main sources of help;
6. Where the thesis is based on work done by myself jointly with others, I have made clear exactly what was done by others and what I have contributed myself;
7. Parts of this work have been published as:

Journal Publications:

S. K. Sahoo, H. Marín-Moreno, L. J. North, I. Falco-Suarez, Madhusudhan B.N, A. I. Best and T. A. Minshull (2018), Presence and consequences of co-existing methane gas with hydrate under two phase water-hydrate stability conditions, Journal of Geophysical Research: Solid Earth, doi: 10.1029/2018JB015598

Marín-Moreno, H., S. K. Sahoo, and A. I. Best (2017), Theoretical modelling insights into elastic wave attenuation mechanisms in marine sediments with pore-filling methane hydrate, Journal of Geophysical Research: Solid Earth, doi:10.1002/2016JB013577.

Conference proceedings:

S. K. Sahoo, H. Marín-Moreno, L. J. North, T. A. Minshull, B. N. Madhusudhan, S. Ahmed, I. Sinclair & A. I. Best (2017) Effect of Methane Hydrate Saturation and Morphology on the Geophysical Properties of Sub-Seafloor Sediments, 9th Int. Conf. Gas Hydrates, Denver, USA.

S. K. Sahoo, H. Marín-Moreno, L. J. North, I. Falco-Suarez, T. A. Minshull and A. I. Best (2017) Laboratory formation of non-cementing hydrate using excess water and temperature cycling, supported by rock physics modelling. Fourth International Workshop on Rock Physics, Trondheim, Norway.

Signed: .....

Date: .....

Acknowledgements

I sincerely thank my supervisors Dr Angus Best and Prof Tim Minshull for their guidance, encouragement and time for the scientific discussion without which this thesis would not have been possible. I also want to thank Dr Hector Marín-Moreno who has also spent a lot of his time in supervising and guiding me. Special thanks to Angus who have always kept his door open for discussions and believing in my science decision. Angus has always motivated and inspired me to look for the light at the end of the tunnel, eventually leading me to completion of this thesis. A PhD has moments of extreme joy and frustrations. Whenever I went through such a frustrating time, a small discussion with Angus and/or Hector brings back the energy. It was a great pleasure and honour to have Angus and Hector attend my wedding in India in December 2016.

Special thanks to Dr Laurence North for helping me in the laboratory. Without Laurence, none of the experiments would have been possible. Laurence has spent lot of time and energy in teaching me the operation of all the laboratory measurement systems, and data processing. Dr Goawei Hu was visiting our laboratory when I started my PhD and he gave me some tips on hydrate formation. Many thanks to Dr Ismaeil Falcon Saurez for his guidance during the experiments. I am very thankful to Dr Madhusudhan B N Murthy for his help with synchrotron imaging; it would not have been possible without him. I also want to thank Dr Karen Weitemeyer who was initially one of my supervisors before she left the University of Southampton. She was my first point of contact and helped me a lot during the application process of the PhD program.

My mom, dad, mamu, mayein and brother have always been there and very supportive. I love it when my dad tries to understand my experiments and results. I can never thank enough my sweet wife *Sheetal* who left India and her job just to join me here in the UK. It has been a pleasure to have her with me.

I like to thank my office mates and friends in Southampton and our coffee group 'The un-respectful 10' for being there when I needed. All the discussions during coffee breaks, lunch breaks, unplanned breaks in corridors……, which have helped relieve stress during my PhD. To Hector, Carla, Max, Deb bhai, Sulekha, Saisha, Mrinal bhai and Ankita thanks for being like a family in a foreign country.

I acknowledge funding from the UK Natural Environment Research Council and GSNOCS, University of Southampton

It looks like my PhD story is coming to an end…… It has been an enjoyable and unforgettable experience.

Chapter 1 Introduction

1.1 Gas hydrates

‘‘Gas hydrate’’ is a commonly used term for naturally occurring crystalline compounds consisting of a solid but open lattice of water molecules with various entrapped and appropriately sized gas molecules without chemical bonding (Sloan and Koh, 2007). Gas hydrates are a class of clathrates (from clatratus, the Latin for cage) and are also known as clathrate hydrate. Gas hydrates come in three crystallographic lattice structural types: body centred cubic (structure I), diamond cubic (structure II) and hexagonal (structure H) (Sloan and Koh, 2007). The structure depends mainly on the size of the guest molecules. Gas hydrates are stable at specific pressures and temperatures, depending on several factors like chemical composition of the gas, pore water salinity, etc. (Sloan and Koh, 2007) (Figure 1.1). If these conditions are not maintained, then the solid hydrate dissociates to gas and water. The predominant gas in natural hydrate is methane (Kvenvolden, 1993). The occurrence of natural gas hydrate is controlled mainly by the availability of gas, and suitable pressure and temperature conditions. In marine sediments, hydrates tend to occur along continental margins in water deeper than about 300 m, with bottom water temperatures of about 3 °C. Natural gas hydrates have also been found in terrestrial and offshore permafrost, and in the deep water sediments of inland lakes and seas. The worldwide distribution of hydrate is show in Figure 1.2.

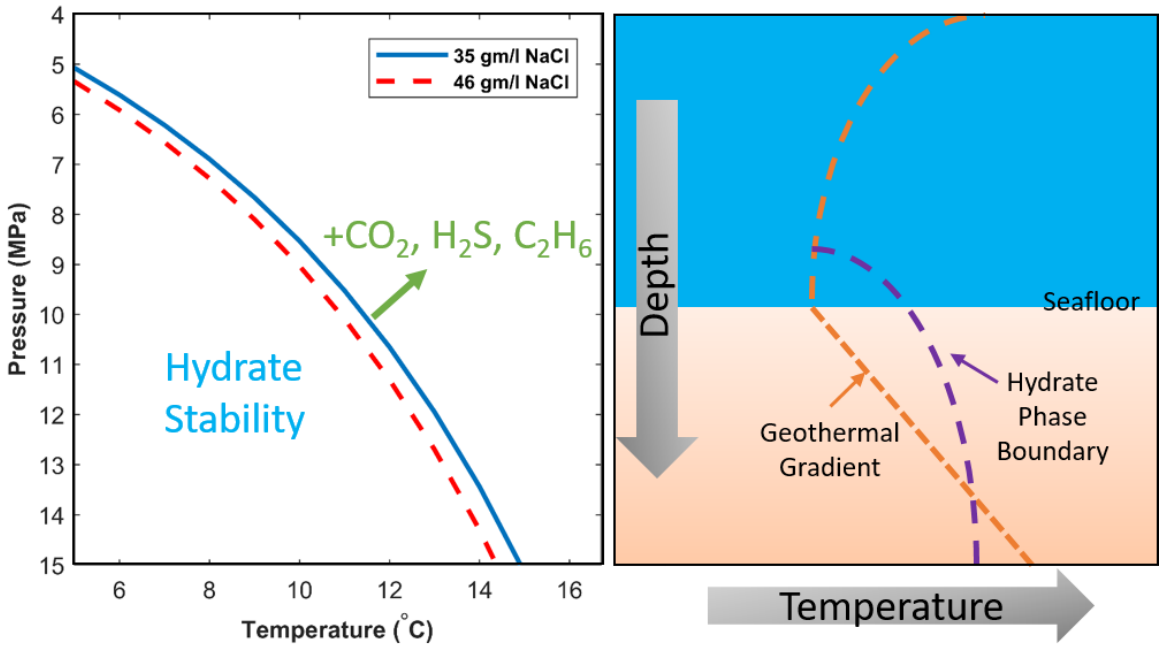

Figure 1.1 Left, methane hydrate phase boundary for two pore water salinities, calculated using Tohidi et al., (1995). Green arrow shows the direction in which the phase boundary would shift if other hydrocarbon gases forms hydrate. Right, conceptual diagram showing typical gas hydrate phase boundary in marine settings

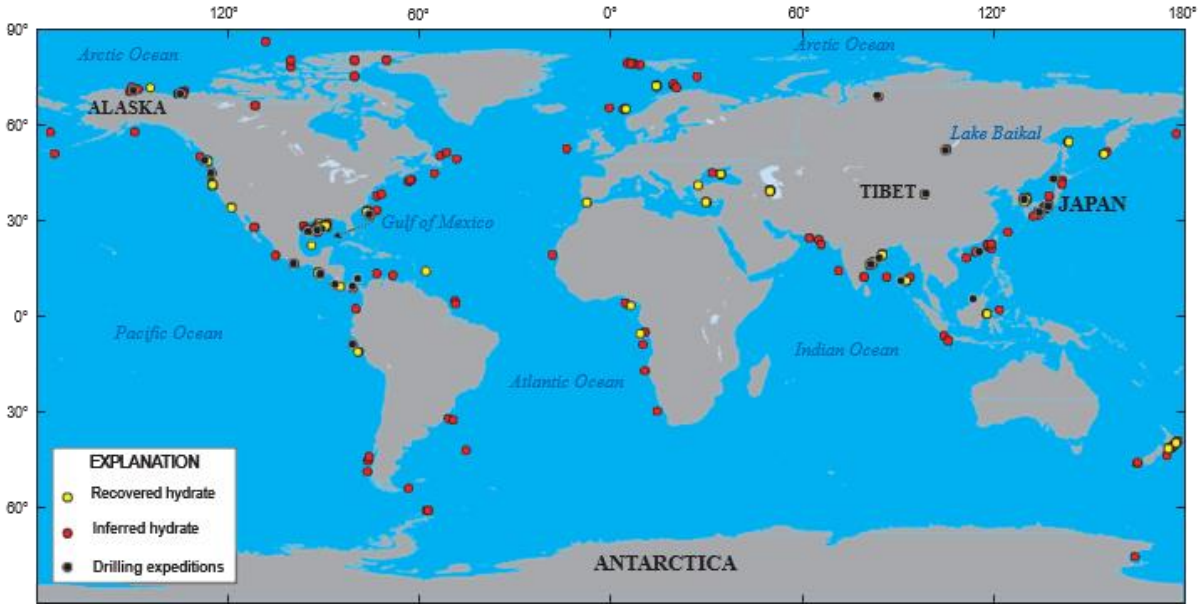

Figure 1.2 Distribution of known and inferred locations of gas hydrate around the world. Red dots show the locations where hydrate has been inferred from geophysical data, yellow dots show the locations where hydrate has been recovered and black dots mark the location of hydrate drilling expeditions (Ruppel, 2018).

1.2 Initial research

Initial research into gas hydrates started as a scientific curiosity when they were first formed in the laboratory in 1778 by Joseph Priestley (1790, p.359). In 1934, Hammerschmidt determined that gas hydrates were blocking gas transmission lines at temperatures above the ice point (Hammerschmidt, 1934) . This discovery led to the recognition of the importance of hydrate to industry, and it was the beginning of the extensive research on hydrate. Oil and gas wells always produce undesired water alongside hydrocarbons. These can form hydrate that may plug transmission lines, causing costly production stoppages, sometimes for as long as months, in large pipelines (Sloan, 2011). Such hydrate formation can also cause safety concerns if the blockage leads to pipe blowouts (Sloan, 2011). Safety concerns also remain during hydrate plug removal, during which large amounts of gas trapped in the hydrate can be released (Sloan, 2011). This thesis will focus on natural gas hydrates and we will not discuss further hydrate research related to pipeline flow assurance.

In 1963, Makogon provided evidence for the existence of natural hydrate from the analysis of thermodynamic conditions in the Markhinskaya gas well in Yakutia, Russia (Makogon, 1981). The first seafloor gas hydrates were recovered almost a decade later from 6.5 m below the seafloor in the Black Sea in water depths of about 2000 m (Yefremova and Zhizhchenko, 1974). A useful summary of early worldwide distribution (inferred and sampled) of gas hydrates is given in Table 1 (Kvenvolden et al., 1993). Several gas hydrate drilling campaigns have been carried out to date and more are planned in near future (Figure 1.3).

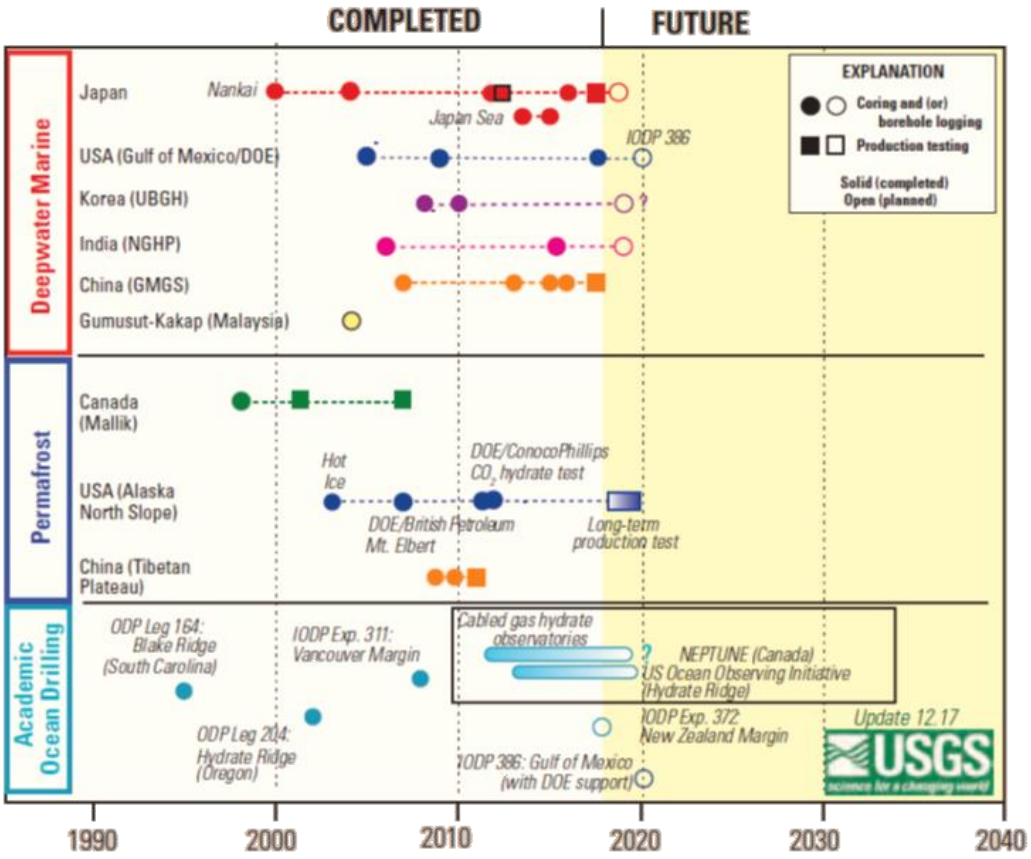

Figure 1.3 Timeline showing past and future coring and drilling of natural gas hydrates up to late 2017 compiled by USGS. After Ruppel, (2018). Please note that this figure does not show all the locations where hydrate has been drilled or cored. DOE refers to the U.S. Department of Energy. ODP refers to Ocean Drilling Program. IODP refers to the Integrated Ocean Drilling Program up to 2013 and thereafter the International Ocean Discovery Program. UBGH refers to the Ulleung Basin Gas Hydrates project, Korea. NGHP refers to the National Gas Hydrates Project, India. GMGS refers to the Guangzhou Marine Geological Survey, China.

1.3 Relevance of natural gas hydrates

1.3.1 Energy

Several independent estimates have shown that a large fraction of the Earth's fossil fuels are stored in the form of gas hydrates. Estimates vary widely between about 10^{15} to 10^{18} m^3 at standard temperature and pressure, compared to known conventional gas reserves estimated to be 8.2 x 10^{12} to 1.86 x 10^{14} m^3 (Boswell and Collett, 2011; Council, 2016; Klauda and Sandler, 2005; Kvenvolden, 1999; Milkov, 2004). The predominant gas in natural hydrate is methane (Kvenvolden,

1993), hence seafloor hydrate is a relatively clean fossil fuel resource. Some maritime nations are investigating the potential use of offshore hydrate reserves to meet rising energy demands while helping to offset CO_2 emissions during the transition to renewable energy in future. Even though all types of sediment can host gas hydrate, hydrate-bearing sands presently offer the most commercially attractive hydrate reservoirs, whether on the seafloor or in terrestrial permafrost regions (Boswell and Collett, 2011). This is because of the relatively high porosity and permeability of reservoir sands, which make gas extraction more feasible.

A number of countries, including the USA, Japan, India, China, Korea, Germany and others, have national programs for studying the industrial production of natural gas from hydrates. However, safe and efficient methane production from hydrate reservoirs remains a major technical challenge. Potential techniques of gas recovery include hydrate dissociation by depressurization, thermal stimulation and inhibitor injection (Collett, 2003; Dallimore et al., 2005; Holder et al., 1984), as well as CO_2-CH_4-exchange (Lee et al., 2003; Ohgaki et al., 1996; Schicks et al., 2011).

In 2002, pilot drilling, characterization and production testing of permafrost hydrate-bearing sands was concluded in the Mallik Well in Canada (Dallimore et al., 2005). Several hydrate production tests have been conducted across the globe since then, providing new insights into the nature and occurrence of gas hydrate and associated gas production challenges (Figure 1.2). An offshore methane hydrate production test was successfully conducted in 2013 at the Nankai Trough, offshore Japan, although it had to be stopped after few days due to excess sand production (K. Yamamoto et al., 2014).

1.3.2 Environmental impact

Methane is a potent greenhouse gas that is 20 times more effective at retaining atmospheric heat than carbon dioxide. Additionally, methane oxidizes to carbon dioxide in about a decade, which then continues to impact climate for many millennia (Archer and Brovkin, 2008). As methane hydrate is only stable at low temperature and high pressure, changes in sea level and temperature can cause hydrate to dissociate. Large scale methane release can have enhance warming through positive feedbacks (Archer and Buffett, 2005), although there may be a delay between methane dissociation and its release to the atmosphere/ocean floor which would limit such positive feedback (Minshull et al., 2016). The release of methane can also accelerate ocean acidification (Biastoch et al., 2011) and de-oxygenation (A. Yamamoto et al., 2014), and affect climate if large amounts of methane reaches the atmosphere (Kvenvolden, 1993), although this scenario is unlikely in deeper waters (McGinnis et al., 2006). There is some evidence that connects gas hydrate dissociation to past events of global climate change. For example, isotopic evidence of a 2 to 3 ‰ decrease in $\delta^{13}C$ has been used to describe the connection between the Paleocene–Eocene Thermal Maximum

(PETM; ~55.6 Ma) and a voluminous release of methane from gas hydrate contained in marine continental sediments (Dickens, 2011; Dickens et al., 1995). Similarly, carbon isotope evidence also suggests that episodic methane release due to hydrate dissociation contributed to late Quaternary climate change (Kennett, 2003). Hesselbo et al. (2000) have attributed hydrate dissociation to a Jurassic ocean anoxic event and Jahren et al. (2001) linked it to a severe period of global warming in the Mesozoic. Some methane plumes are also currently present at the ocean floor (Andreassen et al., 2017; Bünz et al., 2012; Darnell and Flemings, 2015; Smith et al., 2014; Westbrook et al., 2009) and could be due to hydrate dissociation or escape of free gas from below the gas hydrate stability zone. Andreassen et al. (2017) reported a cluster of km-scale blow out craters in the seafloor of Barent Sea. They suggest that these craters are formed by abrupt release of methane from hydrate dissociation, implying potential dissociation of subglacial gas hydrate reservoirs beneath contemporary ice sheets in the future.

When considering methane hydrate dissociation due to global temperature change, how much of this dissociated hydrate remains within the sediment and how much and how fast it is released into ocean needs to be considered. The timescale of response depends upon the effective permeability, the initial distribution of hydrate (Thatcher et al., 2013), and biogeochemical consumption (e.g., Boetius and Wenzhöfer, 2013). Thermohydraulic modelling suggests that even though hydrate dissociation could have been rapid during the PETM, the methane released from hydrate dissociation is modest and could take hundreds to thousands of years to reach the ocean floor, with up to half the dissociated methane remaining within marine sediments or the seafloor (Minshull et al., 2016).

1.3.3 Slope stability

Formation of a sufficient concentration of solid hydrate in sediments significantly increases their strength. Hydrate dissociation leads to the replacement of solid hydrate with gas and water, which generally reduces sediment strength. Massive hydrate dissociation, either due to changes in sea level and/or temperature or due to manmade activity (drilling, pipe lines, etc.,) may lead to seafloor instability (e.g., Pauli et al., 2003; Sultan et al., 2004).

1.4 Quantification

To properly assess the potential impacts of gas hydrates in nature, it is important to obtain accurate estimates of the amount and distribution of *in situ* gas hydrate. Global Estimates of the amount of gas stored in gas hydrates vary widely over three orders of magnitude, from 10^{15} to 10^{18} m^3 (at standard temperature and pressure) (e.g., Kvenvolden, 1999; Milkov, 2004; Klauda and Sandler,

2005; Boswell and Collett, 2011). Such global estimates are an important and necessary initial step in the understanding of natural gas hydrate systems and their implications. However, as revealed by several recent field-tests (Figure 1.2, 1.3), natural gas hydrate occurs under a wide range of conditions. Gas hydrates are known to occur at the seafloor to depths of more than 3000 m below sea-level, within and below permafrost, at temperatures ranging from sub-zero to more than 20 ^{o}C, and at concentrations from 1% to more than 90% of the host sediment's pore space (Collett et al., 2009). Such profound differences have significant implications for both the potential gas production from gas hydrates and how gas hydrates may respond to any given change in the natural environment.

1.4.1 Hydrate morphology

Hydrate morphology refers to the habit of hydrate within the sediment matrix. Broadly, hydrate can be divided into two basic types: sediment grain displacing or pore-fluid displacing (disseminated hydrate within the sediment pore space) (e.g., Holland et al., 2008). Once a hydrate grain fills the available space in a given sediment pore, its growth is constrained by the presence of the sediment grains. Further growth can occur either by displacing the sediment grains or by invading neighbouring pores. This depends on the balance between the local effective pressure and the capillary pressure developed by the hydrate grains (Dai et al., 2012) .

In the literature, sediment grain displacing is also referred to as "grain displacing". The main feature of sediment grain displacing hydrate is that it pushes sediment grains apart, creating hydrate volumes that are bigger than the size of the sediment pores in the form of veins, layers, and lenses of hydrate. The sediment grain displacing morphology commonly exists in the case of finer sediment grain sizes such as clay (Table 1 in Dai et al., 2012) . The morphology can be either (a) nodules or chunks with grains displaced in all directions, or (b) veins and lenses with grains displaced in particular directions.

On the other hand, pore fluid displacing hydrate grows only within the sediment pores. Most pore-fluid displacing natural hydrate has been observed in borehole cores of coarse-grained silty or sandy layers such as those from the NGHP-1 Well (Collett et al., 2015) and IODP Exp. 311 (Riedel et al., 2010). In this thesis, we perform experiments on sand and sandstone to study pore-fluid displacing hydrate.

Pore-fluid displacing hydrate can be sub-divided into cementing and non-cementing morphologies (e.g., Ecker et al., 1998). The cementing morphology forms when hydrate bonds or coats intergranular contacts (e.g., Ecker et al., 1998). Non-cementing hydrate forms when hydrate grows away from the sediment grains contacts (e.g., Ecker et al., 1998). The cementing morphology has a

much greater effect on the elastic properties of hydrate-bearing sediments when compared to the non-cementing morphology (Best et al., 2013; Ecker et al., 1998; Priest et al., 2009; Waite et al., 2004). However, the non-cementing morphology is thought to dominate natural hydrate systems and has been sampled or inferred at locations such as Mallik, Mackenzie Delta (Uchida et al., 2000), the Nankai Trough (e.g., Fujii et al., 2015), Alaminos Canyon, Gulf of Mexico (Boswell et al., 2009), and Mount Elbert, Alaska North Slope (Stern et al., 2011). Hydrate morphologies found at various sites around the world have been summarized by Holland et al., 2008 and Dai et al., 2012. If non-cementing hydrate grows in pores without bridging neighbouring sediment grains, then it is called (partially) pore-filling, or pore-floating. If it bridges neighbouring sediment grains then it's called frame supporting or load bearing (e.g., Waite et al., 2009). If the saturation of pore filling hydrate is high enough (25 - 40%) to completely fill the pore or bridge neighbouring sediment grains, then it becomes load bearing or frame supporting (Priest et al., 2009; Waite et al., 2009).

1.4.2 Exploration techniques

In general, the presence of hydrate tends to increase the seismic velocity (Helgerud et al., 1999) and electrical resistivity (Edwards, 1997) of the host sediments, depending on hydrate morphology and saturation. Seismic/sonic velocity and electrical resistivity anomalies in particular have been used to quantify hydrates locally in marine sediments. This is achieved through the choice of rock physics models that can relate the hydrate content to the measured geophysical properties (e.g., Edwards, 1997; Helgerud et al., 1999; Ecker et al., 2000; Collett, 2001).

Most natural gas hydrate deposits are inferred from seismic reflection data with detection of the high amplitude bottom simulating reflector (BSR) (e.g., Figure 1.4, Shipley et al., 1979). The impedance contrast between gas hydrate bearing sediments above and water or gas bearing sediments below gives rise to the BSR, with opposite polarity to that of the seafloor. The BSR corresponds to the base of the gas hydrate stability zone, which often mimics the seafloor and may crosscut stratigraphic horizons (e.g., Shipley et al., 1979). Hydrates have also been found in the absence of a clear BSR in seismic data (e.g., Holbrook et al., 1996; Wood and Ruppel, 2000); this may occur if the hydrate bearing sediments do not have enough acoustic impedance contrast (Holbrook et al., 1996). Double BSRs have also been reported in some locations (Andreassen et al., 2006; Foucher et al., 2002). Sometimes, hydrate bearing sediment layers above the BSR show low reflection amplitudes compared to sediments below the BSR, known as "blanking effect" (Lee et al., 1993). Some studies associate blanking to the reduction of impedance contrast due to cementation of sediments by hydrate (Lee et al., 1993), while others suggest it is caused by lithological homogeneity (Holbrook et al., 1996). The blanking effect depends on both the nature of the sediment and hydrate saturation (Chand and Minshull, 2003). While BSRs are helpful in

identifying gas hydrate, quantification of the hydrate deposit is not possible solely with the observation of BSR. Generally, hydrate content is estimated from the increase in seismic P wave velocity (V_p)(compared to background velocity) obtained from inversions of multi-channel seismic streamer data (e.g., Singh et al., 1993). A high resolution multi-channel seismic streamer system has also been used for hydrate quantification (Jegen et al., 2014; Petersen et al., 2010). It is often difficult to have accurate estimates of hydrate content from V_p alone, especially at low hydrate saturation (e.g., Ecker et al., 2000; Lee et al., 1996). Additionally, the presence of coexisting gas with hydrate makes hydrate quantification from V_p more difficult as gas reduces V_p (Lee and Collett, 2006). Arrays of Ocean Bottom Seismometers (OBS) have enabled P- and S- wave measurement, as they are in direct contact with seafloor and so provide additional constraints on hydrate quantification (Kumar et al., 2007; Petersen et al., 2007; Westbrook et al., 2008). The presence of gas has also been identified from a decrease in P-wave velocity (e.g., Guerin et al., 1999; Schnurle et al., 2004; Lee and Collett, 2006; Fohrmann and Pecher, 2012).

Sub-seabed electrical resistivity can be measured using borehole logging (e.g., Miyakawa et al., 2014) or marine controlled source electromagnetic (CSEM) methods (e.g., Weitemeyer et al., 2006). Edwards (1997) was the first to use CSEM for hydrate studies. The advantage of CSEM over borehole logging is that it allows resistivity measurements without disturbing the sediments, although borehole resistivity logs are often used to ground truth CSEM data. While the current CSEM technique cannot provide the detailed structural information of seismic methods, it can provide an independent measure of hydrate saturation (Schwalenberg et al., 2010a; Weitemeyer et al., 2006). An example of CSEM based gas hydrate identification is shown in Figure 1.5. It may also be capable of identifying hydrate in areas where no BSR can be identified (Yuan and Edwards, 2000).

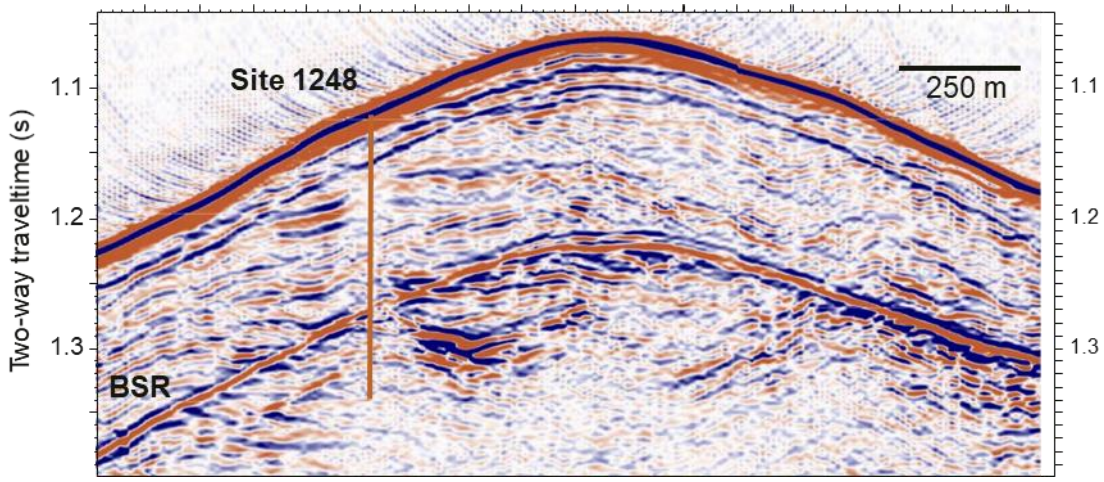

Figure 1.4 An example of an inferred Bottom Simulating Reflector from 2D seismic reflection data collected at the Hydrate Ridge, offshore Oregon, USA. “Site 1248” marks the location of IODP drilling (Shipboard Scientific Party, 2003).

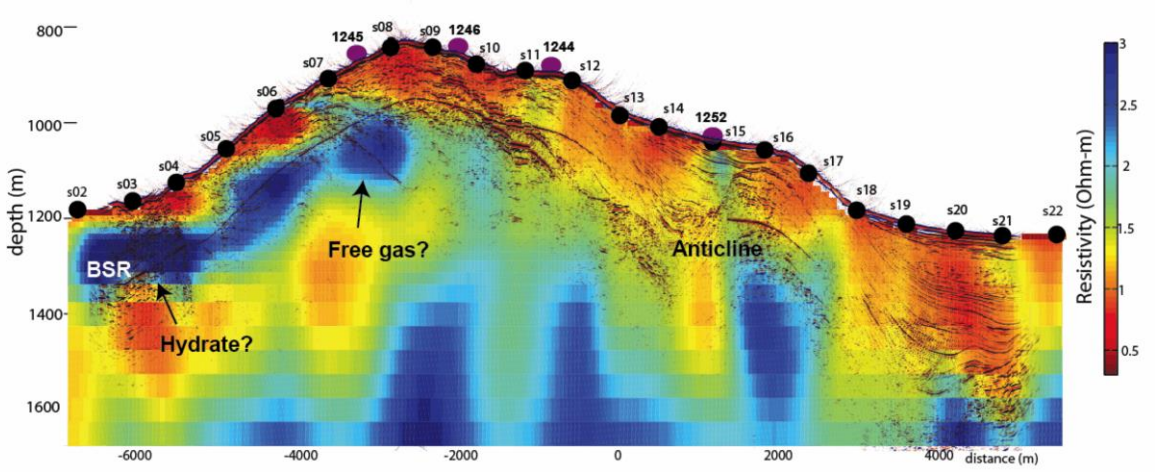

Figure 1.5 An example of CSEM data inversion collected from Hydrate Ridge, offshore Oregon, USA. The BSR obtained from reflection seismic data is also overlaid on the inversion. Note that both hydrate and free gas show high resistivity, and the high resistivity area below the seismic BSR is gas (Weitemeyer et al., 2010).

Hydrate content is often estimated from the increase in electrical resistivity compared to background sediments with no hydrates (e.g., Weitemeyer et al., 2006; Lee and Collett, 2008; Schwalenberg et al., 2010; Hsu et al., 2014). The challenge with the resistivity (both logging and CSEM) method is that both gas and hydrate are resistive compared to conductive sea water (e.g., Lee and Collett, 2008). As discussed above, even though seismic data may be generally useful in detecting/identifying the base of a gas hydrate deposit, it is generally difficult to unambiguously quantify hydrate deposits from seismic data alone as they may not always have distinctive seismic signatures. So collocated seismic and CSEM studies have been recently done, with CSEM being more sensitive to saturation of hydrate or gas and seismic providing high resolution structural information (Attias et al., 2016; Goswami et al., 2015; Schwalenberg et al., 2017, 2010b). Gas bearing sediments can be identified by high resistivities and low P-wave velocities, whereas hydrate bearing sediments have high resistivities and high P-wave velocities.

1.4.3 Discrepancy between elastic and electrical quantification

Ideally, hydrate saturation estimates from elastic and electrical method should match. However, some field studies show discrepancies between the hydrate saturations derived from resistivity and seismic/sonic methods (Table 3.1). This difference is a potential source of uncertainty in the carbon inventory stored in hydrate, as well as in resulting assessments of well stability and methane production from hydrate reservoirs that rely on geophysical remote sensing. Some researchers have associated this discrepancy to the coexistence of gas and hydrate, as the presence of gas can reduce the seismic velocity of sediments but not the electrical resistivity (e.g., Lee and Collett, 2006;

Miyakawa et al., 2014; Attias et al., 2016). The presence of co-existing hydrate and gas within the gas hydrate stability zone (GHSZ) has been inferred in several locations but remains open to interpretation. Recently, joint interpretation of CSEM and seismic data indicated a range of possible saturation values for coexisting gas in the GHSZ offshore Norway (Attias et al., 2016; Goswami et al., 2015).

1.4.4 Rock physics models

Accurate quantification of *in situ* methane hydrates from geophysical datasets depends on rock physics models that can relate hydrate content to measured geophysical properties (e.g., Archie, 1942; Best et al., 2013; Chand et al., 2006; Ecker et al., 2000, 1998; Helgerud et al., 1999). Such models are hampered by our limited understanding of the effects of hydrate content and distribution, along with sediment type, porosity, permeability, and pore fluid salinity, on the measured seismic and electrical properties (Waite et al., 2011). These models often require various assumptions about hydrate morphology (e.g., Ecker et al., 1998) and the micro structure of hydrate such as inclusions (e.g., Best et al., 2013; Marín-Moreno et al., 2017). These assumptions need testing. For example, Chand et al. (2004) compared 4 different elastic velocity models and used these to calculate velocities of two field studies of natural hydrates (Mallik 2L-38 well and ODP leg 164 Blake Ridge). They showed that the models gave different variations of velocity with hydrate saturation, although the ranges were similar and the variations of velocity with porosity and clay content were different.

The P and S wave velocities of sediments hosting cementing hydrate are significantly higher than those of the sediment without hydrate, even for low hydrate saturations below approximately 40% (e.g., Priest et al., 2009, 2005; Waite et al., 2009). In contrast, sediments hosting pore- floating hydrate with saturations below approximately 25–40% do not show significant changes in P and S wave velocities (Priest et al., 2009; Waite et al., 2009; Dai et al., 2012). This is because the hydrate is suspended within the water, and hence only increases the bulk modulus of the effective pore fluid (Ecker et al., 1998). For pore-floating hydrate saturations above 25–40%, hydrate starts bridging sediment grains and the elastic frame moduli and associated P and S wave velocities progressively increase (Dai et al., 2012; Waite et al., 2009). However, current economically exploitable hydrate-bearing sand reservoirs are likely to have hydrate saturations above 40% and thus unlikely to present, initially, a pore-floating hydrate morphology habit. Even in this case, when hydrate saturations fall below about 40% during methane gas production, pore-floating hydrate may become an important habit. Also, laboratory experiments on cementing and pore-bridging hydrate show that repeated cycles of hydrate dissociation and formation tend to create a pore-filling distribution in an excess water environment (Choi et al., 2014). This behaviour is also likely to

occur during production because of hydrate reformation. P and S wave attenuation may be used as an alternative indirect geophysical parameter to estimate hydrate saturation (Best et al., 2013; Guerin and Goldberg, 2002; Priest et al., 2006) and is an attractive alternative, especially in pore-filling hydrate-bearing reservoirs where traditional P and S wave velocity methods are not effective.

While there have been extensive studies on the effect of hydrate on elastic wave velocity of hydrate-bearing sediments, the number of studies on elastic wave attenuation are relatively few (Best et al., 2013; Chand and Minshull, 2004; Dewangan et al., 2014; Dvorkin and Uden, 2004; Guerin and Goldberg, 2002; Marín-Moreno et al., 2017; Priest et al., 2006; Rossi et al., 2007; references in Waite et al., 2009). Attenuation is the process by which a part of the mechanical wave energy is lost inside the propagating medium, leading to a reduction in wave amplitude and frequency content (Toksöz and Johnston, 1981). Attenuation is generally much more challenging to measure than velocity as corrections must be made for geometric spreading and impedance mismatches in spatially heterogeneous media (Huang et al., 2009). Sonic logs from the Mallik 5L-38 well showed that significant apparent attenuation can be caused by imperfect source coupling to the geological formation (Lee and Waite, 2007). Apart from measurement difficulties, interpretation of attenuation measurements is made more difficult by multiple coexisting energy loss mechanisms that are likely to be present in hydrate bearing sediments (Best et al., 2013; Chand and Minshull, 2004; Marín-Moreno et al., 2017; Matsushima, 2006). Adding potential confusion to complexity, some studies suggest that hydrate reduces attenuation in sediments (Dewangan et al., 2014; Dvorkin et al., 2003a; Westbrook et al., 2008), while others suggest it increases attenuation (Dvorkin and Uden, 2004; Guerin and Goldberg, 2002; Pratt et al., 2005; Matsushima, 2006; Priest et al., 2006; Sun et al., 2016). This is likely due to different attenuation mechanisms and unconstrained measurements (e.g., spatial averaging of several heterogeneous materials dictated by measured volume resolution). Moreover, traditionally, attenuation models have treated wave velocity and attenuation independently (Lee, 2006) which potentially contravenes the Kramers-Kronig relations of causality (e.g., Mavko et al., 1998) and may lead to predictions of unphysical behaviour. There are few gas hydrate rock physics models which do not treat velocity and attenuation independently (Guerin and Goldberg, 2005; Marín-Moreno et al., 2017). There is clearly scope for further studies into the elastic wave attenuation of hydrate-bearing sediments.

Rock physics models for calculating hydrate saturation from electrical resistivity often use the increase in resistivity of hydrate bearing sediments compared to background sediments with no hydrates. Electrical conduction in sediments can be divided into pore fluid conduction and surface conduction (e.g., Bussian, 1983; Revil and Glover, 1998; Waxman and Smits, 1968). Surface conduction can be negligible compared to pore fluid conductivity in the presence of high

conductivity pore fluid and the absence of clay rich sediments (e.g., Simandoux, 1963; Waxman and Smits, 1968; Clavier et al., 1984; Revil et al., 1998). Generally, gas hydrate saturation estimation from electrical resistivity use Archie's empirical equations (Archie, 1942) to calculate pore water saturation (e.g., Weitemeyer et al., 2006; Lee and Collett, 2008; Schwalenberg et al., 2010; Hsu et al., 2014). Archie's equations only account for pore fluid conductions and other modified equations (e.g., Simandoux, 1963; Waxman and Smits, 1968) may be used when surface conductions are significant. While these equations are empirical, there are several effective medium models for electrical conductivity that potentially account for the effect of important parameters like grain-shape distribution, grain alignment, shalyness (a review of such effective models is given in Gelius & Wang, 2008). Another class of models are based on joint elastic and electrical properties (Carcione et al., 2007; Han et al., 2011a) which has been recently applied to gas hydrate studies (Attias, 2017; Ellis, 2008). The advantage of joint elastic and electrical rock physics models over individual elastic or electrical models is similar to the collocated CSEM and seismic studies of gas hydrates discussed in Section 1.4.2.

1.4.5 Need for laboratory studies and limitations

The effects of hydrate on geophysical properties of sediments are difficult to understand unambiguously from natural samples alone because of spatial averaging and lack of information of the sub-surface. Moreover, using samples of natural hydrate-bearing sediments for laboratory studies of geophysical and geomechanical properties is often challenging because: a) coring is technically difficult and requires expensive drill ships with autoclave sampling capability; and b) absolute preservation of *in situ* conditions is not currently possible (Tulk, 1999), e.g., *in situ* pressures can be preserved, but not temperature. Hence, controlled laboratory experiments on synthetic hydrate samples offer a viable alternative approach to gain insight into the physical properties of hydrate-bearing sediments. Synthetic hydrate samples allow potentially the full range of hydrate saturations and morphologies to be explored for different sediment types, although laboratory methods have their own challenges.

All laboratory rock physics experiments must address the issue of upscaling from laboratory scale to field scale. Even though laboratory experiments help to understand the effects of hydrate from the micro to centimetre or meter scale, the geophysical properties estimated by field-scale surveys are impacted by additional factors, such as complex averaging of heterogeneity at the scale of the survey and artefacts introduced through data inversion. Reservoir geometry and thickness also affect field measurements. Natural gas hydrates are often found in a mixture of sediments, such as alternate layers of sand and mud, whereas laboratory experiments are generally done on one sediment type. In such a case, rock physics models can be used to upscale laboratory findings to

field scale, with certain limitations. A composite medium approach can also be applied for upscaling to field scale. The composite medium can be defined as a heterogeneous region of the subsurface consisting of component volumes (layers) with varying lithologies, porosities, or pore fluids. The rock physics models for gas hydrates also show that pore scale hydrate morphology can affect the bulk properties. For example Ecker et al. (2000) showed that the location of hydrate at grain contacts or away from grain contacts can affect the bulk elastic wave velocities. Best et al. (2013) showed that inclusions in hydrate could affect the bulk attenuation measurements at the seismic frequency range. Rock physics models that use laboratory measurements also face certain challenges in determining valid relationships to use at the field-scale, but with proper parameterization this is possible. For example, the rock physics model of Chand et al. (2006) was able to predict/match both laboratory measurements and field scale measurement at the Mallik gas hydrate well. Archie's equations (Archie, 1942) for estimating pore water saturation from electrical resistivity, developed originally in the laboratory for sand, has been applied to several field studies with appropriate changes in parameters (e.g., Collett et al., 2003; Miyakawa et al., 2014; Shankar and Riedel, 2011; Weitemeyer et al., 2011, 2006). Some laboratory experiments also try to increase the sample size, to have better understanding of upscaling issues. For example, the Large Reservoir Simulator (LARS) for resistivity tomography and gas production studies of gas hydrate bearing sand has a diameter of 0.45 m and a length of 1.35 m (Priegnitz et al., 2015). The Pulse tube system at National Oceanography Centre, Southampton for P wave velocity and attenuation measurements has a sample size of 70 mm diameter by 0.66 m length. While these example show that laboratory studies have been helpful in the understanding of field scale measurements (e.g., Gregory, 1977), researchers must consider the pertinent upscaling issues (averaging, data collection and its effects, rock physics parameters, etc.). The rock physics models also generally require parameters that are site- and case specific. Both laboratory and fields studies help to calibrate and constrain these parameters.

Thus, there is a great need for extended laboratory studies of gas hydrate-bearing sediments in order to understand the effect of hydrate on geophysics properties. This knowledge is needed in turn to calibrate and constrain the theoretical rock physics models on which geophysical data inversions rely, with the limitation of appropriate upscaling from laboratory to field scale.

1.5 Methods

Each science chapter of this thesis is written as an independent research paper, and hence each includes its own methods section. In this section, to orient the reader, I provide an overview of the

main methods I used in this thesis, and compare these methods with other existing methods. I also refer the reader to the relevant thesis sections for more information.

1.5.1 Laboratory gas hydrate formation

Gas hydrate formation needs the hydrate former (CH_4, C_2H_6, CO_2, etc.) to be in contact with water at hydrate stability conditions. Laboratory hydrate formation methods aim to imitate aspects of natural hydrates as far as possible. Laboratory formation methods can be broadly grouped into those using dissolved gas or free gas. In the former methods, gas dissolved in pore water is used for hydrate formation, while in the latter; a free gas phase is introduced into the pores with water to form hydrate. The solubility of methane is very low and so forming significant hydrate saturation from dissolved methane is challenging and has had limited success (Spangenberg et al., 2005; Winters et al., 2003). Buffett & Zatsepina (2000) showed that they could make CO_2 hydrate from dissolved gas without a free gas phase, as the solubility of CO_2 is higher than that of CH_4. Tohidi et al. (2001) attempted to form methane hydrate from dissolved methane, but were unsuccessful. Tohidi et al. (2001) also made hydrate from dissolved carbon dioxide, although they used a micromodel of etched glass to observe the process, rather than sediment samples. Spangenberg et al. (2005)succeeded in forming methane gas hydrate out of solution by flowing water containing dissolved methane into a “sediment” made from glass beads. Spangenberg and Kulenkampff managed to achieve hydrate saturations of 95% of the pore space in 55 days. Recently, Priegnitz et al. (2015) used this method to have 89.5% hydrate saturation in a sand sample in 73 days. This method also suffers from the additional problem of clogging of the pore fluid pipe; hydrate can form near the fluid inlet pipe, where methane concentration is highest. Also, this method gives poor control on the hydrate distribution (Priegnitz et al., 2015).

To overcome these limitations, laboratory studies have been conducted by forming hydrate from the free gas phase. The undissolved/free gas methods can be further subdivided into excess gas and excess water method based on the dominant and limiting phases in the sample pore space. In the excess gas method, the limiting phase is water and dominant phase is gas. In the excess water method, the limiting phase is gas and dominant phase is water. Excess gas methods causes preferential growth of hydrate at grain contacts (cementing morphology), producing a large increase in sediment strength and wave velocities, even at low hydrate saturations of the order of 3 – 5% (e.g., Priest et al., 2005; Stoll & Bryan, 1979; Waite et al., 2004). Comparison of such results to natural hydrate systems is problematic, as natural hydrates are mainly non-cementing (Section 1.4.1).

Hydrate growth initiates at the contact between gas and water (Tohidi et al., 2001). In the excess gas method, when the water saturation is low, water tends to coat the grains, concentrating at

grain contacts, or bridges adjacent grains; hence, a proportion of the resulting hydrate forms at the grain contacts, giving the cementing morphology. In the excess water method, as the water saturation in the sample pore space increases, the hydrate formation shifts into the pore space, resulting in pore-floating or pore bridging morphology (Priest et al., 2009; Tohidi et al., 2001). Another approach used to form non-cementing hydrate is to firstly form hydrate using the excess gas method and then pump methane saturated brine into the sample converting the cementing hydrate to non-cementing hydrate (Waite et al., 2011). Rydzy (2014) showed the transition of hydrate growth at grain contacts to away from grain contacts into the pore space with increase in water saturation; hence, we use a high brine saturation of >80% in this work. The excess water method can be achieved by either firstly injecting methane gas or brine into a dry sample, as long as the water is the dominant phase in the pores. We chose to firstly inject water, as we wanted the water to wet the sample and allow enough time for the water to distribute within the sample before injecting gas. An earlier study by Ellis (2008) also used the excess water method in the same experimental setup, and firstly injected gas; electrical resistivity distribution measurements showed that more hydrate formed in one corner of the sample, opposite the fluid inlet port. As the fluid inlet port in our experimental setup is at the bottom of the sample, firstly injecting gas and then injecting water is likely to push the gas to top of the sample. This could have happened also if hydrate moved up, as water was being constantly pushed into the sample from below to maintain pressure. Ellis (2008) measured electrical resistivity distribution using a 2D method, so we could not be sure if the high resistivity was distributed along the height of the sample or only on the top. We chose to firstly inject water and then gas, allowing enough time for water to distribute in the sample before gas injection. This is thought to be similar to natural hydrate systems with gas charging from below the gas hydrate stability zone. The hydrate formation method is described in Chapter 3 and Chapter 4 showing changes in pressure temperature and ultrasonic velocity along with hydrate formation.

Some hydrate formation studies use carbon dioxide and tetrahydrofuran (THF) instead of methane (e.g., Malone, 1990; Pearson et al., 1986; Tohidi et al., 2001). The solubility of carbon dioxide is higher and it forms same Structure I hydrate as methane, also at lower pressures. THF has the advantage that it is much easier to form hydrate from solution, but it forms a Structure II hydrate. THF hydrate does not dissociate to a gaseous phase, meaning many production-related processes are difficult to study with THF hydrate. We choose to use methane, as methane is the most abundant hydrate forming gas in nature and our aim is to compare the properties of the laboratory formed hydrate with that of natural hydrate.

1.5.2 Hydrate saturation calculations

Generally in both excess gas and excess water methods, it is assumed that the limiting phase is completely used up in hydrate formation and this assumption is used to calculate hydrate saturation (e.g., Priest et al., 2009, 2005; Sultaniya et al., 2015; Waite et al., 2004). This assumption is based on the thermodynamic phase stability conditions, which states hydrate forms when water and hydrate former (CH_4 in our case) are (i) in contact and (ii) in hydrate stability conditions. In experiments where the hydrate stability conditions are not met, the limiting phase may not be completely used up resulting is coexisting gas, hydrate and water, and the hydrate saturation calculations have had accounted for this (e.g., You et al., 2015). The limiting phase may not be completely used up, even if the hydrate stability conditions are met, if there is not physical contact between the remaining gas and water. Recent studies showed the porous nature of hydrate in both laboratory and natural samples (e.g., Murshed et al., 2008; Schicks et al., 2006; Suess et al., 2001) which could trap gas/water inclusions. Such trapped gas/water may not allow hydrate formation to continue until the limiting phase is completely used up. This may lead to error in saturation calculations with the assumption that the limiting phase is completely used up in hydrate formation. Therefore, we used the PT Method where we calculated continuously the saturations of the three phases (gas, brine, hydrate) from the changes in pore fluid pressure and temperature using the Peng–Robinson equation of state (Peng and Robinson, 1976). These measurements were done at one minute intervals during the experiments. One advantage of this method is that it assumes neither that hydrate formation continues until the limiting phase is exhausted (e.g., Sultaniya et al., 2015), nor that coexistence occurs only under three-phase stability conditions (e.g., You et al., 2015).

We also calculated hydrate saturation independently from electrical resistivity (ERT Method). The ERT method cannot differentiate between gas, ice and hydrate as all are resistive compared to brine. While ice is not present in our experiments or in marine hydrate, it is possible to have ice in permafrost hydrate or during fast pressurization that results in secondary ice formation. Use of ice in laboratory hydrate formation (e.g., Priest et al., 2009) also affects resistivity based saturation calculations.

The PT and ERT methods are described in detail in Chapter 3. In the synchrotron imaging experiment (Section 1.5.5), we used a density segmentation technique to calculate the saturation of gas, water and brine. Such a segmentation technique has been used in several hydrate-related studies (e.g., Hu et al., 2014; Kneafsey et al., 2007; Rees et al., 2011), including natural samples (e.g., Rees et al., 2011). The density segmentation method is discussed in Chapter 4.

1.5.3 Elastic wave measurements

Pearson et al. (1986) measured ultrasonic velocity of THF hydrate bearing sandstone sample including Berea using the pulse transmission method (Mattaboni and Schreiber, 1967), where the acoustic velocity is just the measured arrival time delay divided by the sample length. Several other ultrasonic velocity measurements of hydrate also use the pulse transmission method. For example, the GHASTLI system (Waite et al., 2004; Winters et al., 2003) also used ultrasonic pulse transmission for velocity measurements on sand sample with methane hydrate. Pulse transmission methods, generally are unable to measure attenuations. Our ultrasonic rig, uses reflections, the pulse echo method (Winkler and Plona, 1982), for P- and S-wave velocity and attenuations. A significant advantage of the pulse-reflection method over pulse-transmission is its repeatability and accuracy, particularly for attenuation measurements (McCann and Sothcott, 1992). For instance, signal amplitudes are sensitive to the coupling between the transducer and the sample, and a change in the thickness of the couplant would change this coupling, thereby affecting the pulse amplitude. This would introduce errors in the calculation of attenuation using the pulse-transmission method, as this requires two separate measurements (one on the rock and another on a reference material). The pulse- reflection method does not suffer from this drawback as measurements depend on a single measurement of the amplitudes from the top and base of the rock sample. As such, any variations due to the transducer couplant affect both reflections equally. The main limitation of our ultrasonic rig is that it was designed for rock samples and cannot accept loose sediments like sand although recently our system was adapted successfully to use loosely cemented sand samples (Falcon-Suarez et al., 2018).

While the laboratory methods generally use ultrasonic frequencies due to the limitation of sample size, field studies involve measurement at much lower seismic frequencies. Priest et al. (2005) developed the Gas Hydrate Resonant Column (GHRC), at the University of Southampton, which measures P and S wave velocity and attenuations at seismic frequencies. The velocities are determined from the frequency of vibration at resonance of the sediments using flexural and torsional excitation. Also the uncertainty in GHRC attenuations is relatively high (Best et al., 2013).

We used the custom built joint ultrasonic-resistivity rig (originally used by Ellis, 2008) which is capable of measuring both electrical resistivity and ultrasonic P-and S-wave velocity and attenuation. An overview of the system is given here as a detailed description of the entire system and its calibration can be found in McCann and Sothcott (1992), and in Best (1992).

In the pulse-reflection system, the sample is sandwiched between two cylindrical Perspex buffer rods of same diameter as the sample. Ultrasonic transducers (compressional or shear) transmit pulses through the buffer rod into the rock sample, and into the second buffer rod. The same

transducer is used to receive the reflections from the Perspex-rock interfaces, from which the velocity and attenuation can be calculated. A schematic of the system is shown in Figure 1.6.

We used a piezoelectric single combined P and S wave transducer (type D7105; nominal frequency of 1 MHz) so that measurements to be made sequentially without having to dismantle the rig to change the transducer. Another possible configuration is to use single P and S wave transducers and buffer rods on either end of the sample, but this would obstruct the fluid inlet pipe. The transducer was placed is a steel housing to protect it from high pressure. The entire system made up of the transducer's steel housing, the Perspex buffer rods, and the rock sample is enclosed in a rubber jacket and placed inside a high-pressure cell (Wykeham Farrance design). An Avtech pulse generator was used to provide pulses with frequency content between 100 to 1500 kHz. The pulses were displayed using a LeCroy digital oscilloscope and stacked 1024 times to improve the signal to noise ratio. The broadband signals were then saved onto a computer for subsequent velocity and attenuation calculation. Typical waveforms are shown in Figure 1.7.

The sources of error in the pulse-reflection system are well discussed by Best (1992). Absolute errors can arise due to sample swelling (e.g., in clay rich samples) or sample compression, resulting in a change in sample length which could lead to errors in measurements if not accounted for. The other errors are systematic, and include sample flatness and parallelism, side wall reflections, and diffraction effects. Sample flatness and parallelism is needed to ensure a good welded contact between the buffer rods and the samples when under pressure. Side wall reflections due to beam spreading could cause the pulse to reflect off the walls and interfere with the direct pulses. However, this effect is expected to be significant only at low frequencies in this present setup, and it is possible to calculate the lowest frequency where side wall reflections are not expected (Best, 1992). Diffraction effects, which also introduce errors in the pulse-reflection system are discussed below. The systematic errors were quantified by careful calibration using aluminium and brass samples, and it was found that velocity could be measured to an accuracy of ± 0.3% and attenuation to ± 0.2 dB/cm (see Best, 1992). Errors in calculations using the measured velocities or attenuations can be obtained by propagating the uncertainties in individual measured values (e.g., Taylor, 1997).

1.5.3.1 Diffraction (Beam spreading) corrections

The finite size of ultrasonic transducers causes diffraction. This wave interference effect causes phase and amplitude distortions, which are a function of the transducer radius, the wave frequency and path length (effective distance from the transducer). The effect of the phase distortion is an apparent decrease in travel time (thus higher velocity). The effect of the amplitude distortion due to diffraction is an apparent amplitude reduction, leading to higher values of attenuation than the true value.

Papadakis (1972) formulated attenuation and phase corrections for ultrasonic pulses from a transducer of radius *a*, at a distance *z* from the source, and a wavelength of λ with corresponding velocity *V* and frequency *f*. He defined a normalised distance *S* as:

$$S = \frac{\lambda z}{a^2} = \frac{zV}{a^2 f}, \tag{1.1}$$

The diffraction corrections Δt (μs) and Δα (dB/cm) for the travel times and attenuation coefficients respectively are

$$\Delta t = \frac{\beta(S_B - S_T)}{2\pi f}, \tag{1.2}$$

$$\Delta\alpha = \frac{\alpha(S_B - S_T)}{2L}, \tag{1.3}$$

Where β is the diffraction phase shift, L is the Berea sample length, S_T and S_B are the normalised distances for the top and base reflections, respectively.

The diffraction corrected travel time and attenuation coefficients are $\Delta t = t' + \Delta t$,

$$\Delta\alpha = \alpha' - \Delta\alpha, \tag{1.4}$$

where t' and α' are measured travel time and attenuation coefficient, respectively.

Benson and Kiyohara (1974) tabulated values of β and Δα using the above equations of Papadakis (1972). Although these corrections are strictly valid for P-waves propagating through an infinite medium, the same corrections have been shown to be reliable for S-waves (Best, 1992, McCann and Sothcott, 1992).

1.5.3.2 Velocity and attenuation calculations

The velocity and attenuation was measured using the method of North, (2017). The ultrasonic measurement system may be described by a 1D frequency domain transmission line model (Figure 1.6)

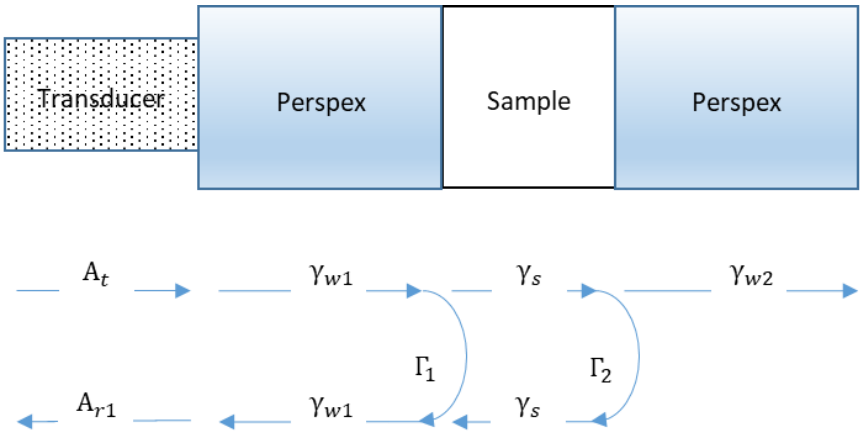

Figure 1.6 Signal flow diagram of the pulse echo ultrasonic measurement. After North et al., (2013)

Where the complex transmit and receive functions of the transducers are denoted by A_t and A_{r1} respectively. The propagation coefficients of the Perspex, adjacent to the sample, are given by:

$$\gamma_{w1} = e^{-i\omega\frac{d_1}{v_w}} \tag{1.5}$$

$$\gamma_{w2} = e^{-i\omega\frac{d_2}{v_w}}, \tag{1.6}$$

where ω is angular frequency, d_1 and d_2 are the lengths of the Perspex buffer rods and $v_w$is the complex velocity of the Perspex buffer rods or delay lines. The imaginary component of velocity describes loss, and no material is a perfect lossless medium. However, Perspex is approximated by a real number in this work because the loss is so low as to be negligible over the 5 cm length of the of delay line. The propagation coefficient of the sample, γ_s, is given by:

$$\gamma_s = e^{-i\omega\frac{d_s}{v_s}}, \tag{1.7}$$

where d_s is the length of the sample and v_s is the complex velocity of the sample. The reflection coefficient, Γ_1, is given by;

$$\Gamma_1 = \frac{z_s - z_w}{z_s + z_w}, \tag{1.8}$$

where the acoustic impedances, z_s and z_w, of the sample and delay line perspex respectively are defined as:

$$z_s = v_s\rho_s, \tag{1.9}$$

$$z_w = v_w\rho_w, \tag{1.10}$$

$$\Gamma_2 = -\Gamma_1. \tag{1.11}$$

If the first and second reflections from the proximal and distal boundaries of a sample are sufficiently temporally compact they may be separated/isolated by time domain gating yielding the time series $\tilde{r}_1$ and $\tilde{r}_2$.

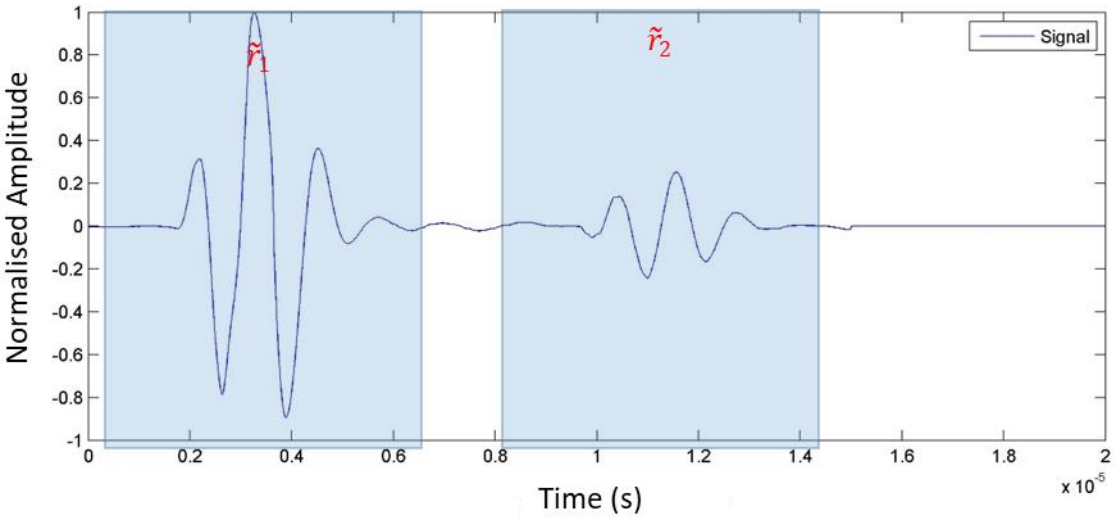

Figure 1.7 A typical reflected time domain series showing the two windowed portions of signal used in the pulse echo technique. From North et al., (2013)

The gated time domain series $\tilde{r}_1$ and $\tilde{r}_2$ may then be transformed to the frequency domain via a Fast Fourier Transform (FFT), yielding the complex frequency dependent variables R_1 and R_2, representing the first and second reflections respectively. From the 1D transmission line model (Figure 1.6) R_1 and R_2 are given by:

$$R_1 = A_t A_{r1} \gamma_{w1}^2 \Gamma_1,$$

and (1.12)

$$R_2 = A_t A_{r1} \gamma_{w1}^2 \gamma_s^2 (1 - \Gamma_1^2) \Gamma_2. \tag{1.13}$$

Winkler and Plonar (1982) derived an approximate explicit solution for the frequency dependant complex velocity (velocity and attenuation) of a sample from the ratio R_2/R_1. They stated that this approximate solution is strictly valid only for plane waves reflecting off perfectly bonded plane interfaces between elastic materials; as laboratory measurements deal with inelastic materials, the reflection coefficients will be complex. So we used the method of North (2017), which uses complex reflection coefficients.

$$R_2/R_1 = -\gamma_s^2(1-\Gamma_1^2) = R_m, \tag{1.14}$$

where R_m is a measured quantity from which complex velocity is derived. In this work, we solve for the complex sample velocity numerically using non-linear optimisation. The objective function H that is minimised and given by:

$$H = [\mathbf{Re}(S_{obs} - S_{mod})]^2 + [\mathbf{Im}(S_{obs} - S_{mod})]^2 \tag{1.15}$$

The minimisation routine used in this work is the Nelder-Mead simplex implementation in MatLab. An example of the optimised real and imaginary components of S and the resultant vale of the error function H are shown in Figure 1.8.

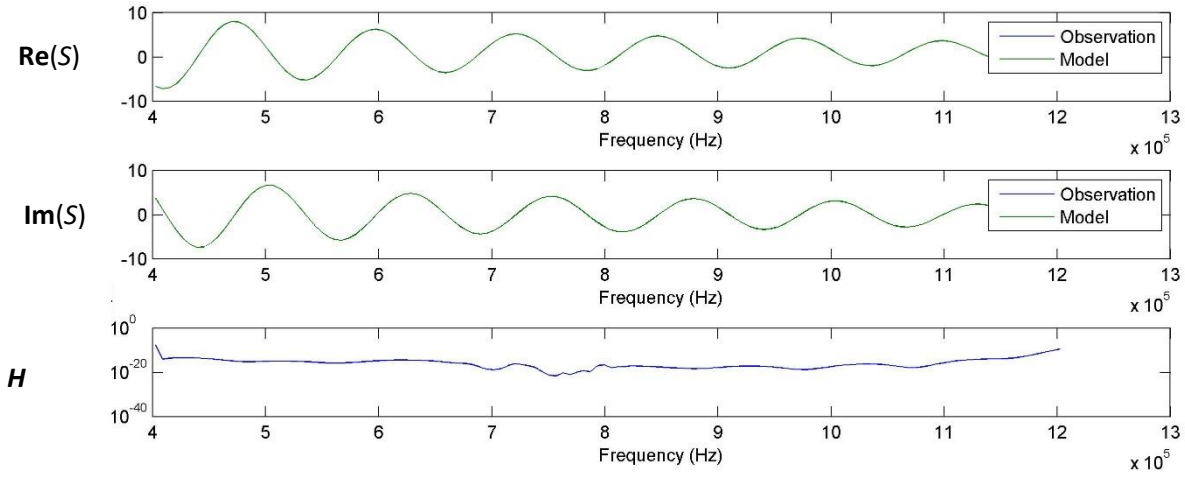

Figure 1.8 Top and middle pane show the real and imaginary components of spectral ratio S (Equation 1.14). The bottom pane shows the error function, H, value after optimisation. From North et al. (2013)

1.5.4 Electrical resistivity measurements

Pearson et al. (1986) measured the electrical resistivity of THF hydrate bearing sandstone samples including Berea using a two-electrode system (Collett and Katsube, 1973). In the two-electrode system, the sample is sandwiched between two planar electrodes. This configuration would give a single resistivity value for the bulk sample. This two-electrode system is still in use by researchers today (Du Frane et al., 2015; Lim et al., 2017). To measure resistivity distribution in the sample, more electrodes need to be used. One such modification is to add two more ring electrodes equally spaced along the height of the sample, along with two electrodes on the top and bottom of the sample (e.g., Spangenberg et al., 2005). A similar four-electrode system is also used in the GHASTLI rig (Waite et al., 2004; Winters et al., 2003). As this four electrode system has the electrodes along the length/height of the sample, it gives a one dimensional distribution. Ellis (2008) used a 12-pin

electrode system radially distributed around the sample and was able to obtain a planar resistivity distribution. Here we choose to use radially distributed electrodes in two planes to obtain a 3D tomography. Our electrical resistivity tomography (ERT) system uses 16 electrodes (8 electrodes in 2 rings) and gives more detailed information on the resistivity distribution (North et al., 2013). The LARS system has a much bigger sample size (210 litre volume) with similar multi-layer electrodes (375 electrodes arranged in 25 circular rings with 15 electrodes in each ring) and was recently used for gas hydrate experiments on sand (Priegnitz et al., 2015). The limitation of LARS is that elastic wave velocity measurements is still under development (Spangenberg et al., 2017).

The inner rubber sleeve in our rig that prevents direct contact between the mineral oil used as confining fluid and the rock sample is perforated by 16 stainless steel electrodes (2 rings of 8 electrodes each) for electrical resistivity tomography (ERT) measurements. North et al. (2013) developed this ERT system at the National Oceanography Centre, Southampton, which is a typical tetra-polar electrode configuration Electric Impedance Tomography (EIT) measurement system (Boone and Holder, 1996). This electrode configuration overcomes measurement artefacts caused by electrode polarization (Mazzeo, 2009; Olhoeft, 1985; Schwan and Ferris, 1968). The system comprises an arbitrary function generator, voltage controlled current source, current and voltage measurement devices and a multiplexer to connect source and measurement devices to the 16 measurement electrodes. A 80 Hz sinusoidal input current was used to minimise total measurement time. The same electrodes are used for both current injection and boundary voltage probing. The measurement pattern of current injection and voltage probing electrodes used in this work is of the off- set adjacent type with an offset of 2 (North et al., 2013)). Current is injected, and voltage probed, between electrode pairs spaced 2 electrodes apart (Figure 1.10). For each current injection pair, 13 surface volt- age measurements are made between all the other pairs of offset electrodes in both rings that do not include a current injection electrode. Similar sets of 13 measurements are made with all offset electrode pairs carrying current during the measurement run. This results in 208 measurements. The measurement signal to noise ratio is increased by time domain averaging and frequency domain filtering of the current and voltage waveforms (16 times averaging and frequency filtering at 80 Hz with Fast Fourier Transform bin size of 0.5 Hz). A finite element algorithm Electrical Impedance Tomography and Diffuse Optical Tomography Reconstruction (EIDORS) package in Matlab (Polydorides and Lionheart, 2002) is used to retrieve the internal resistivity distribution from the measured voltages. North et al. (2013) discussed that current injection and measurement pattern can be altered which would affect the performance of the system, so we chose to use the same measurement pattern as used by North et al. (2013).

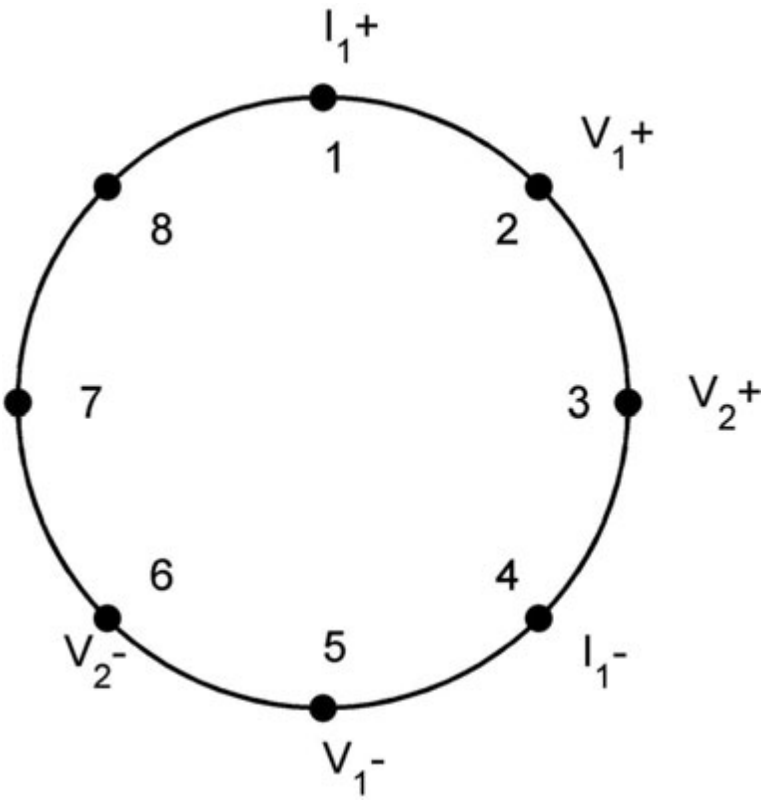

Figure 1.9 A schematic diagram electrode configuration for the top ring of 8 electrodes used for resistivity tomography. The position of the electrodes (numbered 1 to 8), the current injection electrodes, I_1+ and I_1-, and the voltage measurement electrodes for the first (V_1+ and V_1-) and second (V_2+ and V_2-) measurements. From North et al. (2013)

This system is suitable for heterogeneous rocks where it is difficult to obtain resistivity tomography without bias from sample selection and heterogeneity. North et al. (2013) showed that under typical operating conditions the non-systematic (noise) and systematic (component impedances and non-linear distortion) errors result in a resistance measurement error of ≤ 0.1% (1 - 500 Hz) for samples with a conductivity between 1 and 10^{-2} Sm^{-1}.

1.5.5 Pore scale hydrate imaging

Tohidi et al. (2001) imaged hydrate formation and dissociation in glass micromodel using optical microscopy in 2D. They provided time-lapse information on pore scale gas hydrate formation and dissociation mechanism and reported hydrate formation starts at the interface between water gas and not at the hydrophilic glass surface. They also showed the presence of water film between hydrate and glass micromodel. Optical microscope was also used to compare the hydrate morphology with different hydrate formation methods (Spangenberg et al., 2015, 2008). They showed that non-cementing hydrate forms when water is dominant pore phase with small gas bubbles. To increase the resolution, researchers have used more sophisticated conventional X-ray Computer tomography to observe both synthetic and preserved natural hydrate samples (Kneafsey

et al., 2007; Rees et al., 2011). To increase the resolution further synchrotron radiation X-ray computed tomography (SR-XCT) has been used to study both natural and synthetic hydrate (e.g., Chaouachi et al., 2015; Kerkar et al., 2014; Klapp et al., 2007; Murshed et al., 2008; Yang et al., 2016). For example, Murshed et al. (2008) used SR-XCT for 3D microstructure of preserved natural gas hydrates sampled from the Gulf of Mexico. Several researchers have stressed the need for time-resolved tomography (4D-tomography) to aid a better understanding of hydrate systems (Kuhs et al., 2004; Murshed et al., 2008). 4D SR-XCT have been used to study both natural and synthetic hydrate, but not for methane hydrate in sand with brine (Chaouachi et al., 2015; Kerkar et al., 2014; Yang et al., 2016). Kerkar et al. (2014) used methane hydrate with 5 w.t.% BaCl2 solution as the pore fluid in glass beads, while Chaouachi et al. (2015) and Yang et al. (2016) used xenon hydrate without any salt in sand. As our aim is study natural hydrate, we attempted to use methane hydrate in sand with 35gm/l NaCl solution. We used a custom built set up for 4D SR-XCT imaging on small (2mm diameter, 23mm length) sand samples, described in Chapter 4. Synchrotron imaging was performed at the TOMCAT Swiss Light Source (SLS) facility in Switzerland.

1.6 Thesis organization

1.6.1 Scope of the thesis

The aim of my PhD is to understand the effect of hydrate formation and dissociation on elastic and electrical properties of host sediments. Such insights will eventually help to improve our current knowledge of methane hydrates in natural systems, and also suggest ways to improve hydrate quantification methods using geophysical remote sensing.

I have tried to answer and gain understanding of the following important three questions:

1. How does methane hydrate morphology change in detail as hydrate grows inside porous rocks and sediments, and during dissociation, under excess water conditions typical of natural systems?
2. Can gas co-exist with hydrate under hydrate stability conditions, as suggested by some field studies?
3. What effect, if any, do hydrate morphology and co-existing gas have on elastic wave velocity and attenuation, and electrical resistivity?

With support from the supervisory team and other researchers, I conducted a series of hydrate formation and dissociation experiments at different differential pressures with measurements of electrical resistivity, and ultrasonic P and S wave velocity and attenuation. I calculated the continuous evolution of gas, hydrate and brine saturation during hydrate formation and

dissociation from pore fluid pressure and temperature observations. To understand the micro structural changes during hydrate formation and dissociation I performed time resolved (4D) synchrotron X-ray computed tomography of methane hydrate formation. I also contributed to the development of a rock physics model for understanding the effect of hydrate content and morphology on elastic wave velocity and attenuation at different measurement frequencies.

1.6.2 Chapter outline

Each science chapter of this thesis (2, 3, 4 and 5) is written as an independent research paper with its own description of the relevant literature, methods, results and conclusions. These papers list several co-authors and hence I use the first person plural form in the text; I am the lead author of all papers except the one presented in Chapter 2.

In **Chapter 2**, we present a rock physics model for calculating frequency dependent velocity and attenuation of hydrate bearing sediments. We need to use such model to have a better understanding of the complicated behaviour of hydrate bearing sediments. This chapter addresses the point discussed earlier in Section 1.4, that there is scope for more rock physics models for understanding the effect of hydrate saturation and morphology on elastic wave velocity, and especially attenuation, of the hydrate bearing sediment. This model includes elastic wave energy losses caused by (i) squirt flow between fluid inclusions in hydrate and the pores, (ii) squirt flow between different aspect ratio pores, (iii) inertial motion of the frame with respect to the pore fluid (Biot's type attenuation), and (iv) gas bubble damping. This chapter was published in the Journal of Geophysical Research: Solid Earth (Marín-Moreno et al., 2017). I participated in the discussion for the development of the conceptual model for seismic attenuation generated by hydrate growth-related secondary porosity and associated micro squirt flow, based on my experience in laboratory formation of hydrates. I also contributed by running some models for various particular attenuation mechanisms to assess their different behaviours and by providing feedback to the manuscript.

In **Chapter 3,** we address the question of whether gas and hydrate can co-exist under hydrate stability conditions, and how relevant is the effect of such co-existing gas on hydrate quantification. As discussed earlier in Section 1.4.3, there has been speculation over coexisting gas and its effect on resistivity based hydrate quantification; we address those aspects in this chapter. We calculated continuously the evolution of gas, hydrate and brine saturation during hydrate formation and dissociation using thermodynamics from pore fluid pressure and temperature. Hydrate saturation was obtained independently from electrical resistivity. We also discuss possible mechanism for such co-existing gas. This chapter is in review with Journal of Geophysical Research: Solid Earth (Sahoo et al., 2018). I designed and did these experiments with help of Best and Minshull. I also analysed and developed the PT method with help of Marin Moreno and Best. I wrote the manuscript with

corrections by the co-authors. North and Falcon-Suarez helped me with the laboratory set up and conducting the experiments. Madhusudhan did the synchrotron imaging processing of the Berea sample.

In **Chapter 4**, we discuss the way hydrate morphology changes with saturation and how these changes relate to measurable geophysical properties. We use ultrasonic P and S wave velocities measured during hydrate formation in Berea sandstone, and link them to changes in hydrate morphology and saturation using the rock physics model of Marín-Moreno et al. (2017), presented in Chapter 2. We also use high resolution synchrotron imaging to visually observe changes in hydrate morphology and saturation during hydrate formation in Leighton Buzzard sand. We also use the imaging to verify co-existence of gas and hydrate and understand formation mechanisms. This chapter is in preparation for submission to a geophysical research journal. I designed and did these experiments with help of Best. North and Falcon-Suarez helped me with the laboratory set up and conducting the elastic wave experiments. Madhusudhan, North, Ahmed and I did the synchrotron imaging experiments. Madhusudhan and I processed and analysed the synchrotron imaging results. I wrote the manuscript with corrections by the co-authors.

In **Chapter 5**, we try to understand the complicated behaviour of elastic wave attenuation of hydrate bearing sediments. We discussed earlier, in Section 1.4.4, about the limited number of measurements and complicated nature of elastic wave attenuation of hydrate bearing sediments. We discuss the measured ultrasonic P and S wave attenuation at 450 – 800 kHz during hydrate formation in Berea sandstone. Again, we used the rock physics model of Marín-Moreno et al. (2017), presented in Chapter 2, to understand the dominant attenuation mechanisms at these measurement frequencies. I designed and did these experiments as part of my PhD with help of Best. North and Falcon-Suarez helped me with the laboratory set up and conducting the elastic wave experiments. I analysed the data and wrote the manuscript with help from Best, Marin-Moreno and Minshull.

In **Chapter 6**, I summarise the advances in knowledge resulting from the work presented in this thesis, and discuss their significance and wider implications.

Chapter 2 Theoretical modelling insights into elastic wave attenuation mechanisms in marine sediments with pore-filling methane hydrate

This chapter forms a published paper: Marín-Moreno, H., S. K. Sahoo, and A. I. Best (2017), Theoretical modelling insights into elastic wave attenuation mechanisms in marine sediments with pore-filling methane hydrate, Journal of Geophysical Research: Solid Earth, doi:10.1002/2016JB013577.

Abstract

The majority of presently exploitable marine methane hydrate reservoirs are likely to host hydrate in disseminated form in coarse grain sediments. For hydrate concentrations below 25-40%, disseminated or pore-filling hydrate does not increase elastic frame moduli, thus making impotent traditional seismic velocity-based methods. Here, we present a theoretical model to calculate frequency dependent P- and S-wave velocity and attenuation of an effective porous medium composed of solid mineral grains, methane hydrate, methane gas, and water. The model considers elastic wave energy losses caused by: local viscous flow both i) between fluid inclusions in hydrate and pores, and ii) between different aspect ratio pores (created when hydrate grows); the inertial motion of the frame with respect to the pore fluid (Biot's type fluid flow); and gas bubble damping. The sole presence of pore-filling hydrate in the sediment reduces the available porosity and intrinsic permeability of the sediment affecting Biot's type attenuation at high frequencies. Our model shows that attenuation maxima due to fluid inclusions in hydrate are possible over the entire frequency range of interest to exploration seismology (1-10^6 Hz), depending on the aspect ratio of the inclusions, whereas maxima due to different aspect ratio pores occur only at sonic to ultrasound frequencies (10^4-10^6 Hz). This frequency response imposes further constraints on possible hydrate saturations able to reproduce broadband elastic measurements of velocity and attenuation. Our results provide a physical basis for detecting the presence and amount of pore-filling hydrate in seafloor sediments using conventional seismic surveys.

2.1 Introduction

Methane stored in seafloor hydrate is a relatively clean fossil fuel resource that has the potential to ease the transition to renewable energy in future. Methane stored in hydrate-bearing sands presently forms the most commercially attractive hydrate reservoirs (Boswell and Collett, 2011), whether on the seafloor or in terrestrial permafrost regions. Natural hydrates hosted in sediments commonly exist in several forms: (i) disseminated hydrate grows freely in the pore space away from grain contacts and is known as pore-filling hydrate; (ii) hydrate contacting neighbouring mineral grains, known as load-bearing hydrate, is common for pore-filling hydrate saturations exceeding 25-40%; and (iii) hydrate forming cement between mineral grains, known as cementing hydrate (Figure 2.1; Waite et al., (2009)). In coarse grain deposits, hydrates are prone to exhibit a disseminated pore-filling habit (Zhao et al., 2015) for hydrate saturations below 40% when formed from dissolved methane (Spangenberg and Kulenkampff, 2006). Pore-filling hydrates have been directly observed and/or inferred from geophysical surveys in fine to coarse sands in locations such as Mallik, Mackenzie Delta (Uchida et al., 2000), the eastern Nankai Trough (Konno et al., 2015; Priest et al., 2015; Santamarina et al., 2015), the Ulleung Basin, East Sea of Korea (J Y Lee et al., 2013), the Okushiri Ridge, Japan Sea (Tamaki et al., 1990), Alaminos Canyon, Gulf of Mexico (Boswell et al., 2009), and Mount Elbert, Alaska North Slope (Stern et al., 2011; Winters et al., 2011). As such, pore-filling hydrate could account for a significant proportion of global seafloor- and permafrost-hosted methane hydrates.

While the stability field of natural hydrates is readily determined, the saturation of hydrate within it is not. Estimates come from direct sampling, well-log data, or remote geophysical data (e.g., Ecker et al., 1998; Ecker et al., 2000; Guerin and Goldberg, 2002; Matsushima, 2006; Weitemeyer et al., 2006; Westbrook et al., 2008; J Y Lee et al., 2013; Goswami et al., 2015; Konno et al., 2015). Good indirect estimates rely entirely in our conceptual understanding of how P and S-wave velocity and attenuation (M W Lee, 2002; Yun et al., 2005; Chand et al., 2006; Priest et al., 2006; Waite et al., 2009; Dai et al., 2012; Best et al., 2013), and electrical resistivity (Spangenberg, 2001; Spangenberg and Kulenkampff, 2006) relate to hydrate saturation and habit, and in the associated effectiveness of our models. The P and S-wave velocities of sediments hosting cementing hydrate, both when hydrate coats and cements grain contacts or when hydrate forms only at grain contacts, are higher than those of the sediment without hydrate because the hydrate contributes to support any pressure loading. This is reflected in an increase of the composite's bulk and shear moduli (Ecker et al., 1998) even for low hydrate saturations below ca. 40% (Priest et al., 2009; Waite et al., 2009; Dai et al., 2012). In contrast, sediments hosting pore-filling hydrate with saturations below ca. 25-40% do not show significant changes in P- and S-wave velocities (Priest et al., 2009; Waite et al., 2009; Dai et al., 2012) because the hydrate is suspended within the water and hence only increases the

bulk modulus of the effective pore fluid (Ecker et al., 1998). For pore-filling hydrate saturations above 25-40%, hydrate starts bridging sediment grains and the elastic frame moduli and associated P- and S-wave velocities progressively increase (Waite et al., 2009; Dai et al., 2012).

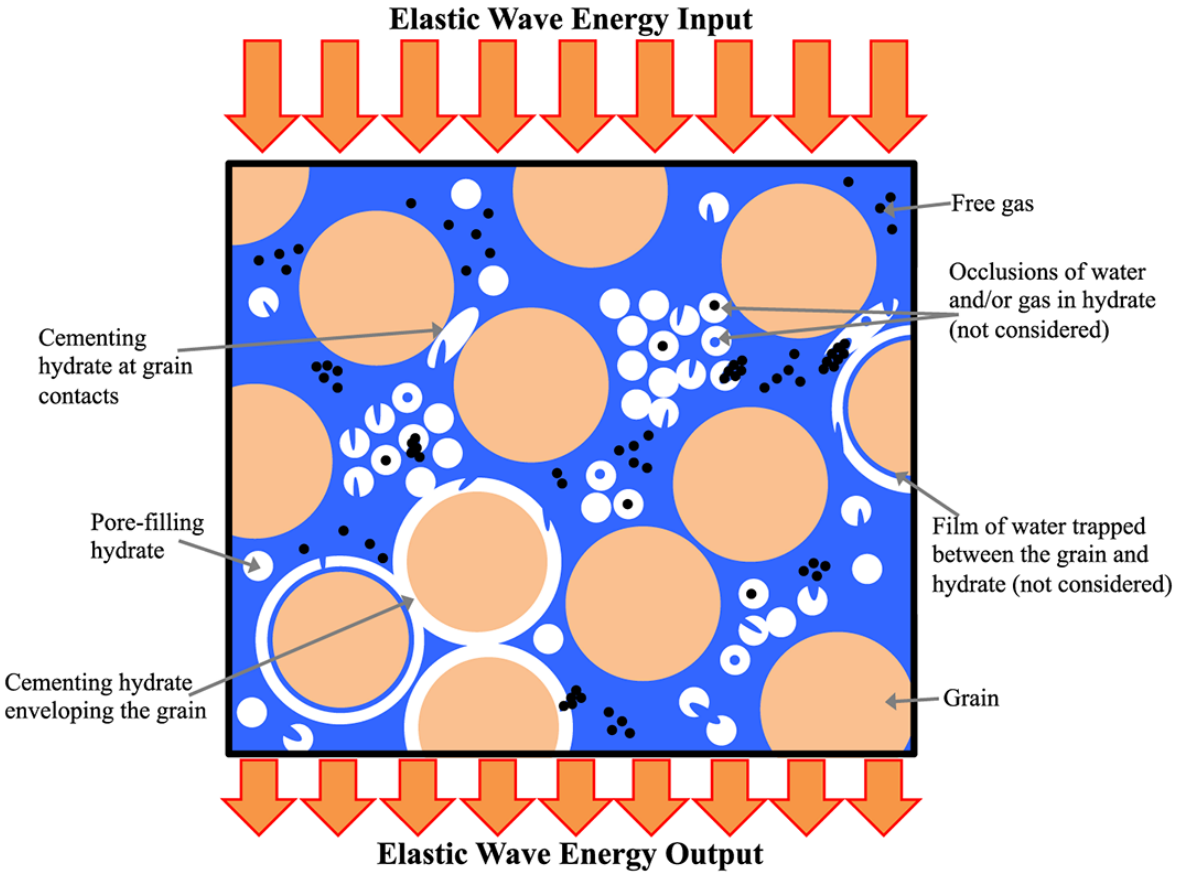

Figure 2.1 Idealized conceptual illustration of the micro-structure of hydrate-bearing sediments (not to scale).

P- and S-wave attenuation may be used as an alternative indirect geophysical parameter to estimate hydrate saturation (Guerin and Goldberg, 2002; Priest et al., 2006; Best et al., 2013) and it is indeed an attractive alternative especially in pore-filling hydrate-bearing reservoirs where traditional P- and S-wave velocity methods are not effective. However, current economically exploitable hydrate-bearing sand reservoirs are likely to have hydrate saturations above 40% and thus unlikely to present, initially, a pore-filling hydrate habit. Even in this case, though, sediment shearing occurs during hydrate production (Hyodo et al., 2013) and when hydrate saturations start to be less than ca. 40%, it is sensible to think that pore-filling hydrate may become an important habit. Also, laboratory experiments on cementing and load-bearing hydrate show that repeated cycles of hydrate dissociation and formation tend to create a pore-filling distribution in an excess water environment (Choi et al., 2014). This behaviour is also likely to occur during production because of hydrate re-formation.

In-situ measurements of elastic wave energy losses caused exclusively by the presence of hydrate in sediments are challenging because (i) it is difficult to isolate elastic wave energy losses within the sediment from elastic wave scattering in spatially heterogeneous media (Huang et al., 2009), and (ii) our understanding of the multiple energy loss mechanisms co-existing in hydrate-bearing sediments is still limited (Priest et al., 2006; Best et al., 2013). Here, to overcome the above limitations, we work with attenuation differences between the hydrate-bearing sediment and the host sediment without hydrate and present a novel approach, the Hydrate-Bearing Effective Sediment (HBES) model, to integrate state-of-the art understanding and models of attenuation mechanisms occurring in hydrate-bearing sands (Figure 2.2). Our method calculates frequency dependent P- and S-wave velocity and attenuation and includes elastic wave energy losses caused by (i) squirt flow between fluid inclusions in hydrate and the pores, (ii) squirt flow between different aspect ratio pores, (iii) inertial motion of the frame with respect to the pore fluid (Biot's type attenuation), and (iv) gas bubble damping (Figure 2.2). Other energy loss mechanisms possibly acting in gas hydrate systems but not implemented in our model may include, wave-induced fluid flow at the mesoscale (White, 1975) and wave-induced gas exsolution-dissolution (Tisato et al., 2015). The HBES model also considers how different hydrate habits affect both velocity and attenuation, and allows representing cases where methane gas co-exists with hydrate under hydrate stability conditions (Milkov et al., 2004; Lee and Collet, 2006; Paganoni et al., 2016). First, we validate our model with published experimental P- and S-wave velocities and attenuations of hydrate-bearing sediments, and then we illustrate the sensitivity of P- and S-wave velocities and attenuations to input parameters in sediments with pore-filling hydrate. We show that different hydrate-related attenuation mechanisms may act at different elastic wave frequency ranges.

2.2 The Hydrate-bearing effective sediment model

The Hydrate-Bearing Effective Sediment (HBES) model calculates frequency dependent P- and S-wave velocity and attenuation of hydrate-bearing sediments (Figure 2.2). Here we describe the main theoretical concepts in which the HBES model is based, but the detailed description and complete mathematical formulation is given in the supplementary information (Appendix A).

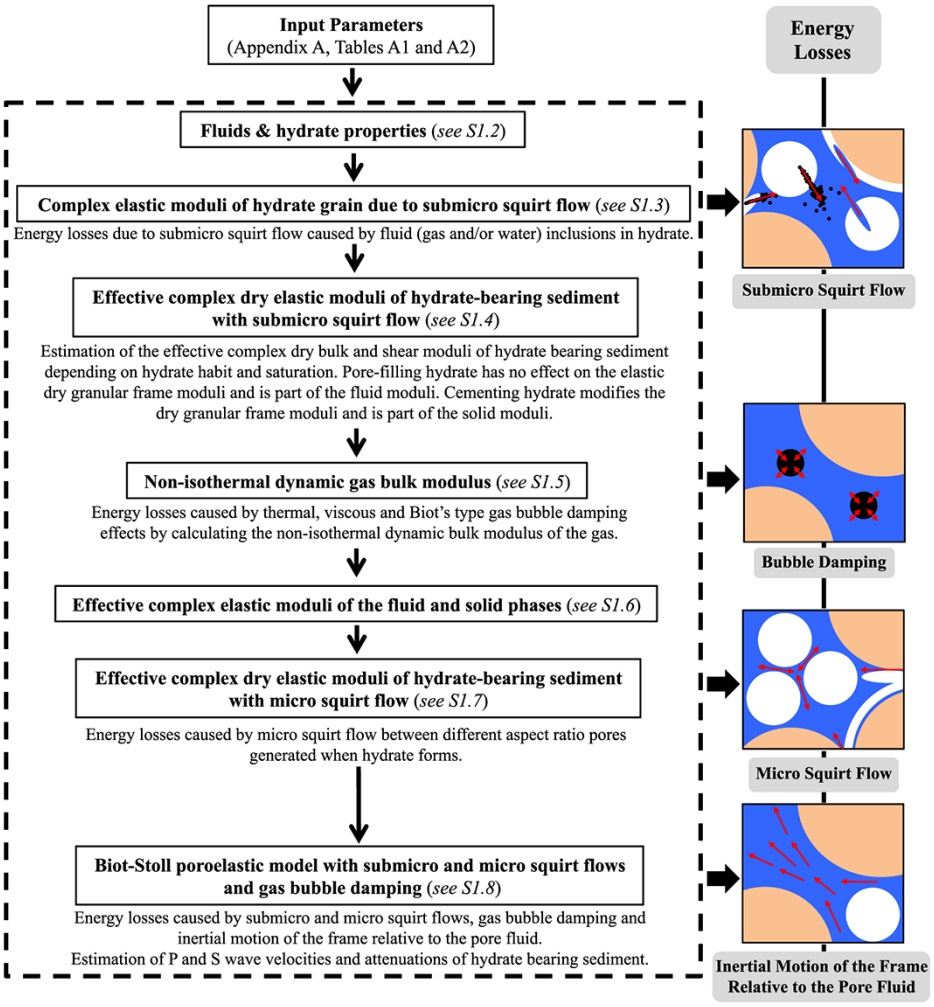

Figure 2.2 Workflow of the Hydrate-Bearing Effective Sediment (HBES) model. The idealized conceptual illustrations on the right show the different individual attenuation mechanisms (not to scale). The total energy loss in the sediment with hydrate is given by the contribution of each of the attenuation mechanisms. The text in italics at the end of each box indicates the section in the Appendix B with the detailed description of each procedure and its mathematical formulation.

Experiments on natural and synthetic hydrates show a micro-porous structure (Kuhs et al., 2004; Zhao et al., 2015), and hence hydrates can be understood as a compliant material, due to inclusions of water and/or gas, and with a behavior resembling that of clay minerals (Best and McCann, 1995; Leurer, 1997). Moreover, elevated P- and S-wave attenuations have been detected on hydrate-bearing sands (Guerin and Goldberg, 2002; Matsushima, 2006; Priest et al., 2006). Based on the above experiments and ideas, Priest et al. (2006) hypothesized that these elevated attenuations could be explained by (i) local viscous fluid flow (squirt flow) between low aspect ratio pore layers of water, bound to mineral grain surfaces when cementing hydrate forms, and the pores, and (ii) viscous squirt flow between connected low aspect ratio micro pores inside the hydrate grains and the sediment pores. Best et al. (2013) considered the attenuation due to the latter type of squirt

flow in their hydrate effective grain (HEG) model. They calculated the complex shear and bulk moduli of hydrate applying the formulation from Johnston et al. (1979) which was later adapted by Leurer (1997) and Leurer and Brown (2008) to represent squirt flow between the structural water of clay minerals one-sided connected to water in the pores. Best et al. (2013) adopted this formulation for fluid inclusions in hydrate, and substituted the clay mineral bulk and shear moduli for those of the hydrate; for simplicity, they assumed single aspect ratio fluid inclusions in hydrate completely filled with either methane or water. The new HBES model employs Best et al's. (2013) model framework and introduces: (i) pressure-temperature dependent density, bulk compressibility and viscosity of methane and water; (ii) the possible co-existence of one-side connected ellipsoidal water and gas inclusions in hydrate, in which each phase can occupy micro pores with different aspect ratios; (iii) local viscous squirt flow between two-side connected ellipsoidal pores generated when hydrate forms (defined as type-2 pores in the formulation; see Appendix B) and the initial pores, in which each hydrate habit can create a different aspect ratio pore and; (iv) wave-induced frequency dependent oscillating gas bubbles in a dilute gas-liquid mixture considering viscous, thermal and Biot's type damping (Smeulders and van Dongen, 1997).

To distinguish between the two local viscous squirt flows considered in the HBES model, here we use the term sub-micro squirt flow for that between fluid inclusions in hydrate and the pores, and micro squirt flow for that between hydrate-generated pores and the initial (e.g., pores of sand grain framework host) pores. First, we calculate the complex bulk and shear moduli of the hydrate grain considering sub-micro squirt flow, similar to Best et al. (2013), and introduce these into Ecker et al.'s (1998; 2000) formulation to obtain the complex dry elastic moduli of cementing and pore-filling hydrate-bearing sediment. Second, we calculate the non-isothermal frequency dependent complex bulk modulus of the gas to consider energy losses caused by gas bubble damping. Third, we calculate the effective complex moduli of the pore fluid and solid phases. As assumed by Ecker et al. (1998), pore-filling hydrate is treated as part of the pore fluid and does not modify the elastic moduli of the dry granular frame, but modifies the pore fluid bulk modulus. Therefore, the effective bulk modulus of the pore fluid can be complex and frequency dependent because sub-micro squirt flow and gas bubble damping generate a hydrate and gas, respectively, complex frequency dependent bulk modulus. The effective bulk and shear moduli of the solid phase can also be complex and frequency dependent due to sub-micro squirt flow in cementing hydrate. Fourth, we consider micro squirt flow by applying the formulation from Leurer (1997) and Leurer and Brown (2008) and (i) substitute the bulk and shear moduli of the clay mineral by the real parts of the effective complex dry frame moduli of hydrate-bearing sediment, (ii) use the real part of the effective complex bulk modulus of the pore fluid and (iii) assume two-sided connected and hydrate-generated ellipsoidal pores. We calculate the final effective complex dry elastic moduli of the

hydrate bearing sediment by assuming superposition of squirt flow mechanisms. This means that the imaginary parts of the effective complex dry frame moduli caused by sub-micro squirt flow are added to the imaginary parts caused by micro squirt flow. Finally, we introduce the final effective complex dry frame moduli and the effective complex bulk modulus of the pore fluid (water, gas and pore-filling hydrate) and solid (sediment grains and cementing hydrate) phases into the Biot-Stoll poroelastic model (Biot, 1956a; b; Stoll and Bryan, 1970) to calculate P- and S-wave velocity and attenuation.

2.3 HBES model performance: results

2.3.1 Comparison with experimental data

We used the experimental measurements of P- and S-wave velocity (V_P, V_S) and attenuation (Q_P^{-1}, Q_S^{-1}) presented by Priest et al. (2006) to evaluate and validate the performance of the HBES model. Priest et al. (2006) formed hydrate under excess-gas conditions (methane saturated pore space) using a resonant-column apparatus, and measured peaks in attenuation at hydrate saturations between 3-5% at seismic frequencies. They attributed these peaks to either squirt flow caused by monolayers of adsorbed water remaining at grain contacts when cementing hydrate forms (this mechanism belongs to our more general concept of micro squirt flow) or nano porosity/inclusions of methane and/or water in hydrate (here named as sub-micro squirt flow). Our model captures the location of the peak in both Q_P^{-1} and Q_S^{-1} at hydrate saturations below 5% when considering (i) the presence of methane and water inclusions in hydrate and (ii) that a fraction of hydrate grows at grain contacts and the initial fraction of pore-filling hydrate in the model decreases linearly with hydrate saturation, and thus cementing hydrate in contact with the grains increases accordingly (Figure 2.3). In these experiments, at 3 to 5% hydrate saturation, sand grains are cemented by hydrate (Priest et al., 2005), consistent with our assumed hydrate habit distribution (see table in Figure 2.3). This habit distribution also captures the change in slope of P- and S-wave velocity observed at hydrate saturations below 5% and the magnitude of seismic velocity change with hydrate saturation (Figure 2.3a).

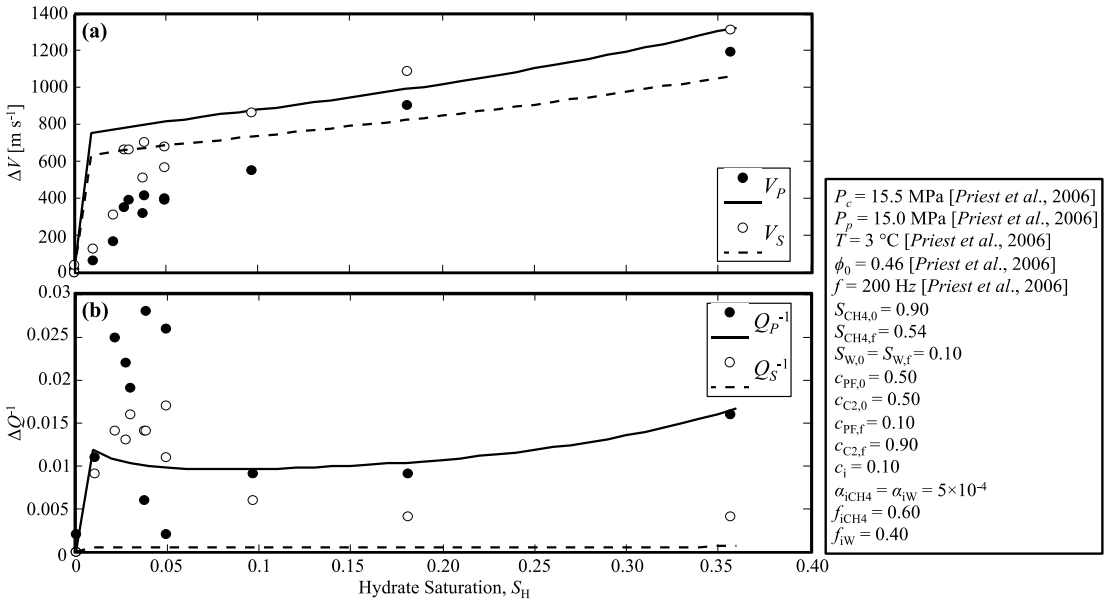

Figure 2.3 Comparison between measured values (dots) (Priest et al., 2006) and values calculated with the HBES model (lines) of P- and S-wave (a) water saturated velocity and (b) methane saturated attenuation, in sediment with hydrate relative to the values without hydrate. Modelled attenuation caused by sub-micro squirt flow and Biot's type global fluid flow, but the relative contribution from the latter at 200 Hz is negligible. Measured results correspond to the excess gas method and the P- and S-wave velocities were converted to water saturated samples using Gassmann's equation (Priest et al., 2006). The input parameters listed in the table and default input parameters are defined in Appendix A (Tables A1 and A2). The sub-scripts 0 and f in the table mean initial and final conditions.

The model suggests that Q_P^{-1} is more sensitive to the presence of hydrate than Q_S^{-1}, as also measured experimentally. However, it gives smaller increments in attenuation than those measured, especially for Q_S^{-1} (Figure 2.3b). Lower changes in Q_S^{-1} than in Q_P^{-1} due to sub-micro squirt flow caused by inter-crystalline water layers in clay minerals are also obtained by Leurer and Brown (2008). Discrepancies between measured and modelled attenuations may be explained by (i) other possible attenuation mechanisms acting at seismic frequencies and not considered in our model, such as wave-induced fluid flow at the mesoscale (White, 1975) and/or wave-induced gas exsolution-dissolution (Tisato et al., 2015) and (ii) the idealized nature of our analytical effective approach, including the geometries considered and their distributions. More notable, the model is able to capture the trend in observed Q_P^{-1} and Q_S^{-1} changes with hydrate saturation in the range between 0 to 35% (Figure 2.3b). We also tested if the observed changes in V_P, V_S, Q_P^{-1}, Q_S^{-1} could be caused by micro squirt flow only, but we were not able to obtain any sensible match to the data. Sub-micro squirt flow due to methane and water inclusions could partly explain the attenuation

behaviour observed in Priest et al. (2006) samples and, at seismic frequencies, may be the primary hydrate-related attenuation mechanism.

2.3.2 Elastic behaviour of sediments with pore-filling hydrate

Here we present model results for pore-filling hydrate-bearing sediments (see justification in the Introduction and Discussion sections) and for P-wave velocity and attenuation only. Similar to Leurer and Brown's (2008) results for sub-micro squirt flow caused by inter-crystalline water layers in clay minerals, we found that frequency-related changes in S-wave velocity and attenuation caused by pore-filling hydrate-generated squirt flow are smaller than those from P-waves, and are not discuss further here. To isolate intrinsic hydrate-related processes, we use the absolute difference between the P-wave velocity and attenuation of the sediment with pore-filling hydrate and those from the host sediment only.

The sole presence of pore-filling hydrate in the sediment reduces the porosity and intrinsic permeability of the sediment and these produce two opposite effects in the maximum P-wave attenuation at high frequencies. If the available porosity reduces, the surface contact area between the fluid in the pores and the solids increases. This results in higher attenuation values caused by higher viscous drag between the solids and global fluid flow (Biot's type attenuation mechanism) and a attenuation peak located at a frequency independent of pore-filling hydrate saturation. If the intrinsic permeability reduces, so does Biot's type attenuation (less global fluid flow), and the attenuation peak moves to higher frequencies (see inset in Figure 2.4). The net effect on attenuation depends on the rate at which intrinsic permeability decreases with porosity, and so with pore-filling hydrate saturation, which in our formulation is controlled by the n_{kPF} parameter, here assumed to be 2 (Appendix A Table 1, and Appendix B Eq. 23). In Figure 2.4, the increase in attenuation caused by the reduction in porosity dominates over the decrease caused by the reduction in intrinsic permeability, and so the attenuation increases with pore-filling hydrate saturation.

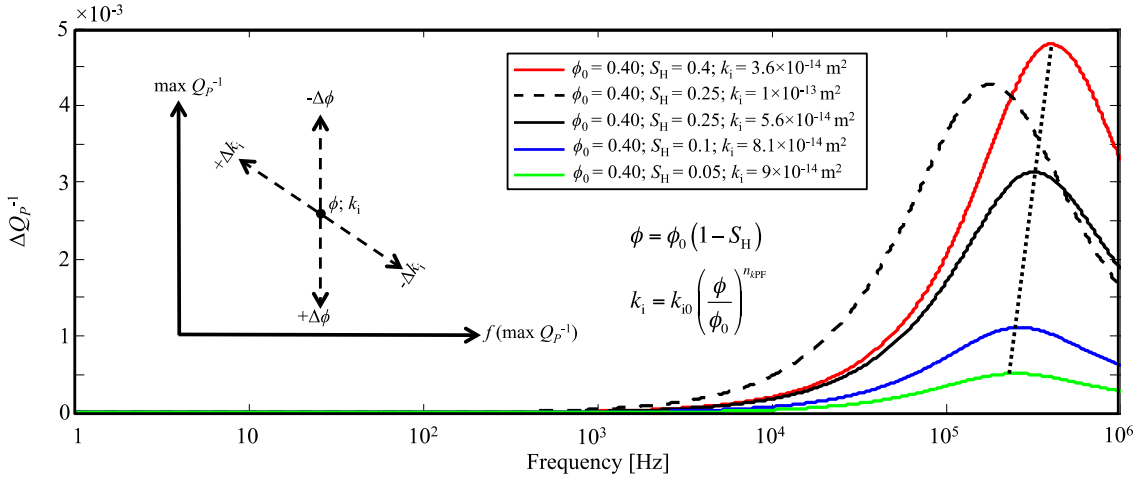

Figure 2.4 Variation in P-wave attenuation with frequency in sediment with pore-filling hydrate relative to the values without hydrate. Results for partially water saturated pores (S_w = 1- S_h). Attenuation caused by Biot's type global fluid flow, without considering hydrate-related squirt flow mechanisms. The black dotted line joining the attenuation peaks shows the translation of the peaks towards higher frequencies with the reduction in intrinsic permeability. The inset shows a conceptual diagram of how changes in intrinsic permeability and porosity affect the maximum attenuation and the frequency at which the maximum attenuation occurs. Input parameters are defined in Appendix A, Tables 1 and 2.

From a phenomenological perspective, the Kramers-Kronig relations state that any change in attenuation needs to be related with a change in velocity dispersion (e.g., Mavko et al., 2009). That is, larger attenuations are necessarily linked with larger velocity dispersions, and zero attenuation requires zero velocity dispersion. Our HBES model predicts frequency related changes in velocity at frequencies where attenuation changes also occur (Figure 2.5). In Figure 2.5b, attenuation peaks shown at seismic frequencies are caused by fluid inclusions in hydrate (sub-micro squirt flow) whereas at ultrasound frequencies they are caused by both the reduction in the available porosity due to pore-filling hydrate and the presence of different aspect ratio pores.

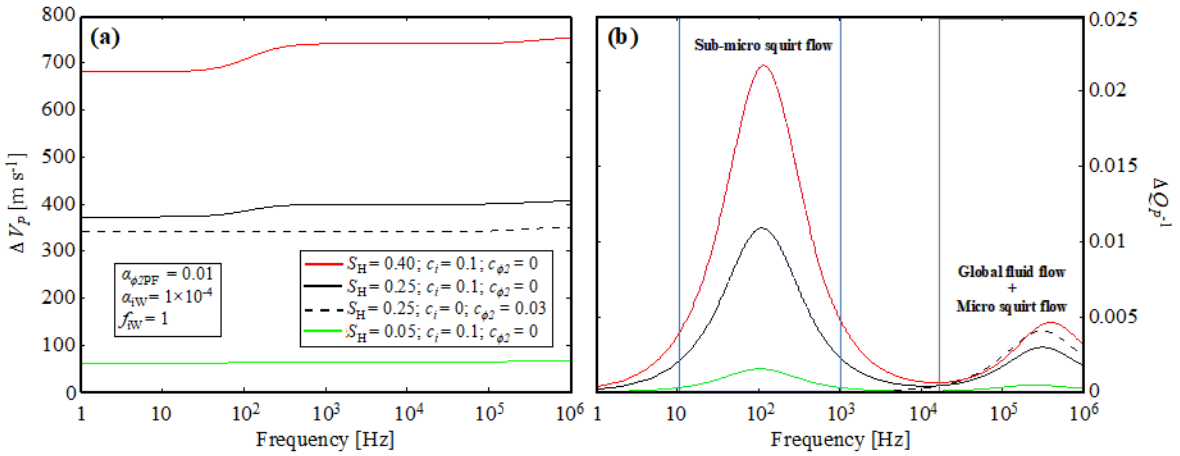

Figure 2.5 Variation in P-wave (a) velocity and (b) attenuation with frequency in sediment with pore-filling hydrate relative to the values without hydrate. Results for partially water saturated pores (S_W = 1- S_h). Attenuation caused by Biot's type global fluid flow and sub-micro and micro squirt flows. Input parameters are defined in Appendix A, Tables 1 and 2.

Attenuation maxima due to sub-micro squirt flow generated by fluid inclusions in hydrate occur over the whole frequency range, depending on both the aspect ratio and type of fluid in the inclusions (Figure 2.6a, b), whereas peaks due to micro squirt flow generated by different aspect ratio pores occur at sonic to ultrasound frequencies, independent of the aspect ratio of pores (Figure 2.6c). In our formulation, micro squirt flow is related with the composite's dry effective moduli. This means that micro squirt flow contributes to the attenuation generated by the global fluid flow in the pore network, and hence is more significant at high frequencies. This frequency distinction imposes further constraints on hydrate saturations that can reproduce broadband elastic measurements. For a given frequency, maximum changes in P-wave velocity and attenuation are observed for a particular aspect ratio and type of fluid inclusion in hydrate (Figures 2.6a, b and 2.7a, b). For a fixed aspect ratio, the magnitude of these changes depends on the fluid type and concentration of inclusions (Figures 2.6b and 2.7c, d). Essentially, the type of fluid inclusion in hydrate controls both the magnitude of attenuation changes and the frequency at which the attenuation peak is located. In contrast, the aspect ratio of fluid inclusions in hydrate controls only the frequency dependence of the attenuation peak, and the concentration of inclusions controls only the magnitude of attenuation.

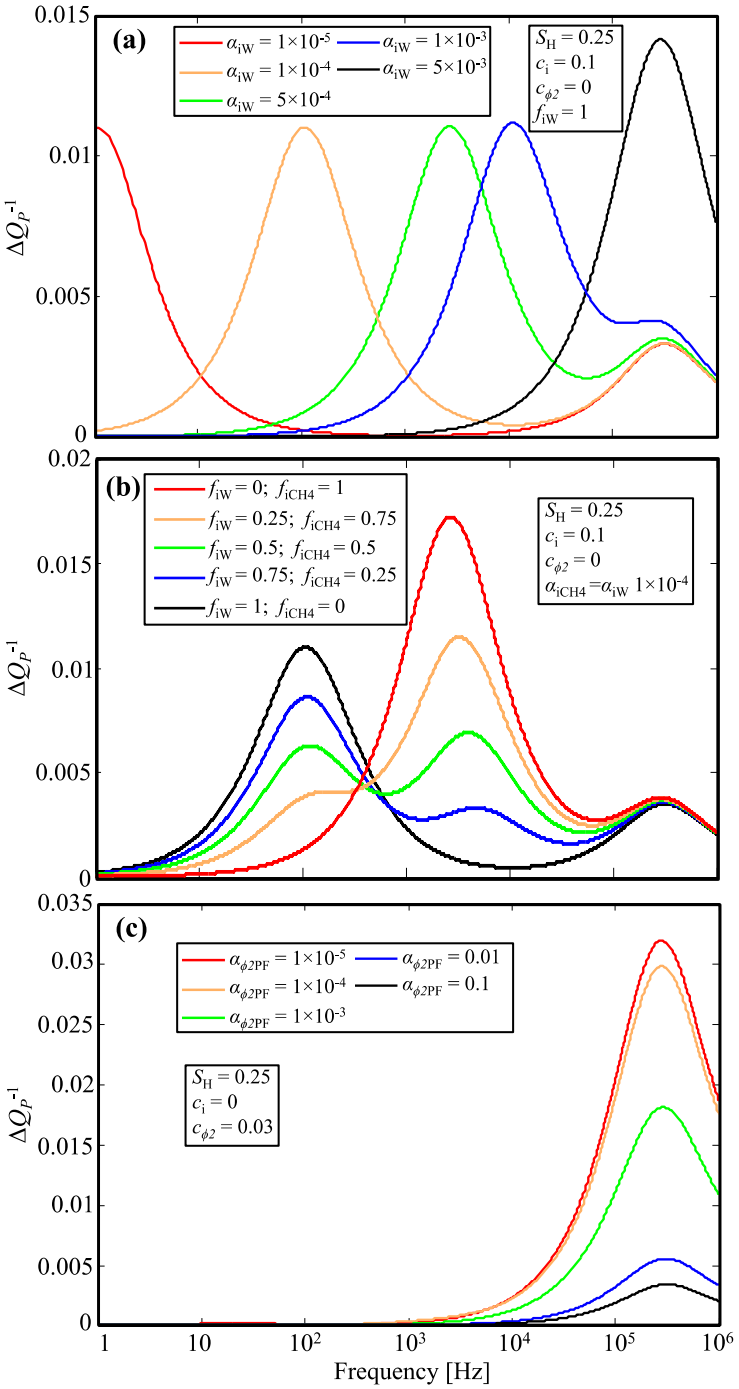

Figure 2.6 Variation in P-wave attenuation with frequency in sediment with pore-filling hydrate relative to the values without hydrate. Results for partially water saturated pores (S_w = 1- S_h) and for a hydrate saturation (S_h) of 0.25. (a and b) Attenuation caused by Biot's type global fluid flow and sub-micro squirt flow and (c) Biot's type global fluid flow and micro squirt flow. Input parameters are defined in Appendix A, Tables 1 and 2.

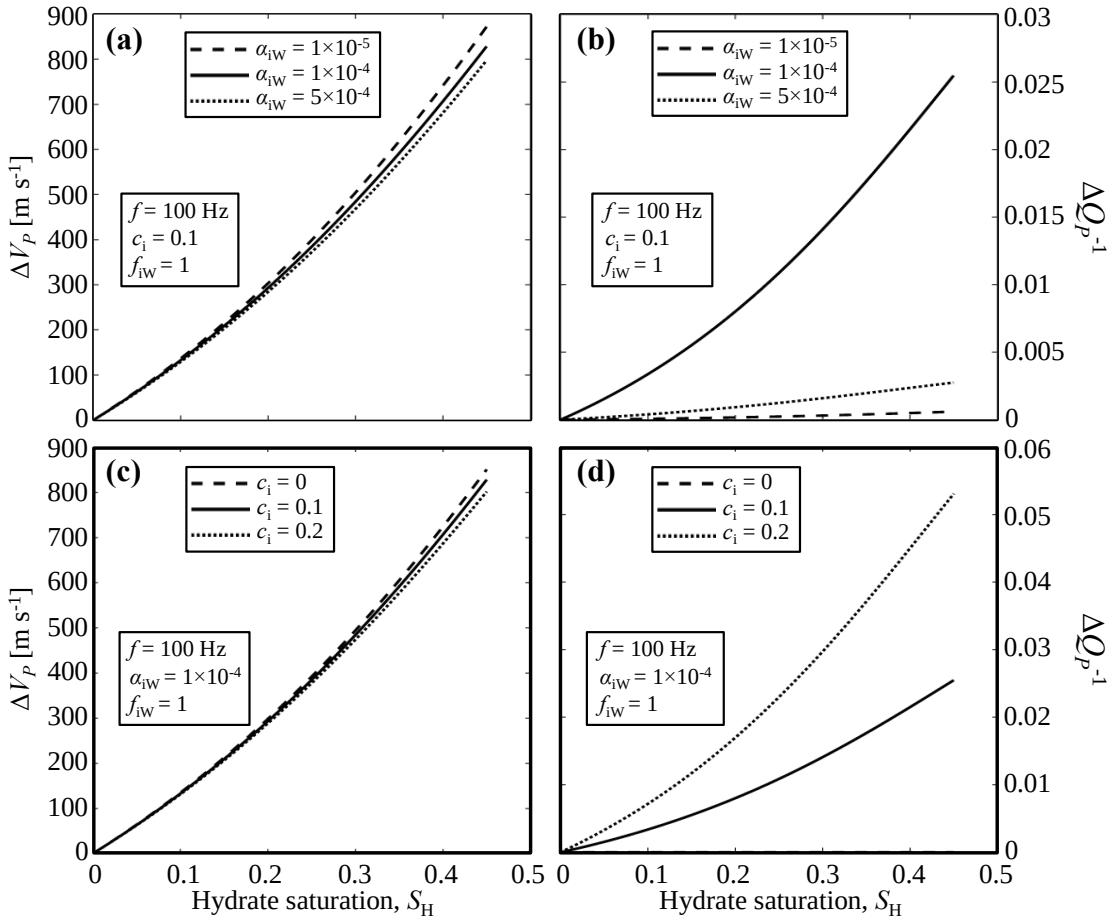

Figure 2.7 Variation in P-wave (a and c) velocity and (b and c) attenuation with pore-filling hydrate saturation in sediment relative to the values without hydrate. Results are shown for partially water saturated pores (S_w = 1- S_h) and fully water saturated inclusions in hydrate (f_{iW} = 1), and for a frequency (f) of 100 Hz. Attenuation caused by sub-micro squirt flow and Biot's type global fluid flow, but the relative contribution from the latter at 100 Hz is negligible. Input parameters are defined in Appendix A, Tables 1 and 2. Note that in (d) the dashed line is not visible, is overlapping the x-axis, because the concentration of fluid inclusions in hydrate (ci) is zero and hence no variation in attenuation occurs due to sub-micro squirt flow.

In the results described above we have assumed that the sediment pores are only occupied by water and hydrate to better understand and isolate pore-filling hydrate-related changes in elastic wave attenuation. However, several gas hydrate fields have shown evidence of co-existing methane gas and hydrate in sediments within the gas hydrate stability zone (e.g., Lee and Collet, 2006). The HBES model can also be used to study frequency dependent changes in attenuation caused by gas bubbles in the pores. At low frequencies, the presence of methane gas bubbles in the pores reduce considerably the P-wave velocity, whereas at high frequencies the P-wave velocity is higher than that for the fully water saturated case (Figure 2.8a). At the high frequency limit, the P-wave velocity tends exactly to that of the fully water saturated case, as stated by Smeulders and van Dongen

(1997). When hydrate is present in the pores, at low frequencies there is a smaller decrease in P-wave velocity due to gas bubbles (Figure 2.8a, solid red and black lines). Two distinctive peaks in attenuation at ~5 Hz and between 10-30 kHz are obtained with a gas bubble radius of 0.001 m, and the latter attenuation peak moves to higher frequencies when decreasing the bubble radius (Figure 2.8b). The greater high frequency attenuation peak observed for a free methane gas saturation of 10% and pore-filling hydrate, in comparison to that without hydrate (Figure 2.8b, solid red and black lines), is caused by hydrate-driven reduction in porosity generating higher Biot's type global fluid flow attenuation.

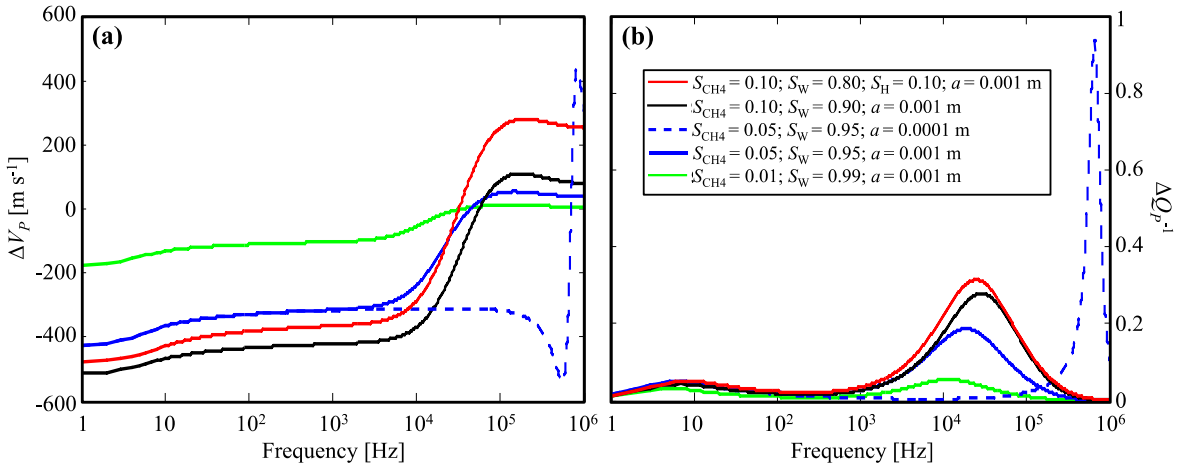

Figure 2.8 Variation in P-wave (a) velocity and (b) attenuation with frequency in sediment with gas bubbles and pore-filling hydrate relative to the values with fully water saturated pores. Results for two methane bubble sizes (*a* of 0.001 m and 0.0001 m) and different combinations of water, free methane gas and hydrate saturations. Attenuation caused by gas bubble damping and Biot's type global fluid flow. Hydrate-related squirt flow attenuation is not considered in the model run with pore-filling hydrate (red lines). Input parameters are defined in Appendix A, Tables 1 and 2.

2.4 Discussion

There is general consensus in the literature on the physical mechanisms explaining the effects of different hydrate habits on P- and S-wave velocities. Pore-filling hydrate-bearing sediments do not show significant changes in P- and S-wave velocities with respect to the host sediment (Priest et al., 2009; Waite et al., 2009; Dai et al., 2012), because hydrate floats in the pore fluid and thus only increases the bulk modulus of the pore fluid (Ecker et al., 1998). Load-bearing and cementing hydrate-bearing sediments show higher P- and S-wave velocities than those of the host sediment (Priest et al., 2009; Waite et al., 2009; Dai et al., 2012;) because hydrate increases the composite's

bulk and shear moduli (Ecker et al., 1998). In contrast, the way in which different hydrate habits affect attenuation is an open scientific question. Some studies suggest that the presence of hydrate in the sediments reduces attenuation (Dvorkin et al., 2003; Westbrook et al., 2008; Dewangan et al., 2014), while others suggest it increases attenuation (Dvorkin and Uden, 2004; Guerin and Goldberg, 2002; Pratt et al., 2005; Matsushima, 2006; Priest et al., 2006; Sun et al., 2016). Also, part of the enhanced attenuations measured in hydrate-bearing sediments may be due to a source-coupling effect (Lee, 2006). When the hydrate grains are larger than the sediment grains, hydrate forms nodules or veins, and this can cause either a negligible effect on attenuation, such in the Blake Ridge (Wood et al., 2000), or a reduction, such offshore west of Svalbard (Westbrook et al., 2008) and in the KG Basin (Dewangan et al., 2014). Our results are consistent with the experimental (e.g., Priest et al., 2006) and field studies where attenuation increased and hydrate was in pore-filling morphology within sand dominated sediments (e.g., Mallik well, Pratt et al., 2005).

Several studies have speculated (e.g., Milkov et al., 2004; Miyakawa et al., 2014; Goswami et al., 2015), proposed (Darnell et al., 2015) and demonstrated experimentally (Sahoo et al., 2018; Chapter 3) that gas can coexist with hydrate within the hydrate stability zone (HSZ). This gas can (i) fill inclusions in hydrate allowing local viscous flow between those and the pores (sub-micro squirt flow), (ii) stay in the pores allowing local viscous flow due to different aspect ratio pores generated when hydrate grows (micro squirt flow), and (iii) stay in the pores allowing gas bubble damping effects. Priest et al. (2006) presents a mechanism in which local viscous fluid flow occurs between monolayers of water remaining at grain contacts (when cementing hydrate forms) and the pores. This idea can be extended to the formation of pore-filling hydrate as, in principle, the formation of pore-filling hydrate can also generate micro squirt flow (Figure 2.2). However, the mechanism presented by Priest et al. (2006) is likely to produce higher attenuations, as the monolayers of adsorbed water are likely to have lower aspect ratios (Figure 2.6c). It is sensible to expect that both sub-micro and micro squirt flows can occur in sediments with hydrate independent of hydrate habit.

The main drawback to the use of P- and S-wave attenuation as a parameter for estimating hydrate saturation is that, traditionally, attenuation models have treated wave velocity and attenuation independently (Lee, 2006) which potentially contravenes the Kramers-Kronig relations of causality (e.g., Mavko et al., 2009). Our proposed HBES model is causal and includes several important hydrate systems-related features affecting P- and S-wave velocity and attenuation such as: derivation of fluid properties from equations of state, coexistence of gas and hydrate within the HSZ, sub-micro and micro squirt flows of gas and/or water, gas bubble damping, possible coexistence of different hydrate habits, and the ability to alter global fluid flow energy losses due to porosity and intrinsic permeability changes. The HBES model adds valuable insights to those

already learned from the limited number of published causal attenuation models (e.g., Guerin and Goldberg, 2005; Best et al., 2013).

2.5 Conclusions

The sole presence of pore-filling hydrate affects both the porosity and intrinsic permeability of the sediment, and hence the attenuation caused by the inertial motion of the grains with respect to the fluid in the pores at high frequencies above 10^4 Hz. Moreover, local sub-micro and micro squirt flows can also explain enhanced attenuations in pore-filling hydrate-bearing sediments at frequencies from 1 to 10^6 Hz that spans the entire frequency range of interest to exploration seismology. In methane rich systems within the HSZ, the absence of a distinctive increase in seismic-wave velocity from that expected of the host sediment only suggests that cementing or load-bearing hydrates are unlikely to be present in the system. However, this does not exclude the possible presence of pore-filling hydrate. From a conventional seismic exploration point of view, enhanced attenuation caused by fluid inclusions in hydrate may be the only hydrate-related loss mechanism able to produce the seismic signal contrasts needed to detect whether a reservoir sand is likely to have pore-filling hydrate, or not. If no distinctive peak in attenuation is observed, this can also mean that pore-filling hydrate still exists but it does not contain sufficient and/or adequate inclusions to create a detectable change in attenuation at seismic frequencies. Overall, our results provide a physical basis for interpreting seismic attenuation observations in sediments with pore-filling methane hydrate.

Acknowledgments

We acknowledge funding from the United Kingdom Natural Environment Research Council (NE/J020753/1). The data used are listed in the references, tables, figures, and in an Excel spreadsheet in the Appendix B. The references Berryman (1995), Bishop (1959), Dvorkin et al. (1998), Hovem and Ingram (1979), Ishii and Mishima (1984), Kuster and Toksöz (1974), Mahabadi et al. (2016), Mindlin (1949), and Reuss (1929) refer only to the Appendix B. We thank Nicola Tisato and an anonymous reviewer for their detailed and constructive comments.

Chapter 3 Presence and consequences of co-existing methane gas with hydrate under two phase water-hydrate stability conditions

This chapter forms a published paper: S. K. Sahoo, H. Marín-Moreno, L. J. North, I. Falco-Suarez, Madhusudhan B.N, A. I. Best and T. A. Minshull (2018), Presence and consequences of co-existing methane gas with hydrate under two phase water-hydrate stability conditions, Journal of Geophysical Research: Solid Earth, doi: 10.1029/2018JB015598

Abstract

Methane hydrate saturation estimates from remote geophysical data and borehole logs are needed to assess the role of hydrates in climate change, continental slope stability, and energy resource potential. Here, we present laboratory hydrate formation/dissociation experiments in which we determined the methane hydrate content independently from pore pressure and temperature, and from electrical resistivity. Using these laboratory experiments, we demonstrate that hydrate formation does not take up all the methane gas or water even if the system is under two phase water-hydrate stability conditions and gas is well distributed in the sample. The experiment started with methane gas and water saturations of 16.5% and 83.5% respectively; during the experiment, hydrate saturation proceeded up to 26% along with 12% gas and 62% water remaining in the system. The co-existence of hydrate and gas is one possible explanation for discrepancies between estimates of hydrate saturation from electrical and acoustic methods. We suggest that an important mechanism for this co-existence is the formation of a hydrate film enveloping methane gas bubbles, trapping the remaining gas inside.

3.1 Introduction

Hydrate is a naturally occurring ice-like, crystalline solid comprising a hydrogen-bonded water lattice with trapped gas molecules, that forms in seafloor sediments at high pressures and low temperatures (Kvenvolden, 1993). Nearly all the gas in natural hydrates is methane, with the remainder comprising higher order hydrocarbons such as ethane (Kvenvolden, 1993). Remote geophysical methods are used to quantify seafloor methane hydrates over broad areas. Typically these methods exploit the increase in seismic velocity (e.g., Fohrmann and Pecher, 2012; Lee and Collett, 2006; Schnurle et al., 2004) and electrical resistivity (e.g., Hsu et al., 2014; Schwalenberg et al., 2010a; Weitemeyer et al., 2006) caused when hydrate replaces saline water in sediment pores. However, accurate quantification of methane hydrate saturation is hampered by uncertainties in the relationship between these parameters and hydrate content (e.g., Goswami et al., 2015; Hsu et al., 2014; Lee and Collett, 2008; Schnurle et al., 2004).

Sub-seabed electrical resistivity can be measured using borehole logging (e.g., Miyakawa et al., 2014) or marine controlled source electromagnetic (CSEM) methods (e.g., Weitemeyer et al., 2006). Some field locations show discrepancies between hydrate saturations derived from resistivity and seismic/sonic methods (Table 1). This difference is a potential source of uncertainty in estimates from geophysical data of the carbon inventory stored in hydrate and in resulting assessments of well stability and methane production from hydrate reservoirs.

Hydrate content is often estimated from the increase in electrical resistivity compared to background sediments with no hydrates (e.g., Weitemeyer et al., 2006; Lee and Collett, 2008; Schwalenberg et al., 2010; Hsu et al., 2014). However, this method does not differentiate between gas and hydrate because both have higher resistivity than conductive pore fluid (e.g., Lee and Collett, 2008). Hereafter, the term gas is used to describe methane that is not stored in hydrate or dissolved in water, and may be mobile or immobile. In seismic data, gas and hydrate have been identified from a decrease and increase in P-wave velocity, respectively (e.g., Guerin et al., 1999; Schnurle et al., 2004; Lee and Collett, 2006; Fohrmann and Pecher, 2012). Because of their strong effect on P wave velocity (White, 1977), the presence of even small amounts of gas can obscure any increase in velocity caused by the presence of hydrate. In this case, estimates of hydrate content based on P wave velocity may differ significantly from those based on resistivity.

The presence of co-existing hydrate and gas within the gas hydrate stability zone (GHSZ) has been inferred in several locations away from seabed methane plumes (e.g., Guerin et al., 1999; Milkov et al., 2004; Lee and Collett, 2006; Miyakawa et al., 2014). Such field studies have attributed this presence of gas within the GHSZ to: (i) influx of gas into the GHSZ along fracture/faults (Gorman et

al., 2002; Lee and Collett, 2006; Miyakawa et al., 2014); (ii) local deviations from two phase water-hydrate stability conditions (pressure-temperature-salinity) resulting in local hydrate dissociation within the GHSZ (Guerin et al., 1999; Milkov et al., 2004); or (iii) hydrate formation kinetics (Torres et al., 2004). Drilling activities may also dissociate hydrates around a well, releasing gas within the GHSZ (Lee and Collett, 2006).

Table 3.1 Hydrate saturations from resistivity and seismic/sonic methods

Location	Hydrate Saturation (%)		References	Comments
	Resistivity	Seismic/ Sonic		
Good Weather Ridge, Taiwan	15-16	0-10	1, 2	Seismic: broad area
Hikurangi Margin, NZ	~34	~25	3, 4	Maximum
ODP Leg 204, USA			5	
Site 1244	6.5 ± 3.9	10.2 ± 3.7		
Site 1245	7.9 ± 5.5	10.4 ± 5.6		
Site 1247	4.5 ± 2.8	6.1 ± 3.2		
Kumano Basin, Japan	0-80	0-30	6	Parts of well
Nyegga, Norway	38	14-27	7, 8	In chimney
Vestnesa Ridge, Norway	20-30	~11	9, 10	Outside chimney

Note: [1] Schnurle et al., 2004; [2] Hsu et al., 2014; [3] Fohrmann and Pecher, 2012; [4] Schwalenberg et al., 2010; [5] Lee & Collett, 2006; [6] Miyakawa et al., 2014; [7] Attias et al., 2016; [8] Plaza-Faverola et al., 2010; [9] Goswami et al., 2015; [10] Hustoft et al., 2009.

At Site 1245 of ODP Leg 204, the amount of gas within the GHSZ was inferred independently from NMR logs and sonic velocity logs, with four times less gas inferred from sonic logs than from NMR logs (Lee and Collett, 2006). In the Kumano basin, Nankai Trough, offshore Japan, the presence of co-existing gas within the GHSZ was inferred from velocity and resistivity logs: in certain parts of

the well, velocity decreased with no corresponding decrease in resistivity, probably due to the presence of gas (Miyakawa et al., 2014). In both these locations, transport of gas into the GHSZ along faults or local hydrate dissociation during drilling has been inferred (Lee and Collett, 2006; Miyakawa et al., 2014). Milkov et al. (2004) explained the presence of gas within the GHSZ at Site 1249 of ODP Leg 204 by high residual pore water salinity, that limited further hydrate formation (Hesse and Harrison, 1981; Liu and Flemings, 2006; Milkov et al., 2004). At Site 995 of ODP Leg 164, co-existing gas and hydrate in the base of the GHSZ have been explained by hydrate dissociation in smaller pores because of capillary effects along with hydrate stability in bigger pores (Guerin et al., 1999). Elsewhere, several locations do not show any evidence of co-existing hydrate and gas within the GHSZ (e.g., Fujii et al., 2015).

However, gas can also be present in two phase water-hydrate stability conditions due to two mechanisms. Firstly, hydrate can contain inclusions of gas (Schicks et al., 2006), which could either be connected or disconnected to the pore network. Disconnected inclusions (occlusions) could remain in the hydrate or could also be a pre-hydrate phase, where hydrate formation is still in process (Schicks et al., 2006). Occlusions of gas may be removed over time by diffusion, but in a dynamic pore fluid system with gas production, diffusion is unlikely to dominate due to its relatively slow rate (Milkov et al., 2004; Suess et al., 2001). Secondly, hydrate formation can block contacts between gas and water within sediment pores, and form pockets of gas (which could include several pores) (e.g., Chaouachi et al., 2015; Yang et al., 2016). Kinetic modelling of hydrate formation and dissociation in porous media suggests that it is highly unlikely that hydrate can achieve true equilibrium because there are too many phases in the system (e.g., Vafaei et al., 2014). Therefore, the limiting phase (methane in excess water conditions; water in excess gas conditions) is unlikely to be completely used up to form hydrates even if two phase water-hydrate stability conditions prevail.

Here, we present results from a laboratory experiment of methane hydrate formation and dissociation in Berea sandstone. We calculated continuously the evolution of the brine, gas and hydrate saturations during hydrate formation and dissociation from pore pressure and temperature. Our calculation method does not assume that hydrate formation continues until the limiting phase is exhausted, and we show that about 12% gas co-exists with 26% hydrate under pressure, temperature and salinity conditions favourable for more hydrate formation.

3.2 Hydrate formation and dissociation experiments

We conducted laboratory experiments involving repeated cycles of methane hydrate formation and dissociation inside a high-pressure cell under excess water conditions.

3.2.1 Sample properties and experimental setup

For the test, we selected a 2 cm height, 5 cm diameter core sample of Berea sandstone. The porosity was 0.22 and the absolute permeability was 448 mD (~4.5×10^{-13} m^2) at atmospheric conditions. The permeability was measured with (gas) permeameter and the porosity with a pycnometer.

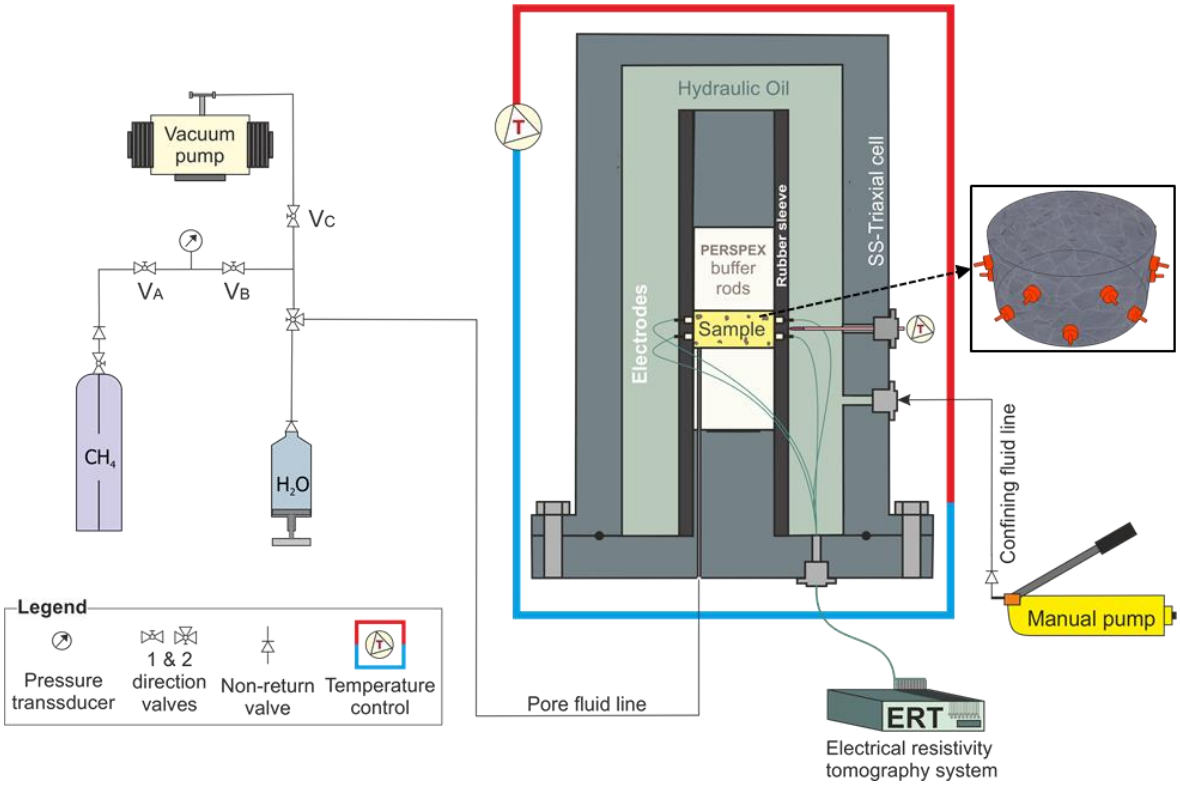

Figure 3.1 Schematic diagram of the experimental setup, also showing the arrangement of electrodes around the Berea rock sample. Scales are approximate.

The experiment was conducted in a stainless steel triaxial cell core holder, designed to host and pressurize 5 cm diameter rock samples up to 65 MPa of confining and pore pressure (Figure 3.1), and instrumented to monitor temperature (both sample and ambient) (Ellis, 2008). The inner sleeve that prevents the direct contact between the mineral oil used as confining fluid and the rock sample is perforated by 16 electrodes coupled to a data acquisition system. Under typical operating conditions the relative error in resistivity measurement is < 0.1% (at frequencies 1 - 500 Hz) for homogenous and isotropic samples in the electrical resistivity range 1-100 Ω m (North et al., 2013). Axially, perspex buffer rods electrically isolate the sample from the cell. The inner temperature sensor was placed on the outer side-wall of the sleeve at the sample height, to provide accurate monitoring of the sample temperature. The pore fluid pipe line is triply connected to (i) a pumping-syringe containing a 35 g/L NaCl solution in deionized-deaerated water, (ii) a vacuum pump and (iii) a CH_4-bottle pressurized at 12 MPa (see Figure 3.1).

3.2.2 Method of hydrate formation

We followed the method of Waite et al. (2004) with an initial brine saturation of 83.5% which allowed an excess water condition (Ellis, 2008; Priest et al., 2009). Our hydrate formation method and experimental set up represent gas hydrate systems where localized gas reaches the base of the GHSZ in fine-grained sediments.

The sample was firstly oven-dried at 60˚C, placed in the high pressure cell, then subjected to a hydrostatic confining pressure of 10 MPa. A vacuum up to 1 Pa was applied to the sample to remove air from the pore space. The presence of air affects the saturation calculation and any other gas present in the air, such as CO_2, can form hydrate. Brine (35 g/L NaCl solution in deionized and deaerated water) was injected to fill 83.5% of the sample pore space. We left the sample for three days so that the pore fluids could re-distribute throughout the sample by capillary forces. The remaining pore space (16.5%), which was previously under vacuum, may have been occupied by water vapor and/or remaining air.

Methane gas was then injected to achieve a pore fluid pressure of 11.9 MPa (Figure 3.2), and, simultaneously, the confining pressure was increased to 21.9 MPa to maintain a constant differential pressure of 10 MPa during the whole experiment. The pore fluid system was sealed, keeping the reservoir between the sample and valve V_A (Figure 3.1) filled with methane gas, which is free to move in and out of the sample as a result of potential pore pressure variations. Finally, four cycles of hydrate formation/dissociation were triggered by cooling/heating the setup in a controlled manner, i.e., in and out from the gas hydrate stability conditions (GHSC).

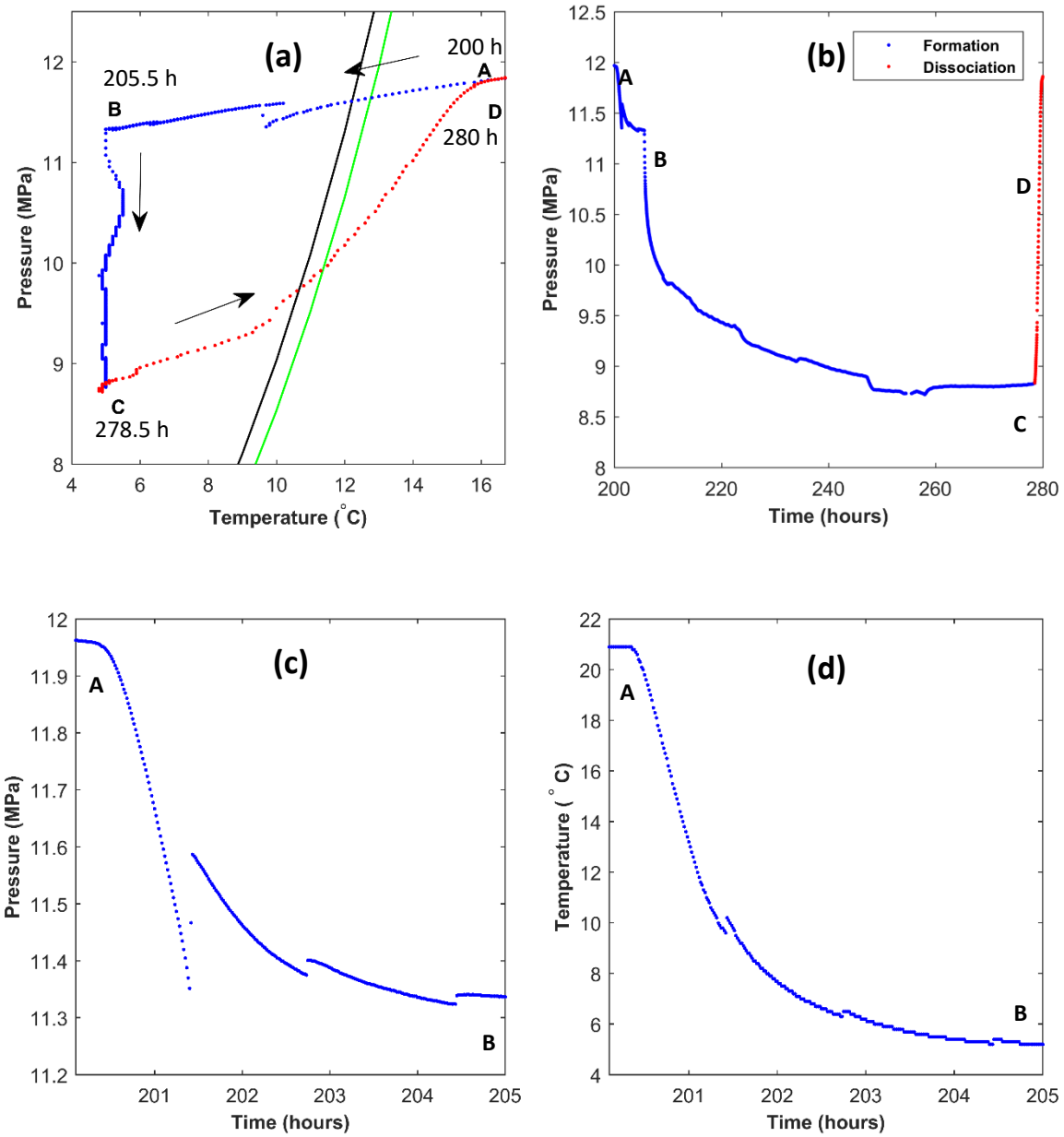

Figure 3.2 Changes of a) pressure versus temperature, and b) pressure with time during methane hydrate formation and dissociation in Berea sandstone. Only the second cycle of hydrate formation and dissociation is shown for clarity. The green and black lines are the pure methane hydrate phase boundary for 35 g/L and 46 g/L salinity respectively, calculated using the approach of Tohidi et al. (1995). Blue dots represent cooling and red dots represent heating. In a) time is shown in hours (h). Trajectory ABC marks cooling of the system to 5 °C and hydrate formation. Trajectory CD shows hydrate dissociation. c) and d) show pressure and temperature change with time during trajectory AB. See text for further details.

The cooling of the system into the GHSC, to a set temperature of 5˚C, generated a reduction in pore pressure (Figure 3.2) that can be explained mainly by hydrate formation, with some contribution from methane gas contraction and increased gas solubility. The pressure reduction appears to take place in two stages (Figure 3.2). On trajectory A-B the system is cooled rapidly (in 5.5 hours). Here, the pressure drops due both to cooling and to hydrate formation. On trajectory B-C the temperature remains around 5˚C and only the pressure drops. Here, the pressure drop is mainly due to hydrate formation and takes much longer (73 hours) than on trajectory A-B. The formation of hydrate also generates a slight increase in temperature caused by exothermic hydrate formation (Hwang et al., 1990). This increase is very clear on trajectory B-C. On trajectory A-B, at around 201.4 h, there is a sudden pore fluid pressure and temperature increase (Figure 3.2). This pressure increase is likely due to the interplay between the cooling of the system and the exothermic effect of hydrate formation. Cooling and the consumption of pore fluids due to hydrate formation both lead to a decrease in pressure. However, hydrate formation also leads to an increase in temperature, which can result in a slight increase in pressure (Figure 3.2c and d). The net effect depends on the balance between the rate of cooling and the rate of hydrate formation. Once hydrate formation ceased, indicated by the end of the pore pressure decrease (point C in Figure 3.2), the system was left at that pressure and temperature for several hours to ensure maximum hydrate formation, evidenced by the horizontal asymptotic behaviour of the pore pressure (Figure 3.2b) and of the saturation lines for each cycle (Figure 3.3).

Hydrate dissociation was initiated by increasing the temperature above the GHSC to room temperature. We also did a separate experiment under identical conditions in which we left the sample under hydrate stability conditions at 5˚C (point C in Figure 3.2a) for 1 month and saw that maximum saturation of methane hydrate occurred in the first 75 hours. This experiment also resulted in 22% hydrate saturation. The differential pressure was held at 10 MPa in the first and second cycles of hydrate formation and dissociation, and then increased to 55 MPa for the third and fourth cycles. This was done to explore the effects of micro-cracks on acoustic properties (included in future work) that are generally open at lower differential pressures (10 MPa) and closed at higher pressures (55MPa), based on previous resistivity and ultrasound data for Berea (Han et al., 2011b). The initial pore fluid pressure for the third cycle was 11.98 MPa (0.08 MPa above that for the first cycle).

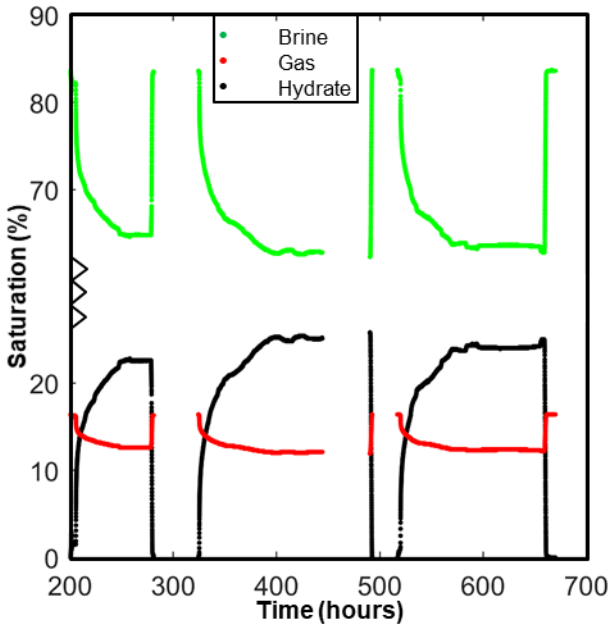

Figure 3.3 Evolution of water, methane gas and methane hydrate saturation during three hydrate formation and dissociation cycles in Berea sandstone. The saturations were calculated from the changes in pore pressure and temperature (Section 3.3.1). We used a hydration number of 6.39 corresponding to 90% cage occupancy (Sloan & Koh, 2007). Note the contracted y-axis scale. The first cycle is not shown because the pressure logger malfunctioned. Relative error in saturation is less than 0.5%.

3.3 Saturation calculations

We tracked the evolution of the saturations of gas, brine and hydrate from the changes in pore fluid pressure and temperature using the real gas equation (the PT method), and independently from electrical resistivity measurements (the ERT method).

3.3.1 PT method

We calculated continuously the saturations of the three phases (gas, brine, hydrate) from the changes in pore fluid pressure and temperature using the real gas equation. These measurements were recorded at one minute intervals during the experiment. This method does not assume that hydrate formation continues until the limiting phase is exhausted (Sultaniya et al., 2015) nor that coexistence occurs only under three-phase stability conditions (e.g., You et al., 2015). This allows us to deduce the physical processes that occur throughout the cycle of hydrate formation and dissociation.

Our method assumes a closed system and conservation of the molar mass of methane and water in the sample pore space. Methane can be present in hydrate, dissolved in brine or as gas. Water can be present as liquid in the pore space (brine) or in hydrate (pure water). The pore volume in the sample and inner volume of the input gas pipe were measured before starting the experiment, and were assumed to remain constant throughout the experiment. A change in effective pressure can change the sample's pore volume, but for the magnitude of the dynamic stresses applied, this change is negligible (< 0.3% for Berea sandstone) (Rutter and Glover, 2012). So we assumed the volume of the input gas pipe remains constant because it is always at ambient pressure and the ambient temperature was controlled to 20 ± 2 °C. The pores of the Berea sandstone can be occupied by gas, water or hydrate. Hydrate can only form in the pore space of the sample and no hydrate forms in the gas input pipe because it is outside hydrate stability conditions.

The non-ideal gas law is:

$$p\,V = n\,\mathrm{R}\,T\,Z\,, \tag{3.1}$$

where *p* is gas pressure, *V* is volume, *n* is the number of moles of methane gas, R is the universal gas constant and *T* is temperature. *Z* is an empirical compressibility factor calculated using the Peng–Robinson equation of state (Peng and Robinson, 1976), and varies with temperature and pressure. Initially there was no hydrate in the sample. The sample pore volume V_{ts} was independently measured with a pycnometer, and a known volume of water V_{w0}, measured using a syringe pump, was injected into the sample. The initial number of moles of water is given by

$$n_{w0} = \frac{V_{w0}\,D_{w0}}{\mathrm{M_w}}\,, \tag{3.2}$$

where D_{w0} is the density of brine at 35 g/L salinity and $\mathrm{M_w}$ is the molar mass of this brine. For the pipe, from equations 3.1 we have

$$p_0\,V_p = n_{p0}\,R\,T_{p0}\,Z_{p0}\,, \tag{3.3}$$

where p_0 is initial gas pressure, which is the same in both the sample and the pipe, V_p is the volume inside the pipe, n_{p0} is the initial number of moles of methane gas in the pipe, T_{p0} is the temperature in the pipe, and Z_{p0} is the compressibility factor of methane under the initial pipe P-T conditions.

For the sample, equations 3.1 gives

$$p_0\;V_{ms0} = n_{s0}\,R\,T_{s0}\,Z_{s0}\,, \tag{3.4}$$

$$V_{ms0} = V_{ts} - V_{w0}\,, \tag{3.5}$$

where V_{ms0} is the initial volume of methane gas in the sample, n_{s0} is the initial number of moles of methane gas in the sample, T_{s0} is the initial temperature of the sample, and Z_{s0} is the compressibility factor of methane under the initial sample P-T conditions. In our method, we accounted for the dependency of methane solubility in water, denoted by b, on temperature and salinity (Tishchenko et al., 2005) and that of hydrate and brine densities on pressure and temperature (Lu and Sultan, 2008; Millero et al., 1980) using the equation:

$$n_{sw0} = V_{w0}\, D_{w0}\, b_0, \tag{3.6}$$

where n_{sw0} is the initial number of moles of methane in solution and b_0 is the initial solubility. The total number of moles of methane in the system n_t was therefore

$$n_t = n_{p0} + n_{s0} + n_{sw0}. \tag{3.7}$$

Once the temperature decreases below that for hydrate stability, hydrate starts to form from the methane and water in the sample's pore space. This process reduces the sample's gas pressure, generating an inflow of methane gas from the pipe to regain equilibrium of pore fluid pressure. The net result is an overall decrease in the gas pressure. From this new gas pressure and the pipe and sample temperatures, T_p and T_s, we can calculate the number of methane moles in each phase. For a gas pressure *p*

$$V_h = n_h \frac{\mathrm{M_h}}{D_h}, \tag{3.8}$$

$$V_w = (n_{w0} - n_h \cdot \mathrm{c}) \frac{\mathrm{M_w}}{D_w}, \tag{3.9}$$

$$V_{ms} = V_{ts} - V_w - V_h, \tag{3.10}$$

$$p\, V_p = n_p\, R\, T_p\, Z_p, \tag{3.11}$$

$$p\, V_{ms} = n_s\, R\, T_s\, Z_s, \tag{3.12}$$

$$n_{sw} = V_w\, D_w b, \tag{3.13}$$

where V_h is the volume of hydrate, n_h is the number of moles of hydrate, $\mathrm{M_h}$ is the molecular mass of hydrate, D_h is the density of hydrate and c is the hydration number (i.e., the number of water

molecules required to form hydrate per molecule of methane). The total number of moles of methane in the system remains constant, so n_h can be obtained from

$$n_h = n_t - n_p - n_s - n_{sw}. \tag{3.14}$$

The hydrate saturation is given by

$$S_h = \frac{V_h}{V_{ts}}. \tag{3.15}$$

Combining Equations 3.8 - 3.15, we obtain:

$$S_h = \frac{\left(\frac{p_0\ V_{p0}}{R\ T_{p0}\ Z_{p0}} + \frac{p_0\ (V_{ts} - V_{w0})}{R\ T_{s0}\ Z_{s0}} + V_{w0}\ D_{w0}\ b_0 - \frac{p\ V_p}{R\ T_p\ Z_p} - \frac{p\ V_s}{R\ T_s\ Z_s} - V_w\ D_w b\right)\frac{M_h}{D_h}}{V_{ts}}. \tag{3.16}$$

All the symbols defined in this section are listed in Table 3.2 and constants are listed in Table 3.3.

Table 3.2 Parameters used in the PT method

Description	Symbol*
Number of moles of methane hydrate	n_h
Saturation of methane hydrate	S_h
Pore fluid Pressure	p
Total pore space in the sample	V_{ts}
Volume of methane gas in the sample	V_{ms}
Volume of liquid water in the sample	V_w
Volume of hydrate in the sample	V_h
Volume of pipe	V_p
Total number of moles of methane in the system	n_t
Number of moles of methane gas in pipe	n_p
Number of moles of methane gas in sample	n_s

Description	Symbol*
Number of moles of methane in solution	n_{sw}
Number of moles of water in liquid phase	n_w
Temperature in the pipe	T_p
Temperature in the sample	T_s
Compressibility of methane gas in the pipe	Z_p
Compressibility of methane gas in the sample	Z_s
Density of Brine	D_w
Density of Hydrate	D_h
Solubility of methane	b

***I**nitial values for these parameters are denoted in the text with a subscript 0

Table 3.3 Constants use in the PT method.

Description	Symbol	Values
Ratio of water to methane in hydrate (Sloan and Koh, 2007)	c	6.39
Molar mass of brine (35 g/L)	$\mathrm{M_w}$	0.0186 Kg
Molar mass of hydrate (structure I)	$\mathrm{M_h}$	0.1312 Kg
Universal gas constant	R	8.314 $\mathrm{Jmol^{-1}K^{-1}}$

3.3.2 ERT method

We estimated the saturation of resistive material in the pore space from measured bulk resistivity of the sample. As both hydrate and gas are resistive compared to the conductive brine, it is not possible to obtain the individual saturations of gas and hydrate separately by this approach.

To determine this saturation, the first step is to calculate the saturation of brine. Several approaches can be used to estimate the saturation of brine from measured electrical resistivity (Archie, 1942; Bussian, 1983; de Lima and Sharma, 1990; Glover, 2010; Revil et al., 1998; Simandoux, 1963; Waxman and Smits, 1968). This interpretation is complicated in the presence of clay minerals as they have charge deficiency. The 'counter ions' required to balance this charge deficiency are in the double layer. These counter ions can move along the grain water surface under the influence of an external electric field. Hence, the macroscopic electrical conduction in a saturated/partially saturated porous medium with clay can be via a) bulk conduction caused by the movement of ions of the conducting pore fluid, and b) surface conduction in the vicinity of the fluid/grain interface (e.g., Bussian, 1983; Revil and Glover, 1998; Waxman and Smits, 1968). A wide variety of formulations have been developed to account for both surface and bulk conduction. The earlier models described the effect of surface conduction in terms of the volume of shale, while more recent models attempt to account for the physics of the diffuse ion double layer surrounding clay particles (e.g., Simandoux, 1963; Waxman and Smits, 1968; Clavier et al., 1984; Revil et al., 1998). We choose to use the Waxman-Smits formula for partial brine saturation (Waxman and Smits, 1968).

$$S_w = \left(\frac{\Phi^{-m} \rho_w}{\rho_t (1 + \rho_w B Q_v / S_w} \right)^{\frac{1}{n}}, \tag{3.17}$$

$$B = 4.6 \left(1 - 0.6 e^{-\frac{1}{1.3 \rho_w}} \right), \tag{3.18}$$

$$Q_v = \frac{\mathrm{CEC}(1 - \Phi) D_O}{\Phi}, \tag{3.19}$$

where S_w is brine saturation, ρ_t is the measured sample resistivity, ρ_w is brine resistivity and Φ is porosity. Q_v is the concentration of clay exchange cations or counter ions per unit pore volume of the rock, and should be measured ideally in the laboratory by analyzing several samples with different brine saturations (Waxman and Smits, 1968). B represents the average mobility of the counter ions near the grain surfaces, CEC is the cation exchange capacity, and D_o is mineral grain density . The empirical parameters *m* and *n* are the cementation coefficient and the saturation exponent, respectively.

Zhan et al., (2010) showed experimentally for a similar porosity Berea sandstone (22.98 - 23.60%) that the Waxman-Smits model gives reliable results for our salinity (Figure 6 of Zhan et al., 2010). Glover et al. (1994) presented laboratory data on the variation of Berea sandstone conductivity with fluid conductivity. They showed that, for low pore fluid conductivity (< 0.001 S/m), bulk conductivity is independent of pore fluid conductivity, and tends to be constant. For higher pore fluid conductivity (< 1 S/m), the saturated rock conductivity is controlled mainly by the movement of ions through the bulk fluid, and seems to be independent of any surface conduction effect. As we used brine of 35 g/l (measured conductivity at 25 ^{o}C temperature is 5.2 S/m), we are in the higher pore fluid conductivity zone where surface conduction effects have only a small effect on bulk rock conductivity.

However, the experiments of Glover et al. (1994) and Zhan et al. (2010) did not involve hydrate. Hence, our approach assumes implicitly that hydrate surface conductivity effects are negligible and that hydrate behaves as a resisitive component. Several studies have also shown that surface conduction contributes substantially to the macroscopic conductivity at low salinity and/or high temperature, even in low clay content sandstone (Bussian, 1983; Revil and Glover, 1998; Waxman and Smits, 1968). Since our sample has a low clay content of 2.3% by weight (XRD analysis; Han et al., 2015), the pore fluid has a high salinity (35gm/l NaCl with conductivity of 5.22 S/m at 25 ^{o}C), and the temperature is low (5 ^{o}C), we conclude that the Waxman-Smits model should be applicable in our case

As natural hydrate can be found also in clay rich sediments, appropriate clay conduction models should be used in such studies. We used the Waxman-Smits model but several modifications, refinements, or other models exist. For example, Clavier et al. (1984) proposed the dual water model, a modified form of the Waxman-Smits model with two types of pore water, of which only one is affected by surface conduction. Kan and Sen (1987) modelled clays as periodic arrays of charged insulating cylinders or spheres, immersed in symmetrical monovalent electrolyte. Revil and Glover (1998) discussed the theoretical framework of surface conduction predictions. Revil et al. (1998) accounted for the difference in behaviour of anions and cations. de Lima & Sharma (1990) discussed a model based on shape and occurrence of clay, such as clay coating the sand grains or as individual clay grains. For a more detail review on conductivity models refer to, for example, Doveton (2001); Glover (2010); de Lima & Sharma (1990); Mavko et al. (1998).

The resistivity of brine is temperature-dependent and we calibrated it using the following expression (e.g., McCleskey et al., 2012):

$$\rho_w = \frac{\rho_{25}}{1+\alpha(\mathrm{T}-25)}\,, \tag{3.20}$$

where, T (°C) is temperature, α is the temperature compensation factor, and ρ_{25} (Ωm) is the resistivity of brine at 25 °C. Values of ρ_{25} were measured using a conductivity meter with α = 1.9%, similar to other studies (e.g., McCleskey et al., 2012). For a mixture of sand and clay, the CEC can be calculated from

$$CEC = m_c \sum \chi_i \mathrm{CEC}_i \,, \tag{3.21}$$

where, m_c is the mass fraction of clay minerals in the whole rock, χ_i is the relative volume fraction of each clay mineral, and CEC_i is the cation exchange capacity of each clay mineral. The cation exchange capacity of quartz can be neglected due to its large size (hence small amount of surface change per unit mass) in comparison to clay minerals (Ellis and Singer, 2007).

This method of calculating CEC assumes a mixture of sand and clay, and does not account for the various clay morphologies (e.g., clay as cement or grains) in Berea sandstone. We used 0.09 meq/g CEC for authigenic illite (Thomas, 1976). A value of 2 was used for *n* (Waxman and Smits, 1968). The value of *m* was determined by fitting the initial resistivity for the known initial brine saturation, found to be 2.84, which is within the range of 1.3 to 4 reported by Jackson et al., (1978). As hydrate forms, the value of m increases (Chen et al., 2008; Spangenberg, 2001), but the exact form of this increase is not known. To account for this change, we assumed slightly higher value of *m* = 3.10 for hydrate saturations above 5% (Chen et al., 2008; Spangenberg, 2001). The increase in *n* simulates a reduction in fluid flow as hydrate blocks pore throats (Chen et al., 2008). The maximum hydrate saturation calculated from the PT method was 26%, unlikely to be sufficient to block pore throats; hence, we did not vary further the value of *n*.

3.4 Results and discussion

3.4.1 Three phase co-existence

The results of the PT method provide evidence for the co-existence of methane gas, methane hydrate and brine in our experiments. When the pressure and temperature reached stability conditions, methane hydrate nucleation and growth started, followed by an increase in hydrate saturation and a decrease in gas and brine saturation (Figure 3.3). Even though we allowed enough time (80 - 180 h) for hydrate formation to continue (see Section 3.2 for further details), and there was always stoichiometrically sufficient methane gas and brine available for more methane hydrate formation, the reaction stabilized at a maximum methane hydrate saturation between 23-26% and methane gas saturation between 12-13% of the pore space (Figure 3.3). The maximum relative error in saturation calculated using the PT method is less than 0.5%. This phenomenon was

observed also in two additional cycles of methane hydrate formation and dissociation, indicating the co-existence of three phases (gas, brine and hydrate) with similar maximum methane hydrate and methane gas saturations, and an asymptotic behaviour of the saturation curves during hydrate formation in each cycle (Figure 3.3). At the maximum hydrate saturation, application of small perturbations in the confining pressure could have ruptured hydrate shells, trapping gas and allowed further hydrate formation (Fu et al., 2017). Such perturbations were not applied, so our estimate of co-existing gas may represent an upper bound for our experimental set up.

Methane hydrate is a non-stoichiometric solid with variable cage occupancy (Sloan and Koh, 2007). We used a hydration number of 6.39, corresponding to 90% cage occupancy (Sloan and Koh, 2007) for the calculation shown in Figure 3.3. If the cage occupancy is 100%, *c* is 5.75 (Sloan and Koh, 2007) and the resulting maximum hydrate saturation decreases by 2%.

In Section 3.1, we listed several mechanisms allowing three phase coexistence of methane gas with hydrate. Here, we discuss some of the mechanisms that are relevant to our experimental study. Methane hydrate may form when methane gas and water are in contact and have conditions favourable for hydrate formation. Our experimental pressure and temperature conditions of 8.8 MPa and 5 ^{o}C were well within the hydrate stability field for 35 g/L brine, but the salinity of the remaining pore water increases due to hydrate formation. Our experiments started with 35 g/L salinity, and a 26% hydrate saturation would have increased the mean salinity to about 46 g/L. At this salinity, our experimental pressure and temperature conditions are still within the GHSC (Figure 3.2a), as calculated using the approach of Tohidi et al., (1995). This calculation does not consider the effect of porous medium properties such as pore size, surface structure and mineral composition that can all affect the GHSC (e.g., Handa and Stupin, 1992; Clennell et al., 1999; Henry et al., 1999). Some experimental results suggest that surface structure and mineral composition may have little effect on GHSC (Riestenberg et al., 2003), while capillary effects due to pore size can be important (Clennell et al., 1999; Uchida et al., 2004). Therefore, we consider only capillary effects.

Clennell et al., (1999) argued that methane hydrate behavior can be analogous to that of ice, as also suggested by other authors (e.g., Handa and Stupin, 1992). The freezing point of ice is lower in a fine-grained porous medium, such as soil, than in bigger pores, such as in sand. This is due to curved water-ice interfaces that increase the free energy of pore water (Everett, 1961). In small pores, the curvature is high and the excess free energy is also high. In big pores, the curvature is low, and so is the excess free energy. Clennell et al. (1999) calculated the decrease in the freezing point of ice inside a pore relative to the bulk freezing point (in a pore of infinite pore radius), and extrapolated that to methane hydrate. We rearranged equation 8 of Clennell et al. (1999) to calculate the

minimum pore radius for which hydrate can form under our experimental conditions of 8.8 MPa and 5 °C.

$$r_e = \frac{2\gamma_{iw} T_{i,bulk} \cos\theta_{iw}}{\rho_w \Delta H_{f,i} \Delta T_{i,pore}}, \quad (3.22)$$

where, r_e is the radius of the pores, γ_{iw} is the specific surface energy between ice and water, $T_{i,bulk}$ is the absolute melting temperature of ice (without considering pore radius effects), θ_{iw} is the wetting angle, ρ_w is the density of water, $\Delta H_{f,i}$ is the specific enthalpy of formation of ice and $\Delta T_{i,pore}$ is the change in melting temperature due to pore size effects. For our experimental pressure of 8.8 MPa, the hydrate-water phase boundary temperature ($T_{i,bulk}$) is 9.8 °C (calculated using the approach of Tohidi et al., 1995), and therefore $\Delta T_{i,pore}$ is -4.8 °C , giving a minimum pore radius of 9.5 nm for γ_{iw} = 26.7 mJ m^{-2} , θ_{iw} = 180 degrees, $\rho_w = 1000$ kgm^{-3} , $\Delta H_{f,i}$ = 333 kJ Kg^{-1} (Clennell et al., 1999).

We also measured the pore size distribution using X-ray computed tomography at the Swiss Light Source (SLS) at the Paul Scherrer Institute. The optical objective used for imaging was 20x, which provided 325 nm voxel resolution. The pore size varied from 11.39 µm to 73.11 µm, so capillary effects in our sample should not have limited the formation of hydrate. Note that only a small part (7.27 mm diameter and 8 mm high) of the sample was studied in the CT scan, and we assumed that the observed pore size distribution is representative of the whole sample. Clennell et al.'s (1999) equation is for pure water, while our pore fluid had an average salinity of up to 46 g/L at maximum hydrate saturation. Sun and Duan (2007) developed a thermodynamic model for the effect of pore size and salinity on hydrate stability. We used their open online calculator (models.kl-edi.ac.cn/models.htm) and found a minimum pore radius of less than 3.2 nm, confirming the minor effect of pore size for our experimental conditions. We note also that it is very unlikely that hydrate formation can reduce the effective pore size to values close to the minimum pore radius because that could only happen when the pore is almost completely occupied by hydrate.

When hydrate forms, it can create a physical barrier between methane gas and water that prevents further hydrate formation. This physical barrier can be of various types:

a) Hydrate may form and dissociate only near the inlet pipe if the methane gas/brine is not distributed in the sample. This scenario is highly unlikely because the sample was vacuumed and then 83% of the pore space was filled with brine. These conditions were kept for three days, allowing the brine to spread within the sample. The gas would also be distributed within the sample before hydrate forms because: (i) the inlet pipe is on the lower surface of the sample, and methane gas would likely move upwards due to buoyancy; and (ii) methane gas was injected into the sample

at room temperature and left for three days to complete its upward migration before cooling the system into the hydrate stability field.

b) Isolated pockets of gas or brine could exist in some pores. This can be due to gas reaching a pore that is not connected in the flow direction, and/or capillary trapping. If such a pore is blocked in the flow direction, hydrate formation can trap the gas (Figure 3.4, A). Similarly, hydrate formation in connected pores could also disconnect them, trapping brine/gas (Figure 3.4, B). Capillary trapping can occur when the gas pressure is less than the capillary entry pressure of a given pore, which depends on its radius, resulting in the fluid being unable to move through that pore (Figure 3.4, C). The formation of hydrate can enhance this trapping mechanism by decreasing the effective pore radius, resulting in higher threshold capillary pressures needed for gas invasion (Figure 3.4, D).

c) Unconnected pores (occlusions) of gas/water can occur within hydrates (Figure 3.4, E). In our experiment, the maximum hydrate and gas saturations are around 26% and 12% of the pore space, respectively. Near seafloor sediments on the southern summit of Hydrate Ridge (offshore Oregon, USA) contain porous hydrates that likely formed when methane gas bubbles became coated with a hydrate film as they moved upwards within the sediments and coalesced together (Suess et al., 2001). A sufficiently thick hydrate film enveloping the methane bubbles disconnects the gas remaining inside the hydrate film from the pore water outside (Figure 3.4, F). Hence, gas remains trapped within the hydrate film, even though hydrate stability conditions prevail. Such porous hydrates have 55 ± 5% of their bulk volume filled with gas (Suess et al., 2001). We propose that this is the dominant mechanism for co-existing gas in our experimental setup. This mechanism does not involve three phase thermodynamic equilibrium, as the trapped methane gas inside the hydrate shell is not in physical contact with water outside the shell.

Gas trapped within hydrate films would diffuse out over geological time scales, so our experimental results might not reproduce well hydrate formation in nature. However, in a dynamic natural system with ongoing gas flow into the GHSZ, methane bubbles with a hydrate film enveloping them can also be present. Samples collected from the shallower sediments at Hydrate Ridge show that the residence time of such hydrate enveloped-methane bubbles may be less than the time needed for diffusion (Suess et al., 2001).

Further evidence for such gas trapping comes from a laboratory study of methane production by hydrate dissociation by heating that showed an abrupt peak in methane production rate, while the rate of water production remained almost constant (Tang et al., 2005), perhaps due to release of co-existing methane gas. A similar abrupt peak in methane production has been observed also using depressurization (Xiong et al., 2012).

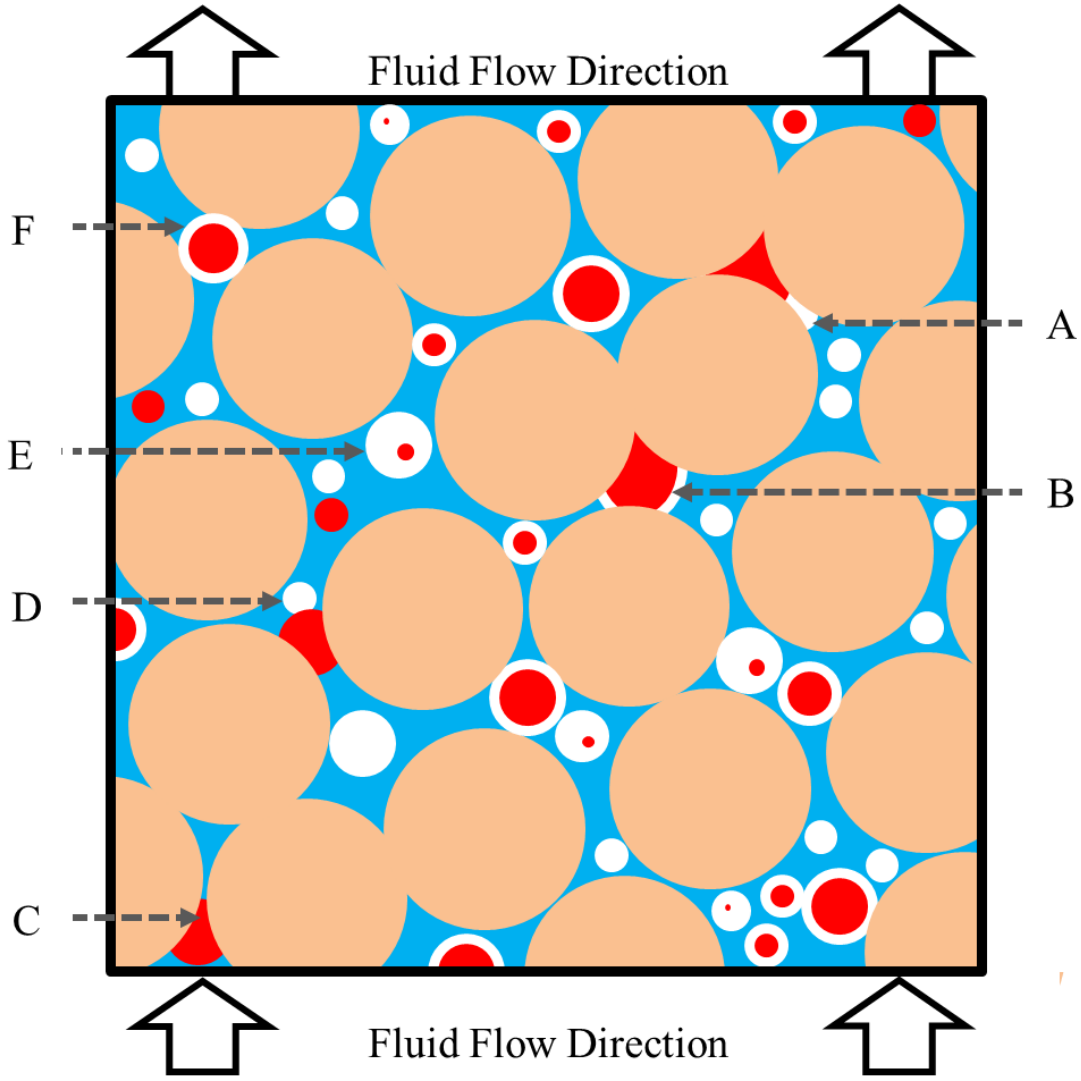

Figure 3.4 Conceptual model showing various mechanisms (marked A to F) for co-existence of methane gas and hydrate even when methane hydrate stability conditions prevail in the system. Red is methane gas, white is hydrate, brown is sand and blue is saline water (brine). A, B: pore blocked by hydrate formation. C: capillary pressure of pore not allowing the gas to move through it. D: capillary pressure of the pore increased by hydrate formation, not allowing further passage of gas. E: occlusions (unconnected inclusions) of gas within hydrate. F: hydrate film enveloping the gas bubble.

3.4.2 Effect of co-existing gas within the GHSZ on hydrate saturation estimates

Resistivity based methods for determining hydrate saturation do not differentiate between gas and hydrate; all resistive material in the pore space within the GHSZ is generally interpreted as hydrate (e.g., Hsu et al., 2014; Schwalenberg et al., 2010; Weitemeyer et al., 2006). Similarly, in our experiment, if we interpret all resistive material in the pore space as hydrate, the ERT method over-

estimates the hydrate saturation because both gas and hydrate are resistive compared to brine (Figure 3.5). Small apparent fluctuations in the total amount of resistive material inferred from ERT results come from uncertainty when selecting the empirical parameters in Equation 3.17 (Section 3.3.2). The PT method can differentiate between methane gas and hydrate because gas and hydrate have different volumetric densities (Section 3.3.1). In our laboratory experiment, up to 36% of the resistive material remained as gas. In a borehole offshore Japan, the difference between hydrate saturation from resistivity methods and from sonic methods was *c.* 50%, likely due to co-existing gas (Miyakawa et al., 2014). Table 3.1 lists other field studies with differences in hydrate saturation inferred from resistivity methods and seismic/sonic methods.

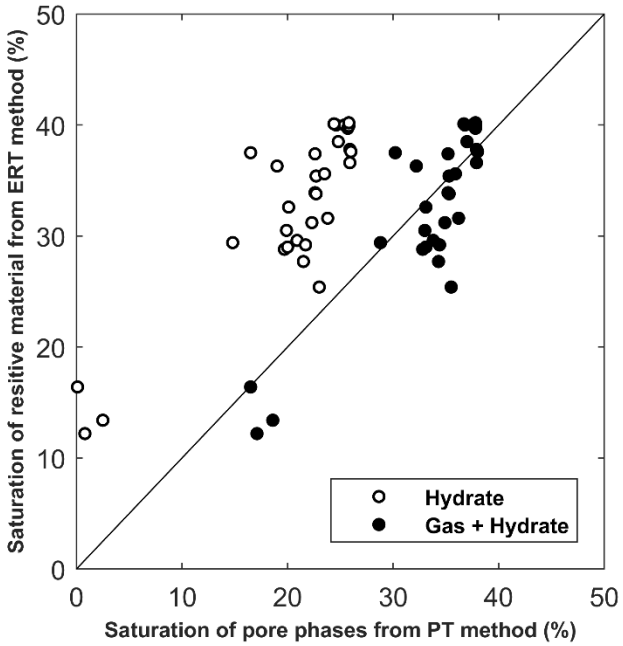

Figure 3.5 Total methane gas and methane hydrate saturations (volume percentage of pore space) from the pressure temperature (PT) method plotted against saturation of all resistive material deduced from the resistivity (ERT) method. Relative errors in the saturations calculated from the ERT and PT methods are less than 2% and 0.5%, respectively.

Further uncertainties in methane quantification based on resistivity data can occur due to such co-existing gas. The methane content per unit volume of the gas phase is different to that of the hydrate phase. The difference depends on the molar volumes of hydrate and gas, which in turn depend on pressure and temperature, with greater variations in the gas phase than in the hydrate phase. Hence, the uncertainty in the methane inventory is larger in shallower water depths where gas molar volumes are higher. The methane content of the GHSZ is over-estimated in shallower waters (e.g., less than *c*. 1250 m depth for the Arctic Ocean) and under-estimated in deeper waters, where the molar volume of methane gas is less than that of hydrate.

If the amount of co-existing gas within the GHSZ is significant, then it can affect the carbon content, and the geophysical and mechanical properties of the hydrate bearing sediments. Current numerical models that simulate the behaviour of natural and laboratory hydrate systems do not account for this type of co-existing gas. Additional work is needed to support further our results, such as performing a similar study on different types of samples, and/or synchrotron X-ray computed tomography of hydrate- and gas-bearing samples.

3.5 Conclusions

In repeated cycles of hydrate formation and dissociation, our experimental results demonstrate the co-existence of up to 26% hydrate with about 12% gas. We infer that not all of the methane gas and water formed hydrate even when the two phase water-hydrate stability conditions were satisfied. We suggest such co-existence occurs when methane gas bubbles become enveloped in hydrate films. A sufficiently thick hydrate film would isolate the gas trapped inside from the brine outside, even when hydrate stability conditions prevail. Such methane bubbles enveloped in hydrate films have also been observed in samples from Hydrate Ridge, offshore Oregon USA, with up to 55% of the bulk hydrate volume made up of co-existing gas. Our experimental results show that hydrate formation from methane in the gas phase results in up to 36% co-existing gas (as a percentage of the bulk hydrate volume).

Our results support the idea that co-existing gas may be present within the gas hydrate stability zone in natural gas hydrate systems, with gas influx through fractures in fine-grained sediments**.** We suggest that this co-existence of gas and hydrate is one possible explanation for the differences in hydrate saturation estimates between resistivity and seismic/sonic observations of natural hydrate systems.

Acknowledgments

We acknowledge funding from the UK Natural Environment Research Council (grant no NE/J020753/1). Hydrate phase boundaries were calculated by the Centre for Gas Hydrate Research at Heriot-Watt University (http://www.pet.hw.ac.uk/research/ hydrate), using the Heriot-Watt Hydrate and Phase Behaviour Programme (HWHYD). We thank K. Amalokwu and E. Attias for their advice on experimental troubleshooting. We thank P. J. Talling for his valuable comments on the manuscript. T. A. Minshull was supported by a Royal Society Wolfson Research Merit award. We also thank the editor Andre Revil, associate editor Ludmila Adam and two anonymous reviewers for their valuable comments.

Chapter 4 Insights into laboratory methane hydrate formation morphologies from 4D synchrotron X-ray computed tomography and their effect on elastic wave velocity

This chapter forms a manuscript in preparation: Sourav K. Sahoo, Madhusudhan B.N, Hector Marín-Moreno, Laurence J. North, Sharif Ahmed, Ismael Falcon-Suarez, Tim A. Minshull and Angus I. Best.

Abstract

We studied the evolution of methane hydrate morphology with hydrate saturation in sandstone and sand, and its effect on elastic wave velocities. These observations could be important for seismic data interpretation in terms of hydrate content and sediment strength, needed for natural resource and geohazard assessments. In the laboratory experiment on Berea sandstone, we measured ultrasonic P- and S-wave velocity (also electrical resistivity tomography, pressure and temperature) during four methane hydrate formation and dissociation cycles, at both 10 MPa and 55 MPa differential pressures (confining minus pore pressure). In a separate experiment, we performed synchrotron high resolution (0.325 µm), time lapse (4D), X-ray computed tomography imaging of methane hydrate formation and dissociation in Leighton Buzzard sand. Initially, hydrate forms by enveloping gas bubbles while, synchronously, gas escapes from these bubbles via diffusion and/or the rupture of the hydrate shell caused by pressure and temperature variations. This gas either forms smaller bubbles or more hydrate. This process generates a transition from pore-floating to pore-bridging hydrate at the scale of individual pores. Finally, the pore-bridging hydrate connects with that from adjacent pores creating a hydrate framework that interlocks with the sand grain framework. In agreement with previous studies, we observed the microporous structure of hydrate and thin water films enveloping sand grains, even after 48 hours of hydrate formation. Coexisting gas was observed even when the system had sufficient water and was under two phase hydrate stability conditions. By inference, and through the use of a rock physics model, the ultrasonic velocities of Berea sandstone appear to be sensitive to these morphology transitions with hydrate growth. We conclude that interlocking hydrate pore frameworks, porous hydrate, and co-existing gas with hydrate under hydrate stability conditions are all likely to be found in natural hydrate-bearing sediments with continuous gas charge.

4.1 Introduction

Gas hydrates are naturally occurring ice like clathrate compounds that form when sufficient gas (generally methane) and water coexist under low temperatures and high pressures, generally found in marine and permafrost environments (Kvenvolden, 1993). Currently, seafloor gas hydrates are being considered as a viable alternative energy resource (Boswell and Collett, 2011), and may have an important role in future climate change (Archer et al., 2009), carbon dioxide sequestration (Jung et al., 2010) and continental slope stability (Sultan et al., 2004). As such, it is important to obtain accurate estimates of the amount and distribution of gas hydrates, which relies mainly on geophysical remote sensing technologies and data interpretation. The latter depends on knowledge of hydrate formation processes and how they affect geophysical properties. In general, the presence of hydrate increases the seismic velocity (Helgerud et al., 1999) and electrical resistivity (Edwards, 1997) of host sediments, depending on hydrate morphology and saturation of the pore space. In particular, elastic wave velocity and electrical resistivity anomalies have been used to quantify hydrates in marine sediments, based on rock physics models that relate hydrate content to velocity (e.g., Collett, 2001; Ecker et al., 2000; Edwards, 1997; Helgerud et al., 1999).

Accurate quantification of *in situ* methane hydrates using rock physics models are hampered by our limited understanding of the effects of hydrate content, morphology and distribution, along with sediment type, porosity, permeability, and pore fluid salinity (e.g., Waite et al., 2009). These effects are difficult to understand unambiguously from studies of natural samples alone because of spatial averaging and lack of information of the sub-surface. Moreover, using natural samples for laboratory studies of geophysical and geomechanical properties is often challenging because: (i) coring is technically difficult and requires expensive drill ships with autoclave sampling capability; and (ii) absolute preservation of *in situ* conditions is not possible currently (Tulk, 1999), e.g., *in situ* pressures can be preserved, but, to our knowledge not temperature. Hence, controlled laboratory experiments on synthetic hydrate samples offer a viable alternative to gain insight into the physical properties of hydrate-bearing sediments. Synthetic hydrate samples allow potentially the full range of hydrate saturations and morphologies to be explored for different sediment types, although laboratory methods have their own challenges.

Several laboratory studies have provided insight into effects of hydrate content and distribution on geophysical and geomechanical properties of hydrate bearing sediments (e.g., Handa, 1990; Kerkar et al., 2014; Priegnitz et al., 2015; Priest et al., 2009; Tohidi et al., 2001), but further research is needed to better understand in particular i) the discrepancy between hydrate saturation estimates from seismic/sonic methods and from electrical resistivity methods (e.g., Attias et al., 2016; Goswami et al., 2015; Lee & Collett, 2006; Miyakawa et al., 2014) (referred to here as the seismic-

electrical discrepancy); and ii) the effect of methane hydrate saturation and morphology on seismic/sonic velocity of the hydrate bearing sediments. Some studies associate the seismic-electrical discrepancy to the coexistence of gas and hydrate, as the presence of gas can reduce the seismic velocity but not the electrical resistivity of the sediment (e.g., Lee and Collett, 2006; Miyakawa et al., 2014; Attias et al., 2016). This discrepancy could also be due to incorrect assumptions about the morphology or distribution of hydrate within the pores.

Natural hydrates commonly exist in several morphologies (or habits) within the host sediments. The term morphology is used here to mean the shape and distribution of the solid hydrate grains within the host sediment. Some published definitions of hydrate morphology (e.g., cementing, non-cementing, load bearing, pore-filling, etc.) were based on how hydrate morphology affects elastic wave properties in particular. Morphology can be divided broadly into two types: sediment grain displacing or pore-fluid displacing (e.g., Holland et al., 2008). Sediment grain displacing hydrate physically moves apart sediment grains, forming solid hydrate volumes larger than the sediment pore size; examples include hydrate veins, layers, and lenses. Pore fluid displacing hydrate grows inside the intact structure of sediment pores. Most pore fluid displacing natural hydrate has been observed in cores from coarse-grained silty or sandy layers, such as those from NGHP1 (Collett et al., 2015) and IODP Expedition 311 (Riedel et al., 2010), which show pore fluid displacing hydrate in coarse-grained layers. We used sandstone in our experiments, so we shall only discuss pore-fluid displacing hydrate.

Pore-fluid displacing hydrate can be sub-divided into cementing or non-cementing morphologies (e.g., Ecker et al., 1998). Cementing morphology occurs when hydrate bonds host mineral grain contacts (Ecker et al., 1998); this was modelled theoretically as either hydrate located exclusively at grain contacts or hydrate evenly coating mineral grains, a proportion of which bonds grain contacts (Ecker et al., 1998; Helgerud et al., 1999). In fact, several studies (e.g., Chand et al., 2006; Priest et al., 2005) have shown that hydrate forms cement under excess gas conditions by coating the mineral grains, with a fraction of the hydrate saturation acting as cement. By contrast, non-cementing hydrate forms when hydrate grows away from the sediment grain contacts (Ecker et al., 1998). The cementing morphology has a much greater effect on the elastic properties of hydrate-bearing sediments compared to the non-cementing morphology (Best et al., 2013; Ecker et al., 1998; Priest et al., 2009; Waite et al., 2004). However, the non-cementing morphology is thought to dominate natural hydrate systems, and has been sampled, or inferred, at locations such as Mallik, Mackenzie Delta (Uchida et al., 2000), the Nankai Trough (e.g., Fujii et al., 2015), Alaminos Canyon, Gulf of Mexico (Boswell et al., 2009), and Mount Elbert, Alaska North Slope (Stern et al., 2011). A useful summary of observations of hydrate morphologies at various sites around the world was provided by Holland et al. (2008) and Dai et al. (2012).

If non-cementing hydrate grows in the pore space without bridging neighbouring sediment grains, then it is termed pore-floating (Hu et al., 2014) or pore-filling hydrate (i.e. hydrate may be partially filling the pore, but not contacting more than one grain of the sand frame). In this manuscript we use the term "pore-floating" for such hydrate morphology. If hydrate bridges neighbouring sediment grains (i.e. contacts more than one grain in the sand frame) then this is termed "frame-supporting" or "load-bearing" or "pore-bridging" hydrate. We will use the term "pore- bridging" to describe this morphology, which has been reported for pore-floating hydrate saturations greater than 25 - 40% (Hu et al., 2014; Priest et al., 2009; Waite et al., 2009).

Note that solid hydrate may not make solid-solid contact with host mineral grains, if the mineral grain surfaces are wet. Most likely bound water envelopes the water wet silica grain surfaces under excess water conditions, meaning that a thin film of water is always present between the solid host mineral grain and the solid hydrate (Chaouachi et al., 2015; Tohidi et al., 2001). This effect should apply to both cementing and pore-bridging hydrate. However, the above definitions are derived both conceptually and from observations of changes in elastic wave velocity for hydrate at different saturations. While cementing and pore-bridging hydrate are both associated with an increase in the elastic moduli of the composite sediment, pore-floating hydrate does not affect the sediment's frame moduli.

Priest et al. (2009) deduced a pore-bridging morphology for methane hydrate formed in sand under excess water conditions from observed increases in seismic velocity at hydrate saturations higher that 30%; for saturations of 10% and 15%, the seismic velocity was between those for pore-bridging and pore-floating hydrate (Priest et al., 2009). Yun et al. (2005) showed that tetrahydrofuran (THF) hydrate grows in the pore-floating morphology up to 40% hydrate saturation; for higher saturations, the measured velocity was much higher than that predicted for the pore-floating morphology, qualitatively consistent with a pore-bridging morphology.

Hydrate formation does not take up all the methane gas or water even if the system is under two phase water-hydrate stability conditions (Sahoo et al., 2018; Chapter 3). Here we present laboratory methane hydrate formation and dissociation results from P- and S-wave velocity analysis, electrical resistivity tomography, and 4D time-resolved synchrotron radiation X-ray computed tomography (SR-XCT) to support our previous observations and track the evolution of hydrate morphology during formation. Several researchers have stressed the need for time-resolved tomography (4D-tomography) to aid a better understanding of hydrate systems (Kuhs et al., 2004; Murshed et al., 2008). SR-XCT (Klapp et al., 2007; Murshed et al., 2008) and 4D SR-XCT (Chaouachi et al., 2015; Kerkar et al., 2014; Yang et al., 2016) have been used to study both natural and synthetic hydrate.

To increase the X-ray contrast between methane hydrate and water, which is low, Kerkar et al. (2014) used methane hydrate with 5 w.t. % $BaCl_2$ solution as the pore fluid, while Chaouachi et al. (2015) and Yang et al. (2016) used xenon hydrate. As natural hydrate are generally composed of methane gas and found in marine sediments (e.g., Kvenvolden, 1993), we choose to use methane gas in 35gm/l NaCl solution. We used a density based approach to differentiate the different pore phases, which is discussed in Section 4.3.5.

Our results provide further evidence on how methane hydrate saturation relates to hydrate morphology, on how this morphology influences elastic wave velocity and electrical resistivity, and on the presence of coexisting methane gas. The synchrotron imaging dataset is novel and has been only partly used here to study the changes in hydrate morphology. We plan to discuss the synchrotron results in more details in a separate paper.

4.2 Methods

4.2.1 Ultrasonic velocity and electrical resistivity measurements

We used a stainless steel high-pressure cell, designed to host 5 cm diameter rock samples under hydrostatic confining pressure up to 65 MPa (see Figure 4.1a) (Ellis, 2008). The cell was instrumented to monitor pore fluid pressure, and the inner and outer (ambient) cell temperature. The inner temperature sensor was placed on the outer surface of the rubber sleeve to indicate the sample temperature. The inlet pore pressure pipe was connected via a three-way valve to a vacuum pump, a methane gas cylinder (with pressure regulator) and a brine reservoir. A syringe pump was used to inject brine into the sample in a controlled manner, while the temperature of the system was regulated by a controlled cooling circuit.

The inner cell was configured for ultrasonic pulse-echo measurements of P- and S-wave velocity (V_p and V_s) with an accuracy ± 0.3%; see methods outlined by Best et al. (1994). The single pulse-echo piezoelectric transducer insonifies a central cylindrical part of the sample, as indicated in Figure 4.1a.

The inner rubber sleeve that prevents direct contact between the mineral oil used as confining fluid and the rock sample is perforated by 16 electrodes for electrical resistivity tomography (ERT) measurements (North et al., 2013). Under typical operating conditions, the resistivity measurement error is ≤ 0.1% (at A/C frequencies 1 - 500 Hz) for samples in the electrical resistivity range 1 - 100 Ω m (North et al., 2013). Electrodes were in tetra-polar configuration, radially distributed in two rings around the sample. This system does not allow simultaneous ultrasonic and electrical measurements because the ultrasonic system gives a ground path for the electrical system. Hence,

whenever the ERT readings were taken, the ultrasonic cables had to be disconnected. The ERT system took nearly one hour for each measurement, so we have fewer ERT measurements.

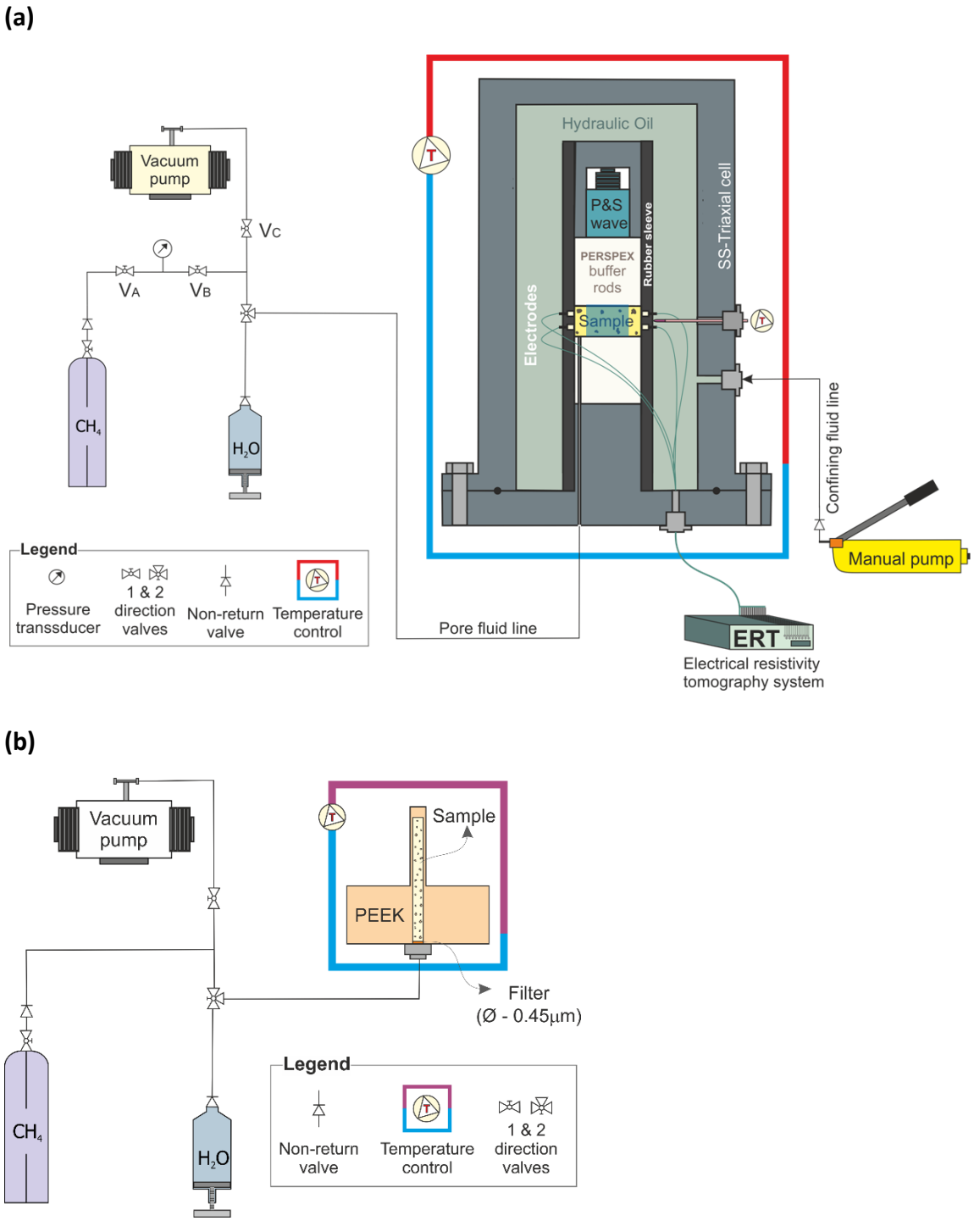

Figure 4.1 Schematic representation of the experimental setup: a) ultrasonic rig; b) synchrotron rig. In a), the blue region inside the sample marks the insonified zone of the sample.

4.2.2 Synchrotron X-ray CT imaging

We designed and manufactured a miniature cylindrical hydrate rig for use at the TOMCAT Swiss Light Source (SLS) facility in Switzerland. It was made from monolithic PEEK plastic by precision lathe and drilling machines (see Figure 4.1b). The rig had an internal diameter of 2 mm, a wall thickness of 0.8 mm and sample scan height of 10 mm (23 mm total height). The gas hydrate formation and dissociation process was imaged through computed tomography (CT) using monochromatic X-rays from a synchrotron source (TOMCAT SLS). Beam energy of 21 keV, 81 mm propagation distance, 200 ms exposure time with 1.25 x, 4 x and 10 x objectives were chosen after trial runs to obtain images at 1.625 µm, 0.625 µm and 0.325 µm resolution, respectively. Figure1b shows details of the hydrate rig including the pore fluid injection system and temperature control. The TOMCAT facility uses phase shifts of the X-rays as they pass through the sample (Fitzgerald, 2000; Stampanoni et al., 2002). We used the phase reconstruction algorithm described by Paganin et al. (2002). Reconstructed CT data were post-processed using ImageJ and visualized using Amira-Avizo® 3D software.

Each voxel is much smaller than the sand grains, which have a mean grain size (d_{50}) of 100 µm. We calibrated the grey scale values in the CT data to known standard densities (sand, brine, hydrate and methane gas; e.g., Kneafsey et al., 2007). We implemented a segmentation technique to give a better visualization. This allows for a range of density values, shown as grey scale colors, to be highlighted for enhanced visual contrast. Such a segmentation technique has been used in several hydrate-related studies (Hu et al., 2014; Kneafsey et al., 2007; Rees et al., 2011). For example, Rees et al. (2011) studied a natural gas hydrate sample collected in NGHP-1 using this segmentation technique.

4.2.3 Porous media

We used a cylindrical sample (4.97 cm diameter and 2.06 cm height) of Berea sandstone with a porosity of 0.22, permeability of 448 mD (4.48×10^{-13} m^2) as a stable, inert, and well-characterized porous medium for the ultrasonic experiment (the pulse-echo system was configured for rock samples, not loose sand). The grain size is about 100 µm, similar to observations by other researchers (e.g., Minagawa et al., 2008). X-ray diffraction analysis of the sample Berea rock by (Han et al., 2015) showed 1.7% illite and 3.3% K feldspar in volume. For the synchrotron imaging, we weighed and tamped Leighton Buzzard sand (a mean grain size d_{50} =100 µm) directly into the cylindrical hydrate rig (2 mm diameter and 23 mm height) to obtain a sample of 35% porosity (typical permeabilities are several Darcies for such sand packs).

4.2.4 Hydrate formation

We followed the method of Waite et al. (2004) with high initial brine saturation (83.5% for ultrasonic and 90% for synchrotron sample) giving excess water conditions (Ellis, 2008; Priest et al., 2009). Our experimental setup with gas injected from the base of the sample represents gas hydrate systems with localized gas flow, such as at the base of the gas hydrate stability zone (GHSZ), or near to gas chimneys.

Each sample was firstly oven-dried at 60 ˚C before placing in their respective rigs. A hydrostatic triaxial confining pressure of 10 MPa was applied to the Berea sample in the ultrasonic rig while only pore fluid pressure was applied to the sand in the synchrotron rig. A pore fluid line vacuum of 1 Pa was applied to each sample to remove as much air as possible from the pore space. Brine (35 gm/l NaCl solution in deionized and deaerated water) was injected to partially fill the sample pore spaces. The samples were left for 3 days so that the pore fluids could re-distribute by capillary action. The remaining pore space (16.5% for ultrasonic and 10% for synchrotron), which was previously under vacuum, is assumed to become occupied by water vapour and any remaining air.

Methane gas was then injected to achieve a pore fluid pressure of 11.9 MPa and simultaneously, the confining pressure was increased to 21.9 MPa to maintain a constant differential pressure of 10 MPa. The pore fluid system was then sealed, keeping the pore fluid line between the sample and valve V_A (Figure 4.1a) filled with methane gas, which is free to move in and out of the sample as a result of potential pore pressure variations. Finally, hydrate was formed by cooling the system to fall within the gas hydrate stability conditions (GHSC). After hydrate formation, dissociation was achieved by heating the system to fall outside the GHSC.

The hydrate formation procedure was similar in both experiments with slight variations as described below.

Ultrasonic P- and S-wave velocities of Berea sandstone are known to be sensitive to changes in differential pressure due to micro cracks in the framework of mineral grains (e.g., Nur and Simmons, 1969). Hence, a constant differential pressure was maintained in the ultrasonic rig to rule out any such effects. This approach ensured that any change in velocity could be attributed to changes in pore fluids and hydrate formation only. Four cycles of hydrate formation and dissociation were completed in the ultrasonic rig; a differential pressure of 10 MPa was maintained for cycles 1 and 2, and 55 MPa for cycles 3 and 4. Hydrate, gas and brine saturation were calculated from the measured pressure and temperature changes of the system using a thermodynamic method (Sahoo et al., 2018; Chapter 3).

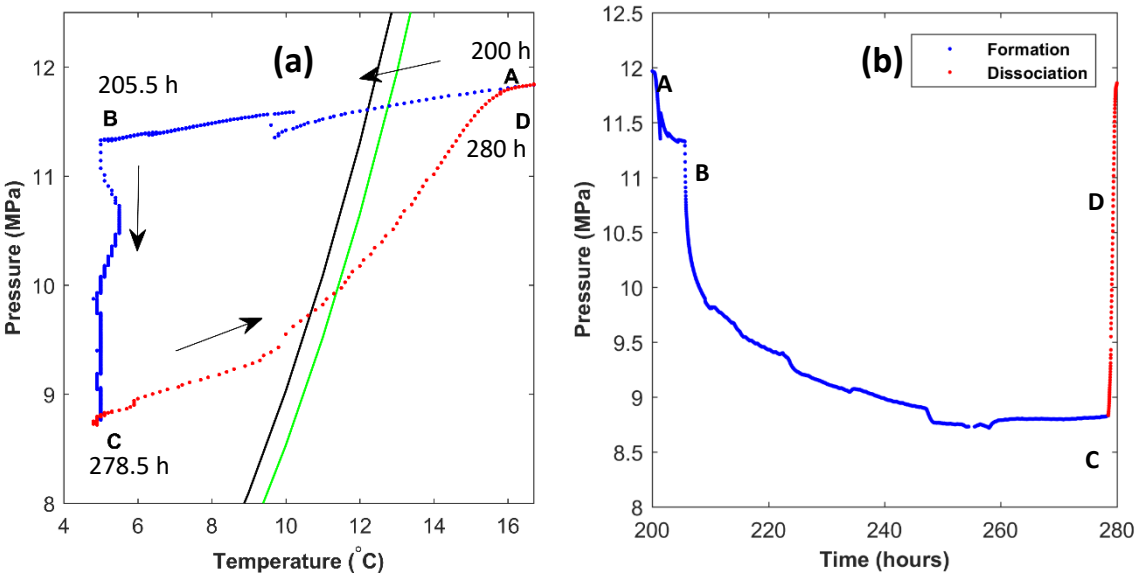

Figure 4.2 Changes of a) pressure versus temperature, and b) pressure with time during methane hydrate formation and dissociation in Berea sandstone. Only the second cycle of hydrate formation and dissociation is shown for clarity. The green and black lines are the pure methane hydrate phase boundary for 35 g/L and 46 g/L salinity respectively, calculated using the approach of Tohidi et al. (1995). Blue dots represent cooling and red dots represent heating. In a) time is shown in hours (h). Trajectory ABC marks cooling of the system to 5 °C and hydrate formation. Trajectory CD shows hydrate dissociation. c) and d) show pressure and temperature change with time during trajectory AB. See text for further details.

In the synchrotron rig, the differential pressure was assumed equal to the applied pore fluid pressure, with the PEEK cell providing rigid confinement. We applied 10 MPa of methane pressure directly through the injection inlet, filling the pore fluid pipe and sand sample volume with a pre-calculated amount of brine solution. We then left the rig for three days for the pore fluids to redistribute within the pore space. Only one cycle of hydrate formation and dissociation was performed.

4.3 Results and discussions

4.3.1 Electrical resistivity tomography (ERT)

We use the ERT results to deduce changes in fluid distribution in the Berea sandstone experiments (Figure 4.3).

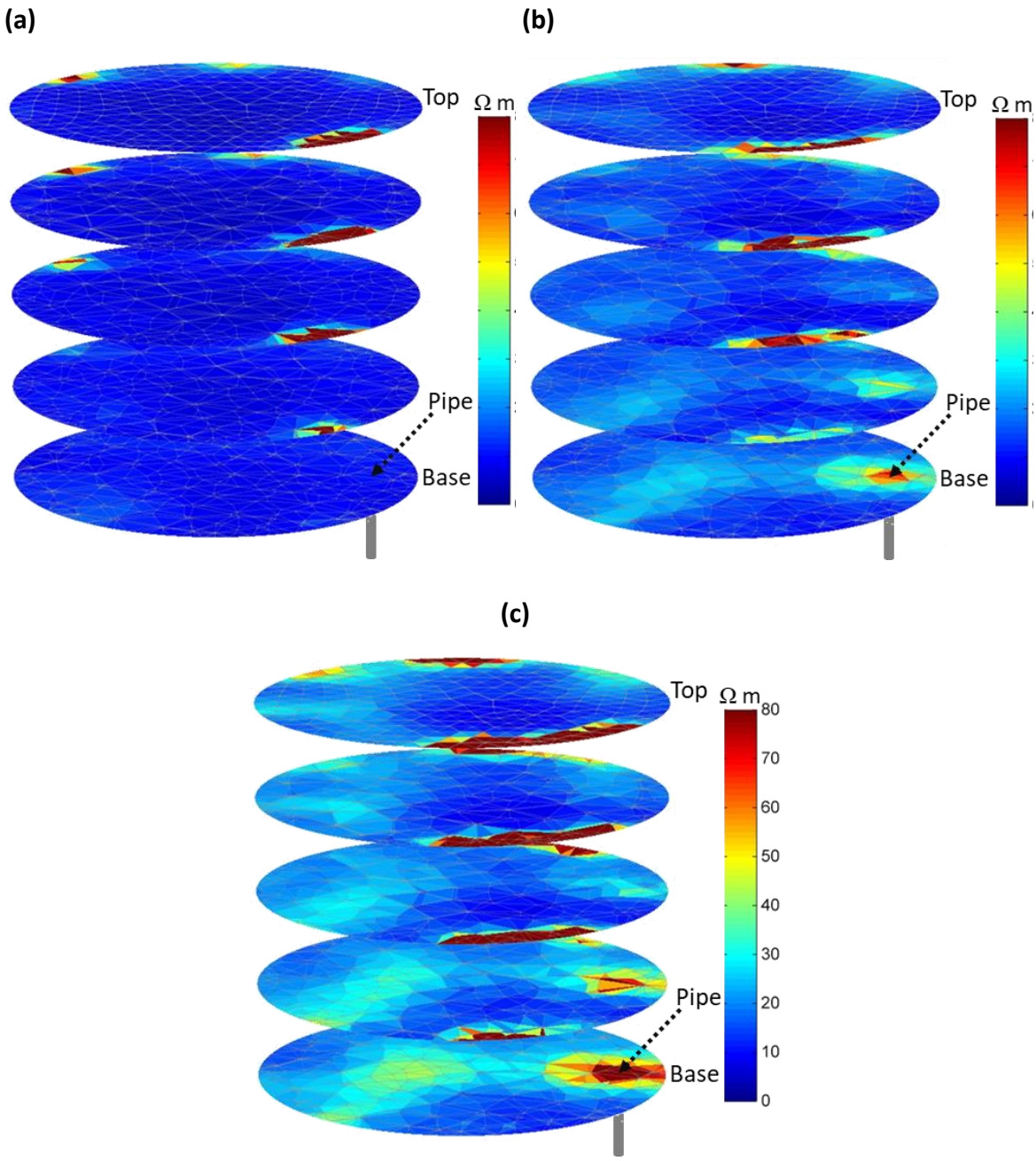

Figure 4.3 Electrical resistivity tomography results for Berea sandstone, using the methods of (North et al. (2013), showing distributions of resistive phases in the pore space during various stages of hydrate formation in cycle 1: a) after water injection; b) after gas injection (pore space has both gas and water); c) after maximum hydrate formation (pore space has hydrate, gas and water). The grey line shows the position of the pore fluid inlet at the base of the sample. Resistivity values above 75 Ωm, seen around the boundaries of the sample on all images, are possibly artefacts due to the poor electrode contacts at those locations; see text for details.

The ERT results indicate a homogeneous distribution of water, apart from a few small high resistivity patches at the edges, 3 days after water injection (Figure 4.3a). These patches could be caused by

water vapour (water saturation was 83% of the pore volume, injected after a vacuum was formed; see methods above). Resistivity values above 75 Ωm, seen around the boundaries of the sample on all images, are possibly artefacts due to the poor electrode contacts at those locations. If an electrode loses physical contact with the sample or its contact is obstructed by gas or hydrate, this loss of contact can give rise to such artefacts. Priegnitz et al. (2015) showed such cases of hydrate formation on some electrodes. Figure 4.3b shows the sample at 33 hours after methane gas injection, with gas patches indicated by increases in resistivity above 25 - 30 Ωm. The ERT images illustrate that the gas migrated upwards through the sample from the inlet pipe at the base (indicated in Figure 4.3b), with decreasing gas concentration indicated by higher resistivity values (lighter blue) at the base and lower values (darker blue) at the top. A high resistivity path (marked by light green to green colour) is discernible in the lower part of the sample, which seems to be a high permeability path allowing lateral gas migration. Figure 4.3c shows the sample after maximum hydrate formation (75 hours after the onset of cooling). The ERT results suggest that hydrate formed mainly around the areas of high gas content seen in Figure 4.3b, indicated by the elevated resistivity values above 15 Ωm in Figure 4.3c. As both gas and hydrate are resistive compared to brine, high resistivity could also be due to co-existing gas with hydrate. However, the overall increase in sample resistivity after maximum hydrate formation (bulk average resistivity of 56 ± 0.06 Ωm), compared to partial gas/water saturation resistivity of 25 ± 0.03 Ωm, suggests that the increase is mainly due to hydrate growth, with minor contribution from flow of additional gas from pipe to sample. This is supported by thermodynamic calculations from changes in pore pressure and temperature (Sahoo et al., 2018; Chapter 3) giving up to 26% gas hydrate co-existing with 12% methane gas.

4.3.2 Ultrasonic velocity changes during hydrate formation and dissociation.

The cooling of the system into the GHSC to a temperature of 5 ˚C generated a reduction in pore pressure as shown in Figure 4.2, points ABC. The pressure drop can be explained mainly by hydrate formation, with some contribution from methane gas contraction and increased gas solubility. A slight increase in temperature can also be seen in Figure 4.2a between points B and C, caused by the exothermic reaction of hydrate formation (Hwang et al., 1990). Figure 4.4 shows rapidly increasing P- and S-wave velocities (V_p and V_s, respectively) during the initial 10 hours of hydrate formation, followed by a more gradual increase thereafter. Once hydrate formation ceased, indicated by the end of the pore pressure decrease at about 260 hours (Figure 4.2b), the system was left at that pressure and temperature to ensure complete hydrate formation. The horizontal asymptotic behavior of the pore pressure in Figure 4.2b, and of V_p and V_s in Figures 4a & b is

evidence that no further hydrate formation took place. Similar indicators were adopted by other researchers (e.g., Waite et al., 2004).

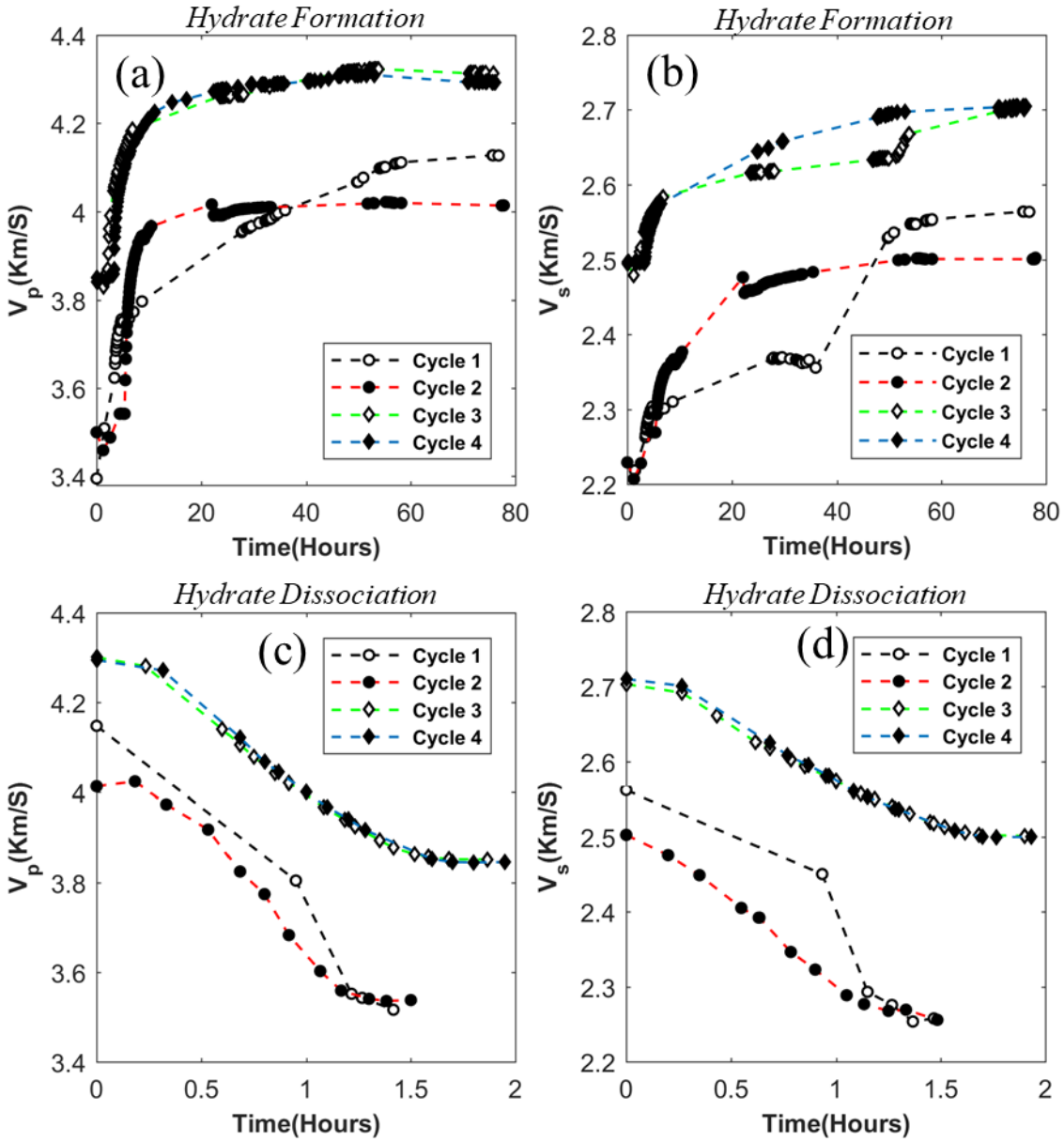

Figure 4.4 Changes in ultrasonic (667 kHz) P- and S-wave velocity (V_p, V_s) during hydrate formation (a, b) and dissociation (c, d). Differential pressure was 10 MPa for cycles 1 & 2 was, and 55 MPa for cycles 3 & 4. Although the cycles are continuous and sequential, we have normalized the time axis for easy comparison. Zero time for a given cycle marks the beginning of cooling or heating for hydrate formation or dissociation respectively.

Figure 4.4a and b show that the initial (start of hydrate formation cycle) V_p and V_s for the first and second cycles were lower than those for the third and fourth cycles. This is expected and is consistent with the differential pressure of 10 MPa for the first two cycles, and 55 MPa for the last

two cycles (e.g., see typical velocities for water-or brine-saturated Berea sandstone in Prasad and Manghnani, 1997). The time taken to reach the maximum velocity in the first cycle is longer than that of the subsequent cycles, which may be due to a methane hydrate formation memory effect (Ohmura et al., 2003; Sloan and Koh, 2007; Takeya et al., 2000), although some researchers dispute the hydrate memory effect (Buchanan et al., 2005). Instead, it may be due to an increase in the contact area of the gas/brine interfaces after the first formation and dissociation cycle, associated with a more even distribution of smaller gas bubbles. Smaller spheres have a larger surface area per unit volume than larger ones, and this change could increase the reaction surface. Interestingly, the maximum V_p and V_s in cycle 1 are larger than those of cycle 2, and we discuss this observation in Section 4.3.3. The increase in Vs with hydrate formation in cycles 1 and 3 shows two distinct segments, with an initial increase followed by a plateau, followed by a renewed velocity increase up to a plateau at the maximum V_s. Cycles 1 and 3 can be considered as the first cycles at each differential pressure, 10 MPa for cycle 1 and 55 MPa for cycle 3. By contrast, V_s of cycles 2 and 4, and V_p of all cycles, do not show this two segment increase. Since the horizontal axis of Figure 4.4 is time, it is difficult to rule out the effect of hydrate formation rate. These observations are discussed further in Section 4.3.3.

As the system was taken out of the GHSC by heating, there was an increase in pore pressure (trajectory CD in Figure 4.2) and a decrease in V_p and V_s (Figure 4.4 c, d). There is a notable difference between the curves of the first and second cycles, while the third and fourth cycles are very similar. Such differences could be due to similar reasons as described for hydrate formation, and will be discussed further in Section 4.3.3.

4.3.3 Morphology of hydrate from ultrasonic velocity

The observed increases in V_p and V_s in Figure 4.4a & b depend on both hydrate saturation and morphology. Here, we apply the hydrate bearing effective sediment (HBES) model of Marín-Moreno et al., (2017) to our experimental results with the aim of relating changes in velocity to changes in hydrate saturation and morphology. We adapted the HBES model for pore-bridging hydrate using the approach of Ecker et al., (2000), which considers that pore bridging hydrate reduces the porosity and affects the elastic properties of the solid phase.

The HBES model input parameters are given in Table 1. As our sample was not pure quartz (1.7 volume % illite and 3.4 volume % k-feldspar), we first used the Voigt–Reuss–Hill average to calculate the bulk and shear modulus of the grains, which were then used as an inputs to the HBES model. The saturation of hydrate, gas and brine in the pore space was calculated from changes in pore pressure and temperature using the thermodynamics approach of Sahoo et al. (2018; Chapter 3).

We used these calculated saturations of gas, water and hydrate for the HBES model. This saturation calculation showed the presence of co-existing gas even at maximum hydrate saturation, and hence we included the bubble resonance effect in the HBES model. The pore size in our Berea sample varied from 11 µm to 73 µm, measured from SR-XCT, and we choose to use 20 and 40 µm bubble diameter in the HBES model. We expect that initially the bubble size would almost fill the pore and with formation of hydrate the bubble size would reduce, this is based on observation from synchrotron images (Section 4.3.5). The aspect ratio and concentration of secondary porosity created due to hydrates (Marín-Moreno et al., 2017), was chosen based on the values used in Marín-Moreno et al., (2017) with both attenuation and velocity data matching of 448 – 782 kHz as discussed in Chapter 5. The concentration of inclusions in hydrate was set to zero, as they have negligible effect on V_p in our measurement frequency band (Chapter 5). Other parameters were kept same as that used by Marín-Moreno et al. (2017).

Table 4.1 Values used in the HBES model runs. Only those parameters with different values to those listed in Marin-Moreno et al. (2017) are given here, with the remaining parameters the same.

Parameter	**Values**
Critical porosity (Mavko et al., 2009)	0.36
K Feldspar bulk modulus (Mavko et al., 2009)	37.5×10^9 Pa
K Feldspar shear modulus (Mavko et al., 2009)	15×10^9 Pa
Illite bulk modulus (Mavko et al., 2009)	62.21×10^9 Pa
Illite shear modulus (Mavko et al., 2009)	25.70×10^9 Pa

Small increases in V_p and V_s for hydrate saturations (S_h) up to about 5% are well represented by implementing a pore-floating hydrate morphology in the HBES model (Figure 4.5). As hydrate saturation increases above 5%, the observed V_p increases more steeply and approaches the pore-bridging morphology model results at about S_h = 15%. It is generally accepted that when saturation of pore-floating hydrate increases, it eventually starts bridging the pores (Priest et al., 2009; Waite et al., 2009). Above S_h = 15%, the gradient of increasing V_p becomes shallower, and actually diverges

below the predicted pore-bridging increase of the HBES model. This observation indicates that, for saturations above 15%, only a small proportion of the newly formed hydrate is adding to bridging of the pores. Similarly, V_s continues to track the pore-floating HBES model up to S_h of 5%. For S_h > 5%, in contrast to V_p, V_s falls below the HBES model for pore-bridging morphology. A possible explanation is that when hydrate fills the pores in our experiments, it does not make solid-solid bonds to the host sand grains, as assumed in the HBES pore-bridging model. Instead, a thin, bound water layer may exist between the water wet sand grains and the hydrate. For example, Tohidi et al. (2001) showed a thin film of water always exists between methane hydrate and glass, irrespective of the method of hydrate formation. Chaouachi et al. (2015) showed a similar water film for xenon hydrate and sediment grains. A similar result for our methane hydrate and sand grains is supported by the X-ray CT images in Section 4.3.5.

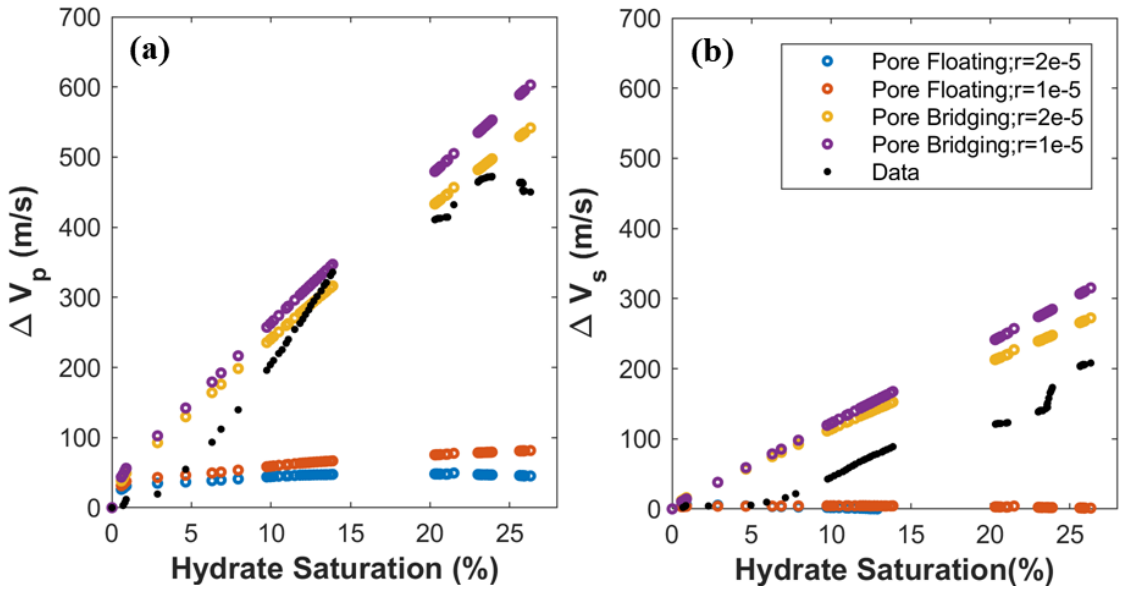

Figure 4.5 Comparison of measured and modelled change in a) P- and b) S-wave velocity with hydrate formation. The experimental data is that of the third cycle of hydrate formation with a differential pressure of 55MPa. The modelled velocities were obtained using the HBES model (Marín-Moreno et al., 2017); two bubble radii of 2 x 10^{-5} m and 1 x 10^{-5} m were used in model calculations, shown in the legend. The error in the experimental data is small compared to the symbol size.

We can extend the above concepts to methane hydrate formation in Berea sandstone during our ultrasound experiments. The presence of the water film could increase the Berea's frame bulk modulus in a similar manner to the pore-bridging model, but not the frame shear modulus. Only when sufficient hydrate has grown to interlock the sand grains, would the frame shear modulus increase, and then still less than for solid-solid contacts. This phenomenon could explain the rise of V_s above the pore-floating model line, but below the pore-bridging model line.

There is a steep increase in V_s around S_h = 23% in Figure 5.5b, with a less pronounced increase in V_p (Figure 4.5a). This behaviour was described earlier as a two-segment increase of V_s in cycles 1 and 3, not seen for Vp (Figure 4.4a and b). Cycles 1 and 3 are the first cycles at each differential pressure (10 MPa in cycles 1 and 2; 55 MPa in cycles 3 and 4). The steep increase in cycle 1 and 3 (at 39 hours for cycle 1, and 47 hours for cycle 3, in Figure 4.4b), might occur when sufficient hydrate has grown to interlock extensively the sediment. The sudden increase in V_s could indicate a threshold of interlocking when the rock frame shear modulus is stiffened significantly. Such a steep increase in not seen in V_p in Figure 5.4a, suggesting that the increase in bulk modulus is dominated by replacement of pore-fluid with pore-bridging hydrate, irrespective of whether the hydrate significantly interlocks or not. However, there is a less steep increase of V_p at S_h = 21% compared to the steep increase of V_s at S_h = 23% (Figure 4.5).

A possible explanation for the absence of such behaviour in cycles 2 and 4 could be a reduction in gas bubble size that results in pore-bridging aggregates formed of smaller hydrate “grains”. Hydrate forms on gas bubble surfaces, and smaller gas bubbles would result in smaller hydrate grains. With more hydrate formation, such hydrate grains would aggregate to eventually bridge the pores and interlock the rock frame, as discusses earlier. The smaller the grains forming the hydrate aggregate, the more discontinuities there are, giving a smaller shear modulus than for larger hydrate grains. Hence, aggregation of smaller hydrate grains may lead to a weaker effect on V_s. As discussed earlier, hydrate dissociation can lead to more uniform distribution of methane gas and a reduction in bubble size. So it is possible that bubble size is lower in cycles 2 and 4 than in cycles 1 and 3. The patterns of change of V_s and V_p for first and third cycles are similar, and the patterns are also similar between the second and fourth cycle (Figure 4.4 a, b). As expected, the magnitude of changes is higher for lower differential pressures (cycles 1 and 2).

The observation that V_p matches the pore-bridging HBES model but not V_s, likely due to the presence of water films between hydrate and sand, adds another level of complexity to the effect of hydrate morphology on elastic wave velocities. We no longer should view hydrate as pore-bridging in the sense of solid-solid contacts, but as a three-phase system of interlocking solid hydrate and host grain frameworks separated by water. Indeed, the presence of a thin water film between sand grains and hydrate is consistent with the Leclaire et al. (1994) three phase Biot model adapted for hydrate by Guerin & Goldberg (2005) and Carcione & Tinivella (2000). Best et al. (2013) found that this model gave reasonable predictions of shear wave attenuation (although velocity results were not shown). This observation also implies that the hydrate cementing model concept (i.e. solid-solid bonding at grain contacts or grain coating; see definitions in introduction) may need to be revisited to include this water layer effect. However, Priest et al. (2005) found that, under excess gas conditions, the grain coating cement model made equally good V_p and V_s predictions,

which both increase steeply for small amounts of hydrate (Sh < 5%); see also Chand et al. (2006). Priest et al. (2006) also invoked the presence of a thin water film between sand grains and cementing hydrate to explain the attenuation results from the same experiments described in Priest et al. (2005), where the velocity results were presented.

We see higher maximum V_p and V_s for cycle 1 than for cycle 2, while those for cycle 3 and 4 are similar (Figure 4.4). The difference in maximum V_p between cycles 1 and 2 is about double that of Vs. Different maximum velocities between cycles 1 and 2 can be explained by (i) higher hydrate saturation in cycle 1 than in cycle 2, and/or (ii) reduction in bubble size in cycle 2. In cycle 1, S_h could not be calculated due to a malfunctioning pressure gauge, and in cycles 2, 3 and 4 the maximum S_h values were 23%, 26% and 25%, respectively. The HBES model shows that a slight increase of pore-bridging S_h of 3% - 4% units could account for the observed discrepancies in maximum V_p and V_s between cycles 1 and 2 (Figure 4.5). A reduction in bubble size (pore-bridging curves in Figure 4.5) can cause a similar reduction. The latter mechanism is also consistent with a redistribution of methane gas and a change in bubble size occurring during hydrate dissociation and reformation, as discussed above.

4.3.4 Effect of differential pressure

The rate of change in V_p and V_s with Sh, for Sh of 10% - 15%, is much higher at a differential pressure of 10 MPa, than at 55 MPa (Figure 4.6). The onset of the rapid increase in V_p and V_s occurs at a lower S_h at 10 MPa than at 55 MPa. This behaviour might be due to the presence of microcracks at 10 MPa that are mostly closed at 55 MPa (e.g., Prasad and Manghnani, 1997; Han , 2010 PhD Thesis). When the microcracks are open at lower pressures, hydrate formation is likely to cause a much more dramatic initial stiffening of the rock frame bulk moduli than when the microcracks are closed at higher pressures, leading to a steeper increase in V_p and V_s, because the frame moduli are initially weaker. This effect is similar in magnitude to the normal velocity-pressure dependence reported for Berea and similar sandstones with microcracks, where velocity increases more rapidly at lower than at higher pressures (e.g., Eberhart-Phillips et al., 1989; Han et al., 2011; Prasad & Manghnani, 1997).

For cycle 2 only, an interesting step-increase in V_p and V_s is observed between S_h of 0 and 7% (Figure 4.6). This looks similar to the discontinuity of bulk modulus versus water/gas saturation discussed by Amalokwu et al. (2017). They attributed this discontinuity to one of two mechanisms associated with patchy gas saturation, related to either capillary or squirt flow effects. The latter is related to partially saturated micro cracks that become fully saturated with the wetting phase as saturation increases; the wetting phase is brine in our case, and the non-wetting phase is methane gas. Their

data were collected using a similar ultrasonic pulse-echo system. As the S_h is very low, and such a step increase is not seen at higher differential pressures, we think this effect may not be related to hydrate formation, but rather to partially saturated micro cracks, as discussed by Amalokwu et al. (2017).

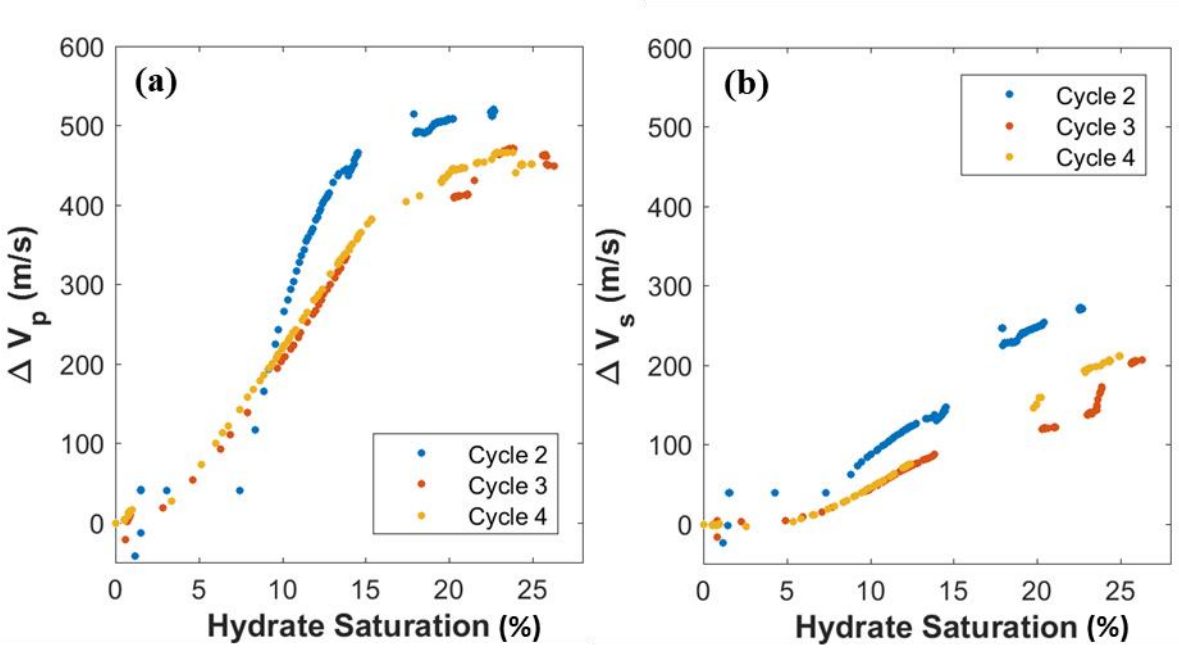

Figure 4.6 Comparison of change in a) P- and b) S-wave velocity with hydrate formation at differential pressures of 10 MPa (cycle 2) and 55 MPa (cycles 3 and 4). Saturations could not be calculated for cycle 1.

4.3.5 Synchrotron imaging of hydrate formation.

An example of density segmentation is shown in Figure 4.7. As hydrate formation continues from 23 h 30 min to 45 h 10 min, the bubble size reduces (Figure 4.7a, b) and also the grey scale count increases (Figure 4.7c). The increase in grey scale count indicates an increase in density, which is most likely due to conversion of methane gas to hydrate.

(a) Time: 23h 30min

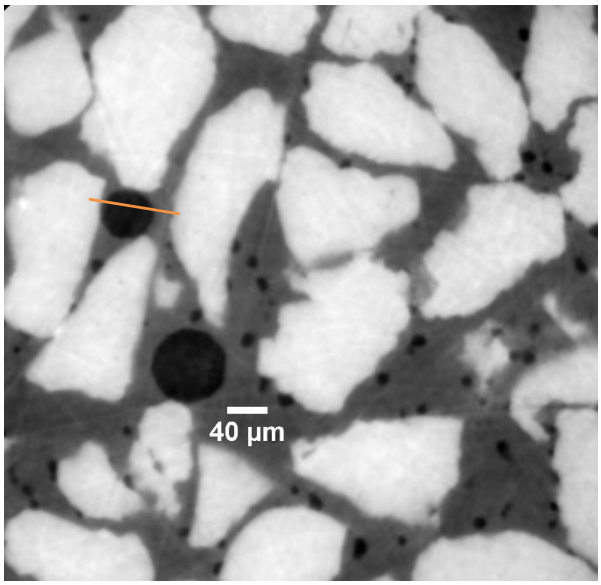

(b) Time: 45h 10min

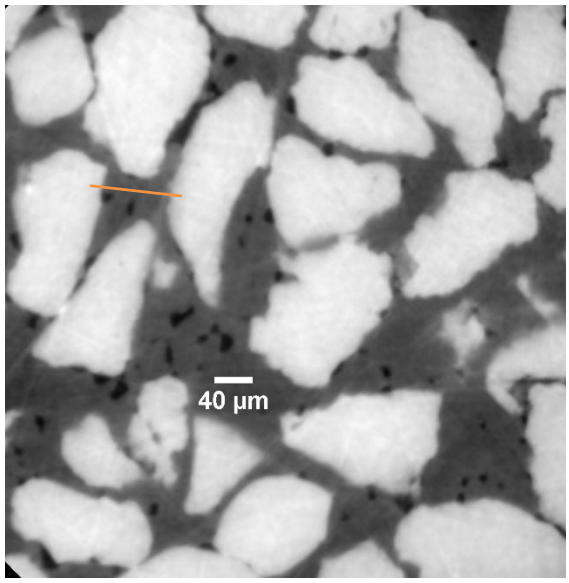

(c)

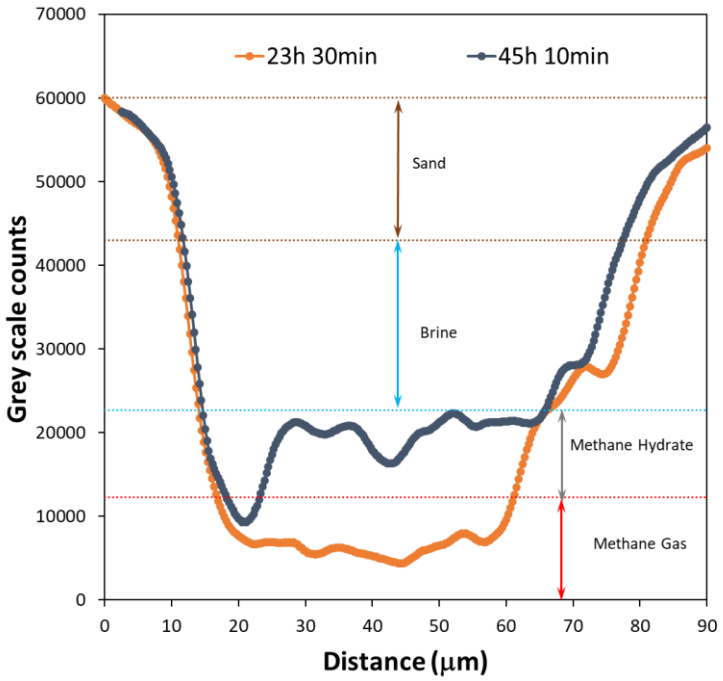

Figure 4.7 2D phase reconstructed CT slices from synchrotron imaging of the hydrate/sand sample after a) 23hr 30m, b) 45hr 10m. c) Cross section through grey scale images indicating evolution of hydrate formation extracted at the same locations shown in a, b. marked in yellow. Also shown are the grey levels of the four phases methane gas, methane hydrate, brine and sand obtained by density normalization.

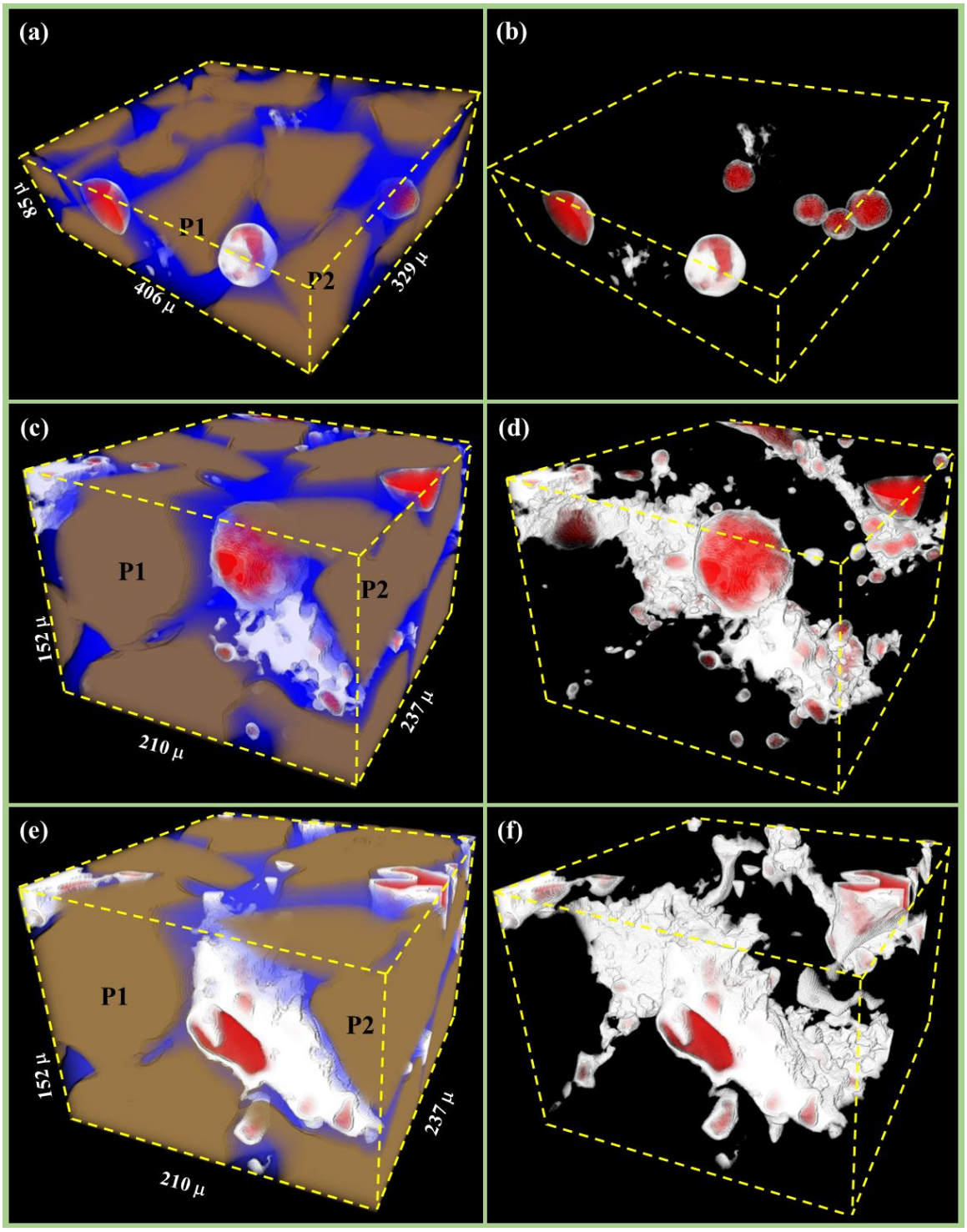

Figure 4.8 3D Synchrotron radiation X-ray computed tomography images at different times during hydrate formation in sand. Red is gas, brown is sand, white is hydrate and blue is water. P1 and P2 marked in a, b and c are two arbitrarily selected sand grains to aid visual comparison. Times are: 16hr 42 m (a and b), 23h 30m (c and d), 45h 10m (e and f). a), c) and e) show all four phases while b), d) and f) show only gas and hydrate for the same data volumes, respectively.

After inspecting the extensive X-ray CT dataset (9 Terabytes of data), we selected a series of images to illustrate the key hydrate formation processes that we observed in a typical 3D volume (Figure 4.8). Hydrate grows initially as a shell around gas bubbles scattered throughout the pore space, as also reported for methane hydrate formation in water without sediments (e.g., Klapp et al., 2012). The gas is sparsely distributed as sub-spherical "bubbles" with a range of sizes; some gas bubbles almost completely fill the pores, while others occupy part of the pore only (Figure 4.8a, b). Hydrate films that develop on bubbles at some point seem to rupture, and the trapped gas escapes (Figure 4.8c, d). Hydrate formation consumes methane, reducing the pore fluid pressure and is also an exothermic reaction; this may lead to bubble expansion and/or rupture of the hydrate shell. The escaped gas either forms smaller bubbles and/or forms more hydrate (Figure 4.8 c, d). Hydrate growing in adjacent pores then starts to coalesce as the pores are further filled with hydrate creating a pore framework structure interlocking with the sand grain framework (Figure 4.8c, d). While we cannot directly compare our two experiments because of the different host media and volumes that will give different hydrate formation/dissociation rates, the coalescence of hydrate from adjacent pores creating an interlocking hydrate framework could be linked with the rapid increase in velocities seen in Figure 4.4a, b. The spherical shapes of bubbles distort due to further hydrate growth into the gas bubble. Ultimately the gas remains as isolated pockets surrounded by hydrate, while hydrate occupies most of the pore space in patches throughout the volume (Figure 4.8e, f). Such distorted bubble shapes and uneven, porous hydrate distribution could have an impact on elastic wave propagation mechanisms, see (Section 4.3.3). The presence of such pockets of gas confirms the hypothesis of co-existence of water, hydrate and methane gas proposed by Sahoo et al. (2018; Chapter 3) from ERT and thermodynamic calculations. A film of brine is evident between hydrate and sand even at maximum hydrate saturation (Figure 4.8e).

The highest hydrate content occurs where the porosity is highest, but the lowest hydrate content is not where the porosity is lowest (Figure 4.9). The depth variation of S_h increases as the average S_h increases (Figure 4.9); at 45h 10 min, S_h varies between 38 and 60%, about 44% of the mean saturation.

We note the following caveats when comparing these results to the ultrasonic experiments: porosity, permeability, and sample size are different as described in Section 4.2.2; also, the inlet pipe in the synchrotron imaging rig is in the centre of the sample, while it is off-centre for the ultrasonic rig (Figure 4.1). The ratio of diameter of the sample to that of the pore fluid inlet pipe is 24.5 and 15.7 for the ultrasonic rig and the imaging rig, respectively. This difference might have affected the distribution of the gas and hydrate in the sample. However, we expect the observed hydrate formation morphologies and their

time evolution to be similar in other laboratory experiments and in natural hydrate systems, especially for coarse grained host sediments with similar pore dimensions that are fed by free gas from below.

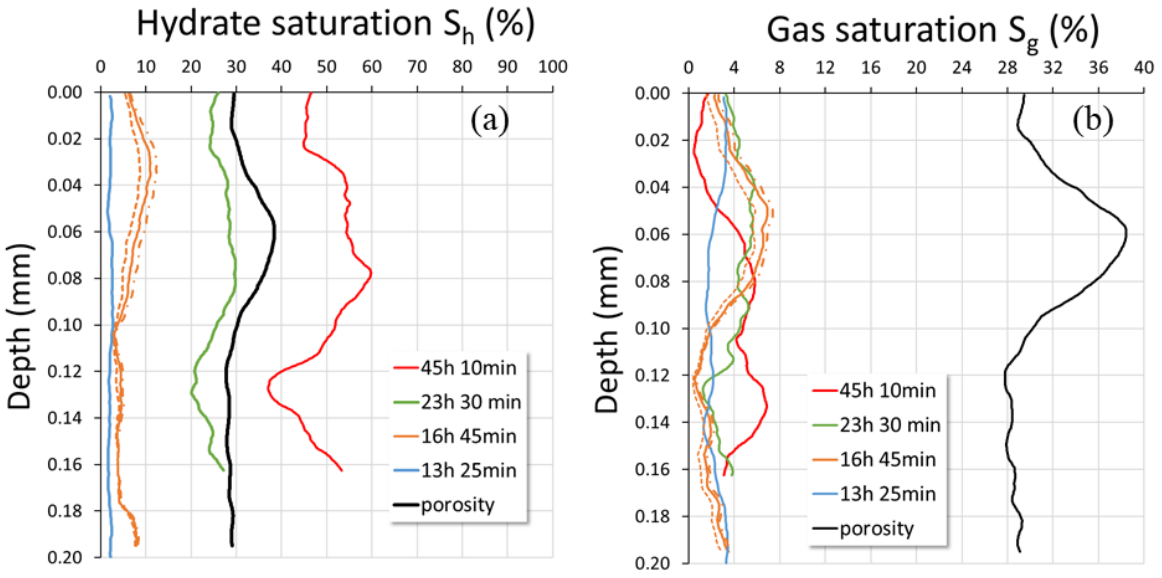

Figure 4.9 Area average distribution of a) hydrate and b) gas with depth in the sample at different times during hydrate formation, obtained from X-ray CT analysis. Porosity distribution is also shown, the same curve in a) and b) at different scales. Note that the gas is continuously charged form below during hydrate formation. Dashed and dotted orange lines shows the upper and lower error bounds for 16h 45m; errors bound at other times are similar.

4.4 Conclusions

Estimates of hydrate content from seismic data and of hydrate related geohazards depend on an understanding of the morphology and formation process of non-cementing hydrate in porous media. We conclude the following:

1. Our time resolved/lapse (4D) SR-XCT images show that hydrate grows initially in a pore-floating morphology and transitions to a pore-bridging morphology. Then, eventually, it forms a hydrate pore-framework that interlocks with the sand grain framework, although separated by thin water films.
2. Using rock physics modelling, we were able to link these morphological transitions to changes in the rate of increase of elastic wave P- and S- wave velocity with hydrate saturation.

3. While P wave velocities match the modelled velocity for pore-bridging hydrate, S wave velocities are higher than the pore-floating model and lower than the pore-bridging model, likely due to presence of water film between hydrate and the rock frame.
4. The SR-XCT images confirm the occurrence of a hydrate film around methane gas bubbles, trapping gas inside, as the mechanism of co-existence of gas with hydrate under hydrate stability conditions. SR-XCT images show that water films occur between hydrate and sand when using methane and brine for hydrate formation. They also confirm the previously inferred porous nature of hydrate.
5. Both ultrasonic velocities and imaging results indicate that hydrate-bearing sediment is a system of interlocking solid hydrate and host grain frameworks separated by water films, with isolated pockets of gas within the hydrate.

These observations are likely to be typical of natural hydrate-bearing sediments charged by gas from below. Such pore-bridging hydrate frameworks and co-existing gas, if widespread in nature, should be considered when estimating *in situ* hydrate contents from elastic wave velocities.

Acknowledgments

The authors are grateful to the Swiss Light Synchrotron Radiation for access to TOMCAT-X02DA beamline, to the assistance of Dr. Anne Bonnin and Mr. Thomas Steigmeier. Thanks to μ-VIS at the University of Southampton for the computer analysis facilities, and particularly to Prof. Ian Sinclair for his help with the proposal to TOMCAT. We acknowledge funding from the UK Natural Environment Research Council (grant no NE/J020753/1). Madhusudhan was supported by the NERC Landslide-Tsunami risk to the UK (NE/K00008X/1). T. A. Minshull was supported by a Royal Society Wolfson Research Merit award.

Chapter 5 Laboratory observations of frequency-dependent ultrasonic velocity and attenuation during methane hydrate formation and dissociation in Berea sandstone.

Abstract

Knowledge of how seismic wave attenuation is affected by methane hydrate saturation and morphology in sediments and rocks could help reduce ambiguity in seafloor hydrate content estimates from seismic velocities. These are needed for seafloor resource and geohazard assessment, as well as to improve predictions of greenhouse gas fluxes into the water column in a warming world. In particular, at lower hydrate saturations in excess water systems found in nature, seismic velocity is relatively insensitive to hydrate content, and so attenuation may provide useful additional information. Hence, we conducted laboratory ultrasonic measurements of P- and S-wave velocity and attenuation over four successive cycles of methane hydrate formation and dissociation in Berea sandstone (porosity 22%, permeability 448 mD) at differential (confining minus pore) pressures of 10 and 55 MPa, up to a maximum hydrate saturation of 26%. We observed systematic and repeatable changes with hydrate saturation in the velocity and attenuation frequency spectra between 448 and 782 kHz. Having established the coexistence of methane gas bubbles with solid hydrate and brine in the pore space, and using a rock physics model, we were able to link the spectral changes to a decrease in methane gas bubble radius and an increase in secondary porosity with hydrate formation. The results show that at 55 MPa, attenuation can increase or decrease at low hydrate saturations (< 15%) depending on the measurement frequency. For higher hydrate saturations (> 15%), attenuation increases over the whole measured frequency band. The results also support earlier experimental observations of attenuation peaks at specific hydrate saturations, and that these peaks also depend on frequency.

5.1 Introduction

Gas hydrates are ice like, naturally occurring, clathrate compounds of gas (generally methane) trapped in a lattice of water, that form in low temperature and high pressure conditions in marine and permafrost environments (Sloan and Koh, 2007). Currently, seafloor gas hydrates are being considered as a viable alternative energy resource (Boswell and Collett, 2011), and may have an important role in future climate change (Archer et al., 2009), carbon dioxide sequestration (Jung et al., 2010) and continental slope stability (Sultan et al., 2004). Methane hydrates formed in seafloor and/or permafrost sand deposits offer the most commercially attractive hydrate reservoirs (Boswell and Collett, 2011).

Natural hydrates commonly exist in several morphologies within host sediments: (i) hydrate forming cement between mineral grains, known as cementing hydrate; (ii) disseminated hydrate growing freely in the pore space away from grain contacts, known as pore-floating or pore-filling hydrate; (iii) hydrate contacting neighbouring mineral grains, known as pore-bridging or load bearing or frame supporting hydrate (e.g., Holland et al., 2008). When the saturation of pore-floating hydrate is high enough to fill a pore or bridge neighbouring sediment grains, then it becomes pore-bridging (Priest et al., 2009; Waite et al., 2009). We will use pore-floating and pore-bridging hereafter to describe the physical shape, or morphology, of hydrate in the pore space. Pore-floating and pore-bridging morphologies are types of non-cementing morphology. In coarse-grained deposits, hydrates are prone to exhibit a non-cementing habit (Zhao et al., 2015). The cementing morphology has a much greater effect on the mechanical, elastic and electrical properties of hydrate-bearing sediments than the non-cementing morphology (Best et al., 2013; Ecker et al., 1998; Priest et al., 2009; Waite et al., 2004). However, the non-cementing morphology is thought to dominate natural hydrate systems, and has been sampled and/or inferred at locations such as Mallik, Mackenzie Delta (Uchida et al., 2000), the Nankai Trough (e.g., Fujii et al., 2015), Alaminos Canyon, Gulf of Mexico (Boswell et al., 2009), and Mount Elbert, Alaska North Slope (Stern et al., 2011).

As such, it is important to obtain accurate estimates of the amount and distribution of gas hydrate. While the stability field of natural hydrates is readily determined, the quantification of hydrate within it is not. Estimates of saturation come from direct sampling, well log data, or remote geophysical data (e.g., Ecker et al., 1998; Ecker et al., 2000; Guerin and Goldberg, 2002; Matsushima, 2006; Weitemeyer et al., 2006; Westbrook et al., 2008; Lee et al., 2013; Goswami et al., 2015; Konno et al., 2015). Good indirect estimates rely entirely on our conceptual understanding of how the presence of hydrate affects P- and S-wave velocity and attenuation (e.g., Lee, 2002; Best

et al., 2013), and electrical resistivity (e.g., Spangenberg, 2001) of the host sediments, and on the appropriateness of theoretical or empirical models for geophysical data inversion.

P- and S-wave velocities of sediments hosting cementing hydrate show a significant increase even for low hydrate saturations of about 5% (e.g., Priest et al., 2009; Waite et al., 2009; Dai et al., 2012) mainly attributed to increase in frame bulk and shear moduli (Ecker et al., 1998). In contrast, sediments hosting non-cementing hydrate (both pore-floating and pore-bridging) do not show significant changes in P-and S-wave velocities (e.g., Priest et al., 2009) because the hydrate is suspended within the pore water, and hence only increases the bulk modulus of the effective pore fluid (e.g., Ecker et al., 1998). However, the elastic frame moduli and associated velocities increase progressively as pore-bridging hydrate starts to connect the sediment grains, although at much lower values than for cementing hydrate (e.g., Priest et al., 2009).

P- and S-wave attenuation has also been used for indirect estimates of hydrate saturation (e.g., Best et al., 2013; Chand and Minshull, 2004; Guerin and Goldberg, 2002; Priest et al., 2006; Westbrook et al., 2008). In contrast to velocity, attenuation shows more complex variations with hydrate saturation for both cementing and non-cementing hydrate (e.g., Best et al., 2013; Marín-Moreno et al., 2017). While some studies on natural hydrate bearing samples suggest that hydrate reduces attenuation (Dvorkin et al., 2003; Westbrook et al., 2008; Dewangan et al., 2014), others suggest it increases attenuation (Dvorkin and Uden, 2004; Guerin and Goldberg, 2002; Pratt et al., 2005; Matsushima, 2006; Priest et al., 2006; Sun et al., 2016). Laboratory studies by Priest et al. (2006) and Best et al. (2013) showed significant variation of seismic (200 Hz) P- and S-wave attenuation with hydrate saturation, including distinct attenuation peaks. Best et al. (2013) demonstrated that these peaks could be explained by local viscous fluid flow related to the microporous structure of hydrate containing gas and water inclusions (Schicks et al., 2006). Recent studies have shown that gas can co-exist with hydrate within the gas hydrate stability zone (Lee and Collett, 2006; Milkov et al., 2004), and that the presence of co-existing gas with hydrate can itself have a strong effect on attenuation (Anderson and Hampton, 1980a, 1980b; Marín-Moreno et al., 2017).

In general, attenuation in fluid saturated porous media depends on measurement frequency, owing to the viscous interaction of pore fluids and porous solid (Biot, 1956a, 1956b). Partial and patchy saturation of gas and hydrates adds further complexity (e.g., Murphy, 1982; Rubino and Holliger, 2013; White, 1975). While it is often difficult to relate unambiguously attenuation measured from remote seismic data and sonic well logs to specific hydrate contents (e.g., because of spatial averaging effects), they can be related in the laboratory, which and characterising this relationship could offer greater insight into attenuation mechanisms.

Here, we present results from laboratory experiments combining the highly accurate ultrasonic pulse-echo method for measuring velocity and intrinsic attenuation with controlled methane hydrate formation and dissociation in Berea sandstone. By comparison with the rock physics model of Marín-Moreno et al. (2017), we were able to explain systematic variations in attenuation caused by hydrate content and morphology, and gas bubble resonance.

5.2 Experimental methods

5.2.1 High pressure rig and sample

We used a stainless steel high-pressure cell, designed to host 5 cm diameter rock samples under hydrostatic confining pressure of up to 65 MPa (see Figure 5.1). The cell was instrumented to monitor pore fluid pressure, and inner and outer (ambient) cell temperature. The inlet pore pressure pipe was connected via a three-way valve to a vacuum pump, a methane gas cylinder (with pressure regulator) and a brine reservoir. A syringe pump was used to inject brine into the sample in a controlled manner, while the temperature of the system was regulated by a controlled cooling circuit.

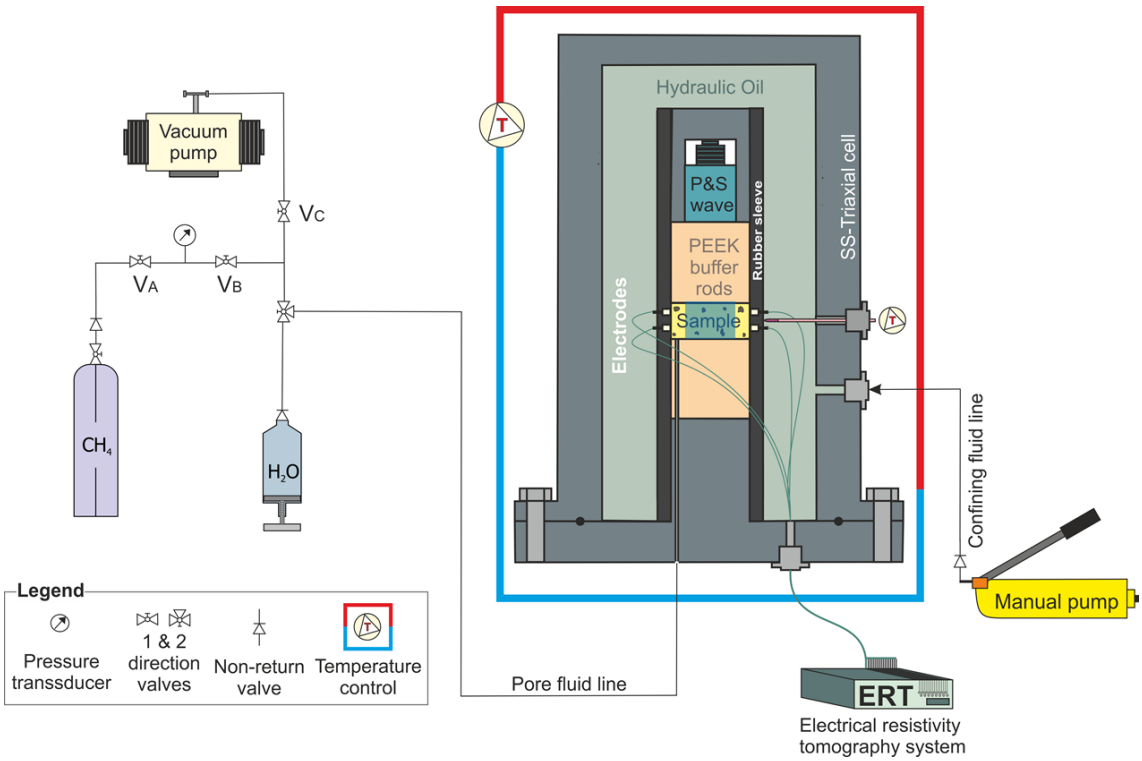

Figure 5.1 Experimental setup. The blue region inside the sample marks the insonified zone of the sample.

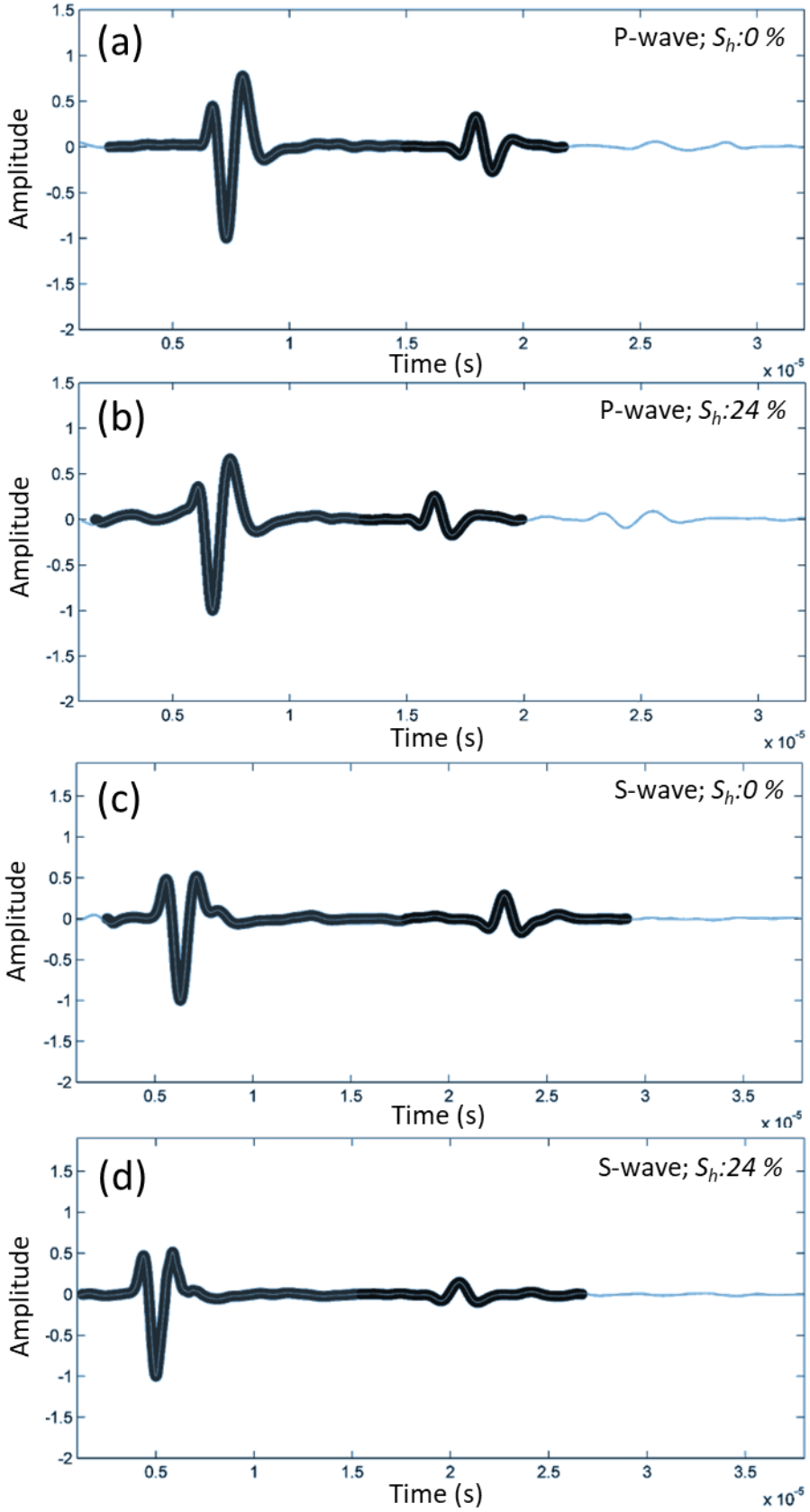

Figure 5.2 Typical examples of P and S wave signals measured during hydrate formation in Berea sandstone at a differential pressure of 55 MPa. Black outlines show the time domain gated signal used for calculating velocity and attenuation.

The inner cell was configured for ultrasonic pulse-echo measurements of P- and S-wave velocity (V_p and V_s) and attenuation (Q_p^{-1} and Q_s^{-1}). A useful feature of the pulse-echo system is the broad signals, giving velocity and attenuation data at frequencies between 448 and 782 kHz. Examples of P- and S-wave signals are shown in Figure 5.2 for zero and 24% hydrate saturation, collected at 55 MPa differential pressure in Berea sandstone. These examples illustrate the data quality and obvious decrease in signal amplitude with hydrate growth. The pulse-echo data analysis method corrects for amplitude changes due to interface reflection coefficients and diffraction, giving the intrinsic attenuation coefficient spectra of the sample, with an accuracy at each frequency of ± 0.2 dB/cm (Best et al., 1994), converted to inverse quality factor. The sampling interval was 4×10^{-10} seconds. The shortest time domain gate was 9 microseconds, for the reflection from the bottom of the sample, giving a frequency resolution of 111 kHz. Each spectrum contains 4 data points; while it is possible to increase the frequency resolution on the plots, this essentially entails interpolation, and so we choose to show the actual raw data only.

We used a cylindrical sample (4.97 cm diameter and 2.06 cm height) of Berea sandstone with a porosity of 22% and a permeability of 448 mD (4.48×10^{-13} m^2) as a stable, inert, and well-characterized porous medium.

5.2.2 Hydrate formation

The sample was first oven dried at 60˚C, placed in the high pressure cell and then subjected to a hydrostatic confining pressure of 10 MPa. A vacuum of 1 Pa was applied to the sample to remove air from the pore space. The presence of air affects the saturation calculation and any other gas present in the air, such as CO_2, can form hydrate. We followed the method of Waite et al. (2004) with an initial brine saturation of 83.5% which allowed an excess water condition (Ellis, 2008; Priest et al., 2009). We left the sample for three days so that the pore fluids could re-distribute throughout the sample by capillary forces. The remaining pore space (16.5%), which was previously under vacuum, may have been occupied by water vapour and/or any remaining air.

Methane gas was then injected to achieve a pore fluid pressure of 11.9 MPa, and the confining pressure was increased to 21.9 MPa to maintain a constant differential. The pore fluid system was isolated by closing valve A in Figure 5.1, keeping the pipe between the sample and the pressure gauge filled with methane gas. This gas could potentially move in and out of the sample in response to changes in pore pressure, which represents a hydrate system fuelled from below, such as those commonly found near gas chimneys (e.g., Petersen et al., 2010) or at the base of the GHSZ. Finally, four cycles of hydrate formation and dissociation were achieved by cooling then heating the system in and out of the gas hydrate stability conditions (Figure 5.3).

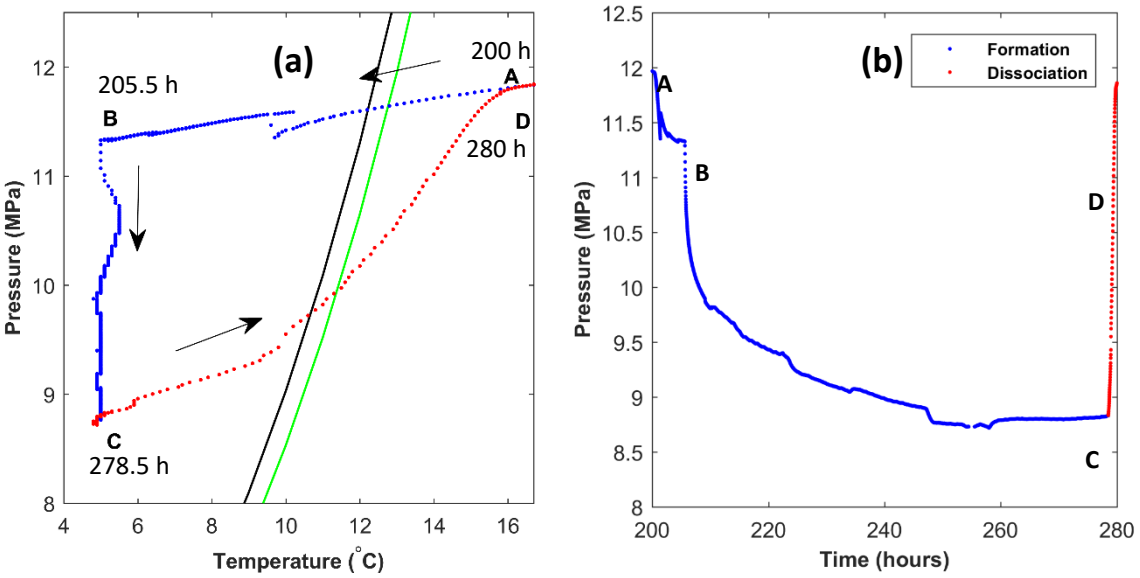

Figure 5.3 Changes of a) pressure versus temperature, and b) pressure with time during methane hydrate formation and dissociation in Berea sandstone. Only the second cycle of hydrate formation and dissociation is shown for clarity. The green and black lines are the pure methane hydrate phase boundary for 35 g/L and 46 g/L salinity respectively, calculated using the approach of Tohidi et al. (1995). Blue dots represent cooling and red dots represent heating. In a) time is shown in hours (h). Trajectory ABC marks cooling of the system to 5°C and hydrate formation. Trajectory CD shows hydrate dissociation. c) and d) show pressure and temperature change with time during trajectory AB. See text for further details.

The differential pressure (confining minus pore fluid pressure) was held at 10 MPa in the first and second cycles of hydrate formation and dissociation, and then increased to 55 MPa for the third and fourth cycles. This was done to explore the effects of micro-cracks on ultrasonic properties that are generally open at lower differential pressures (10 MPa) and closed at higher pressures (55 MPa), based on previous resistivity and ultrasound data for Berea (Han et al., 2011). The initial pore fluid pressure for the third cycle was 11.98 MPa (0.08 MPa above that for the first cycle). Hydrate, gas and brine saturation were calculated from the measured pore fluid pressure and temperature changes of the system using a thermodynamic method (Sahoo et al., 2018; Chapter 3).

5.3 Results

5.3.1 Comparison of velocity and attenuation changes during hydrate formation and dissociation

Presence of micro crack affects the velocity and attenuations in Berea and are generally closed in high differential pressure of 55 MPa. To exclude any micro crack effects, and focus on hydrate effects, we only discuss the data of cycle 3 and 4 with differential pressure of 55 MPa. We compare the ultrasonic attenuation results to the velocity results already discussed in Chapter 4, both at 667 kHz, presented as variations with hydrate saturation for two hydrate formation and dissociation cycles at 55 MPa differential pressure (Figure 5.4). As shown in Chapter 4, the main changes in velocity during hydrate formation can be attributed to hydrate floating within brine in the pore space, thus increasing the pore fluid bulk modulus, and hydrate bridging across pores, thus increasing the frame elastic moduli. Most notably, changes in gradient of increasing P-wave velocity (V_p) are seen at S_h = 3 - 4% and 18-20%, and at S_h = 7 - 8% and 20 - 24% for S-wave velocity (V_s) in Figure 5.4a & b. The gradient change in V_s was observed at slightly higher S_h than that for V_p. This change occurs only when a sufficient amount of hydrate has grown to interlock the sand grains, thus increasing the frame shear modulus, as discussed in Chapter 4.

The attenuation results for P-waves (Q_p^{-1}) and S-waves (Q_s^{-1}) in Figures 5.4c & d also show increasing values with hydrate formation, with changes in gradient at S_h = 3 - 4% and 18 - 20% for Q_p^{-1} and S_h =7 - 8% and 20 - 24% for Q_s^{-1} (note some overnight S-wave data are missing for cycle 4 for S_h = 15 – 18%). These changes in gradient correspond to those seen for velocity and hence can be associated with the above changes in hydrate morphology from pore-floating to pore-bridging (Chapter 4). While the velocities show an increase in gradient at these transition S_h values, the attenuations instead show peaks. This behaviour is similar to the occurrence of attenuation peaks (both Q_s^{-1} and Q_p^{-1}), measured at 200 Hz, at specific saturation during hydrate formation by Best et al. (2013). These results had insufficient attenuation (Best et al., 2013) and velocity (Priest et al., 2009) data points to resolve changes in velocity gradient such as those seen in our data. Best et al. (2013) attributed such peaks to the formation of different aspect ratio inclusions in hydrate, to give attenuation peaks at different saturations.

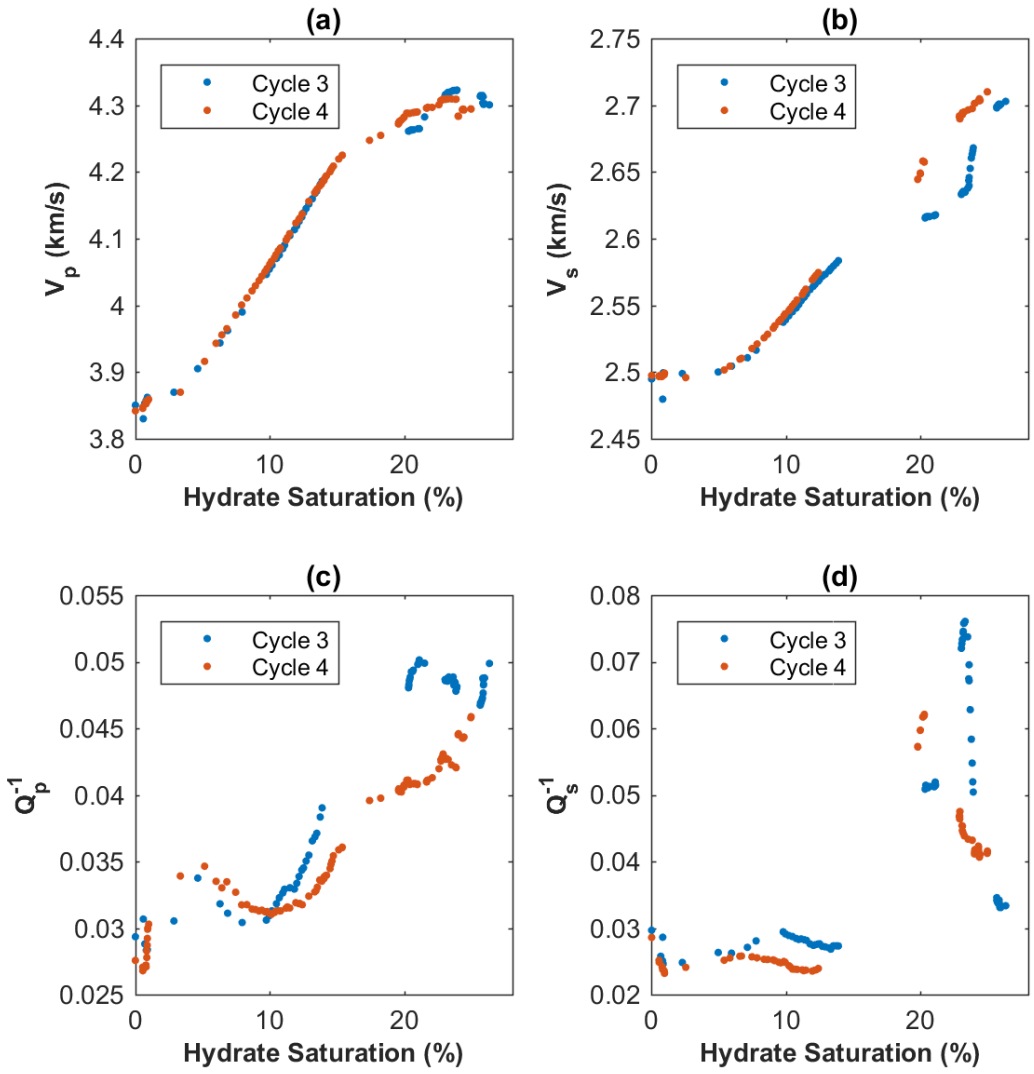

Figure 5.4 Changes in ultrasonic (667 kHz) a) P-wave velocity, b) S-wave velocity, c) P-wave attenuation and d) S-wave attenuation during hydrate formation. The differential pressure was 55 MPa for both Cycles 3 & 4.

The velocities of both P- and S-waves decrease uniformly with dissociation, as seen in Figure 5.5, while P- and S-wave attenuations each show a small increase with initial hydrate dissociation, followed by a large decrease (exception is cycle 4 in Figure 5.5d for Q_s^{-1} that shows a small drop, then plateau at low hydrate saturations). The decreases in Q_p^{-1} and Q_s^{-1} are not uniform like the velocities, but rather peaks are seen, similar to those seen during hydrate formation.

As expected from causality, the changes in velocities (both P and S wave) during hydrate formation and dissociation match corresponding changes in attenuation (Figure 5.4, 5.5). One important aspect to note is the relatively high change in attenuation compared to velocity, suggesting that attenuation changes with hydrate content are more likely to be detectable in elastic wave data

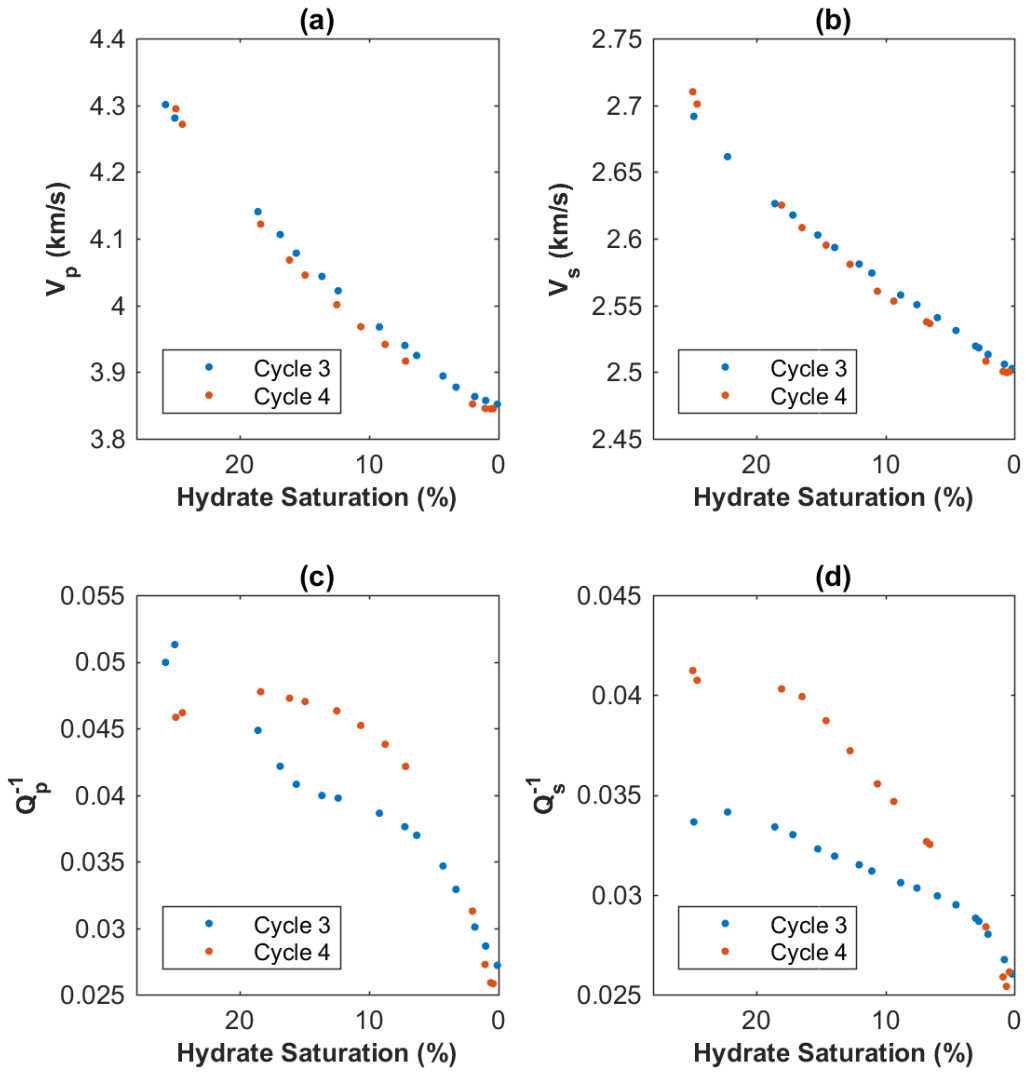

Figure 5.5 Changes in ultrasonic (667 kHz) a) P-wave velocity, b) S-wave velocity, c) P-wave attenuation and d) S-wave attenuation during hydrate dissociation in Berea sandstone. The differential pressure was 55 MPa for both Cycles 3 & 4.

5.3.2 Changes in velocity and attenuation frequency spectra during hydrate formation and dissociation

Here, we present P- and S-wave velocity and attenuation spectra measured during various stages of hydrate formation during cycle 2 (10 MPa, Figure 5.6), cycle 3 (55 MPa, Figure 5.7) & cycle 4 (55 MPa, Figure 5.8); the values vary between cycles but cover similar ranges. Cycle 1 is not shown as the pressure gauge was not working, and hence hydrate saturation could not be calculated. We also plot V_p/V_s and Q_s/Q_p ratios only for those S_h where both P and S wave data were collected with S_h difference of 0.02% or less (Figures 5.5, 5.6 and 5.7).

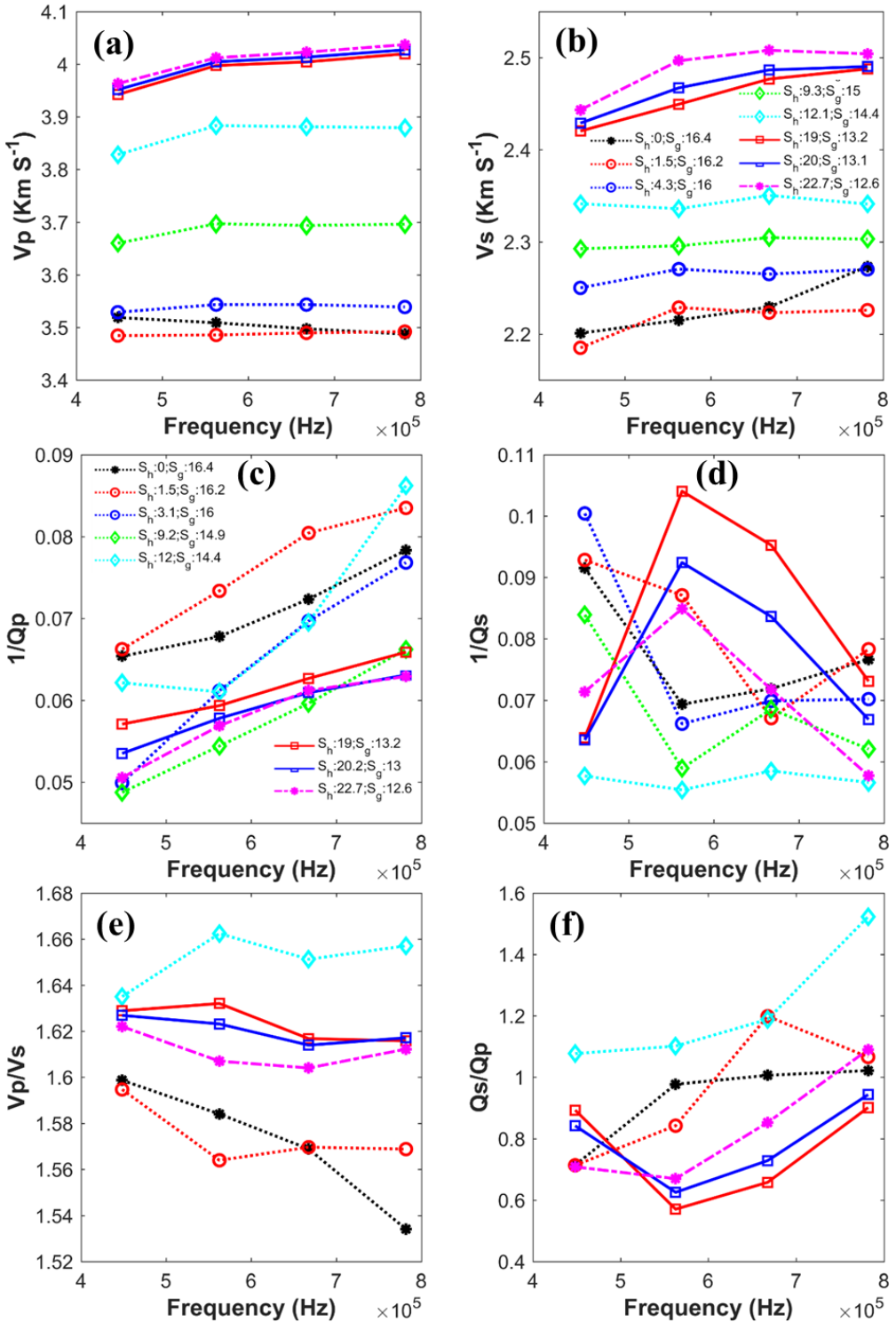

Figure 5.6 Variation of elastic properties with frequency for various hydrate saturations for Cycle 2 of hydrate formation at a differential pressure of 10 MPa in Berea sandstone.

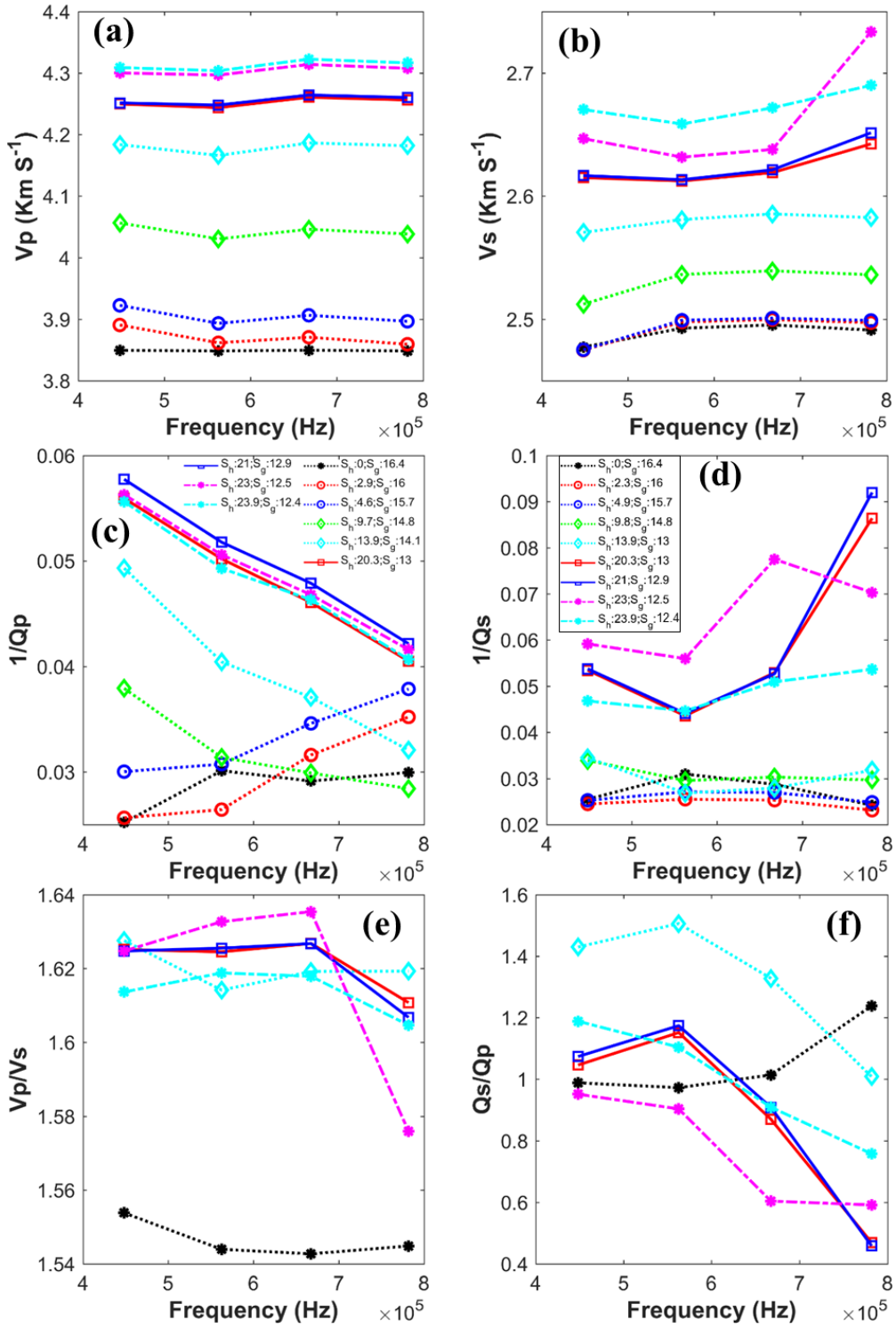

Figure 5.7 Variation of elastic properties with frequency for various hydrate saturations for Cycle 3 of hydrate formation at a differential pressure of 55 MPa in Berea sandstone.

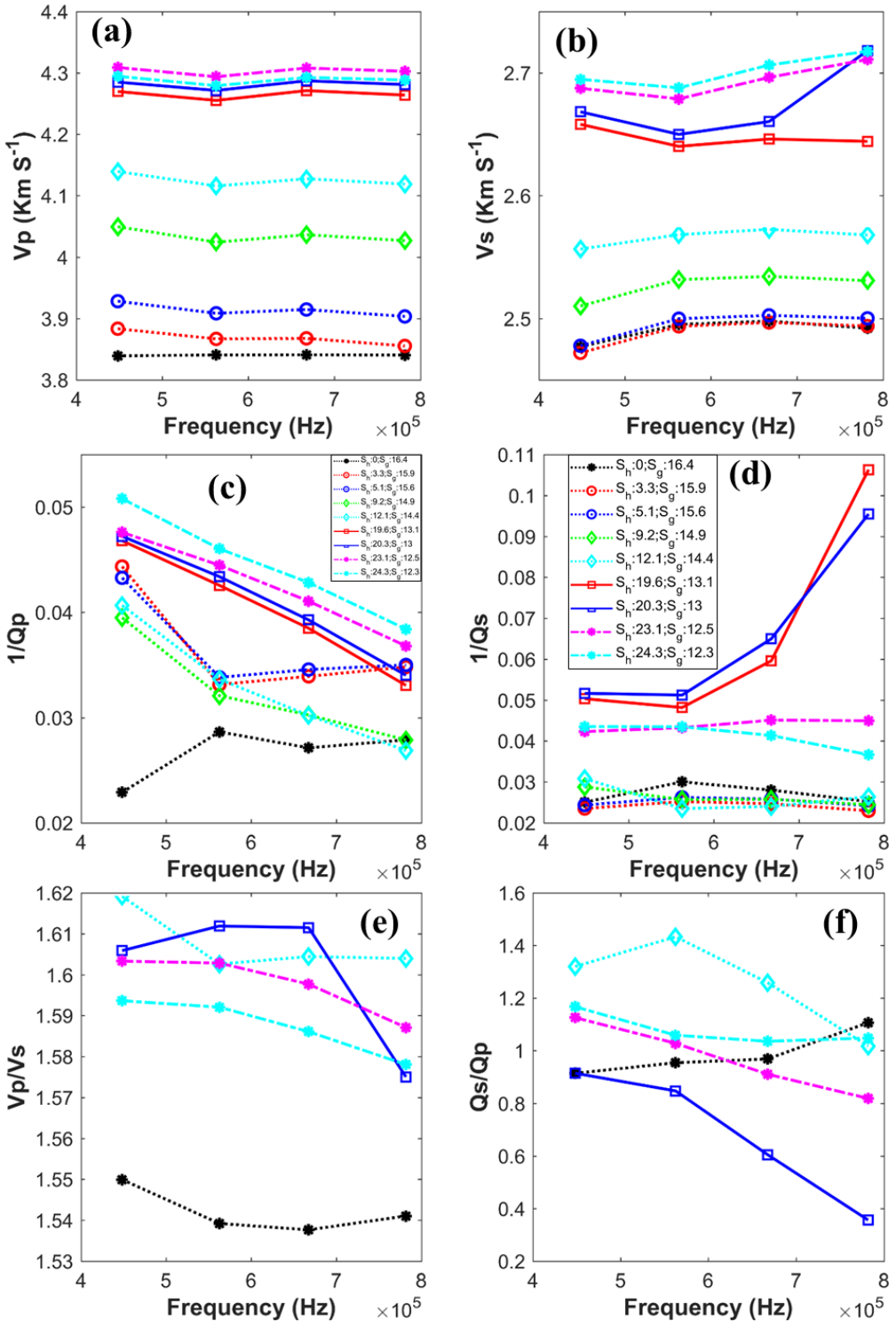

Figure 5.8 Variation of elastic properties with frequency for various hydrate saturations for Cycle 4 of hydrate formation at a differential pressure of 55 MPa in Berea sandstone.

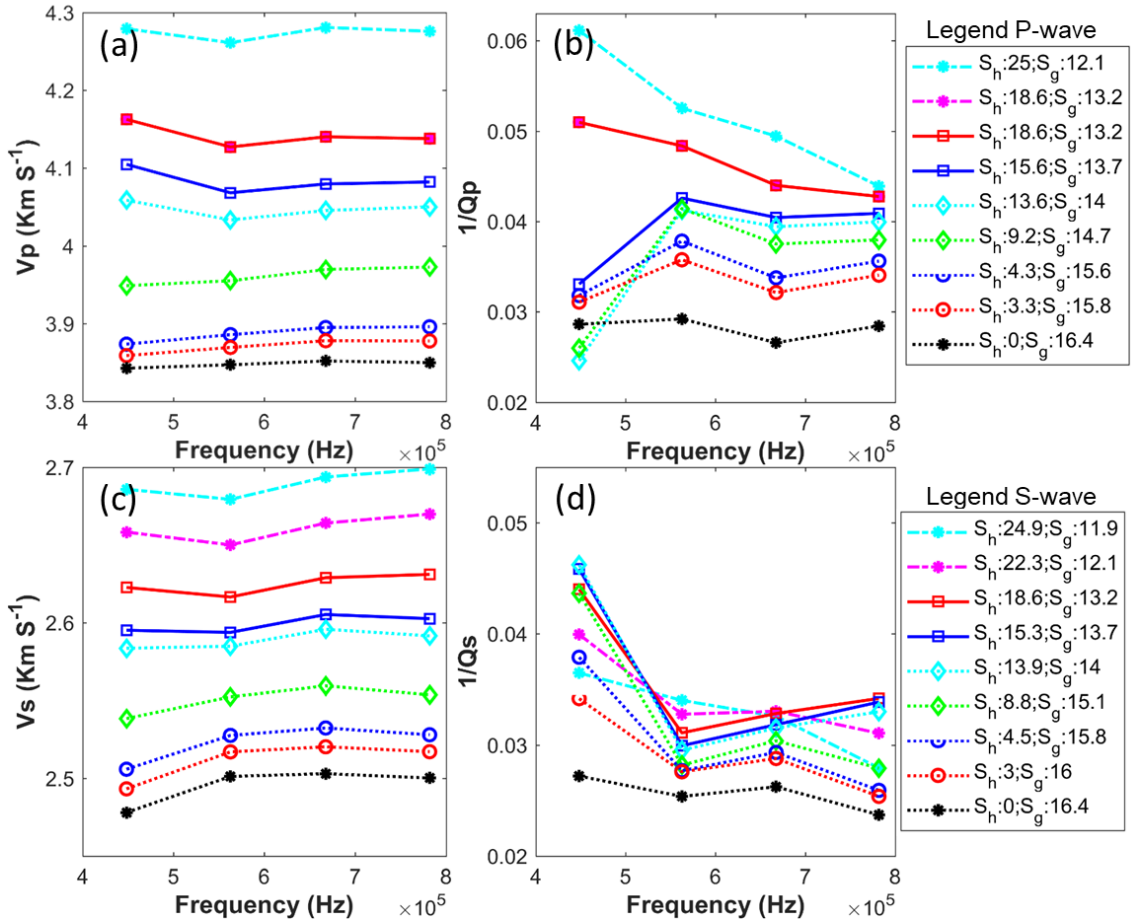

Figure 5.9 Variation of elastic properties with frequency for various hydrate saturations for Cycle 3 of hydrate dissociation at a differential pressure of 55 MPa in Berea sandstone. Note that V_p/V_s and Q_p^{-1}/Q_s^{-1} ratios are not shown because dissociation occurred very rapidly (within 2 hours), and hence both P and S waves could not be measured at the same hydrate saturations.

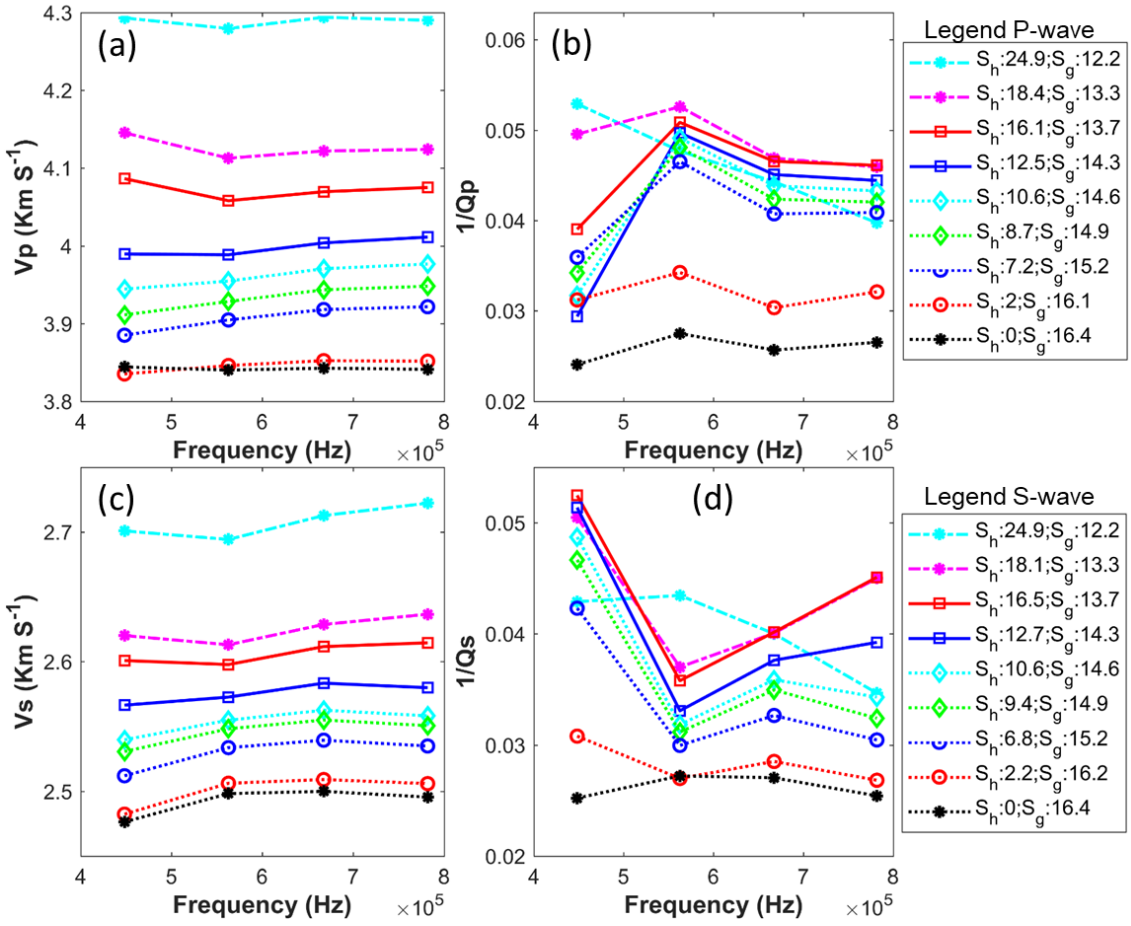

Figure 5.10 Variation of elastic properties with frequency for various hydrate saturations for Cycle 4 of hydrate dissociation at a differential pressure of 55 MPa in Berea sandstone. Note that V_p/V_s and Q_p^{-1}/Q_s^{-1} ratios are not shown because dissociation occurred very rapidly (within 2 hours), and hence both P and S waves could not be measured at the same hydrate saturations.

In general, the velocity spectra in Figures 5.7 & 5.8 show little frequency dependence and will not be discussed further (they are included for completeness and to demonstrate the stability of the ultrasonic results). By contrast, the attenuation spectra show noticeable changes with hydrate formation. Also, there is a distinct difference in the attenuation spectra at high and low differential pressures, possibly related to micro cracks in Berea sandstone that are generally closed at high differential pressures (e.g., Han et al., 2011). Even at zero, hydrate saturation, the attenuation increases significantly with frequency, which is likely due to partial brine and gas saturation. The attenuation spectra for zero hydrate saturation is less frequency-dependent at high differential pressure than at low differential pressure, also likely due to closing of microcracks. Hereafter, we will discuss the results of the third and fourth cycles to exclude any microcrack effects, and focus on hydrate effects.

The attention spectra show broadly similar shapes and magnitudes at different hydrate saturations in both the third and fourth cycles, indicating repeatable data and systematic changes. We can broadly classify the attenuation spectra into three categories based on the shape of the Q_p^{-1} spectra in Figures 6a and 7a and then extend this to Q_s^{-1}. The first category is for zero hydrate ($S_h = 0$) where Q_p^{-1} is relatively constant with frequency (at least above 550 kHz) compared to when hydrate is present; similarly, for Q_s^{-1}. Category two is for $0 < S_h < 6\%$ when the gas saturation decreases as hydrate forms, Q_p^{-1} increases with frequency, at least above 550 kHz. Note that the cut-off frequency (e.g., Winkler & Plona, 1982) for our pulse-echo system is 400 kHz, and so the data at 450 kHz are unlikely to be affected. By contrast, Q_s^{-1} shows relatively little frequency dependence.

Category three is for $S_h > 6\%$, when the Q_p^{-1} versus frequency slope changes from positive to negative as more hydrate forms. By contrast, Q_s^{-1} shows a peak at around 550 kHz (Figures 5.6 and 5.7). These systematic and repeatable changes in spectra of Q_p^{-1} and Q_s^{-1} with hydrate saturation show that there are frequency dependent effects within this bandwidth that change as hydrate and gas saturation change. We will discuss possible Q_p^{-1} and Q_s^{-1} mechanisms in Section 5.4.

The Q_p^{-1} and Q_s^{-1} spectra also show broadly similar and repeatable frequency dependence during hydrate dissociation in both cycle 3 and 4 (Figures 5.9 and 5.10). The shape of the Q_p^{-1} and Q_s^{-1} spectra vary only slightly compared to those during formation in Figures 5.7 & 5.8.

5.4 Discussions

5.4.1 Possible loss mechanisms

Fluid-saturated rocks exhibit different attenuation and velocity dispersion to dry rocks, which have been ascribed to the complex nature of the crack/pore structure of rocks, and to the behaviour of fluids occupying and flowing within the pore structure (e.g., Biot, 1956; Winkler and Murphy, 1995; Mavko et al., 1998). In our experiment, the presence of three pore phases i.e., gas, hydrate and brine, adds to the complexity. Attenuation can occur due to geometric effects and source coupling in addition to intrinsic loss mechanisms in the rock (e.g., Goldber et al., 1984; Lee, 2006). The geometric and source coupling effects are circumvented in the pulse-echo system by calibration/corrections for the former, and intrinsic design for the latter (the top and base reflection signals use the same source coupling). Scattering is another possible source of attenuation, and this can become significant as the wavelength approached the size of heterogeneities, such as the grainsize (e.g., Mavko et al., 1998). The wavelength was always larger than 30 mm in our experiments, while the mean grain size of Berea is around 100 μm, hence we assume the effect is minimal. Therefore, we expect that formation of methane hydrate in our experiments will

predominantly affect the intrinsic attenuation. In this section, we shall discuss some plausible attenuation mechanisms applicable to our experiments.

5.4.1.1 Biot global flow

Attenuation occurs when there is inertial motion of the pore fluid with respect to the rock frame caused by the generation of pressure gradients from a passing elastic wave (Biot, 1956b). This is the result of wavelength-scale pore fluid pressure equilibration between peaks and troughs of a compressional wave. Biot fluid flow may not be significant at seismic exploration frequencies around 10 - 100 Hz but is dominant at ultrasonic frequencies (e.g., Mavko et al., 1998). The formation of solid hydrate in the pores reduces the porosity and intrinsic permeability of the sediment. This reduction produces two opposite effects on the attenuation in our measured frequency range. With the reduction in porosity, the surface contact area between the fluid in the pores and the solids increases. This results in higher viscous drag between the solids and global fluid flow which increases Biot type attenuation. By contrast, a reduction in intrinsic permeability reduces global fluid flow, reducing Biot type attenuation. The net effect depends on the rate at which intrinsic permeability decreases with porosity, and so with hydrate saturation. In our experiment, the maximum hydrate saturation is only 26%, so there is unlikely to be a major permeability effect, provided that hydrate does not preferentially block pore throats. Our hydrate formation method has excess water (64% water saturation), so it is unlikely to preferentially block pore throats. Hence, in our experiments, Biot attenuation is more likely to be dominated by the porosity effect, and we would expect an increase with S_h. Marín-Moreno et al. (2017) showed that the magnitude of increase of Biot type attenuation (Q_p^{-1}) in hydrate bearing sand is in the order of 10^{-3}, and hence significantly smaller than other attenuation mechanisms described below.

5.4.1.2 Squirt flow

Early concepts of hydrate-related attenuation considered hydrate as solid grains replacing pore fluid (gas or water) leading to a reduction in attenuation (Dvorkin et al., 2003b). Contrary to this, several *in situ* and laboratory measurement studies showed increasing attenuation with hydrate content (Dvorkin and Uden, 2004; Guerin and Goldberg, 2002; Pratt et al., 2005; Matsushima, 2006; Priest et al., 2006; Sun et al., 2016). Kuhs et al., (2004) observed the microporous structure of natural hydrates and the same structures in synthetic hydrates formed under similar conditions in the laboratory (pores between 100 nm – 1 µm); they suggested that such gas-filled microporous structures could give rise to heightened attenuation in sediments.

Inclusions

These micro pores comprise fluid inclusions within solid hydrate (e.g., Kuhs et al., 2004; Schicks et al., 2006) that can be either connected or unconnected to the main pore network. Connected inclusion can lead to local (as opposed to global Biot type) viscous fluid flow (known as squirt flow) between these inclusions and the main pore network, leading to an increase in attenuation (e.g., Best et al., 2013). These inclusions can have different aspect ratios, and could contain gas and/or water.

Secondary porosity due to hydrates

Formation of hydrate with the macro pores can also lead to a secondary porosity with a different aspect ratio compared to the initial microporous fluid inclusions discussed above. Squirt flow can also occur in these pores. We refer to this secondary porosity squirt flow as micro squirt flow, and to the inclusion related squirt flow as sub-micro squirt flow. With increasing hydrate saturation, the concentration and aspect ratio(s) of these secondary pores are likely to change. (Priest et al., 2006) hypothesized that the increased attenuation seen in his excess-gas hydrate formation experiments was likely due to squirt flow between low aspect ratio pore layers of water, bound to mineral grain surfaces when cementing hydrate forms, and the pores. This can be treated as a special case of our secondary porosity squirt flow. Some studies have showed that a layer of water is usually present between hydrate and mineral surfaces both in cementing and pore-floating hydrate (Tohidi et al., 2001; Kerkar et al., 2014; Chapter 4), so such squirt flow of bound water could also contribute to attenuation in our experiments.

Both types of pores could have a distribution of different aspect ratios. Also, the grains of our Berea sandstone sample are not uniform in shape (Figure 5.11), giving rise to a range of macro-pore aspect ratios. The attenuation peak frequency due to squirt flow will depend on the aspect ratio of all the pore types, while concentration of a given aspect ratio controls the peak magnitude according to Best et al. (2013) and Marín-Moreno et al. (2017). Hence, attenuation peaks could occur at different frequencies and will produce a cumulative effect through superimposition. As our measurement frequency window is from 400 to 800 kHz, we can capture the effect of only a narrow band of aspect ratios. Without using rock physics models, it is difficult to say which squirt flow mechanism will dominate losses in our measured frequency range; however, we expect squirt flow to be a dominant mechanism in this study. We use a rock physics model in Section 5.4.2

Micro cracks in the Berea sandstone sample can also cause squirt flow (in fact, the original squirt flow concept was developed for micro cracks in rocks by Mavko & Nur (1975), O'Connell & Budiansky (1977), etc.). The micro-cracks in our sample are likely to be closed during cycles 3 and 4

at the high differential pressure of 55 MPa following typical velocity-pressure curves for Berea, such as reported by Han et al. (2011), while they are likely to be open during cycle 2 at the low pressure of 10 MPa; hence, micro-cracks may play a dominant role in the attenuation during cycle 2. This change may explain the differences in attenuation spectra between cycle 2 (10 MPa) and cycles 3 and 4 (55 MPa) in Figure 5.5.

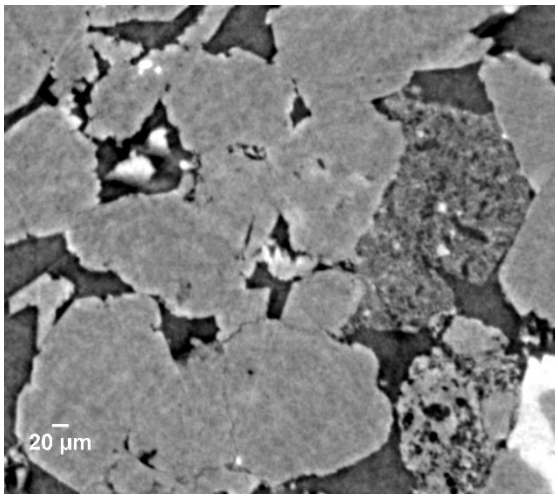

Figure 5.11 2D reconstructed image of a 10 mm diameter subsample of the Berea sandstone used in the study. The CT images were obtained using X-ray imaging of Synchrotron source (SLS, Switzerland). The optical objective used for imaging was 20x, which provided 325 nm voxel size resolution.

5.4.1.3 Co-existing gas

Gas can co-exist with hydrate in the gas hydrate stability zone (GHSZ), as speculated (e.g., Milkov et al., 2004; Miyakawa et al., 2014; Goswami et al., 2015), proposed (Darnell and Flemings, 2015), and demonstrated in the laboratory (Sahoo et al., 2018; Chapter 3) and in natural samples (e.g., Suess et al., 2001; Zhang et al., 2017). Tisato et al. (2015) showed experimentally that presence of gas bubbles in the pore liquid can attenuate seismic waves due to wave-induced gas exsolution and dissolution. It is well known that the presence of gas, even in low concentrations (< 20%), can increase sonic attenuation in rocks significantly (Murphy, 1982), and more generally in marine sediments, for only a few percent gas, due to gas bubble resonance effects (Anderson and Hampton, 1980a, 1980b; Best et al., 2004; Leighton, 2007).

Guerin & Goldberg (2002) speculated that increased attenuation seen on sonic logs at the Mallik 2L-38 research well (Mackenzie Delta) in Canada, could be due to the presence of coexisting gas within the GHSZ, although high attenuation can also be due to scattering and source coupling in addition to intrinsic attenuation (e.g., Lee, 2006). Marín-Moreno et al. (2017) showed that co-

existing gas could also increase attenuation in our experimental frequency range using a theoretical modelling approach. Co-existing gas could appear as (i) as connected inclusions in hydrate allowing local viscous flow between those inclusions and the macropores (sub-micro squirt flow), (ii) as gas-filled cavities in the pores promoting local viscous flow from different aspect ratio pores generated when hydrate grows (micro squirt flow), and (iii) as sub-spherical bubbles in the pores allowing gas bubble resonance damping effects. The peak attenuation frequency and magnitude due to gas bubble damping depends on the concentration of gas bubbles in the pore space and on gas bubble size (e.g., Anderson & Hampton, 1980a, 1980b; Dogan et al., 2017; Marín-Moreno et al., 2017). As gas bubbles can exhibit a distribution of bubble sizes, again a superposition of different frequency attenuation peaks can occur. Moreover, our experiment started with nearly 16.4% gas saturation, and the gas was consumed during hydrate formation, with about 12% gas still remaining at maximum hydrate saturation. Hence, these loss mechanisms related to coexisting gas are likely to be important in our ultrasonic experiments.

Other plausible loss mechanisms not considered in the rock physics model of Marin-Moreno et al., 2017 are the mesoscale patchy gas saturation model of White (1975), and wave induced gas exsolution-dissolution (WIGED) inferred by Tisato et al. (2015). The latter is only likely to occur at very low gas saturations (< 1%), so is unlikely to dominate our results (minimum of 12 % gas).

5.4.1.4 Mesoscale effect

Compressional wave propagation induces pressure gradients and pore fluid flow relative to the rock frame, leading to Biot type attenuation as discussed above. If the pore fluid has an heterogeneous distribution (e.g., pockets of gas and brine, sometime called patchy saturation), then pressure gradients near such inhomogeneities are high, causing mesoscopic scale fluid flow and hence more attenuation (White, 1975). The attenuation at these local inhomogeneities within the rock frame may be averaged over the total volume and produce a large overall attenuation (White, 1975). Inhomogeneities that are larger than the typical pore size and smaller than the wavelength are called meso scale; they can cause significant attenuation in particular frequency ranges controlled by the characteristic length scale of the heterogeneities (e.g., Rubino and Holliger, 2013). Bachrach (1998) analysed the effects of both microscopic and mesoscopic heterogeneities on acoustic velocities for the special case of spherical gas patches, while Chapman (2003) analysed squirt flow in combination with mesoscopic flow due to a set of aligned fractures of the same size. Rubino and Holliger (2013) showed that even microscopic heterogeneities (less that typical pore size) can also affect fluid flow at mesoscopic scales.

In our experiments, assuming minimal mesoscopic heterogeneity of the solid frame (Berea is fairly uniform material), the main cause of mesoscopic fluid flow is likely to be an inhomogeneous pore

fluid distribution. Our ultrasonic measurement system takes a bulk average of the central part of the sample, and does not probe the circumferential boundary (Figure 5.1). ERT images (see Chapter 4) show that there is a fairly homogenous horizontal distribution in the central part of the sample. Also, as no internal reflections are seen in the recorded pulse-echo waveforms in Figure 5.2, the vertical distribution can be considered homogenous. Such internal reflections would be expected because of the high impedance contrast if, for example, hydrate formed only part-way up the sample with gas remaining in the upper part.

5.4.2 Rock physics modelling

Here, we interpret the Berea P-wave attenuation (Q_p^{-1}) frequency spectra at 55 MPa (formation Cycles 3 & 4) using the HBES model of Marin-Moreno et al. (2017). As the pressure and temperature calculation showed co-existing gas with hydrate in our experiments (Sahoo et al., 2018; Chapter 3), we need to include gas effects in our assessment of hydrate attenuation mechanisms. Our understanding is that gas bubble radius is maximum at the beginning of hydrate formation, then the bubble size reduces during hydrate formation due to consumption of methane. We saw a reduction in gas bubble size with hydrate formation using Synchrotron X-ray CT imaging in sand (Chapter 4), and we expect similar processes in Berea sandstone.

As discussed above, we see broadly three categories of Qp^{-1} spectra that are consistent with the spectra for V_p, V_s and Q_s^{-1}; these are defined according to hydrate saturation as no hydrate, $S_h = 0$ (Category 1), very low hydrate, $0\% < S_h < 6\%$ (Category 2), and higher amounts of hydrate, $S_h > 6\%$ (Category 3). Methane gas bubbles occupy most of the pore space in Category 1, while in Category 2, the size of the methane gas bubbles will slowly decrease as hydrate forms. This is supported by analogy to the Synchrotron X-ray CT imaging study of methane hydrate formation in sand of Chapter 4. There may also be some micro squirt flow due to secondary porosity and sub-micro squirt flow due to inclusions. In Category 3, the bubble size would reduce further either due to thickening of the hydrate film or formation of smaller bubbles. Both these effects were seen in Synchrotron X-ray CT imaging of methane hydrate formation in sand. This reduction would produce an increase in concentration of micro squirt flow and the aspect ratio would decrease. We suggest that the aspect ratio and concentration of inclusions (sub micro squirt flow) might be an intrinsic parameter of hydrate formation and growth, similar to observations of Best et al. (2013). It is difficult to predict how the aspect ratio and concentration of inclusions would change with small changes in S_h, so we choose to use the same aspect ratio and concentration of inclusions for both low and high S_h categories, as given by Best et al. (2013).

We measured the pore size distribution in a subsample of our Berea sample at the Synchrotron X-ray CT facility of Swiss Light Source, Switzerland and found the pores to vary between 11 and 73µm. Hence, we chose to use an average bubble size within this range.

Category 1: - The model results for S_h of 0% are shown in Figure 5.12 a and b. For the Berea sandstone mineral bulk and shear moduli, we used the Voigt–Reuss–Hill average (Mavko et al., 1998) of the mineral moduli of the sample constituents, with proportions given by the XRD data of Han et al. (2015). These average moduli do not account for cementation, so we followed the approach of Mavko et al. (1998) where they increased the grain coordination number to 15 (Figure 5.12). We used V_p and Q_p^{-1} at zero hydrate saturation (16.4% gas and 83.6% water in the pore space) and varied the grain co-ordination number n indicated in Figure 5.12 a,b, with n = 12.5 giving the best match to the measured V_p frequency spectrum. The pore size varied from 11 to 73 µm, so we choose to use gas bubble radii of 30 µm (diameter =60 µm) and 50 µm.

However, the best velocity-matched model underestimates Q_p^{-1} at S_h = 0 and adjusting the coordination number hardly changes the model-predicted Q_p^{-1}. Increasing gas bubble radius within the allowable range increases the model Q_p^{-1} slightly, but still grossly underestimates the observed Q_p^{-1}. The HBES model only accounts for gas bubble resonance and not for any micro squirt flow due to only the presence of gas in the pore space (e.g., as invoked by Dvorkin et al., 1993 in their BISQ model). This latter mechanism could likely account for the apparently higher attenuation that was measured. The model also underestimates Q_s^{-1} (not shown). We use a co-ordination number of 12.5 in the following analysis.

Category 2 (Figure 5.12 c, d)*:* - We expect the average gas bubble radius to decrease as the system cools and hydrate starts forming, with the appearance of micro and sub-micro squirt flow related to the hydrate. Attenuation is expected to be relatively low due to the low hydrate concentrations. The HBES model shows a good match for V_p above about 550 kHz, and an excellent match for Q_p^{-1}. The model, at these hydrate and gas saturations (4.6% & 15.7% respectively), is quite sensitive to small changes in gas bubble radius, as shown for r = 20 and 22 µm. The gas bubble radius was decreased from that of category 1, because we saw from the synchrotron imaging that bubble radius reduces with hydrate formation (Chapter 4). The aspect ratio and concentration of inclusions are 3×10^{-4} and 0.48 respectively, as used by Best et al., (2013), and are thought to be intrinsic to hydrates due to its porous structure (e.g., Kerkar et al., 2014; Kuhs et al., 2004). The aspect ratio and concentration of secondary porosity are 0.014 and 0.01 respectively, chosen to fit our measurements but are similar to the ones used by Marín-Moreno et al. (2017). Some of the hydrate may be forming close to the grain contacts, as seen in synchrotron imaging (Chapter 4). So we used arbitrary values (based on velocity match) of 84% of hydrate growing away in pores and 16%

growing near grain contacts. Other parameters in HBES model were as used by Marín-Moreno et al. (2017).

Category 3 (Figure 5.12e, f): - We would expect micro squirt attenuation to increase as the average bubble radius continues to decrease. So we used bubble radius of 9 to 17 μm, which is lower than that of category 2. The aspect ratio of secondary porosity is expected to decrease as more hydrate forms and so we used 0.08 which is lower than that of category 2. Similarly, concentration of secondary porosity would also increase with hydrate saturation and so we used 0.025-0.027. The aspect ratio and concentration of secondary porosity are similar to those used by Marín-Moreno et al. (2017). With increase in S_h, we increased the amount of hydrate growing close to grain contacts, as seen in synchrotron imaging for sand (Chapter 4). We used arbitrary values (based on velocity match) of 60% of hydrate growing in pores and 40% growing near grain contacts. The inclusion aspect ratio and concentration values are from Best et al. (2013) and were same as that for category 2, as its thought to be intrinsic to hydrates due to its porous structure (e.g., Kerkar et al., 2014; Kuhs et al., 2004). We show results for a range of HBES model parameters to indicate their sensitivity (Figure 5.12 e and f). It is possible to obtain a good match to the measured data for both V_p and Q_p^{-1} using reasonable parameter values.

We can see that as the micro squirt flow concentration increases, V_p decreases and Q_p^{-1} increases in Figure 5.12 e and f, allowing an optimum match to be obtained for of both V_p and Q_p^{-1}. If concentration of secondary porosity is set to zero, the model calculates very low attenuation and high velocity. This specific micro squirt flow concentration would vary if other model parameters were changed. However, this duality between velocity and attenuation provides a useful way to constrain the choice of parameters to match micro squirt flow concentration to V_p and Q_p^{-1}. It was also evident that bubble size affects the shape of the spectra for all S_h categories, and this behaviour may be used to better constrain possible bubble size (assuming a dominant, single bubble size rather than a distribution, or an average bubble size). This result shows that broadband measurements can give us better control over the choice of model input parameters, like aspect ratio and concentration (e.g., Chand et al., 2006; Best et al., 2013; Marín-Moreno et al., 2017). Hence, in this way, rock physics models can help to obtain better estimates of the physical properties of natural hydrate bearing samples.

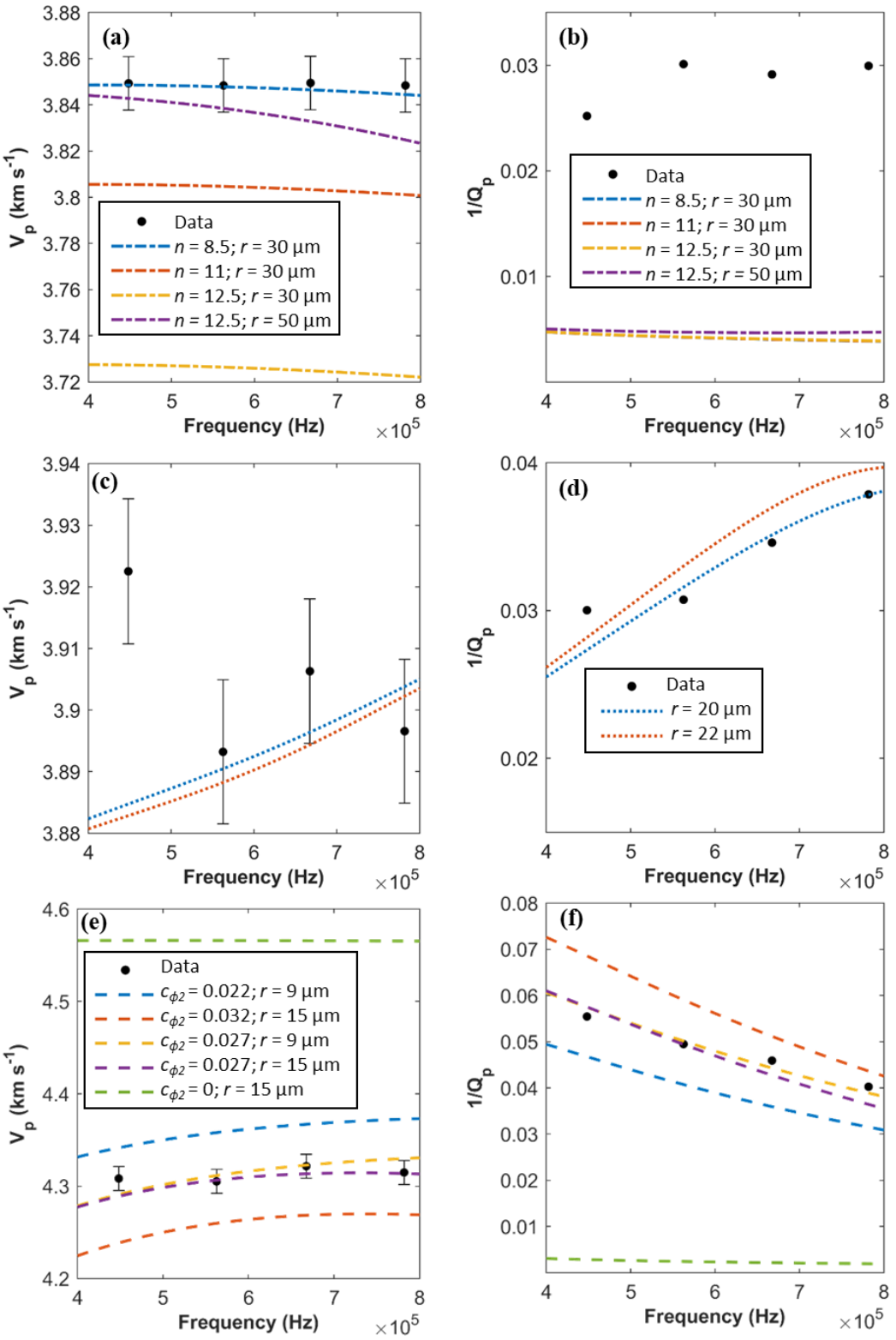

Figure 5.12 Comparison of results from the HBES rock physics model of Marín-Moreno et al. (2017) to measured V_p and Q_p^{-1} for Cycle 3 of hydrate formation in Berea sandstone at different hydrate saturations. Black dots represent the measured data, lines the model results. a) and b) are for zero hydrate saturation; c) and d) are for 4.6% hydrate saturation; e) and f) for 24% hydrate saturation. $C_{\varphi 2}$ is concentration of secondary porosity, r is bubble radius. See text for details.

Our measurements are in ultrasonic frequency range, far above the frequencies used in seismic exploration and sonic well logging. However, having constrained (or calibrated) the HBES model input parameters, we can extend our model to make hypothetical predictions of V_p and Q_p^{-1} behaviour at seismic and sonic frequencies, as shown in Figure 5.13. We compared our model with that of Best et al., 2013 who measured experimentally and modelled Q_p^{-1} at 200 Hz. We used the best fit parameters used in category 3 including the inclusion aspect ratio and concentration of Best et al., 2013.

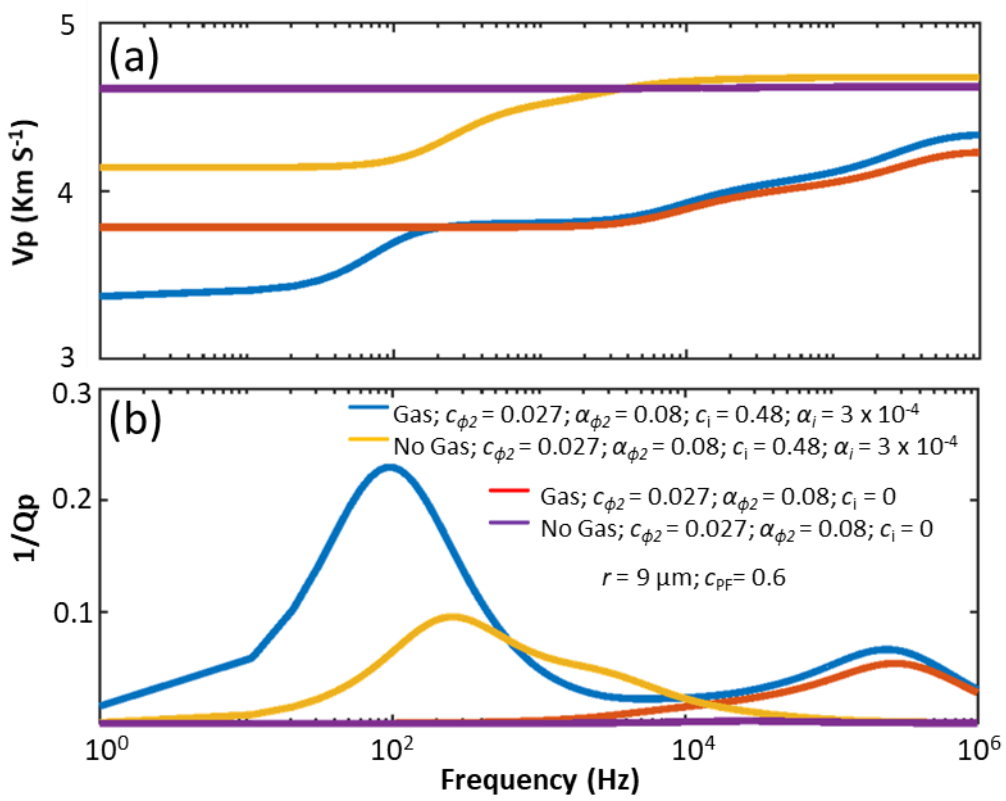

Figure 5.13 HBES rock physics model predictions of V_p and Q_p^{-1} from seismic to ultrasonic frequencies using the parameters calibrated by the ultrasonic Berea data at hydrate saturation of 24% of cycle 3 with differential pressure of 55 MPa. Red and Yellow line have no gas bubble resonance effects. Best et al. (2013) measured attenuations in sand at 200 Hz and found Q_p^{-1} at S_h = 17% is 0.04 ± 0.01 and S_h = 32% is 0.1 ± 0.02.

Encouragingly, in Figure 5.13 our model gives similar Q_p^{-1} magnitudes to measurements of Best et al. (2013), Q_p^{-1} at S_h = 17% is 0.04 ± 0.01 and S_h = 32% is 0.1 ± 0.02; data are from resonant column experiment on Leighton Buzzard sand at 200 Hz. Our model shows that fluid inclusions (for our choice of parameters) do not have much effect on Q_p^{-1} in our measured frequency band, while they are expected to have a strong effect at lower frequencies. Note that we used the fluid inclusion concentrations and aspect ratios indicted by Best et al. (2013), and so we would expect a good match. The HBES model uses a similar concept for modelling hydrate inclusions as used in the

hydrate effective grain (HEG) model presented by Best et al. (2013), i.e. for sub-micro squirt flow. However, the HEG model does not account for micro squirt flow.

We also look at the effect of co-existing gas at both higher and lower frequencies in Figure 5.13. The model results are very sensitive to the chosen bubble size, especially the Q_p^{-1} frequency spectrum shape and peak frequency. Without gas bubble resonance, the magnitude of Q_p^{-1} decreases both for inclusions (sub-micro squirt flow) and secondary porosity (micro squirt flow). These results suggest that gas bubble resonance damping is more dominant at higher frequencies. Sub-micro squirt flow could be an important loss mechanism at seismic and sonic frequencies, producing significant levels of attenuation likely to be detectable on seismic and sonic surveys, but micro squirt flow is significant at higher frequencies (Marín-Moreno et al., 2017).

We used model input parameter estimates based on matching both velocity and attenuation data, exploring values within the range used by Marín-Moreno et al. (2017) and Best et al. (2013). Another approach would be to use the model to invert for micro pore concentrations and aspect ratios. Such an inversion would be needed to explain the changes in gradient and peaks observed in V_p and Q_p^{-1} in Figures 5.4 & 5.5 over the whole range of hydrate saturations. While rock-physics models can help us to understand intrinsic attenuation mechanisms, field measurements of intrinsic attenuation are still a challenge. Geometric spreading and scattering due to impedance mismatches in spatially heterogeneous media can significantly affect field measurements (Huang et al., 2009). For example, acoustic energy from borehole sources can reflect off the borehole wall due to the high stiffness of hydrate- bearing sediments, and not propagate through the hydrate-bearing sediment at all (Lee and Waite, 2007).

5.5 Conclusions

We measured the ultrasonic frequency spectra of V_p, V_s, Q_p^{-1}, Q_s^{-1} during laboratory methane hydrate formation at two differential pressures. At higher differential pressure, where the micro cracks of the sample are closed, we see distinct changes in the shape of the spectra with hydrate formation. We can clearly distinguish two separate trends for high (> 6%) and low hydrate (<6%) saturations. For low hydrate saturations, the attenuation of hydrate bearing samples can be either lower or higher than that of the partially gas and water saturated sample, depending on the measurement frequency. For high hydrate saturations (> 12 %), there is a clear increase in attenuation in the whole measured frequency band of 450 - 800 kHz. Our measurements also support earlier experimental observations of attenuation peaks at specific hydrate saturations that are dependent on measurement frequency. Using rock physics models we were able to explain the measured Q_p^{-1} and V_p variation with a combination of the effects of hydrate formation, including

reduction of gas bubble size, increase in secondary porosity concentration, and decrease in aspect ratio of secondary porosity. Our results show that measurements at ultrasonic frequencies can be used to better constrain the various parameters used in rock physics models, thus providing a means to better constrain *in situ* seismic and sonic data inversions. Also, coexisting gas with hydrate is likely to enhance seismic and sonic wave attenuation, and must be considered when using attenuation to constrain *in situ* hydrate saturation estimates from elastic wave data.

Acknowledgments

We acknowledge funding from the UK Natural Environment Research Council (grant no NE/J020753/1). Bangalore N. Madhusudhan did the synchrotron imaging of the Berea sample at the Swiss Light Synchrotron Radiation for access to TOMCAT-X02DA beamline. T. A. Minshull was supported by a Royal Society Wolfson Research Merit award.

Chapter 6 Conclusions

6.1 Summary of key findings

Controlled laboratory experiments of hydrate formation and dissociation carried out in this thesis provide experimental evidence of the complex nature of gas hydrate bearing sediments. Using high resolution X-ray CT, I was able to image in 3D a system of interlocking solid hydrate and host grain frameworks separated by water films, with isolated pockets of co-existing gas within hydrates. This complex structure has clear implications for geophysical and geomechanical properties. The key findings of this thesis are summarised below.

i) I showed experimentally that all methane gas and water did not form hydrate even when the system is under two phase water-hydrate stability conditions. Co-existing gas was inferred in two separate experiments: a) from pore-pressure temperature calculations and independently from electrical resistivity in consecutive cycles of hydrate formation and dissociation in Berea Sandstone; and b) from high resolution synchrotron X-ray CT imaging of hydrate formation in sand.

ii) The dominant mechanism for co-existing gas was deduced to be the formation of hydrate shells around methane gas bubbles, trapping residual gas inside. Such residual gas can either a) escape when the hydrate shell ruptures due to pressure/temperature variations during hydrate formation, forming smaller bubbles or more hydrate, or b) remain trapped within a sufficiently think hydrate shell or hydrate aggregate.

iii) I demonstrated that the presence of co-existing gas and hydrate can affect hydrate quantification from electrical resistivity. Both gas and hydrate are resistive compared to saline pore fluid, so resistivity based methods cannot differentiate between gas and hydrate. Hence, if all resistive material in the pore space is interpreted as hydrate, this can lead to hydrate quantification errors.

iv) Co-existing gas can cause bubble resonance; using a rock physics model I demonstrated that bubble resonance significantly affects elastic wave velocity and attenuation in the ultrasonic bandwidth 448 – 782 kHz.

v) I demonstrated from high resolution 3D imaging that hydrate growth from undissolved methane in an excess water system can be broadly characterised as a) initially growing in a pore-floating morphology, b) transitioning to a pore-bridging morphology, and c) eventually forming an intra-pore hydrate framework as hydrate growing in adjacent pores coalesces, which in turn interlocks with the sand grain

framework separated by thin water films. This hydrate pore-framework can have isolated pockets of trapped gas.

vi) I also tracked these changes in hydrate morphology from ultrasonic velocity and attenuation, with reference to the newly developed HBES rock physics model for hydrate-bearing porous media. The presence of water films between hydrate and the rock frame has a significant effect on shear wave velocity for pore-bridging hydrate. As expected, the P wave velocity matches the model predictions, but S wave velocity is lower than that pore-bridging model predictions and higher than those for the pore filling model. I infer that the presence of water films between the hydrate and rock frameworks inhibits the transmission of shear forces, leading to a reduced shear modulus and S-wave velocity compared to those expected for solid-solid contacts between hydrate and rock grains.

vii) Hydrate formation and dissociation showed systematic and repeatable changes in attenuation frequency spectra between 450 – 800 kHz. Measurement of elastic wave attenuation at multiple frequencies provides a further constraint on the physical input parameters used for the rock physics model. This helped us to better understand the dominant attenuation mechanisms. I note that the magnitude of relative changes in attenuation with hydrate saturation and morphology is much higher than that of velocity.

viii) I conclude that the dominant wave propagation mechanisms affecting attenuation and velocity at ultrasonic frequencies are i) gas bubble damping related to a decrease in methane gas bubble radius, and ii) squirt flow related to a change in the pore size distribution and shapes during hydrate formation. Squirt flow related to inclusions in hydrate has negligible effect at ultrasonic frequencies, while the model predicts a significant effect at seismic and sonic frequencies used in field studies.

Overall, I have demonstrated that hydrate bearing sediment is a complicated system and quantification of hydrate from elastic and electrical methods needs to account for the above effects. Indeed, multiple and broadband geophysical properties measurements (P and S wave velocities and attenuation, electrical resistivity) are required to accurately quantify natural hydrate systems with low hydrate saturations (< 40%).

6.2 Discussion

The ability to detect and quantify the concentration of hydrate in marine sediments has become increasingly important. The presence of hydrate generally affects the elastic and electrical properties of the sediments and these changes with respect to the hydrate free sediments can be

used to characterise hydrate. While identification of hydrate has been successfully done in the last few decades from seismic data, its quantification is still challenging. Hydrate quantification requires an appropriate model to relate changes in geophysical properties of the sediment to both amount and morphology of hydrate. Both hydrate saturation and morphology have different effects on the geophysical properties of the host sediments and hence rock physics models for hydrate quantification need to account for these. Also, some field studies show a discrepancy between hydrate saturation estimates from elastic and electrical methods, possibly related to the co-existence of gas with hydrate under hydrate stability conditions. Owning to the problems associated with preserving the *in situ* conditions of natural samples, laboratory formed hydrates provide an alternative means to achieve a better understanding of the effects of hydrates on host sediment properties. These issues were discussed in detail in Chapter 1.

From the experimental and modelling results I was able to see how hydrate morphology changes with saturation, and how such changes in saturation and morphology affect P and S wave velocity and attenuation. The key findings are summarised in Section 6.1; here, I shall discuss the possible wider implications of these results.

Our experiments were on a much shorter time scale compared to the formation of natural hydrates. Hence, it is difficult to say whether the gas trapped within hydrates will remain or will diffuse through the hydrate shell over geological time scales. While laboratory time scales are much smaller for diffusion, the observation of porous hydrate with co-existing gas in natural hydrate from Hydrate Ridge, offshore Oregon USA (Suess et al., 2001) shows a possibility of coexisting gas in hydrate. Other field studies in Japan, Norway, and the USA have also shown indirect evidence for, or hypothesise, co-existing gas from resistivity methods (Table 3.1). These samples from the Hydrate Ridge had up to 55% of the bulk hydrate volume as co-existing gas (Suess et al., 2001).

I also saw the change of morphology of hydrate from pore-floating to pore-bridging to intra-pore hydrate framework morphologies. The observed P-wave velocity of pore-bridging hydrate matched the rock-physics model predictions. The S-wave velocity was lower than the pore-bridging model predictions but higher than the pore-floating model predictions (Chapter 4). This is likely to be due to the presence of water films between hydrate and rock frameworks, and when pore-bridging hydrate interlocks with the rock frame, the S-wave velocity increases above that predicted for pore-filling hydrate, but is still less than pore-bridging model predictions (that relies on solid-solid contacts between hydrate and sediment/rock grains). While the presence of a water film has been noted in earlier published imaging studies, my results show that such water film could have a significant effect on geophysical properties. Generally, field hydrate quantification is done from remote P-wave measurements, while our results show that water films affect mainly the S-wave,

and not the P-wave, properties. This also suggests that water films could affect the shear strength of hydrate bearing sediments if water films effects are not properly account for; a key aspect for geohazard assessments.

While our experimental results have added significant new insights into our understanding of the complicated changes of hydrate morphology with saturation, and its effect on geophysical properties, they also point to avenues for further research. The transition of pore-bridging to an intra-pore hydrate framework needs further analysis from both a rock-physics modelling and a laboratory measurement perspective. I was able to observe this transition more clearly in the imaging experiment than in the ultrasonic experiment because the hydrate saturation was higher in the former (max. 50 %) than in the ultrasonic experiment (max. 26%). A higher hydrate saturation would have allowed us to study the effects of these transitions from pore-bridging to intra-pore hydrate framework more clearly. In future, a higher saturation experiment could be planned in the ultrasonic rig. This would provide further insights into how these intra-pore hydrate frameworks affect geophysical properties. To the best of my knowledge, current rock physics models for homogenous hydrate generally treat hydrate in neighbouring pores as non-connected to each other (cementing or pore-floating or pore-bridging), so there is a need to incorporate such a hydrate framework into rock physics modelling. Also, I did not investigate patchy saturation models, that calculate lower velocities than for cementing hydrate, but higher than for pore-bridging hydrate (Dai et al., 2012), which might provide a way forward to model the effect of intra-pore hydrate framework.

I linked changes of P- and S-wave velocities and attenuations to changes in hydrate saturation and morphology (Chapter 4 and 5). Our rock physics model under predicted S wave attenuations, and in future I could modify our rock physics model or use other models to understand the S wave attenuations. It would also have been interesting to link these changes with the bulk resistivity. I had collected fewer resistivity data than for P wave velocity as our system only allows one measurement at a time, and resistivity data take almost one hour for one complete measurement. The changes in gradient of V_p with hydrate saturation matches well that for resistivity. For S_h of about 20% - 24%, both V_p and resistivity increase, and above S_h of 25% both V_p and resistivity decrease (Figure 6.1a). Such changes in resistivity could also be linked to Q_p^{-1}, V_s and Q_s^{-1}, as shown in Chapter 3 and 4 where changes in V_p with S_h matched the changes in Q_p^{-1}, V_s and Q_s^{-1} (Figure 6.1). A possible future work would be to relate elastic and electric measurements, and develop a joint rock physics model. Moreover, our experimental results have velocity and attenuations of both P and S wave, which would be often difficult to unambiguously get from field studies (e.g., references in Waite et al., 2009), and so lend themselves to more detailed analysis of wave propagation phenomena. For example, these measurements of V_p, Q_p^{-1}, V_s, Q_s^{-1} and resistivity could provide a

foundation for the development and validation of a comprehensive joint elastic-electric rock physics model for hydrate-bearing sediments.

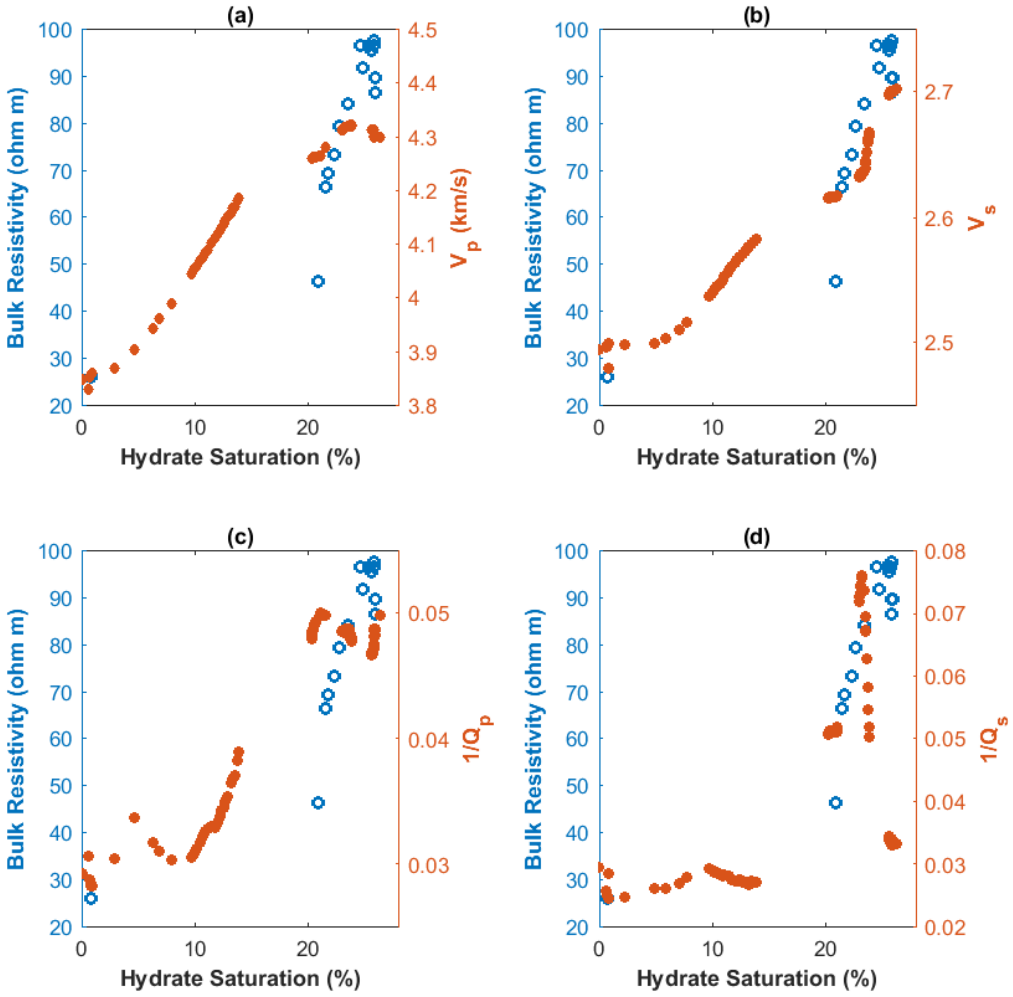

Figure 6.1 Changes in bulk resistivity and P- & S-wave velocity and attenuation with hydrate saturation for cycle 3 of hydrate formation at 55 MPa in Berea sandstone.

Co-located seismic reflection survey and control source electromagnetics have been used to study natural hydrates (e.g., Attias et al., 2016; Goswami et al., 2015; Schwalenberg et al., 2017). While resistivity is effective in finding gas or hydrate saturation within sediments, it cannot differentiate between gas or hydrate which are both resistive compared to saline pore fluid. On the other hand, seismic P wave velocity is effective in identifying the base of hydrate deposits within sediments, although it is difficult to estimate hydrate distribution in sediments from P wave velocity alone. I discussed this recent development of co-located controlled source electromagnetic (CSEM) and P wave studies in Chapter 1. The results of my thesis suggest that, it would be beneficial to design future gas hydrate surveys with co-located broadband frequency P-wave, S-wave and electrical resistivity measurements. Multi-channel seismic streamer methods only measure P-waves, so

complementing these with collocated ocean bottom seismometers (OBSs) and CSEM, would give additional information. These measurements would give additional constraints on estimating gas hydrate morphology, which feeds into inversion for hydrate quantification. Intrinsic attenuations of P and S waves would also give additional insight into gas hydrate morphology and saturation, provided scattering and other possible energy loss sources are properly accounted for. For example, Westbrook et al. (2008) obtained P and S wave quality factor from OBS data. The experimental results of chapter 5 showed that multi frequency measurements can help our understanding and constraint hydrate shape, distribution, and micro-porous structure. Field experiments at the same gas hydrate field using various seismic sources working at different frequencies (e.g., Bolt airguns, GI guns, deep-towed sparker, chirp) can be helpful. Sonic logs, if available, could complement the above experiments. For example, broadband frequency (10 - 1000 Hz) seismic data, collected from different surveys were used to study gas hydrate distribution in Lake Baikal (Vanneste et al., 2001).

Appendix A Input parameters of rock physics model presented in Chapter 2

Table A1 Fixed input parameters used in the model runs (except in Figure 2.3). For more details, refer to the Appendix B.

Parameter	Symbol	Value	Units	Reference
Test Conditions[1]				
Confining pressure	P_c	2.5×10^7	Pa	
Pore fluid pressure	P_p	2.0×10^7	Pa	
Temperature	T	13	°C	
Components Properties				
Hydrate bulk modulus	K_H	7.9×10^9	Pa	(*Best et al.*, 2013)
Hydrate shear modulus	G_H	3.3×10^9	Pa	(*Best et al.*, 2013)
Hydrate Poisson's ratio	ν_H	0.32		
Hydrate density	ρ_H	925	kg m^{-3}	(*Helgerud et al.*, 2009)
Methane bulk modulus	K_{CH4}	$K_{CH4}(P_p, T)$	Pa	(*Millero et al.*, 1980)
Methane density	ρ_{CH4}	$\rho_{CH4}(P_p, T)$	kg m^{-3}	(*Millero et al.*, 1980)
Methane viscosity	μ_{CH4}	$\mu_{CH4}(P_p, T)$	Pa s	(*Millero et al.*, 1980)
Methane irreducible saturation	S_{rCH4}	0.02		(*Reagan and Moridis*, 2008)
Sand/Quartz grain bulk modulus	K_S	36×10^9	Pa	(*Ecker et al.*, 2000)
Sand/Quartz grain shear modulus	G_S	45×10^9	Pa	(*Ecker et al.*, 2000)
Sand/Quartz grain Poisson's ratio	ν_S	0.062		
Sand/Quartz grain density	ρ_S	2650	kg m^{-3}	(*Ecker et al.*, 2000)

Parameter	Symbol	Value	Units	Reference
Sand/Quartz grain diameter	d_S	$1x10^{-4}$	m	(*Best et al.*, 2013)
Sand/Quartz grain coordination number	n	8.5		(*Ecker et al.*, 2000)
Water bulk modulus	K_W	$K_W(P_p, T)$	Pa	(*Setzmann and Wagner*, 1991)
Water density	ρ_W	$\rho_W(P_p, T)$	kg m^{-3}	(*Setzmann and Wagner*, 1991)
Water viscosity	μ_W	$\mu_W(P_p, T)$	Pa s	(*Setzmann and Wagner*, 1991)
Water salinity	s	3.5	% wt	
Water irreducible saturation	S_{rW}	0.2		(*Reagan and Moridis*, 2008)
<u>*Sand Sediment Properties*</u>				
Porosity[1] without hydrate	ϕ_0	0.40		(*Daigle et al.*, 2015)
Critical porosity	ϕ_c	0.38		(*Best et al.*, 2013)
Intrinsic permeability without hydrate	k_0	10^{-13}	m^2	(*Daigle et al.*, 2015)
Intrinsic permeability exponent for cementing hydrate	n_{kC}	3		
Intrinsic permeability exponent for pore-filling hydrate	n_{kPF}	2		
Tortuosity	t	3		based on (*Mavko et al.*, 2009)
van Genuchten's (1980) capillary pressure fitting parameter	m	0.45		(*Reagan and Moridis*, 2008)

Parameter	Symbol	Value	Units	Reference
van Genuchten's (1980) capillary pressure gas entry parameter	P_0	2000	Pa	(*Reagan and Moridis*, 2008)

[1]Test conditions and porosity represent those of a hydrate-bearing sand at about 1500 m water depth and 500 m below the seabed. We have considered the geothermal structure in the northern Gulf of Mexico with a seabed temperature of 4 °C and a geothermal gradient of 17.9 °C km^{-1} (*Daigle et al.*, 2015).

Table A2 Case dependent input parameters used in the model runs. For more details, refer to the Appendix B.

Parameter	Symbol	Units
Aspect ratio of inclusions containing methane or water	$\alpha_{\{iCH4,iW\}}$	
Aspect ratio of type-2 pores created by the formation of cementing hydrate enveloping the grains (C1) and in contact with the grains (C2), and pore-filling hydrate (PF)	$\alpha_{\phi 2\{C1,C2,PF\}}$	
Methane bubble radius	a	m
Concentration of cementing hydrate enveloping the grains (C1) and in contact with the grains (C2), and pore-filling hydrate (PF)	$c_{\{C1,C2,PF\}}$	
Concentration of inclusions in hydrate	c_i	
Concentration of different aspect ratio, type-2, pores	$c_{\phi 2}$	
Frequency	f	Hz
Fraction of cementing hydrate enveloping the grains	f_{C1}	
Fraction of methane and water inclusions in hydrate	$f_{\{iCH4,iW\}}$	
Intrinsic permeability	k	m^2
Porosity	ϕ	
Saturation of hydrate, methane and water in the pore space	$S_{\{H,CH4,W\}}$	

Appendix B Mathematical formulation of rock physics model presented in Chapter 2

This appendix forms a supporting information of a published paper: Marín-Moreno, H., S. K. Sahoo, and A. I. Best (2017), Theoretical modelling insights into elastic wave attenuation mechanisms in marine sediments with pore-filling methane hydrate, Journal of Geophysical Research: Solid Earth, doi:10.1002/2016JB013577.

B.1 Introduction

The approach presented in this work integrates existing models in the literature. This section presents a comprehensive description of the mathematical formulation of the method, sufficient to allow the readers to reproduce our results. For further details about the formulation refer to the original references. The parameters used in the equations below are defined in Table B1 at the end of this document.

Our overarching assumptions are the following (other more detailed assumptions are stated in the text):

i. Fluid inclusions in hydrate affect the elastic moduli of hydrate, of the fluid and solid phases, and of the dry/saturated sediment. Phase saturations in the pore space and hydrate density are independent on the concentration of fluid inclusions in hydrate.
ii. Hydrates are homogeneously distributed in the pore space.
iii. Inclusions are homogeneously distributed in hydrate and independent on hydrate habit. They are open and one-sided connected to the pores.
iv. Load-bearing hydrate habit, as defined by Waite et al. (2009), is not considered. Only pore-filling and cementing hydrate habits, including hydrate at grain contacts and enveloping the grains, as defined by Ecker et al. (1998) and Ecker et al. (2000), are used (see text for more detail).

B.2 Fluids and hydrate properties

Conventional pore pressure sensors used in laboratory samples measure the bulk fluid pressure in the pores (P_p) as they do not distinguish between the pressures of individual fluid phases occupying the pore space. To estimate the pressure of the individual fluid phases, water and methane, we assume known $S_{\{H,CH4,W\}}$ and apply van Genuchten's capillary pressure model (Eq. B1; van Genuchten (1980)) in combination with Bishop's effective stress definition for unsaturated porous media (Eq.B2; Bishop (1959)). We then use the pressure of the individual phases to obtain the properties of water ρ_W, K_W, μ_W (the High Pressure International EOS, Millero et al., (1980)), methane ρ_{CH4}, K_{CH4}, μ_{CH4}, Cp_{CH4}, Cv_{CH4}, k_{thCH4} (Setzmann and Wagner, 1991) and methane hydrate ρ_H (Helgerud et al., 2009). For simplicity, here we assume the same fluid properties for the fluid inclusions in hydrate and for the pore fluids, but those may be different because hydrate could have been formed under different thermodynamic conditions.

$$P_{cap} = P_0 + \left[\left(S^* \right)^{\left(-1/m\right)} - 1 \right]^{1-m} \quad ; \quad S^* = \frac{S_W - \left(S_{rW} + S_{rCH4} \right)}{1 - S_H - \left(S_{rW} + S_{rCH4} \right)} \tag{B1}$$

$$P_p = \frac{S_{\mathrm{W}} P_{\mathrm{W}} + S_{\mathrm{CH4}} P_{\mathrm{CH4}}}{S_{\mathrm{W}} + S_{\mathrm{CH4}}} \tag{B2}$$

$$P_{\mathrm{CH4}} = P_p \frac{S_{\mathrm{W}}}{S_{\mathrm{W}} + S_{\mathrm{CH4}}} P_{cap} \;\; ; \;\; P_{\mathrm{W}} = P_{\mathrm{CH4}} - P_{cap} \tag{B3}$$

In Eq. (B1) m is a fitting parameter obtained experimentally or using pore-network modeling and depends on sediment type, and S_{rW} and S_{rCH4} are the irreducible gas saturations of water and methane, respectively, defined as the saturation of water and methane above which these fluids can flow (e.g., Mahabadi et al., 2016 and references therein).

B.3 Complex elastic moduli of hydrate grain due to submicro squirt flow

The stress induced by the propagation of a seismic wave can generate submicro squirt flow due to the different volume change between inclusions in hydrate with aspect ratios α≈0 and pores with α≈1. The generation of submicro squirt flow due to fluid inclusions in hydrate is considered using the models proposed by Johnston et al. (1979), Leurer (1997) and Leurer and Brown (2008). The frequency dependence of the squirt flow mechanism is added into the expression for the real effective bulk and shear moduli of the grain material from Kuster and Toksöz (1974) by applying the correspondence principle to the bulk and shear moduli of the inclusion material (Eqs. B4)

$$\begin{aligned} K'_{\{\mathrm{iCH4,iW}\}} &= K1_{\{\mathrm{iCH4,iW}\}} + i2\pi f K_{\mathrm{H}} \tau_{\{\mathrm{iCH4,iW}\}} \\ G'_{\{\mathrm{iCH4,iW}\}} &= i2\pi f \mu_{\{\mathrm{iCH4,iW}\}} \end{aligned} \tag{B4}$$

where $K1_{\{\mathrm{iCH4,iW}\}}$ is the effective bulk modulus of the fluids in hydrate inclusions and in the pores and $\tau_{\{\mathrm{iCH4,iW}\}}$ is the relaxation time. These are given by

$$K1_{\{\mathrm{iCH4,iW}\}} = \left(\frac{1-\phi_0 S_{\mathrm{H}} \cdot c_{\mathrm{i}}}{\left(\frac{1}{(1-S_{\mathrm{H}})} \left(\frac{S_{\mathrm{CH4}}}{K_{\mathrm{CH4}}} + \frac{S_{\mathrm{W}}}{K_{\mathrm{W}}} \right) \right)^{-1}} + \frac{\phi_0 S_{\mathrm{H}} \cdot c_{\mathrm{i}} \cdot f_{\{\mathrm{iCH4,iW}\}}}{K_{\{\mathrm{iCH4,iW}\}}} \right)^{-1} \;\; ; \;\; f_{\mathrm{iCH4}} + f_{\mathrm{iW}} = 1$$

$$\tau_{\{\mathrm{iCH4,iW}\}} = \frac{8\mu_{\{\mathrm{iCH4,iW}\}}}{\alpha_{\{\mathrm{iCH4,iW}\}} K1_{\{\mathrm{iCH4,iW}\}} \left(1+\varepsilon_{\{\mathrm{iCH4,iW}\}}\right)} \tag{B5}$$

Note that in Eqs. (B4) the real part of the shear modulus of the fluid inclusion is zero. For the relaxation time in Eqs. (B5), we implicitly assume ellipsoidal inclusions and one-side connected inclusions to the pore space. We estimate the ratio of the volume of inclusions to the pores $\varepsilon_{\{\mathrm{iCH4,iW}\}}$ as

$$\varepsilon_{\{\mathrm{iCH4,iW}\}} = \frac{\phi_0 S_\mathrm{H} \cdot c_\mathrm{i} \cdot f_{\{\mathrm{iCH4,iW}\}}}{\phi} \tag{B6}$$

where the different volumes are defined as

$$\begin{aligned}
&\mathrm{Vol}_\mathrm{Fp} = \phi = \phi_0 \left(1 - S_\mathrm{H}\right) \\
&\mathrm{Vol}_\mathrm{Sp} = 1 - \phi \\
&\mathrm{Vol}_\mathrm{S} = 1 - \phi_0 \\
&\mathrm{Vol}_\mathrm{H} = \phi_0 - \phi = \phi_0 S_\mathrm{H} \\
&\mathrm{Vol}_{\{\mathrm{iCH4,iW}\}} = \phi_0 S_\mathrm{H} \cdot c_\mathrm{i} \cdot f_{\{\mathrm{iCH4,iW}\}}
\end{aligned} \tag{B7}$$

Assuming ellipsoidal/penny crack inclusions as defined by Berryman (1995), the effective complex bulk (Eq. B8) and shear (Eq. B10) moduli of hydrate are given by

$$K'_\mathrm{H} = \frac{K_\mathrm{H} + 4G_\mathrm{H}\left(c_\mathrm{i}\left(f_\mathrm{iCH4} L_{K\mathrm{iCH4}} + f_\mathrm{iW} L_{K\mathrm{iW}}\right)\right)}{1 - 3\left(c_\mathrm{i}\left(f_\mathrm{iCH4} L_{K\mathrm{iCH4}} + f_\mathrm{iW} L_{K\mathrm{iW}}\right)\right)} \tag{B8}$$

where

$$L_{K\,\{\mathrm{iCH4,iW}\}} = \frac{K'_{\{\mathrm{iCH4,iW}\}} - K_\mathrm{H}}{3K_\mathrm{H} + 4G_\mathrm{H}} \left(\frac{K_\mathrm{H}}{K'_{\{\mathrm{iCH4,iW}\}} + \pi \cdot \alpha_{\{\mathrm{iCH4,iW}\}} G_\mathrm{H} \left(\frac{3K_\mathrm{H} + G_\mathrm{H}}{3K_\mathrm{H} + 4G_\mathrm{H}} \right)} \right) \tag{B9}$$

and

$$G'_\mathrm{H} = G_\mathrm{H} \frac{1 + \left(9K_\mathrm{H} + 8G_\mathrm{H}\right)\left(c_\mathrm{i}\left(f_\mathrm{iCH4} L_{G\mathrm{iCH4}} + f_\mathrm{iW} L_{G\mathrm{iW}}\right)\right)}{1 - 6\left(K_\mathrm{H} + 2G_\mathrm{H}\right)\left(c_\mathrm{i}\left(f_\mathrm{iCH4} L_{G\mathrm{iCH4}} + f_\mathrm{iW} L_{G\mathrm{iW}}\right)\right)} \tag{B10}$$

where

$$L_{G\,\{\mathrm{iCH4,iW}\}} = \frac{1}{25} \frac{G'_{\{\mathrm{iCH4,iW}\}} - G_\mathrm{H}}{G_\mathrm{H}\left(3K_\mathrm{H} + 4G_\mathrm{H}\right)} \left(\begin{array}{l} 1 + \dfrac{8G_\mathrm{H}}{4G'_{\{\mathrm{iCH4,iW}\}} + \pi \cdot \alpha_{\{\mathrm{iCH4,iW}\}} G_\mathrm{H} \left(1 + 2\left(\dfrac{3K_\mathrm{H} + G_\mathrm{H}}{3K_\mathrm{H} + 4G_\mathrm{H}} \right) \right)} + \\ +2 \left(\dfrac{3K_{\{\mathrm{iCH4,iW}\}} + 2\left(G'_{\{\mathrm{iCH4,iW}\}} + G_\mathrm{H}\right)}{3K_{\{\mathrm{iCH4,iW}\}} + 4G'_{\{\mathrm{iCH4,iW}\}} + 3\pi \cdot \alpha_{\{\mathrm{iCH4,iW}\}} G_\mathrm{H} \left(\dfrac{3K_\mathrm{H} + G_\mathrm{H}}{3K_\mathrm{H} + 4G_\mathrm{H}} \right)} \right) \end{array} \right) \tag{B11}$$

Note that the effective complex bulk and shear moduli of hydrate are calculated independently. That means the imaginary part of the effective complex bulk modulus of hydrate is not used to calculate its effective complex shear modulus, and viceversa.

B.4 Effective complex dry elastic moduli of hydrate-bearing sediment with submicro squirt flow

The effective complex bulk and shear moduli of hydrate from Eqs. (B8 & B10) are then introduced in the cementing and pore-filling hydrate-bearing sediment models from Ecker et al. (1998; 2000) to calculate the dry bulk and shear effective complex moduli of the sediment with hydrate. The cementing and pore-filling hydrate models were originally defined for cemented and uncemented sands, respectively (Mavko et al., 2009). As mentioned above, here we do not consider the load-bearing hydrate habit. Load-bearing hydrate results from an increase in the saturation of pore-filling hydrate (hydrate that nucleates and grows freely in the pores away from grain contacts) above 25%-40% causing the bridging of neighbouring grains and contributing to the mechanical stability of the granular frame. Existing models for load-bearing hydrate-bearing sands estimate a very small increase in the bulk modulus of the composite sediment with respect to that estimated from a pore-filling hydrate model (e.g., Choi et al. (2014)). In contrast, cementing hydrate nucleates and grows at grain contacts and cements intergranular contacts significantly increasing the elastic properties of the composite sediment (e.g., Waite et al. (2009)). Therefore, by considering end member habits, i.e. pore-filling and cementing hydrates, we cover the range of possible elastic properties values. Following Ecker et al. (1998; 2000), here we also assume that pore-filling hydrate has no effect on the elastic moduli of the granular frame and it is part of the pore fluid. The dry bulk and shear effective complex moduli for the two types of cementing hydrate (hydrate enveloping the grains, C1, and hydrate in contact with the grains, C2) are defined as

$$
\begin{aligned}
K'_{\mathrm{dry}\{\mathrm{C1,C2}\}} &= \frac{n\left(1-\phi_0\right)}{6}\left(K'_{\mathrm{H}}+\frac{4}{3}G'_{\mathrm{H}}\right)S_{n\{\mathrm{C1,C2}\}} \\
G'_{\mathrm{dry}\{\mathrm{C1,C2}\}} &= \frac{K'_{\mathrm{dry}\{\mathrm{C1,C2}\}}}{5}\frac{3n\left(1-\phi_0\right)}{20}G'_{\mathrm{H}}S_{\tau\{\mathrm{C1,C2}\}}
\end{aligned}
\tag{B12}
$$

where S_n and S_τ are given by

$$
\begin{aligned}
S_{n\{\mathrm{C1,C2}\}} &= A_n\left(\Lambda_n\right)r^2_{\{\mathrm{C1,C2}\}}+B_n\left(\Lambda_n\right)r_{\{\mathrm{C1,C2}\}}+C_n\left(\Lambda_n\right) \\
A_n\left(\Lambda_n\right) &= -0.024153\Lambda_n^{-1.3646} \\
B_n\left(\Lambda_n\right) &= 0.20405\Lambda_n^{-0.89008} \\
C_n\left(\Lambda_n\right) &= 0.00024649\Lambda_n^{-1.9864} \\
\Lambda_n &= \frac{2G'_{\mathrm{H}}}{G_{\mathrm{S}}}\frac{\left(1-\nu_{\mathrm{S}}\right)\left(1-\nu_{\mathrm{H}}\right)}{\left(1-2\nu_{\mathrm{S}}\right)}
\end{aligned}
\tag{B13}
$$

$$
\begin{aligned}
&S_{\tau\{\mathrm{C1,C2}\}} = A_\tau\left(\Lambda_\tau, \nu_\mathrm{S}\right) r_{\{\mathrm{C1,C2}\}}^2 + B_\tau\left(\Lambda_\tau, \nu_\mathrm{S}\right) r_{\{\mathrm{C1,C2}\}} + C_\tau\left(\Lambda_\tau, \nu_\mathrm{S}\right) \\
&A_\tau\left(\Lambda_\tau, \nu_\mathrm{S}\right) = -10^{-2}\left(2.26\nu_\mathrm{S}^2 + 2.07\nu_\mathrm{S} + 2.3\right)\Lambda_\tau^{\left(0.079\nu_\mathrm{S}^2 + 0.1754\nu_\mathrm{S} - 1.342\right)} \\
&B_\tau\left(\Lambda_\tau, \nu_\mathrm{S}\right) = \left(0.0573\nu_\mathrm{S}^2 + 0.0937\nu_\mathrm{S} + 0.202\right)\Lambda_\tau^{\left(0.0274\nu_\mathrm{S}^2 + 0..0529\nu_\mathrm{S} - 0.8765\right)} \\
&C_\tau\left(\Lambda_\tau, \nu_\mathrm{S}\right) = -10^{-4}\left(9.654\nu_\mathrm{S}^2 + 4.945\nu_\mathrm{S} + 3.1\right)\Lambda_\tau^{\left(0.01867\nu_\mathrm{S}^2 + 0.4011\nu_\mathrm{S} - 1.8186\right)} \\
&\Lambda_n = \frac{2G'_\mathrm{H}}{G_\mathrm{S}}
\end{aligned}
\tag{B14}
$$

with the parameters r_{C1} and r_{C2} defined as

$$
\begin{aligned}
r_{\mathrm{C1}} &= \left(\frac{2S_\mathrm{H}\left(1-c_\mathrm{PF}\right)\phi_0}{3\left(1-\phi_0\right)}\right)^{0.5} \\
r_{\mathrm{C2}} &= \left(\frac{2S_\mathrm{H}\left(1-c_\mathrm{PF}\right)\phi_0}{3n\left(1-\phi_0\right)}\right)^{0.25}
\end{aligned}
\tag{B15}
$$

Finally, the dry bulk and shear effective complex moduli of cementing hydrate are given by

$$
\begin{aligned}
K'_{\mathrm{dryC}} &= f_{\mathrm{dryC1}}K'_{\mathrm{dryC1}} + \left(1 - f_{\mathrm{dryC1}}\right)K'_{\mathrm{dryC2}} \\
G'_{\mathrm{dryC}} &= f_{\mathrm{dryC1}}G'_{\mathrm{dryC1}} + \left(1 - f_{\mathrm{dryC1}}\right)G'_{\mathrm{dryC2}}
\end{aligned}
\tag{B16}
$$

The effective elastic moduli of the dry granular frame of the sediment with pore-filling hydrate are calculated using a modified Hashin-Shtrikman-Hertz-Mindlin theory (Dvorkin et al., 1999) and are given by

$$
\left\{
\begin{aligned}
K_{\mathrm{dryPF}} &= \left[\frac{\phi/\phi_c}{K_\mathrm{HM} + \frac{4}{3}G_\mathrm{HM}} + \frac{1-\phi/\phi_c}{K_\mathrm{S} + \frac{4}{3}G_\mathrm{HM}}\right]^{-1} - \frac{4}{3}G_\mathrm{HM} \\
G_{\mathrm{dryPF}} &= \left[\frac{\phi/\phi_c}{G_\mathrm{HM} + Z} + \frac{1-\phi/\phi_c}{G_\mathrm{S} + Z}\right]^{-1} - Z \quad ; \quad Z = \frac{G_\mathrm{HM}}{6}\left(\frac{9K_\mathrm{HM} + 8G_\mathrm{HM}}{K_\mathrm{HM} + 2G_\mathrm{HM}}\right)
\end{aligned}
\right\} \quad \phi < \phi_c
$$

$$
\left\{
\begin{aligned}
K_{\mathrm{dryPF}} &= \left[\frac{\left(1-\phi\right)/\left(1-\phi_c\right)}{K_\mathrm{HM} + \frac{4}{3}G_\mathrm{HM}} + \frac{\left(\phi-\phi_c\right)/\left(1-\phi_c\right)}{\frac{4}{3}G_\mathrm{HM}}\right]^{-1} - \frac{4}{3}G_\mathrm{HM} \\
G_{\mathrm{dryPF}} &= \left[\frac{\left(1-\phi\right)/\left(1-\phi_c\right)}{G_\mathrm{HM} + Z} + \frac{\left(\phi-\phi_c\right)/\left(1-\phi_c\right)}{Z}\right]^{-1} - Z \quad ; \quad Z = \frac{G_\mathrm{HM}}{6}\left(\frac{9K_\mathrm{HM} + 8G_\mathrm{HM}}{K_\mathrm{HM} + 2G_\mathrm{HM}}\right)
\end{aligned}
\right\} \quad \phi > \phi_c
\tag{B17}
$$

where the bulk and shear moduli of a dry, dense, random pack of identical spherical grains subject to a effective stress *P** are given by the contact Hertz-Mindlin theory (*Mindlin*, 1949) as

$$K_{\mathrm{HM}} = \left[\frac{n^2 \left(1-\phi_{\mathrm{c}}\right)^2 G_{\mathrm{S}}^2}{18\pi^2 + \left(1-\nu_{\mathrm{S}}\right)^2} P* \right]^{1/3}$$
$$G_{\mathrm{HM}} = \frac{5-4\nu_{\mathrm{S}}}{5\left(2-\nu_{\mathrm{S}}\right)} \left[\frac{3n^2 \left(1-\phi_{\mathrm{c}}\right)^2 G_{\mathrm{S}}^2}{2\pi^2 + \left(1-\nu_{\mathrm{S}}\right)^2} P* \right]^{1/3} \quad \text{(B18)}$$

The effective complex shear and bulk moduli of the dry granular frame are the Reuss average (Reuss, 1929; Mavko et al., 2009) of those of the sediment containing cementing (Eqs. B16) and pore-filling hydrate (Eqs. B17), and are given by

$$K'_{\mathrm{dry}} = \left(\frac{c_{\mathrm{PF}}}{K_{\mathrm{dryPF}}} + \frac{1-c_{\mathrm{PF}}}{K'_{\mathrm{dryC}}} \right)^{-1}$$
$$G'_{\mathrm{dry}} = \left(\frac{c_{\mathrm{PF}}}{G_{\mathrm{dryPF}}} + \frac{1-c_{\mathrm{PF}}}{G'_{\mathrm{dryC}}} \right)^{-1} \quad \text{(B19)}$$

B.5 Non-isothermal dynamic gas bulk modulus

The presence of small concentrations of free gas in the pores can attenuate the propagation of seismic waves. Here we apply the model proposed by Smeulders and van Dongen (1997) to consider the attenuation of seismic waves due to the presence of methane bubbles in the pores in an incompressible fluid-solid system. The authors propose a model to calculate the non-isothermal dynamic bulk modulus of oscillating gas bubbles in a dilute gas-liquid mixture considering viscous, thermal and Biot's type frequency dependent damping caused by a change in pressure far away from the bubbles. (Smeulders and van Dongen, 1997). This model recovers the isothermal quasi-stationary bulk modulus at low frequencies, and at high frequencies gives a bulk modulus that tends to negative infinity (Smeulders and van Dongen, 1997). The methane non-isothermal dynamic complex bulk modulus is given by

$$K'_{\mathrm{CH4}} = \frac{1}{3} a^2 2\pi f \rho_{\mathrm{Fp}} \left(\frac{3n_{th} K_{\mathrm{CH4}}}{a^2 2\pi f \rho_{\mathrm{Fp}}} - 1 \frac{\rho'_{12}}{\phi \rho_{\mathrm{Fp}}} + \frac{4i\mu_{\mathrm{W}}}{a^2 2\pi f} \right) \quad \text{(B20)}$$

where here K_{CH4} is the isothermal and quasi-stationary bulk modulus of methane, and the fluid phase density ρ_{Fp} and the parameter ρ'_{12} are given by

$$\rho_{\mathrm{Fp}} = \frac{\phi_0}{\phi} \left(S_{\mathrm{CH4}} \rho_{\mathrm{CH4}} + S_{\mathrm{W}} \rho_{\mathrm{W}} \right)$$
$$\rho'_{12} = -\left(t-1\right)\phi + \frac{i \cdot b}{2\pi f} \quad \text{(B21)}$$

where

$$b = \frac{\mu_{\mathrm{W}} \phi^2}{k} \tag{B22}$$

and the intrinsic permeability of the hydrate-bearing sediment *k* is given by

$$k = \left(c_{\mathrm{PF}} \Big/ k_0 \left(\frac{\phi_0 (1 - S_{\mathrm{H}})}{\phi_0} \right)^{n_{k\mathrm{PF}}} + (1 - c_{\mathrm{PF}}) \Big/ k_0 \left(\frac{\phi_0 (1 - S_{\mathrm{H}})}{\phi_0} \right)^{n_{k\mathrm{C}}} \right)^{-1} \tag{B23}$$

The complex polytropic exponent n_{th} in Eq. (B20) is defined as

$$n_{th} = \frac{Cp_{\mathrm{CH4}}}{Cv_{\mathrm{CH4}}} \left[\frac{Cp_{\mathrm{CH4}}}{Cv_{\mathrm{CH4}}} - \left(\frac{Cp_{\mathrm{CH4}}}{Cv_{\mathrm{CH4}}} - 1 \right) \left(1 - \frac{4i}{\left(2d_{\mathrm{p}} / 3\delta_{\mathrm{T}} \right)^2} \left(1 + \frac{1}{8} i \left(2d_{\mathrm{p}} / 3\delta_{\mathrm{T}} \right)^2 \right)^{1/2} \right)^{-1} \right]^{-1} \tag{B24}$$

where the thermal depth penetration δ_{T} in Eq. (B24) is given by

$$\delta_{\mathrm{T}} = \left(\frac{2k_{th\mathrm{CH4}}}{2\pi f} \right)^{1/2} \tag{B25}$$

B.6 Effective complex elastic moduli of the fluid and solid phases

We calculate the effective complex bulk modulus of the fluid phase assuming that pore-filling hydrate is part of the fluid phase. We first calculate the Reuss average (Reuss, 1929; Mavko et al., 2009) of the bulk modulus of the fluid as

$$K1'_{\mathrm{Fp}} = \left(\frac{S_{\mathrm{CH4}}}{K'_{\mathrm{CH4}}} + \frac{S_{\mathrm{W}}}{K_{\mathrm{W}}} \right)^{-1} \tag{B26}$$

We then include the effect of the pore-filling hydrate in the bulk modulus of the fluid phase by using the Reuss average of the fluid bulk modulus from Eq. (B26) and the effective complex bulk modulus of the fraction of pore-filling hydrate. Hence, the effective complex bulk modulus of the fluid phase is given by

$$K'_{\mathrm{Fp}} = \left(\frac{S_{\mathrm{CH4}} + S_{\mathrm{W}}}{K1'_{\mathrm{Fp}}} + \frac{S_{\mathrm{H}} c_{\mathrm{PF}}}{K'_{\mathrm{H}}} \right)^{-1} \tag{B27}$$

The effective complex bulk and shear moduli of the solid phase are the Voigt-Reuss-Hill average

(Mavko et al., 2009) of the bulk and shear moduli of the solid grains and the effective bulk and shear moduli of the fraction of cementing hydrate. These are given by

$$K'_{Sp} = \frac{1}{2}\left[f_S K_S + (1-f_S) K'_H + \left(\frac{f_S}{K_S} + \frac{(1-f_S)}{K'_H} \right)^{-1} \right]$$
$$G'_{Sp} = \frac{1}{2}\left[f_S G_S + (1-f_S) G'_H + \left(\frac{f_S}{G_S} + \frac{(1-f_S)}{G'_H} \right)^{-1} \right] \quad \text{(B28)}$$

where the fraction of solid grains in the granular frame f_S is defined as

$$f_S = \frac{(1-\phi_0)}{1-(1-S_H(1-c_{PF}))\phi_0} \quad \text{(B29)}$$

B.7 Effective complex dry elastic moduli of hydrate-bearing sediment with micro squirt flow

The formation of hydrate in the pore space likely creates pores with different shapes, lower aspect ratios, to those originally. We thus assume that the formation of hydrate generates ellipsoidal smaller size pores named here as type 2 pores (the original pores are assumed spherical). Both hydrate habits are allowed to create type 2 pores with different aspect ratios. However, based on the location where these two different hydrate habits form in the pore space, the aspect ratio of type 2 pores generated by the formation of pore-filling hydrate needs to be greater than those created by the formation of cementing hydrate. Similarly, to the generation of submicro squirt flow, micro squirt flow can be generated by different volume changes between type 2 pores and the original pores caused by a seismic wave propagating through the porous media. Here we follow a similar approach to that adopted for submicro squirt flow (see Eqs. B4-B5 and Eqs. B30-B31), and modify the formulations proposed by Johnston et al. (1979), Leurer (1997) and Leurer and Brown (2008) to consider frequency dependent micro squirt flow. This attenuation mechanism is introduced into the effective complex dry bulk and shear moduli of the sediment with hydrate by substituting in Kuster and Toksöz's (1974) expression (i) the real bulk and shear moduli of the grain material with the effective real dry bulk and shear moduli of the sediment containing hydrate (calculated in Eqs. B19 above), and (ii) applying the correspondence principle to the bulk and shear moduli of the fluid phase without pore-filling hydrate

$$K''_{Fp} = \Re\left(K1'_{FP}\right) + i2\pi f \Re\left(K'_{dry}\right) \tau_{FP\{C1,C2,PF\}}$$
$$G''_{Fp} = i2\pi f \mu_{FP} \quad \text{(B30)}$$

where the relaxation time τ_{Fp} is given by

$$\tau_{\mathrm{FP\{C1,C2,PF\}}} = \frac{4\mu_{\mathrm{FP}}}{\alpha_{\phi 2}\Re\left(K1'_{\mathrm{FP}}\right)\left(1+\varepsilon_{\phi 2\{\mathrm{C1,C2,PF}\}}\right)} \tag{B31}$$

and the viscosity of the fluid phase μ_{Fp} is given by modifying Ishii and Mishima's (1984) model to consider the presence of hydrate as

$$\mu_{\mathrm{Fp}} = \mu_{\mathrm{W}}\left(1-\frac{S_{\mathrm{CH4}}}{1-S_{\mathrm{H}}}\right)^{-2.5(1-S_{\mathrm{H}})\mu_r} \tag{B32}$$

where the parameter μ_r is defined as

$$\mu_r = \frac{\mu_{\mathrm{CH4}}+0.4\mu_{\mathrm{W}}}{\mu_{\mathrm{CH4}}+\mu_{\mathrm{W}}} \tag{B33}$$

In the relaxation time defined in Eq. (B30), we assume that type 2 pores have an ellipsoidal shape and are two-side connected to the original pores. Note that the relaxation time depends on aspect ratio and thus on hydrate habit. We define the volumetric ratio of type 2 pores to original pores $\varepsilon_{\phi 2\{\mathrm{C1,C2,PF}\}}$ in Eq. (B31) as

$$\begin{aligned}
\varepsilon_{\phi 2\,\mathrm{PF}} &= \frac{\phi\cdot c_{\phi 2}\cdot c_{\mathrm{PF}}\cdot S_{\mathrm{H}}}{\phi\left(1-c_{\phi 2}\right)} \\
\varepsilon_{\phi 2\,\mathrm{C1}} &= \frac{\phi\cdot c_{\phi 2}\left(1-c_{\mathrm{PF}}\right)\left(1-f_{\mathrm{C1}}\right)S_{\mathrm{H}}}{\phi\left(1-c_{\phi 2}\right)} \\
\varepsilon_{\phi 2\,\mathrm{C2}} &= \frac{\phi\cdot c_{\phi 2}\left(1-c_{\mathrm{PF}}\right)f_{\mathrm{C1}}\cdot S_{\mathrm{H}}}{\phi\left(1-c_{\phi 2}\right)}
\end{aligned} \tag{B34}$$

The effective complex dry bulk modulus of the sediment with hydrate experiencing micro squirt flow is given by

$$K''_{\mathrm{dry}} = \frac{\Re\left(K'_{\mathrm{dry}}\right)+4\Re\left(G'_{\mathrm{dry}}\right)\Lambda_K}{1-3\Lambda_K} \tag{B35}$$

where

$$\Lambda_K = \phi\cdot c_{\phi 2}\cdot S_{\mathrm{H}}\left(c_{\mathrm{PF}}\cdot L_{K\mathrm{PF}}+(1-c_{\mathrm{PF}})f_{\mathrm{C1}}\cdot L_{K\mathrm{C1}}+(1-c_{\mathrm{PF}})\left(1-f_{\mathrm{C1}}\right)L_{K\mathrm{C2}}\right) \tag{B36}$$

with

$$L_{K\{\mathrm{C1,C2,PF}\}} = \frac{K''_{\mathrm{Fp}\{\mathrm{C1,C2,PF}\}} - \Re\left(K'_{\mathrm{dry}}\right)}{3\Re\left(K'_{\mathrm{dry}}\right) + 4\Re\left(G'_{\mathrm{dry}}\right)} \cdot \left(\frac{\Re\left(K'_{\mathrm{dry}}\right)}{K''_{\mathrm{Fp}\{\mathrm{C1,C2,PF}\}} + \pi \cdot \alpha_{\phi 2\{\mathrm{C1,C2,PF}\}} \Re\left(G'_{\mathrm{dry}}\right) \left(\frac{3\Re\left(K'_{\mathrm{dry}}\right) + \Re\left(G'_{\mathrm{dry}}\right)}{3\Re\left(K'_{\mathrm{dry}}\right) + 4\Re\left(G'_{\mathrm{dry}}\right)} \right)} + \right) \tag{B37}$$

and the effective complex dry shear modulus is given by

$$G''_{\mathrm{dry}} = \Re\left(G'_{\mathrm{dry}}\right) \frac{1 + \left(9\Re\left(K'_{\mathrm{dry}}\right) + 8\Re\left(G'_{\mathrm{dry}}\right)\right)\Lambda_G}{1 - 6\left(\Re\left(K'_{\mathrm{dry}}\right) + 2\Re\left(G'_{\mathrm{dry}}\right)\right)\Lambda_G} \tag{B38}$$

where

$$\Lambda_G = \phi \cdot c_{\phi 2} \cdot S_{\mathrm{H}} \left(c_{\mathrm{PF}} \cdot L_{GPF} + (1 - c_{\mathrm{PF}}) f_{\mathrm{C1}} \cdot L_{GC1} + (1 - c_{\mathrm{PF}})(1 - f_{\mathrm{C1}}) \cdot L_{GC2} \right) \tag{B39}$$

with

$$L_{G\{\mathrm{C1,C2,PF}\}} = \frac{1}{25} \frac{G''_{\mathrm{Fp}} - \Re\left(G'_{\mathrm{dry}}\right)}{\Re\left(G'_{\mathrm{dry}}\right)\left(3\Re\left(K'_{\mathrm{dry}}\right) + 4\Re\left(G'_{\mathrm{dry}}\right)\right)} \cdot \left(1 + \frac{8\Re\left(G'_{\mathrm{dry}}\right)}{4G''_{\mathrm{Fp}} + \pi \cdot \alpha_{\phi 2\{\mathrm{C1,C2,PF}\}} \Re\left(G'_{\mathrm{dry}}\right) \left(1 + 2\left(\frac{3\Re\left(K'_{\mathrm{dry}}\right) + \Re\left(G'_{\mathrm{dry}}\right)}{3\Re\left(K'_{\mathrm{dry}}\right) + 4\Re\left(G'_{\mathrm{dry}}\right)} \right) \right)} + \right. \left. + 2 \left(\frac{\frac{3}{2}\Re\left(K1'_{\mathrm{Fp}} + K2'_{\mathrm{Fp}}\right) + 2\left(G''_{\mathrm{Fp}} + \Re\left(G'_{\mathrm{dry}}\right)\right)}{\frac{3}{2}\Re\left(K1'_{\mathrm{Fp}} + K2'_{\mathrm{Fp}}\right) + 4G''_{\mathrm{Fp}} + 3\pi \cdot \alpha_{\phi 2\{\mathrm{C1,C2,PF}\}} \Re\left(G'_{\mathrm{dry}}\right) \left(\frac{3\Re\left(K'_{\mathrm{dry}}\right) + \Re\left(G'_{\mathrm{dry}}\right)}{3\Re\left(K'_{\mathrm{dry}}\right) + 4\Re\left(G'_{\mathrm{dry}}\right)} \right)} \right) \right) \tag{B40}$$

B.8 Biot-Stoll poroelastic model with submicro and micro squirt flows and gas bubble damping

We first assume superposition of submicro and micro squirt flow attenuation mechanisms and the complex bulk and shear effective moduli of the dry granular frame of the sediment containing hydrate are given by

$$K'''_{dry} = \Re\left(K''_{dry}\right) + i\left(\Im\left(K''_{dry}\right) + \Im\left(K'_{dry}\right)\right)$$
$$G'''_{dry} = \Re\left(G''_{dry}\right) + i\left(\Im\left(G''_{dry}\right) + \Im\left(G'_{dry}\right)\right) \quad \text{(B41)}$$

The effective complex dry bulk and shear moduli of the sediment containing hydrate K'''_{dry} and G'''_{dry} (Eqs. B41), and the effective complex bulk modulus of the fluid K'_{Fp} (Eqs. B27) and solid K'_{Sp} (Eqs. B28) phases are now introduced into the Biot-Stoll model (BSM; Stoll and Bryan, (1970)). This model is an extension of Biot's (1956a, b) model to include global friction losses in the skeletal frame of unconsolidated marine sediments besides the classical Biot's global fluid flow losses due to the inertial motion of the frame with respect to pore fluids. The BSM is given by (*Mavko et al*., 2009)

$$\mathrm{P} = -\frac{1}{2}\left(\mathrm{b} + \mathrm{sign}\sqrt{\mathrm{b}^2 - 4\cdot\mathrm{a}\cdot\mathrm{c}}\right)$$
$$\mathrm{S} = \frac{\left(\mathrm{q}\cdot\rho - \rho_{Fp}^2\right)}{\mathrm{q}\cdot G'''_{dry}} \quad \text{(B42)}$$

where ρ is the hydrate-bearing sediment density and is given by

$$\rho = \left(1-\phi_0\right)\rho_S + \phi_0\left(S_H\rho_H + S_W\rho_W + S_{CH4}\rho_{CH4}\right) \quad \text{(B43)}$$

In Eqs. (B42) the parameters a, b, c and sign are given by

$$\mathrm{a} = \mathrm{C}^2 - \mathrm{M}\cdot\mathrm{H}$$
$$\mathrm{b} = \mathrm{H}\cdot\mathrm{q} + \mathrm{M}\cdot\rho - 2\mathrm{C}\rho_{Fp}$$
$$\mathrm{c} = \rho_{Fp}^2 - \rho\cdot\mathrm{q}$$
$$\mathrm{sign} = \begin{cases} -1 \ \text{ if } \ \Re\left(\mathrm{conj}(\mathrm{b})\sqrt{\mathrm{b}^2 - 4\cdot\mathrm{a}\cdot\mathrm{c}}\right) < 0 \\ +1 \ \text{ if } \ \Re\left(\mathrm{conj}(\mathrm{b})\sqrt{\mathrm{b}^2 - 4\cdot\mathrm{a}\cdot\mathrm{c}}\right) > 0 \end{cases} \quad \text{(B44)}$$

and the function conj(b) indicates the complex conjugate of b.

In Eqs. (B44) the parameters C, H, M and q are given by

$$
\begin{aligned}
\mathrm{A} &= K'_{\mathrm{Sp}}\left(1+\phi\left(\frac{K'_{\mathrm{Sp}}}{K'_{\mathrm{Fp}}}-1\right)\right)\\
\mathrm{C} &= \frac{\left(K'_{\mathrm{Sp}}-K'''_{\mathrm{dry}}\right)K'_{\mathrm{Sp}}}{\mathrm{A}\text{-}K'''_{\mathrm{dry}}}\\
\mathrm{H} &= K'''_{\mathrm{dry}}+\frac{4}{3}G'''_{\mathrm{dry}}+\frac{\left(K'_{\mathrm{Sp}}-K'''_{\mathrm{dry}}\right)^2}{\mathrm{A}\text{-}K'''_{\mathrm{dry}}}\\
\mathrm{M} &= \frac{K'^2_{\mathrm{Sp}}}{\mathrm{A}\text{-}K'''_{\mathrm{dry}}}\\
\mathrm{q} &= t\cdot\frac{K'_{\mathrm{Fp}}}{\phi}-\frac{i\cdot\mu_{\mathrm{Fp}}F(\zeta)}{2\pi f\cdot k}
\end{aligned}
\tag{B45}
$$

where the viscodynamic operator $F(\zeta)$ incorporates the frequency dependence of viscous drag and it is defined by

$$
F(\zeta)=\frac{1}{4}\left(\frac{\zeta T(\zeta)}{1+2i\cdot T(\zeta)/\zeta}\right) \tag{B46}
$$

The function $T(\zeta)$ and parameter ζ in Eq. (B46) are defined as

$$
\begin{aligned}
T(\zeta) &= \frac{\mathrm{e}^{i3\pi/4}J_1\left(\zeta\mathrm{e}^{-i\pi/4}\right)}{J_0\left(\zeta\mathrm{e}^{-i\pi/4}\right)}\\
\zeta &= \sqrt{\frac{2\pi f\cdot a_{\mathrm{S}}^2\rho_{\mathrm{Fp}}}{\mu_{\mathrm{Fp}}}}
\end{aligned}
\tag{B47}
$$

where the J_0 and J_1 are the Bessel functions of order 0 and 1, respectively, and a_S is the pore-size parameter which for spherical grains is defined by *Hovem and Ingram* (1979) as

$$
a_{\mathrm{S}}=\frac{\phi\cdot d_{\mathrm{S}}}{3(1-\phi)} \tag{B48}
$$

Finally, from Eqs. (B43 & B45) the fast and slow P wave velocities V_{P1} and V_{P2}, respectively, and S wave velocity V_S are obtained as

$$
\begin{aligned}
V_{P1} &= \Re\left(\sqrt{\mathrm{P}/\mathrm{c}}\right)\\
V_{P2} &= \Re\left(\sqrt{\mathrm{a}/\mathrm{P}}\right)\\
V_S &= \Re\left(\sqrt{1/\mathrm{S}}\right)
\end{aligned}
\tag{B49}
$$

and the fast and slow P wave inverse quality factors Q^{-1}_{P1} and Q^{-1}_{P2}, respectively, and S wave inverse quality factor Q^{-1}_{S} are obtained as

$$Q_{P1}^{-1} = \frac{2\Im\left(\sqrt{\mathrm{P}/\mathrm{c}}\right)}{\Re\left(\sqrt{\mathrm{P}/\mathrm{c}}\right)}$$
$$Q_{P2}^{-1} = \frac{2\Im\left(\sqrt{\mathrm{a}/\mathrm{P}}\right)}{\Re\left(\sqrt{\mathrm{a}/\mathrm{P}}\right)} \quad \text{(B50)}$$
$$Q_{S}^{-1} = \frac{2\Im\left(\sqrt{\mathrm{l}/\mathrm{S}}\right)}{\Re\left(\sqrt{\mathrm{l}/\mathrm{S}}\right)}$$

Table B 1 Nomenclature of the parameters used in the formulation.

Variable	Description
a	= bubble radius
a_S	= pore size parameter as defined by Hovem and Ingram (1979)
$\alpha_{\{iCH4,iW\}}$	= aspect ratio of inclusions containing methane or water
$\alpha_{\phi 2\{C1,C2,PF\}}$	= aspect ratio of type 2 pores created by the formation of cementing hydrate enveloping the grains (C1) and in contact with the grains (C2), and pore-filling hydrate
$C\{p,v\}_{CH4}$	= specific heat of methane at constant pressure and constant volume
c_i	= concentration of inclusions in hydrate
c_{PF}	= concentration of pore-filling hydrate in the pore space
$c_{\phi 2}$	= concentration of type 2 pores
d_S	= diameter of the solid grains
δ_T	= thermal depth penetration in Smeulders and van Dongen's (1997) non-isothermal dynamic gas bulk modulus model
$\varepsilon_{\{iCH4,iW\}}$	= volumetric ratio of methane and water inclusions in hydrate to pores
$\varepsilon_{\phi 2\{C1,C2,PF\}}$	= volumetric ratio of type 2 pores created by the formation of cementing hydrate enveloping the grains (C1) and in contact with the grains (C2), and pore-filling hydrate to original pores
$F(\zeta)$	= viscodynamic operator in the Stoll and Bryan's, (1970) model
f	= frequency
f_{C1}	= fraction of cementing hydrate enveloping the grains
$f_{\{iCH4,iW\}}$	= fraction of methane and water inclusions in hydrate
f_S	= fraction of solid grains in the granular frame (solid grains + cementing hydrate)
$G_{\{S,H\}}$	= shear modulus of solid grains and hydrate

Variable	Description
G'_{H}	= effective complex hydrate shear modulus
$G'_{\{iCH4,iW\}}$	= complex shear modulus of methane and water inclusions in hydrate
G_{dryPF}	= effective dry shear modulus considering pore-filling hydrate only
$G'_{dry\{C,C1,C2\}}$	= effective complex dry shear modulus considering cementing hydrate (C), cementing hydrate enveloping the solid grains only (C1), and cementing hydrate in contact with solid grains only (C2)
G'_{dry}	= effective complex dry shear modulus considering submicro squirt flow only
G''_{dry}	= effective complex dry shear modulus considering micro squirt flow only
G'''_{dry}	= effective complex dry shear modulus considering submicro and micro squirt flow
$G'_{\{Fp,Sp\}}$	= complex shear modulus of the fluid phase and effective complex shear modulus of the solid phase (solid grains + hydrate)
G''_{Fp}	= complex shear modulus of the fluid phase used in the micro squirt flow model
G_{HM}	= Hertz-Mindlin shear modulus
$K_{\{S,H,CH4,W\}}$	= bulk modulus of solid grains, hydrate, and pure methane and water. For methane is the isothermal quasi-stationary bulk modulus.
$K'_{\{H,CH4\}}$	= effective complex hydrate bulk modulus and complex methane bulk modulus. For methane is the non-isothermal dynamic bulk modulus.
$K_{\{iCH4,iW\}}$	= real part of the bulk modulus of methane and water inclusions in hydrate
$K1_{\{iCH4,iW\}}$	= real part of the effective bulk modulus of methane and water inclusions in hydrate and the fluid in the pores used in the submicro squirt flow model
$K'_{\{iCH4,iW\}}$	= complex bulk modulus of methane and water inclusions in hydrate
K_{dryPF}	= effective dry bulk modulus considering pore-filling hydrate only

Variable	Description
$K'_{dry\{C,C1,C2\}}$	= effective complex dry bulk modulus considering cementing hydrate (C), cementing hydrate enveloping the solid grains only (C1), and cementing hydrate in contact with solid grains only (C2)
K'_{dry}	= effective complex dry bulk modulus considering submicro squirt flow only
K''_{dry}	= effective complex dry bulk modulus considering micro squirt flow only
K'''_{dry}	= effective complex dry bulk modulus considering submicro and micro squirt flow
$K'_{\{Fp,Sp\}}$	= effective complex bulk modulus of the fluid (fluids + pore-filling hydrate) and solid (solid grains + cementing hydrate) phases
$K1'_{\{Fp\}}$	= effective complex bulk modulus of the fluid phases in the pores only (without pore-filling hydrate)
K''_{Fp}	= effective complex bulk modulus of the fluid phase used in the micro squirt flow model
K_{HM}	= Hertz-Mindlin bulk modulus
k	= intrinsic permeability of the sediment containing hydrate
k_0	= intrinsic permeability of the sediment without hydrate
k_{thCH4}	= thermal conductivity of methane
m	= experimental fitting parameter for van Genuchten's (1980) capillary pressure model
n	= solid grains coordination number
n_{kC}	= exponent controlling how the intrinsic permeability changes with the formation of cementing hydrate
n_{kPF}	= exponent controlling how the intrinsic permeability changes with the formation of pore-filling hydrate
n_{th}	= complex polytropic exponent in Smeulders and van Dongen's (1997) non-isothermal dynamic gas bulk modulus model

Variable	Description
P_c	= confining pressure
P_p	= pore pressure
P^*	= effective pressure (P_c-P_p)
$P_{\{CH4,W\}}$	= methane and water pressures
P_0	= parameter controlling the air entry pressure in van Genuchten's (1980) capillary pressure model
P_{cap}	= capillary pressure (P_{CH4}-P_W)
$Q^{-1}_{\{P1,P2,S\}}$	= inverse quality factor for fast and slow P wave velocities (P1 & P2, respectively) and S wave velocities (S)
$r_{\{C1,C2\}}$	= ratio of the radius of hydrate enveloping the solid grains (C1) and in contact with solid grains (C2) to solid grain radius
ρ	= density of the sediment
$\rho_{\{S,H,CH4,W\}}$	= density of solid grains, hydrate, methane and water
$\rho_{\{iCH4,iW\}}$	= density of methane and water inclusions in hydrate
ρ_{Fp}	= density of the fluid phase
$S_{\{H,CH4,W\}}$	= saturation of hydrate, methane and water
S_{rCH4}	= irreducible methane saturation
S_{rW}	= irreducible water saturation
S^*	= effective water saturation
S_n	= parameter proportional to the normal stiffness of two cemented grains
S_τ	= parameter proportional to the tangential stiffness of two cemented grains
s	= salinity of water
T	= temperature
t	= tortuosity of the sediment containing hydrate

Variable	Description
ϕ	= porosity of the sediment containing hydrate
ϕ_c	= porosity of a random dense pack of identical spheres
ϕ_0	= potential sediment porosity or porosity for zero hydrate saturation
$\tau_{\{iCH4,iW\}}$	= relaxation time of methane and water inclusions in hydrate
$\tau_{Fp\{C1,C2,PF\}}$	= relaxation time of pore fluid for the habits of cementing hydrate enveloping the grains (C1) and in contact with the grains (C2), and pore-filling hydrate
μ_{Fp}	= fluid phase viscosity
μ_r	= viscosity parameter in Ishii and Mishima's (1984) model
$\mu_{\{CH4,W\}}$	= viscosity of methane and water
$\mu_{\{iCH4,iW\}}$	= viscosity of methane and water inclusions in hydrate
$V_{\{P1,P2,S\}}$	= fast and slow P wave velocities (P1 & P2, respectively) and S wave velocities (S)
$Vol_{\{S,H\}}$	= volume of solid grains and hydrate
$Vol_{\{iCH4,iW\}}$	= volume methane and water inclusions in hydrate
Vol_{Fp}	= volume of the mobile fluid phases (methane + water)
Vol_{Sp}	= volume of the solid phase (solid grains + hydrate)
$\nu_{\{S,H\}}$	= Poisson's ratio of solid grains and hydrate

List of References

Amalokwu, K., Papageorgiou, G., Chapman, M., & Best, A. I. (2017). Modelling ultrasonic laboratory measurements of the saturation dependence of elastic modulus: New insights and implications for wave propagation mechanisms. *International Journal of Greenhouse Gas Control*, *59*, 148–159. https://doi.org/10.1016/j.ijggc.2017.02.009

Anderson, A. L., & Hampton, L. D. (1980a). Acoustics of gas-bearing sediments. II. Measurements and models. *The Journal of the Acoustical Society of America*, *67*(6), 1890–1903. https://doi.org/10.1121/1.384454

Anderson, A. L., & Hampton, L. D. (1980b). Acoustics of gas-bearing sediments I. Background. *The Journal of the Acoustical Society of America*, *67*(6), 1865–1889. https://doi.org/10.1121/1.384453

Andreassen, K., Hubbard, A., Winsborrow, M., Patton, H., Vadakkepuliyambatta, S., Plaza-Faverola, A., … Bünz, S. (2017). Massive blow-out craters formed by hydrate-controlled methane expulsion from the Arctic seafloor. *Science*, *356*(6341), 948–953. https://doi.org/10.1126/science.aal4500

Andreassen, K., Mienert, J., Bryn, P., & Singh, S. C. (2006). A Double Gas-Hydrate Related Bottom Simulating Reflector at the Norwegian Continental Margin. *Annals of the New York Academy of Sciences*, *912*(1), 126–135. https://doi.org/10.1111/j.1749-6632.2000.tb06766.x

Archer, D., & Brovkin, V. (2008). The millennial atmospheric lifetime of anthropogenic CO2. *Climatic Change*, *90*(3), 283–297. https://doi.org/10.1007/s10584-008-9413-1

Archer, D., Buffett, B., & Brovkin, V. (2009). Ocean methane hydrates as a slow tipping point in the global carbon cycle. *Proceedings of the National Academy of Sciences of the United States of America*, *106*(49), 20596–601. https://doi.org/10.1073/pnas.0800885105

Archer, D., & Buffett, B. (2005). Time-dependent response of the global ocean clathrate reservoir to climatic and anthropogenic forcing. *Geochemistry, Geophysics, Geosystems*, *6*(3). https://doi.org/10.1029/2004GC000854

Archie, G. E. (1942). The Electrical Resistivity Log as an Aid in Determining Some Reservoir Characteristics. *Transactions of the AIME*, *146*(1), 54–62. https://doi.org/10.2118/942054-G

Attias, E. (2017, November 20). *Geophysical analysis of marine gas hydrate structures*. PhD Thesis. Retrieved from https://eprints.soton.ac.uk/416892/

Attias, E., Weitemeyer, K. A., Minshull, T. A., Best, A. I., Sinha, M., Jegen-Kulcsar, M., … Berndt, C. (2016). Controlled-source electromagnetic and seismic delineation of subseafloor fluid flow structures in a gas hydrate province, offshore Norway. *Geophysical Journal International*, *206*(2), 1093–1110. https://doi.org/10.1093/gji/ggw188

Bachrach, R. (1998). *High resolution shallow seismic subsurface characterization*. PhD. thesis, Stanford University, Stanford, California. Retrieved from https://pangea.stanford.edu/departments/geophysics/dropbox/SRB/public/docs/theses/SRB_071_SEP98_Bachrach.pdf

Benson, G. C., & Kiyohara, O. (1974). Tabulation of some integral functions describing diffraction effects in the ultrasonic field of a circular piston source. *J. Acoust. Soc. Am.*, *55*(1), 184–185. https://doi.org/10.1121/1.1928147

Berryman, J.G. (1995), Mixture theories for rock properties. In Rock Physics and Phase Relations: a Handbook of Physical Constants, ed. T.J. Ahrens. Washington, DC: American Geophysical Union, pp. 205–228.

Best, A. I. (1992). *The prediction of the reservoir properties of sedimentary rocks from seismic measurements.* PhD Thesis. Retrieved from http://ethos.bl.uk/OrderDetails.do?uin=uk.bl.ethos.331984

Best, A. I., Tuffin, M. D. J., Dix, J. K., & Bull, J. M. (2004). Tidal height and frequency dependence of acoustic velocity and attenuation in shallow gassy marine sediments. *Journal of Geophysical Research B: Solid Earth*, *109*(8), 1–17. https://doi.org/10.1029/2003JB002748

Best, A. I., Priest, J. A., Clayton, C. R. I., & Rees, E. V. L. (2013). The effect of methane hydrate morphology and water saturation on seismic wave attenuation in sand under shallow sub-seafloor conditions. *Earth and Planetary Science Letters*, *368*, 78–87. https://doi.org/10.1016/j.epsl.2013.02.033

Best, A. I., Mccann, C., & Sothcott, J. (1994). The relationships between the velocities , attenuations and petrophysical properties of reselvoi r sedimentary rocksl. *Geophysical Prospecting*, 151–178.

Best, A. I., and C. McCann (1995), Seismic attenuation and pore-fluid viscosity in clay-rich reservoir sandstones, *Geophysics*, *60*(5), 1386-1397, doi:10.1190/1.1443874.

Biastoch, A., Treude, T., Rüpke, L. H., Riebesell, U., Roth, C., Burwicz, E. B., … Wallmann, K. (2011). Rising Arctic Ocean temperatures cause gas hydrate destabilization and ocean acidification.

Geophysical Research Letters, *38*(8). https://doi.org/10.1029/2011GL047222

Biot, M. A. (1956a). Theory of Propagation of Elastic Waves in a Fluid-Saturated Porous Solid. I. Low-Frequency Range. *The Journal of the Acoustical Society of America*, *28*(2), 168–178. https://doi.org/10.1121/1.1908239

Biot, M. A. (1956b). Theory of Propagation of Elastic Waves in a Fluid-Saturated Porous Solid. II. Higher Frequency Range. *The Journal of the Acoustical Society of America*, *28*(2), 179–191. https://doi.org/10.1121/1.1908241

Bishop, A. W. (1959), The principle of effective stress, *Teknisk Ukeblad*, 106 (39), 859–863.

Boetius, A., & Wenzhöfer, F. (2013). Seafloor oxygen consumption fuelled by methane from cold seeps. *Nature Geoscience*, *6*, 725. Retrieved from http://dx.doi.org/10.1038/ngeo1926

Boone, K. G., & Holder, D. S. (1996). Current approaches to analogue instrumentation design in electrical impedance tomography. https://doi.org/10.1088/0967-3334/17/4/001

Boswell, R., & Collett, T. S. (2011). Current perspectives on gas hydrate resources. *Energy Environ. Sci.*, *4*(4), 1206–1215. https://doi.org/10.1039/C0EE00203H

Boswell, R., Shelander, D., Lee, M. W., Latham, T., Collett, T., Guerin, G., … Goldberg, D. (2009). Occurrence of gas hydrate in Oligocene Frio sand: Alaminos Canyon Block 818: Northern Gulf of Mexico. *Marine and Petroleum Geology*, *26*(8), 1499–1512. https://doi.org/10.1016/j.marpetgeo.2009.03.005

Brie, A., F. Pampuri, A. F. Marsala, and O. Meazza (1995), Shear Sonic Interpretation in Gas-Bearing Sands, edited, Society of Petroleum Engineers, doi:10.2118/30595-MS.

Buchanan, P., Soper, A. K., Thompson, H., Westacott, R. E., Creek, J. L., Hobson, G., & Koh, C. A. (2005). Search for memory effects in methane hydrate: Structure of water before hydrate formation and after hydrate decomposition. *Journal of Chemical Physics*, *123*(16). https://doi.org/10.1063/1.2074927

Bünz, S., Polyanov, S., Vadakkepuliyambatta, S., Consolaro, C., & Mienert, J. (2012). Active gas venting through hydrate-bearing sediments on the Vestnesa Ridge, offshore W-Svalbard. *Marine Geology*, *332*, 189–197. https://doi.org/10.1016/j.margeo.2012.09.012

Bussian, A. E. (1983). Electrical conductance in a porous medium. *Geophysics*, *48*(9), 1258–1268. https://doi.org/10.1190/1.1441549

Carcione, J. M., Ursin, B., & Nordskag, J. I. (2007). Cross-property relations between electrical

conductivity and the seismic velocity of rocks. *Geophysics*, *72*(5), E193–E204. Retrieved from http://dx.doi.org/10.1190/1.2762224

Carcione, J. M., & Tinivella, U. (2000). Bottom-simulating reflectors: Seismic velocities and AVO effects. *GEOPHYSICS*, *65*(1), 54–67. https://doi.org/10.1190/1.1444725

Chand, S., Minshull, T. A., Gei, D., & Carcione, J. M. (2004). Elastic velocity models for gas-hydrate-bearing sediments—a comparison. *Geophysical Journal International*, *159*(2), 573–590. https://doi.org/10.1111/j.1365-246X.2004.02387.x

Chand, S., & Minshull, T. A. (2003). Seismic constraints on the effects of gas hydrate on sediment physical properties and fluid flow: A review. *Geofluids*, *3*(4), 275–289. https://doi.org/10.1046/j.1468-8123.2003.00067.x

Chand, S., & Minshull, T. A. (2004). The effect of hydrate content on seismic attenuation: A case study for Mallik 2L-38 well data, Mackenzie delta, Canada. *Geophysical Research Letters*, *31*(14), 2–5. https://doi.org/10.1029/2004GL020292

Chand, S., Minshull, T. A., Priest, J. A., Best, A. I., Clayton, C. R. I., & Waite, W. F. (2006). An effective medium inversion algorithm for gas hydrate quantification and its application to laboratory and borehole measurements of gas hydrate-bearing sediments. *Geophysical Journal International*, *166*(2), 543–552. https://doi.org/10.1111/j.1365-246X.2006.03038.x

Chaouachi, M., Falenty, A., Sell, K., Enzmann, F., Kersten, M., Haberthür, D., & Kuhs, W. F. (2015). Microstructural evolution of gas hydrates in sedimentary matrices observed with synchrotron X-ray computed tomographic microscopy. *Geochemistry, Geophysics, Geosystems*, *16*(6), 1711–1722. https://doi.org/10.1002/2015GC005811

Chapman, M. (2003). Frequency-dependent anisotropy due to meso-scale fractures in the presence of equant porosity. *Geophysical Prospecting*, *51*(5), 369–379. https://doi.org/10.1046/j.1365-2478.2003.00384.x

Chen, M. P., Riedel, M., Spence, G. D., & Hyndman, R. D. (2008). Data report: a downhole electrical resistivity study of northern Cascadia marine gas hydrate. *Proceedings of the Integrated Drilling Program*, *311*. https://doi.org/10.2204/iodp.proc.311.203.2008

Choi, J. H., Dai, S., Cha, J. H., & Seol, Y. (2014). Laboratory formation of noncementing hydrates in sandy sediments. *Geochemistry, Geophysics, Geosystems*, *15*(4), 1648–1656. https://doi.org/10.1002/2014GC005287

Clavier, C., Coates, G., & Dumanoir, J. (1984). Theoretical and Experimental Bases for the Dual-

Water Model for Interpretation of Shaly Sands. *Society of Petroleum Engineers Journal*, *24*(2), 153–168. https://doi.org/10.2118/6859-PA

Clennell, M. Ben, Hovland, M., Booth, J. S., Henry, P., & Winters, W. J. (1999). Formation of natural gas hydrates in marine sediments: 1. Conceptual model of gas hydrate growth conditioned by host sediment properties. *Journal of Geophysical Research: Solid Earth*, *104*(B10), 22985–23003. https://doi.org/10.1029/1999JB900175

Collett, L. S., & Katsube, T. J. (1973). ELECTRICAL PARAMETERS OF ROCKS IN DEVELOPING GEOPHYSICAL TECHNIQUES. *GEOPHYSICS*, *38*(1), 76–91. https://doi.org/10.1190/1.1440336

Collett, T. S. (2001). A Review of Well-Log Analysis Techniques Used to Assess Gas-Hydrate-Bearing Reservoirs. In *Natural Gas Hydrates: Occurrence, Distribution, and Detection* (pp. 189–210). American Geophysical Union. https://doi.org/10.1029/GM124p0189

Collett, T. S. (2003). Natural Gas Hydrate as a Potential Energy Resource. In M. D. Max (Ed.) (pp. 123–136). Dordrecht: Springer Netherlands. https://doi.org/10.1007/978-94-011-4387-5_10

Collett, T. S., Johnson, A., Knapp, C., & Boswell, R. (2009). Natural Gas Hydrates: A Review (pp. 146–219). AAPG Special Volumes. https://doi.org/10.1306/13201101M891602

Collett, T. S., Goldberg, D. S., Janik, A., & Guerin, G. (2003). Downhole Log Assessment of Gas Hydrate and Free-Gas Concentrations on Hydrate Ridge. *American Geophysical Union*. Retrieved from http://adsabs.harvard.edu/abs/2003AGUFMOS51C0876C

Collett, T. S., Riedel, M., Boswell, R., Presley, J., Kumar, P., Sathe, A., … Lall, M. V. (2015). *Indian National Gas Hydrate Program Expedition 01 report*. *Scientific Investigations Report*. Reston, VA. https://doi.org/10.3133/sir20125054

Council, W. E. (2016). *World Energy Resources Natural Gas | 2016*. Retrieved from https://www.worldenergy.org/wp-content/uploads/2017/03/WEResources_Natural_Gas_2016.pdf

Dai, S., Santamarina, J. C., Waite, W. F., & Kneafsey, T. J. (2012). Hydrate morphology: Physical properties of sands with patchy hydrate saturation. *Journal of Geophysical Research*, *117*(B11), B11205. https://doi.org/10.1029/2012JB009667

Daigle, H., A. Cook, and A. Malinverno (2015), Permeability and porosity of hydrate-bearing sediments in the northern Gulf of Mexico, *Marine and Petroleum Geology*, *68, Part A*, 551-564, doi: 10.1016/j.marpetgeo.2015.10.004.

Dallimore, S. R., Collett, T. S., Taylor, A. E., Uchida, T., Weber, M., Chandra, A., … Inoue, T. (2005). Scientific results from the Mallik 2002 gas hydrate production research well program, Mackenzie Delta, northwest territories, Canada: Preface. *Bulletin of the Geological Survey of Canada*, (585). Retrieved from http://pubs.er.usgs.gov/publication/70027941

Darnell, K. N., & Flemings, P. B. (2015). Transient seafloor venting on continental slopes from warming-induced methane hydrate dissociation. *Geophysical Research Letters*, *42*(24), 10765–10772. https://doi.org/10.1002/2015GL067012

Dewangan, P., Mandal, R., Jaiswal, P., Ramprasad, T., & Sriram, G. (2014). Estimation of seismic attenuation of gas hydrate bearing sediments from multi-channel seismic data: A case study from Krishna-Godavari offshore basin. *Marine and Petroleum Geology*, *58*(PA), 356–367. https://doi.org/10.1016/j.marpetgeo.2014.05.015

Dickens, G. R. (2011). Down the Rabbit Hole: Toward appropriate discussion of methane release from gas hydrate systems during the Paleocene-Eocene thermal maximum and other past hyperthermal events. *Climate of the Past*, *7*(3), 831–846. https://doi.org/10.5194/cp-7-831-2011

Dickens, G. R., O'Neil, J. R., Rea, D. K., & Owen, R. M. (1995). Dissociation of oceanic methane hydrate as a cause of the carbon isotope excursion at the end of the Paleocene. *Paleoceanography*, *10*(6), 965–971. https://doi.org/10.1029/95PA02087

Dogan, H., White, P. R., & Leighton, T. G. (2017). Acoustic wave propagation in gassy porous marine sediments: The rheological and the elastic effects. *J. Acoust. Soc. Am.*, *141*(March), 2277–2288. https://doi.org/10.1121/1.4978926

Doveton, J. H. (2001). All Models Are Wrong , but Some Models Are Useful : " Solving " the Simandoux Equation Prolog : The Archie Equation.

Dvorkin, J., M. Prasad, A. Sakai, and D. Lavoie (1999), Elasticity of marine sediments: Rock physics modeling, *Geophysical Research Letters*, *26*(12), 1781-1784, doi:10.1029/1999GL900332.

Dvorkin, J., Helgerud, M. B., Waite, W. F., Kirby, S. H., & Nur, A. (2003). Introduction to physical properties and elasticity models: Chapter 20. In *Natural gas hydrate in oceanic and permafrost environments* (Vol. 5, pp. 245–260). Springer. https://doi.org/10.1007/978-94-011-4387-5_20

Dvorkin, J., Nur, A., Uden, R., & Taner, T. (2003). Rock physics of a gas hydrate reservoir. *The Leading Edge*, *22*(9), 842–847. https://doi.org/10.1190/1.1614153

Dvorkin, J., & Uden, R. (2004). Seismic wave attenuation in a methane hydrate reservoir. *The*

Leading Edge, *23*(8), 730–732. https://doi.org/10.1190/1.1786892

Eberhart-Phillips, D., Han, D.-H., & Zoback, M. D. (1989). Empirical relationships among seismic velocity, effective pressure, porosity, and clay content in sandstone. *GEOPHYSICS*, *54*(1), 82–89. https://doi.org/10.1190/1.1442580

Ecker, C., Dvorkin, J., & Nur, A. (1998). Sediments with gas hydrates: Internal structure from seismic AVO. *GEOPHYSICS*, *63*(5), 1659–1669. https://doi.org/10.1190/1.1444462

Ecker, C., Dvorkin, J., & Nur, A. (2000). Estimating the amount of hydrate and free gas from surface seismic. *Geophysics*, *65*(2), 565–573. https://doi.org/10.1190/1.1820496

Edwards, R. N. (1997). On the resource evaluation of marine gas hydrate deposits using sea-floor transient electric dipole-dipole methods. *GEOPHYSICS*, *62*(1), 63–74. https://doi.org/10.1190/1.1444146

Ellis, D. V., & Singer, J. M. (2007). *Well Logging for Earth Scientists*. (D. V. Ellis & J. M. Singer, Eds.). Dordrecht: Springer Netherlands. https://doi.org/10.1007/978-1-4020-4602-5

Ellis, M. H. (2008). *Joint Seismic and Electrical Measurements of Gas Hydrates in Continental Margin Sediments*. PhD thesis, University of Southampton. Retrieved from http://eprints.soton.ac.uk/id/eprint/63293

Everett, D. H. (1961). The thermodynamics of frost damage to porous solids. *Transactions of the Faraday Society*, *57*(0), 1541. https://doi.org/10.1039/tf9615701541

Falcon-Suarez, I., Papageorgiou, G., Chadwick, A., North, L., Best, A. I., & Chapman, M. (2018). CO2-brine flow-through on an Utsira Sand core sample: Experimental and modelling. Implications for the Sleipner storage field. *International Journal of Greenhouse Gas Control*, *68*, 236–246. https://doi.org/10.1016/J.IJGGC.2017.11.019

Fitzgerald, R. (2000). Phase-Sensitive X-Ray Imaging. *Physics Today*, *53*(7), 23–26. https://doi.org/10.1063/1.1292471

Fohrmann, M., & Pecher, I. A. (2012). Analysing sand-dominated channel systems for potential gas-hydrate-reservoirs using an AVO seismic inversion technique on the Southern Hikurangi Margin, New Zealand. *Marine and Petroleum Geology*, *38*(1), 19–34. https://doi.org/10.1016/j.marpetgeo.2012.08.001

Foucher, J. P., Nouzé, H., & Henry, P. (2002). Observation and tentative interpretation of a double BSR on the Nankai slope. *Marine Geology*, *187*(1–2), 161–175.

https://doi.org/10.1016/S0025-3227(02)00264-5

Du Frane, W. L., Stern, L. A., Constable, S., Weitemeyer, K. A., Smith, M. M., & Roberts, J. J. (2015). Electrical properties of methane hydrate + sediment mixtures. *Journal of Geophysical Research: Solid Earth*, *120*(7), 4773–4783. https://doi.org/10.1002/2015JB011940

Fu, X., Porter, M., Viswanathan, H., Carey, J., & Juanes, R. (2017). Controlled depressurization of a hydrate-crusted gas bubble : Insights from 2D experiments and phase-field modeling. In *The 9th International Conference on Gas Hydrates*. Denver. Retrieved from http://icgh9.csmspace.com/docs/ICGH9_FinalProgram.pdf?062017

Fujii, T., Suzuki, K., Takayama, T., Tamaki, M., Komatsu, Y., Konno, Y., … Nagao, J. (2015). Geological setting and characterization of a methane hydrate reservoir distributed at the first offshore production test site on the Daini-Atsumi Knoll in the eastern Nankai Trough, Japan. *Marine and Petroleum Geology*, *66*, 310–322. https://doi.org/10.1016/j.marpetgeo.2015.02.037

Gelius, L. J., & Wang, Z. (2008). Modelling production caused changes in conductivity for a siliciclastic reservoir: A differential effective medium approach. *Geophysical Prospecting*, *56*(5), 677–691. https://doi.org/10.1111/j.1365-2478.2008.00720.x

Glover, P. W. J. (2010). A generalized Archie's law for n phases. *GEOPHYSICS*, *75*(6), E247–E265. https://doi.org/10.1190/1.3509781

Glover, P. W. J., Meredith, P. G., Sammonds, P. R., & Murrell, S. A. F. (1994). Ionic surface electrical conductivity in sandstone. *Journal of Geophysical Research: Solid Earth*, *99*(B11), 21635–21650. https://doi.org/10.1029/94JB01474

Goldber, D. S., Kan, T. K., & Castagna, J. P. (1984). Attenuation Measurements From Sonic Log Waveforms. In *SPWLA 25th Annual Logging Symposium, 10-13 June*. New Orleans, Louisiana: Society of Petrophysicists and Well-Log Analysts. Retrieved from https://www.onepetro.org/conference-paper/SPWLA-1984-NN

Gorman, A. R., Holbrook, W. S., Hornbach, M. J., Hackwith, K. L., Lizarralde, D., & Pecher, I. (2002). Migration of methane gas through the hydrate stability zone in a low-flux hydrate province. *Geology*, *30*(4), 327. https://doi.org/10.1130/0091-7613(2002)030<0327:MOMGTT>2.0.CO;2

Goswami, B. K., Weitemeyer, K. A., Minshull, T. A., Sinha, M. C., Westbrook, G. K., Chabert, A., … Ker, S. (2015). A joint electromagnetic and seismic study of an active pockmark within the hydrate stability field at the Vestnesa Ridge, West Svalbard margin. *Journal of Geophysical Research: Solid Earth*, *120*(10), 6797–6822. https://doi.org/10.1002/2015JB012344

Gregory, A. R. (1977). Aspects of Rock Physics From Laboratory and Log Data that are Important to Seismic Interpretation: Section 1. Fundamentals of Stratigraphic Interpretation of Seismic Data, *165*, 15–46. Retrieved from http://archives.datapages.com/data/specpubs/seismic1/data/a165/a165/0001/0000/0015.htm#purchaseoptions

Guerin, G., & Goldberg, D. (2002). Sonic waveform attenuation in gas hydrate-bearing sediments from the Mallik 2L-38 research well, Mackenzie Delta, Canada. *Journal of Geophysical Research B: Solid Earth*, *107*(5), EPM 1-1-EPM 1-12. https://doi.org/10.1029/2001JB000556

Guerin, G., & Goldberg, D. (2005). Modeling of acoustic wave dissipation in gas hydrate-bearing sediments. *Geochemistry, Geophysics, Geosystems*, *6*(7), 1–16. https://doi.org/10.1029/2005GC000918

Guerin, G., Goldberg, D., & Meltser, A. (1999). Characterization of in situ elastic properties of gas hydrate-bearing sediments on the Blake Ridge. *Journal of Geophysical Research: Solid Earth*, *104*(B8), 17781–17795. https://doi.org/10.1029/1999JB900127

Hammerschmidt, E. G. (1934). Formation of Gas Hydrates in Natural Gas Transmission Lines. *Industrial & Engineering Chemistry*, *26*(8), 851–855. https://doi.org/10.1021/ie50296a010

Han, T., Best, A. I., Sothcott, J., & Macgregor, L. M. (2011). Pressure effects on the joint elastic-electrical properties of reservoir sandstones. *Geophysical Prospecting*, *59*(3), 506–517. https://doi.org/10.1111/j.1365-2478.2010.00939.x

Han, T., Best, A. I., Sothcott, J., North, L. J., & MacGregor, L. M. (2015). Relationships among low frequency (2Hz) electrical resistivity, porosity, clay content and permeability in reservoir sandstones. *Journal of Applied Geophysics*, *112*, 279–289. https://doi.org/10.1016/j.jappgeo.2014.12.006

Han, T., Best, A. I., MacGregor, L. M., Sothcott, J., & Minshull, T. a. (2011). Joint elastic-electrical effective medium models of reservoir sandstones. *Geophysical Prospecting*, *59*(4), 777–786. https://doi.org/10.1111/j.1365-2478.2011.00956.x

Handa, Y. P. (1990). Effect of hydrostatic pressure and salinity on the stability of gas hydrates. *The Journal of Physical Chemistry*, *94*(6), 2652–2657. https://doi.org/10.1021/j100369a077

Handa, Y. P., & Stupin, D. (1992). Thermodynamic properties and dissociation characteristics of methane and propane hydrates in 70-angstrom-radius silica-gel pores. *Journal of Physical Chemistry*, *96*(21), 8599–8603. https://doi.org/10.1021/j100200a071

Helgerud, M. B., Dvorkin, J., Nur, A., Sakai, A., & Collett, T. (1999). Elastic-wave velocity in marine sediments with gas hydrates: Effective medium modeling. *Geophysical Research Letters*, *26*(13), 2021–2024. https://doi.org/10.1029/1999GL900421

Helgerud, M. B., W. F. Waite, S. H. Kirby, and A. Nur (2009), Elastic wave speeds and moduli in polycrystalline ice Ih, sI methane hydrate, and sII methane-ethane hydrate, *Journal of Geophysical Research: Solid Earth*, *114*(B2), doi:10.1029/2008JB006132.

Henry, P., Thomas, M., & Clennell, M. Ben. (1999). Formation of natural gas hydrates in marine sediments: 2. Thermodynamic calculations of stability conditions in porous sediments. *Journal of Geophysical Research: Solid Earth*, *104*(B10), 23005–23022. https://doi.org/10.1029/1999JB900167

Hesse, R., & Harrison, W. E. (1981). Gas hydrates (clathrates) causing pore-water freshening and oxygen isotope fractionation in deep-water sedimentary sections of terrigenous continental margins. *Earth and Planetary Science Letters*, *55*(3), 453–462. https://doi.org/10.1016/0012-821X(81)90172-2

Hesselbo, S. P., Gröcke, D. R., Jenkyns, H. C., Bjerrum, C. J., Farrimond, P., Morgans Bell, H. S., & Green, O. R. (2000). Massive dissociation of gas hydrate during a Jurassic oceanic anoxic event. *Nature*, *406*(6794), 392–395. https://doi.org/10.1038/35019044

Holbrook, W. S., Hoskins, H., Wood, W. T., Stephen, R. A., Lizarralde, D., & Leg 164 Science Party. (1996). Methane Hydrate and Free Gas on the Blake Ridge from Vertical Seismic Profiling. *Science*, *273*(5283), 1840–1843. https://doi.org/10.1126/science.273.5283.1840

Holder, G. D., Kamath, V. A., & Godbole, S. P. (1984). The Potential of Natural Gas Hydrates as an Energy Resource. *Annual Review of Energy*, *9*(1), 427–445. https://doi.org/10.1146/annurev.eg.09.110184.002235

Holland, M., Schultheiss, P., Roberts, J., & Druce, M. (2008). Observed Gas Hydrate Morphologies in Marine Sediments. In *6th International Conference on Gas Hydrates*.

Hovem, J. M., and G. D. Ingram (1979), Viscous attenuation of sound in saturated sand, *The Journal of the Acoustical Society of America*, *66*(6), 1807-1812, doi:10.1121/1.383653.

Hsu, S. K., Chiang, C. W., Evans, R. L., Chen, C. S., Chiu, S. D., Ma, Y. F., … Wang, Y. (2014). Marine controlled source electromagnetic method used for the gas hydrate investigation in the offshore area of SW Taiwan. *Journal of Asian Earth Sciences*, *92*, 224–232. https://doi.org/10.1016/j.jseaes.2013.12.001

Hu, G., Ye, Y., Liu, C., Best, A. I., & Li, C. (2014). Gas Hydrate Distribution in Sediment Pore Space and Its Impact on Acoustic Properties of Hydrate-Bearing Sediments.

Huang, J. W., Bellefleur, G., & Milkereit, B. (2009). Seismic modeling of multidimensional heterogeneity scales of mallik gas hydrate reservoirs, Northwest territories of Canada. *Journal of Geophysical Research: Solid Earth*, *114*(7), 1–22. https://doi.org/10.1029/2008JB006172

Hustoft, S., Bünz, S., Mienert, J., & Chand, S. (2009). Gas hydrate reservoir and active methane-venting province in sediments on <20 Ma young oceanic crust in the Fram Strait, offshore NW-Svalbard. *Earth and Planetary Science Letters*, *284*(1–2), 12–24. https://doi.org/10.1016/j.epsl.2009.03.038

Hwang, M. J., Wright, D. A., Kapur, A., & Holder, G. D. (1990). An experimental study of crystallization and crystal growth of methane hydrates from melting ice. *Journal of Inclusion Phenomena and Molecular Recognition in Chemistry*, *8*(1–2), 103–116. https://doi.org/10.1007/BF01131291

Hyodo, M., J. Yoneda, N. Yoshimoto, and Y. Nakata (2013), Mechanical and dissociation properties of methane hydrate-bearing sand in deep seabed, *Soils and Foundations*, *53*(2), 299-314, doi:10.1016/j.sandf.2013.02.010.

Ishii, M., and K. Mishima (1984), Two-fluid model and hydrodynamic constitutive relations, *Nuclear Engineering and Design*, *82*(2), 107-126, doi:10.1016/0029-5493(84)90207-3.

Jackson, P. D., Smith, D. T., & Stanford, P. N. (1978). Resistivity-porosity-particle shape relationships for marine sands. *Geophysics*, *43*(6), 1250–1268. https://doi.org/10.1190/1.1440891

Jahren, A. H., Arens, N. C., Sarmiento, G., Guerrero, J., & Amundson, R. (2001). Terrestrial record of methane hydrate dissociation in the Early Cretaceous. *Geology*, *29*(2), 159. https://doi.org/10.1130/0091-7613(2001)029<0159:TROMHD>2.0.CO;2

Jegen, M., Hoelz, S., Swidinsky, A., Sommer, M., Berndt, C., & Chi, W. C. (2014). Electromagnetic and seismic investigation of methane hydrates offshore Taiwan - The Taiflux experiment. *Oceans 2014 - Taipei*, 4–7. https://doi.org/10.1109/OCEANS-TAIPEI.2014.6964461

Jung, J. W., Espinoza, D. N., & Santamarina, J. C. (2010). Properties and phenomena relevant to CH 4 -CO 2 replacement in hydrate-bearing sediments. *Journal of Geophysical Research*, *115*(B10), B10102. https://doi.org/10.1029/2009JB000812

Kan, R., & Sen, P. N. (1987). Electrolytic conduction in periodic arrays of insulators with charges. *The Journal of Chemical Physics*, *86*(10), 5748–5756. https://doi.org/10.1063/1.452502

Kennett, J. P. (2003). Methane Hydrates in Quaternary Climate Change. Retrieved from http://sfx.ethz.ch/sfx_locater?sid=ALEPH:EBI01&genre=book&isbn=9780875902968

Kerkar, P. B., Horvat, K., Jones, K. W., & Mahajan, D. (2014). Imaging methane hydrates growth dynamics in porous media using synchrotron X-ray computed tomography. *Geochemistry Geophysics Geosystems*, *15*, 4759–4768. https://doi.org/10.1002/2014GC005373

Klapp, S. A., Enzmann, F., Walz, P., Huthwelker, T., Tuckermann, J., Schwarz, J. O., … Brewer, P. G. (2012). Microstructure characteristics during hydrate formation and dissociation revealed by X-ray tomographic microscopy. *Geo-Marine Letters*, *32*(5–6), 555–562. https://doi.org/10.1007/s00367-012-0276-0

Klapp, S. A., Klein, H., & Kuhs, W. F. (2007). First determination of gas hydrate crystallite size distributions using high-energy synchrotron radiation. *Geophysical Research Letters*, *34*(13), 1–5. https://doi.org/10.1029/2006GL029134

Klauda, J. B., & Sandler, S. I. (2005). Global Distribution of Methane Hydrate in Ocean Sediment. *Energy & Fuels*, *19*(2), 459–470. https://doi.org/10.1021/ef049798o

Kneafsey, T. J., Tomutsa, L., Moridis, G. J., Seol, Y., Freifeld, B. M., Taylor, C. E., & Gupta, A. (2007). Methane hydrate formation and dissociation in a partially saturated core-scale sand sample. *Journal of Petroleum Science and Engineering*, *56*(1–3), 108–126. https://doi.org/10.1016/j.petrol.2006.02.002

Konno, Y., Y. Jin, J. Yoneda, M. Kida, K. Egawa, T. Ito, K. Suzuki, and J. Nagao (2015), Effect of methane hydrate morphology on compressional wave velocity of sandy sediments: Analysis of pressure cores obtained in the Eastern Nankai Trough, *Marine and Petroleum Geology*, *66, Part 2*, 425-433, doi:10.1016/j.marpetgeo.2015.02.021.

Kuhs, W. F., Genov, G., Goreshnik, E., Zeller, A., Techmer, K. S., & Bohrmann, G. (2004). The Impact of Porous Microstructures of Gas Hydrates On Their Macroscopic Properties. *International Journal of Offshore and Polar Engineering*, *14*(4). Retrieved from http://publications.marum.de/id/eprint/1908

Kumar, D., Sen, M. K., & Bangs, N. L. (2007). Gas hydrate concentration and characteristics within Hydrate Ridge inferred from multicomponent seismic reflection data. *Journal of Geophysical Research: Solid Earth*, *112*(12), 1–11. https://doi.org/10.1029/2007JB004993

Kuster, G. T., and M. N. Toksöz (1974), Velocity and attenuation of seismic waves in two-phase media: Part 1. Theoretical formulations, *Geophysics*, *39*(5), 587-606, doi:10.1190/1.1440450.

Kvenvolden, K. A. (1993). Gas hydrates—geological perspective and global change. *Reviews of Geophysics*, *31*(2), 173. https://doi.org/10.1029/93RG00268

Kvenvolden, K. A. (1999). Potential effects of gas hydrate on human welfare. *Proceedings of the National Academy of Sciences of the United States of America*, *96*(7), 3420–6. https://doi.org/10.1073/PNAS.96.7.3420

Kvenvolden, K. A., Ginsburg, G. D., & Soloviev, V. A. (1993). Worldwide distribution of subaquatic gas hydrates. *Geo-Marine Letters*, *13*(1), 32–40. https://doi.org/10.1007/BF01204390

Leclaire, P., Cohen-Ténoudji, F., & Aguirre-Puente, J. (1994). Extension of Biot's theory of wave propagation to frozen porous media. *The Journal of the Acoustical Society of America*, *96*(6), 3753–3768. https://doi.org/10.1121/1.411336

Lee, M. W. (2002), Biot-Gassmann theory for velocities of gas hydrate-bearing sediments, *Geophysics*, *67*(6), 1711-1719, doi: 10.1190/1.1527072.

Lee, H., Seo, Y., Seo, Y.-T., Moudrakovski, I. L., & Ripmeester, J. A. (2003). Recovering Methane from Solid Methane Hydrate with Carbon Dioxide. *Angewandte Chemie International Edition*, *42*(41), 5048–5051. https://doi.org/10.1002/anie.200351489

Lee, M. W. (2006). *Is Amplitude Loss of Sonic Waveforms Due to Intrinsic Attenuation or Source Coupling to the Medium ? Scientific Investigations Report 2006-5120*.

Lee, M. W., & Collett, T. S. (2006). Gas Hydrate and Free Gas Saturations Estimated from Velocity Logs on Hydrate Ridge, offshore Oregon, U.S.A. In *Proceedings of the Ocean Drilling Program, 199 Scientific Results* (Vol. 204, pp. 1–25). Ocean Drilling Program. https://doi.org/10.2973/odp.proc.sr.204.103.2006

Lee, M. W., & Collett, T. S. (2008). Integrated analysis of well logs and seismic data to estimate gas hydrate concentrations at Keathley Canyon, Gulf of Mexico. *Marine and Petroleum Geology*, *25*(9), 924–931. https://doi.org/10.1016/j.marpetgeo.2007.09.002

Lee, M. W., Hutchinson, D. R., Collett, T. S., & Dillon, W. P. (1996). Seismic velocities for hydrate-bearing sediments using weighted equation. *Journal of Geophysical Research: Solid Earth*, *101*(B9), 20347–20358. https://doi.org/10.1029/96JB01886

Lee, M. W., Hutchinson, D. R., Dillon, W. P., Miller, J. J., Agena, W. F., & Swift, B. A. (1993). Method of estimating the amount of in situ gas hydrates in deep marine sediments. *Marine and Petroleum Geology*, *10*(5), 493–506. https://doi.org/10.1016/0264-8172(93)90050-3

Lee, M. W., & Waite, W. F. (2007). Amplitude loss of sonic waveform due to source coupling to the medium. *Geophysical Research Letters*, *34*(5), 1–4. https://doi.org/10.1029/2006GL029015

Lee, J. Y., J. W. Jung, M. H. Lee, J. J. Bahk, J. Choi, B. J. Ryu, and P. Schultheiss (2013), Pressure core based study of gas hydrates in the Ulleung Basin and implication for geomechanical controls on gas hydrate occurrence, *Marine and Petroleum Geology*, *47*, 85-98, doi:10.1016/j.marpetgeo.2013.05.021.

Leurer, K. C. (1997), Attenuation in fine-grained marine sediments; extension of the Biot-Stoll model by the "effective grain model" (EGM), *Geophysics*, *62*(5), 1465-1479, doi:10.1190/1.1444250.

Leurer, K. C., and C. Brown (2008), Acoustics of marine sediment under compaction: Binary grain-size model and viscoelastic extension of Biot's theory, *The Journal of the Acoustical Society of America*, *123*(4), 1941-1951, doi:10.1121/1.2871839.

Leighton, T. G. (2007). Theory for acoustic propagation in marine sediment containing gas bubbles which may pulsate in a non-stationary nonlinear manner. *Geophysical Research Letters*, *34*(17), 12–15. https://doi.org/10.1029/2007GL030803

Lim, D., Ro, H., Seo, Y., Lee, J. Y., Lee, J., Kim, S.-J., … Lee, H. (2017). Electrical Resistivity Measurements of Methane Hydrate during N 2 /CO 2 Gas Exchange. *Energy & Fuels*, *31*(1), 708–713. https://doi.org/10.1021/acs.energyfuels.6b01920

de Lima, O. a. L., & Sharma, M. M. (1990). A grain conductivity approach to shaly sandstones. *GEOPHYSICS*, *55*(10), 1347–1356. https://doi.org/10.1190/1.1442782

Liu, X., & Flemings, P. B. (2006). Passing gas through the hydrate stability zone at southern Hydrate Ridge, offshore Oregon. *Earth and Planetary Science Letters*, *241*(1–2), 211–226. https://doi.org/10.1016/j.epsl.2005.10.026

Lu, Z., & Sultan, N. (2008). Empirical expressions for gas hydrate stability law, its volume fraction and mass-density at temperatures 273.15 K to 290.15 K. *Geochemical Journal*, *42*(2), 163–175. Retrieved from http://archimer.ifremer.fr/doc/00000/4958/

Mahabadi, N., S. Dai, Y. Seol, T. Sup Yun, and J. Jang (2016), The water retention curve and relative permeability for gas production from hydrate-bearing sediments: pore-network model simulation, *Geochemistry, Geophysics, Geosystems*, *17*(8), 3099-3110, doi:10.1002/2016GC006372.

Makogon, Y. (1981). *Hydrates of Natural Gas*. Tulsa, Oklahoma: Pennwell. Retrieved from https://www.researchgate.net/profile/Y_Makogon/publication/241968293_Hydrates_of_Na

tural_Gas/links/54fa0b2d0cf2040df21b1aa9/Hydrates-of-Natural-Gas.pdf

Malone, R. D. (1990). *Gas hydrates*. United States. Retrieved from http://www.osti.gov/scitech/servlets/purl/6129491

Marín-Moreno, H., Sahoo, S. K., & Best, A. I. (2017). Theoretical modeling insights into elastic wave attenuation mechanisms in marine sediments with pore-filling methane hydrate. *Journal of Geophysical Research: Solid Earth*. https://doi.org/10.1002/2016JB013577

Matsushima, J. (2006). Seismic wave attenuation in methane hydrate-bearing sediments vertical seismic profiling data from the Nankai trough exploratory well, offshore Tokai, central Japan. *Journal of Geophysical Research: Solid Earth*, *111*(10), 1–20. https://doi.org/10.1029/2005JB004031

Mattaboni, P., & Schreiber, E. (1967). Method of pulse transmission measurements for determining sound velocities. *Journal of Geophysical Research*, *72*(20), 5160–5163. https://doi.org/10.1029/JZ072i020p05160

Mavko, G. M., Mukerji, T., & Dvorkin. (1998). The Rock Physics Handbook. Tools for Seismic Analysis in Porous Media. x + 329 pp. Cambridge, New York, Melbourne: Cambridge University Press. Price £40.00, US $64.95 (hard covers). ISBN 0 521 62068 6. *Geological Magazine*, *136*(6), 697–711. https://doi.org/10.1017/S0016756899413329

Mavko, G. M., & Nur, A. (1975). Melt squirt in the asthenosphere. *Journal of Geophysical Research*, *80*(11), 1444. https://doi.org/10.1029/JB080i011p01444

Mazzeo, B. A. (2009). Parasitic capacitance influence of potential-sensing electrodes on four-electrode liquid impedance measurements. *Journal of Applied Physics*, *105*(9). https://doi.org/10.1063/1.3124365

McCann, C., & Sothcott, J. (1992). Laboratory measurements of the seismic properties of sedimentary rocks. *Geological Society, London, Special Publications*, *65*(1), 285–297. https://doi.org/10.1144/GSL.SP.1992.065.01.22

McCleskey, R. B., Nordstrom, D. K., & Ryan, J. N. (2012). Comparison of electrical conductivity calculation methods for natural waters. *Limnology and Oceanography: Methods*, *10*(11), 952–967. https://doi.org/10.4319/lom.2012.10.952

McGinnis, D. F., Greinert, J., Artemov, Y., Beaubien, S. E., & Wüest, A. (2006). Fate of rising methane bubbles in stratified waters: How much methane reaches the atmosphere? *Journal of Geophysical Research*, *111*(C9), C09007. https://doi.org/10.1029/2005JC003183

Milkov, A. V. (2004). Global estimates of hydrate-bound gas in marine sediments: How much is really out there? *Earth-Science Reviews*, *66*(3–4), 183–197. https://doi.org/10.1016/j.earscirev.2003.11.002

Milkov, A. V., Dickens, G. R., Claypool, G. E., Lee, Y. J., Borowski, W. S., Torres, M. E., … Schultheiss, P. (2004). Co-existence of gas hydrate, free gas, and brine within the regional gas hydrate stability zone at Hydrate Ridge (Oregon margin): Evidence from prolonged degassing of a pressurized core. *Earth and Planetary Science Letters*, *222*(3–4), 829–843. https://doi.org/10.1016/j.epsl.2004.03.028

Millero, F. J., Chen, C.-T., Bradshaw, A., & Schleicher, K. (1980). A new high pressure equation of state for seawater. *Deep Sea Research Part A. Oceanographic Research Papers*, *27*(3–4), 255–264. https://doi.org/10.1016/0198-0149(80)90016-3

Minagawa, H., Nishikawa, Y., Ikeda, I., Miyazaki, K., Takahara, N., Sakamoto, Y., … Nairta, H. (2008). Characterization of sand sediment by pore size distribution and permeability using proton nuclear magnetic resonance measurement. *Journal of Geophysical Research: Solid Earth*, *113*(7), 1–9. https://doi.org/10.1029/2007JB005403

Mindlin, R.D. (1949), Compliance of elastic bodies in contact. *Transactions ASME 71*, A-259, doi:10.1007/978-1-4613-8865-4_24.

Minshull, T. A., Marín-Moreno, H., Armstrong McKay, D. I., & Wilson, P. A. (2016). Mechanistic insights into a hydrate contribution to the Paleocene-Eocene carbon cycle perturbation from coupled thermohydraulic simulations. *Geophysical Research Letters*, *43*(16), 8637–8644. https://doi.org/10.1002/2016GL069676

Miyakawa, A., Saito, S., Yamada, Y., Tomaru, H., Kinoshita, M., & Tsuji, T. (2014). Gas hydrate saturation at Site C0002, IODP Expeditions 314 and 315, in the Kumano Basin, Nankai trough. *Island Arc*, *23*(2), 142–156. https://doi.org/10.1111/iar.12064

Murphy, W. F. (1982). Effects of partial water saturation on attenuation in Massilon sandstone and Vycor porous glass. *The Journal of the Acoustical Society of America*, *71*(6), 1458–1468. https://doi.org/10.1121/1.387843

Murshed, M. M., Klapp, S. A., Enzmann, F., Szeder, T., Huthwelker, T., Stampanoni, M., … Kersten, M. (2008). Natural gas hydrate investigations by synchrotron radiation X-ray cryo-tomographic microscopy (SRXCTM). *Geophysical Research Letters*, *35*(23), L23612. https://doi.org/10.1029/2008GL035460

North, L. J. (2017). *Breakthrough Solutions for the Sustainable Exploration and Extraction of Deep Sea Mineral Resources - Laboratory Experiments and Analyses*. Retrieved from http://www.bluemining.eu/download/project_results/public_summary_reports/BLUE-MINING-D2.41-FINAL-Geochemical-results-and-core-descriptions-EXECUTIVE-SUMMARY.pdf

North, L. J., Best, A. I., Sothcott, J., & MacGregor, L. (2013). Laboratory determination of the full electrical resistivity tensor of heterogeneous carbonate rocks at elevated pressures. *Geophysical Prospecting*, *61*(2), 458–470. https://doi.org/10.1111/j.1365-2478.2012.01113.x

Nur, A., & Simmons, G. (1969). The effect of saturation on velocity in low porosity rocks. *Earth and Planetary Science Letters*, *7*(2), 183–193. https://doi.org/10.1016/0012-821X(69)90035-1

O'Connell, R. J., & Budiansky, B. (1977). Viscoelastic properties of fluid-saturated cracked solids. *Journal of Geophysical Research*, *82*(36), 5719–5735. https://doi.org/10.1029/JB082i036p05719

Ohgaki, K., Takano, K., Sangawa, H., Matsubara, T., & Nakano, S. (1996). Methane exploitation by carbon dioxide from gas hydrates. Phase equilibria for CO2-CH4 mixed hydrate system. *JOURNAL OF CHEMICAL ENGINEERING OF JAPAN*, *29*(3), 478–483. https://doi.org/10.1252/jcej.29.478

Ohmura, R., Ogawa, M., Yasuoka, K., & Mori, Y. H. (2003). Statistical Study of Clathrate-Hydrate Nucleation in a Water/Hydrochlorofluorocarbon System: Search for the Nature of the "Memory Effect." *The Journal of Physical Chemistry B*, *107*(22), 5289–5293. https://doi.org/10.1021/jp027094e

Olhoeft, G. R. (1985). Low-frequency electrical properties. *Geophysics*, *50*(12), 2492–2503. https://doi.org/10.1190/1.1441880

Paganin, D., Mayo, S. C., Gureyev, T. E., Miller, P. R., & Wilkins, S. W. (2002). Simultaneous phase and amplitude extraction from a single defocused image of a homogeneous object. *Journal of Microscopy*, *206*(1), 33–40. https://doi.org/10.1046/j.1365-2818.2002.01010.x

Paganoni, M., J. A. Cartwright, M. Foschi, R. C. Shipp, and P. Van Rensbergen (2016), Structure II gas hydrates found below the bottom-simulating reflector, *Geophysical Research Letters*, *43*(11), 5696-5706, doi:10.1002/2016GL069452.

Palmer, I. D., & Traviolia, M. L. (1980). Attenuation by squirt flow in undersaturated gas sands. *Geophysics*, *45*(12), 1780–1792. https://doi.org/10.1190/1.1441065

Papadakis, E. P. (1972). Ultrasonic Diffraction Loss and Phase Change in Anisotropic Materials. *The*

Journal of the Acoustical Society of America, *40*(4), 863–876. https://doi.org/10.1121/1.1910159

Pauli, C. K., Ussler, W., & Dillon, W. P. (2003). Potential Role of Gas Hydrate Decomposition in Generating Submarine Slope Failures (pp. 149–156). Springer, Dordrecht. https://doi.org/10.1007/978-94-011-4387-5_12

Pearson, C., Murphy, J., & Hermes, R. (1986). Acoustic and resistivity measurements on rock samples containing tetrahydrofuran hydrates: Laboratory analogues to natural gas hydrate deposits. *Journal of Geophysical Research*, *91*(B14), 14132. https://doi.org/10.1029/JB091iB14p14132

Peng, D.-Y., & Robinson, D. B. (1976). A New Two-Constant Equation of State. *Industrial & Engineering Chemistry Fundamentals*, *15*(1), 59–64. https://doi.org/10.1021/i160057a011

Petersen, C. J., Papenberg, C., & Klaeschen, D. (2007). Local seismic quantification of gas hydrates and BSR characterization from multi-frequency OBS data at northern Hydrate Ridge. *Earth and Planetary Science Letters*, *255*(3), 414–431. https://doi.org/https://doi.org/10.1016/j.epsl.2007.01.002

Petersen, C. J., Bünz, S., Hustoft, S., Mienert, J., & Klaeschen, D. (2010). High-resolution P-Cable 3D seismic imaging of gas chimney structures in gas hydrated sediments of an Arctic sediment drift. *Marine and Petroleum Geology*, *27*(9), 1981–1994. https://doi.org/10.1016/j.marpetgeo.2010.06.006

Plaza-Faverola, A., Westbrook, G. K., Ker, S., Exley, R. J. K., Gailler, A., Minshull, T. A., & Broto, K. (2010). Evidence from three-dimensional seismic tomography for a substantial accumulation of gas hydrate in a fluid-escape chimney in the Nyegga pockmark field, offshore Norway. *Journal of Geophysical Research: Solid Earth*, *115*(8), 1–24. https://doi.org/10.1029/2009JB007078

Polydorides, N., & Lionheart, W. R. B. (2002). A Matlab toolkit for three-dimensional electrical impedance tomography: A contribution to the Electrical Impedance and Diffuse Optical Reconstruction Software project. *Measurement Science and Technology*, *13*(12), 1871–1883. https://doi.org/10.1088/0957-0233/13/12/310

Pratt, R.G., F. Hou, K. Bauer, and M. Weber (2005), Waveform tomography images of velocity and inelastic attenuation from the Mallik 2002 cross-hole seismic surveys. In: Dallimore, S.R., Collett, T.S. (Eds.), Scientific Results from the Mallik 2002 Gas Hydrate Production Research

Well Program, Mackenzie Delta, Northwest Territories, Canada, *Bulletin of the Geological Survey of Canada*, vol. 585, 14 pp.

Prasad, M., & Manghnani, M. H. (1997). Effects of pore and differential pressure on compressional wave velocity and quality factor in Berea and Michigan sandstones. *GEOPHYSICS*, *62*(4), 1163–1176. https://doi.org/10.1190/1.1444217

Priegnitz, M., Thaler, J., Spangenberg, E., Schicks, J. M., Schrötter, J., & Abendroth, S. (2015). Characterizing electrical properties and permeability changes of hydrate bearing sediments using ERT data. *Geophysical Journal International*, *202*(3), 1599–1612. https://doi.org/10.1093/gji/ggv245

Priest, J. A., Best, A. I., & Clayton, C. R. I. (2005). A laboratory investigation into the seismic velocities of methane gas hydrate-bearing sand. *Journal of Geophysical Research*, *110*(B4), B04102. https://doi.org/10.1029/2004JB003259

Priest, J. A., Best, A. I., & Clayton, C. R. I. (2006). Attenuation of seismic waves in methane gas hydrate-bearing sand. *Geophysical Journal International*, *164*(1), 149–159. https://doi.org/10.1111/j.1365-246X.2005.02831.x

Priest, J. A., Rees, E. V. L., & Clayton, C. R. I. (2009). Influence of gas hydrate morphology on the seismic velocities of sands. *Journal of Geophysical Research: Solid Earth*, *114*(B11), B11205. https://doi.org/10.1029/2009JB006284

Priest, J. A., M. Druce, J. Roberts, P. Schultheiss, Y. Nakatsuka, and K. Suzuki (2015), PCATS Triaxial: A new geotechnical apparatus for characterizing pressure cores from the Nankai Trough, Japan, *Marine and Petroleum Geology*, *66, Part 2*, 460-470, doi:10.1016/j.marpetgeo.2014.12.005.

Priestley, J. (1790). *Experiments and Observations on Different Kinds of Air, And Other Branches of Natural Philosophy, Connected with the Subject.* Birmingham: Thomas Peasron. Retrieved from https://books.google.co.uk/books?hl=en&lr=&id=JU9kAAAAMAAJ&oi=fnd&pg=PA1&ots=ZSBZoyP8rg&sig=w870pgZfla-POQStHnXILEDoFtQ#v=onepage&q&f=false

Reagan, M. T., and G. J. Moridis (2008), Dynamic response of oceanic hydrate deposits to ocean temperature change, *Journal of Geophysical Research: Oceans*, *113*(C12), C12023, doi:10.1029/2008jc004938.

Reuss, A. (1929), Berechnung der Fliessgrenzen vonMischkristallen aufGrund der

Plastizitätsbedingung für Einkristalle. *Journal of Applied Mathematics and Mechanics,* 9, 49–58.

Rees, E. V. L., Priest, J. A., & Clayton, C. R. I. (2011). The structure of methane gas hydrate bearing sediments from the Krishna-Godavari Basin as seen from Micro-CT scanning. *Marine and Petroleum Geology*, *28*(7), 1283–1293. https://doi.org/10.1016/j.marpetgeo.2011.03.015

Revil, A., & Glover, P. W. J. (1998). Nature of surface electrical conductivity in natural sands, sandstones, and clays. *Geophysical Research Letters*, *25*(5), 691–694. https://doi.org/10.1029/98GL00296

Revil, A., Cathles, L. M., Losh, S., & Nunn, J. a. (1998). Electrical conductivity in shaly sands with geophysical applications. *Journal of Geophysical Research*, *103*, 23,925-23,936. https://doi.org/10.1029/98JB02125

Riedel, M., Collett, T. S., & Malone, M. (2010). Expedition 311 Synthesis: scientific findings. In *Proceedings of the IODP, 311* (Vol. 311). Integrated Ocean Drilling Program. https://doi.org/10.2204/iodp.proc.311.213.2010

Riestenberg, D., West, O., Lee, S., McCallum, S., & Phelps, T. J. (2003). Sediment surface effects on methane hydrate formation and dissociation. *Marine Geology*, *198*(1–2), 181–190. https://doi.org/10.1016/S0025-3227(03)00100-2

Rossi, G., Gei, D., Böhm, G., Madrussani, G., & Carcione, J. M. (2007). Attenuation tomography: An application to gas hydrate and free gas detection. *Geophysical Prospecting*, *55*, 655–669.

Rubino, J. G., & Holliger, K. (2013). Research note: Seismic attenuation due to wave-induced fluid flow at microscopic and mesoscopic scales. *Geophysical Prospecting*, *61*(4), 882–889. https://doi.org/10.1111/1365-2478.12009

Ruppel, C. D. (2018). *No Title*. *Fact Sheet*. https://doi.org/10.3133/fs20173080

Rutter, E. H., & Glover, C. T. (2012). The deformation of porous sandstones; are Byerlee friction and the critical state line equivalent? *Journal of Structural Geology*, *44*, 129–140. https://doi.org/10.1016/j.jsg.2012.08.014

Rydzy, M. (2014). *The effect of hydrate formation on the elastic properties of unconsolidated sediment.* PhD Thesis, Colorado School of Mines. Retrieved from http://adsabs.harvard.edu/abs/2014PhDT.....4R

Sahoo, S., H. Marín-Moreno, L. J. North, I. Falco-Suarez, B. N. Madhusudhan, A. I. Best and T. A.

Minshull (2018). Presence and consequences of co-existing methane gas with hydrate under two phase water-hydrate stability conditions, *Journal of Geophysical Research: Solid Earth.* doi: 10.1029/2018JB015598

Santamarina, J. C., et al. (2015), Hydro-bio-geomechanical properties of hydrate-bearing sediments from Nankai Trough, *Marine and Petroleum Geology*, *66, Part 2*, 434-450, doi:10.1016/j.marpetgeo.2015.02.033.

Setzmann, U., and W. Wagner (1991), A New Equation of State and Tables of Thermodynamic Properties for Methane Covering the Range from the Melting Line to 625 K at Pressures up to 100 MPa, *Journal of Physical and Chemical Reference Data*, *20*(6), 1061-1155, doi:10.1063/1.555898.

Schicks, J. M., Spangenberg, E., Giese, R., Steinhauer, B., Klump, J., & Luzi, M. (2011). New approaches for the production of hydrocarbons from hydrate bearing sediments. *Energies*, *4*, 151–172. https://doi.org/10.3390/en4010151

Schicks, J. M., Naumann, R., Erzinger, J., Hester, K. C., Koh, C. A., & Sloan, E. D. (2006). Phase transitions in mixed gas hydrates: Experimental observations versus calculated data. *Journal of Physical Chemistry B*, *110*(23), 11468–11474. https://doi.org/10.1021/jp0612580

Schnurle, P., Liu, C.-S., Hsiuan, T.-H., & Wang, T.-K. (2004). Characteristics of Gas Hydrate and Free Gas Offshore Southwestern Taiwan from a Combined MCS/OBS Data Analysis. *Marine Geophysical Researches*, *25*(1–2), 157–180. https://doi.org/10.1007/s11001-005-0740-6

Schwalenberg, K., Wood, W., Pecher, I., Hamdan, L., Henrys, S., Jegen, M., & Coffin, R. (2010). Preliminary interpretation of electromagnetic, heat flow, seismic, and geochemical data for gas hydrate distribution across the Porangahau Ridge, New Zealand. *Marine Geology*, *272*(1–4), 89–98. https://doi.org/10.1016/J.MARGEO.2009.10.024

Schwalenberg, K., Haeckel, M., Poort, J., & Jegen, M. (2010). Evaluation of gas hydrate deposits in an active seep area using marine controlled source electromagnetics: Results from Opouawe Bank, Hikurangi Margin, New Zealand. *Marine Geology*, *272*(1–4), 79–88. https://doi.org/10.1016/j.margeo.2009.07.006

Schwalenberg, K., Rippe, D., Koch, S., & Scholl, C. (2017). Marine-controlled source electromagnetic study of methane seeps and gas hydrates at Opouawe Bank, Hikurangi Margin, New Zealand. *Journal of Geophysical Research: Solid Earth*, *122*(5), 3334–3350. https://doi.org/10.1002/2016JB013702

Schwan, H. P., & Ferris, C. D. (1968). Four-electrode null techniques for impedance measurement with high resolution. *Review of Scientific Instruments*, *39*(4), 481–485. https://doi.org/10.1063/1.1683413

Shankar, U., & Riedel, M. (2011). Gas hydrate saturation in the Krishna-Godavari basin from P-wave velocity and electrical resistivity logs. *Marine and Petroleum Geology*, *28*(10), 1768–1778. https://doi.org/10.1016/j.marpetgeo.2010.09.008

Shipboard Scientific Party. (2003). Leg 204 Summary. In *Proceedings of the Ocean Drilling Program, 204 Initial Reports* (Vol. 204). Ocean Drilling Program. https://doi.org/10.2973/odp.proc.ir.204.101.2003

Shipley, T. H., Houston, M. H., Buffler, R. T., Shaub, F. J., McMillen, K. J., Ladd, J. W., & Worzel, J. L. (1979). Seismic evidence for widespread possible gas hydrate horizons on continental slopes and rises. *AAPG Bulletin*, *63*(12), 2204–2213. Retrieved from http://aapgbull.geoscienceworld.org/cgi/content/long/63/12/2204

Simandoux, P. (1963). Dielectric measurements in porous media and application to shaly formations. *Rev. Inst. Fr. Petrol.*, *18*(Suppl. issue), 193–215.

Singh, S. C., Minshull, T. A., & Spence, G. D. (1993). Velocity structure of a gas hydrate reflector. *Science (New York, N.Y.)*, *260*(5105), 204–7. https://doi.org/10.1126/science.260.5105.204

Sloan, E. D. (2011). *Natural gas hydrates in flow assurance*. Gulf Professional Pub./Elsevier. Retrieved from https://www.sciencedirect.com/science/book/9781856179454

Sloan, E. D., & Koh, C. A. (2007). *Clathrate hydrates of natural gases.* New York: CRC Press. Retrieved from https://www.crcpress.com/Clathrate-Hydrates-of-Natural-Gases-Third-Edition/Sloan-Jr-Koh/p/book/9780849390784

Smeulders, D. M. J., and M. E. H. van Dongen (1997), Wave propagation in porous media containing a dilute gas–liquid mixture: theory and experiments, *Journal of Fluid Mechanics*, *I343*, 351-373, doi:10.1017/S0022112097005983.

Smith, A. J., Flemings, P. B., Liu, X., & Darnell, K. (2014). The evolution of methane vents that pierce the hydrate stability zone in the world's oceans. *Journal of Geophysical Research B: Solid Earth*, *119*(8), 6337–6356. https://doi.org/10.1002/2013JB010686

Spangenberg, E. (2001). Modeling of the influence of gas hydrate content on the electrical properties of porous sediments. *Journal of Geophysical Research: Solid Earth*, *106*(B4), 6535–6548. https://doi.org/10.1029/2000JB900434

Spangenberg, E., Kulenkampff, J., Naumann, R., & Erzinger, J. (2005). Pore space hydrate formation in a glass bead sample from methane dissolved in water. *Geophysical Research Letters*, *32*(24), L24301. https://doi.org/10.1029/2005GL024107

Spangenberg, E., and J. Kulenkampff (2006), Influence of methane hydrate content on electrical sediment properties, *Geophysical Research Letters*, *33*(24), doi:10.1029/2006GL028188.

Spangenberg, E., Beeskow-Strauch, B., Luzi-Helbing, M., Naumann, R., Rydzy, M., & Schicks, J. (2008). The process of hydrate formation in clastic sediments and its impact on their physical properties. In *6th International Conference on Gas Hydrates*. Vancouver, Canada. Retrieved from http://gfzpublic.gfz-potsdam.de/pubman/faces/viewItemOverviewPage.jsp?itemId=escidoc:237650:3

Spangenberg, E., Heeschen, K., & Schicks, J. M. (2017). Seismic Wave Tomography to Monitor Hydrate Formation and Production Experiments in LARS. In *ICGH 9 - 9th International Conference on Gas Hydrates*. Denver, USA. Retrieved from https://escidoc.gfz-potsdam.de/ir/item/escidoc:2363926/components/component/escidoc:2363924/content

Spangenberg, E., Priegnitz, M., Heeschen, K., & Schicks, J. M. (2015). Are Laboratory-Formed Hydrate-Bearing Systems Analogous to Those in Nature? *Journal of Chemical & Engineering Data*, *60*(2), 258–268. https://doi.org/10.1021/je5005609

Stampanoni, M., Borchert, G., Wyss, P., Abela, R., Patterson, B., Hunt, S., … Rüegsegger, P. (2002). High resolution X-ray detector for synchrotron-based microtomography. *Nuclear Instruments and Methods in Physics Research Section A: Accelerators, Spectrometers, Detectors and Associated Equipment*, *491*(1–2), 291–301. https://doi.org/10.1016/S0168-9002(02)01167-1

Stern, L. A., Lorenson, T. D., & Pinkston, J. C. (2011). Gas hydrate characterization and grain-scale imaging of recovered cores from the Mount Elbert Gas Hydrate Stratigraphic Test Well, Alaska North Slope. *Marine and Petroleum Geology*, *28*(2), 394–403. https://doi.org/10.1016/j.marpetgeo.2009.08.003

Stoll, R. D., and G. M. Bryan (1970), Wave Attenuation in Saturated Sediments, *The Journal of the Acoustical Society of America*, *47*(5B), 1440-1447, doi:10.1121/1.1912054.

Stoll, R. D., & Bryan, G. M. (1979). Physical properties of sediments containing gas hydrates. *Journal of Geophysical Research*, *84*, 1629. https://doi.org/10.1029/JB084iB04p01629

Suess, E., Torres, M. E., Bohrmann, G., Collier, R. W., Rickert, D., Goldfinger, C., … Elver, M. (2001). Sea Floor Methane Hydrates at Hydrate Ridge, Cascadia Margin. In *Natural Gas Hydrates—*

Occurrence, Distribution and Detection (pp. 87–98). American Geophysical Union. https://doi.org/10.1029/GM124p0087

Sultan, N., Cochonat, P., Foucher, J.-P., & Mienert, J. (2004). Effect of gas hydrates melting on seafloor slope instability. *Marine Geology*, *213*(1–4), 379–401. https://doi.org/10.1016/j.margeo.2004.10.015

Sultaniya, A. K., Priest, J. A., & Clayton, C. R. I. (2015). Measurements of the changing wave velocities of sand during the formation and dissociation of disseminated methane hydrate. *Journal of Geophysical Research: Solid Earth*, *120*(2), 778–789. https://doi.org/10.1002/2014JB011386

Sun, R., & Duan, Z. (2007). An accurate model to predict the thermodynamic stability of methane hydrate and methane solubility in marine environments. *Chemical Geology*, *244*(1–2), 248–262. https://doi.org/10.1016/j.chemgeo.2007.06.021

Takeya, S., Hori, A., Hondoh, T., & Uchida, T. (2000). Freezing-memory effect of water on nucleation of CO_2 hydrate crystals. *The Journal of Physical Chemistry B*, *104*(17), 4164–4168. https://doi.org/10.1021/jp993759+

Tamaki, K., K. Pisciotto, Allan J., et. al. (1990), *Proceedings of the Ocean Drilling Program, Initial Reports, 127*, College Station, Texas, doi: 10.2973/odp.proc.ir.127.1990.

Tang, L. G., Xiao, R., Huang, C., Feng, Z. P., & Fan, S. S. (2005). Experimental investigation of production behavior of gas hydrate under thermal stimulation in unconsolidated sediment. *Energy and Fuels*, *19*(6), 2402–2407. https://doi.org/10.1021/ef050223g

Taylor, J. R. (John R. (1997). *An introduction to error analysis : the study of uncertainties in physical measurements*. University Science Books.

Thatcher, K. E., Westbrook, G. K., Sarkar, S., & Minshull, T. A. (2013). Methane release from warming-induced hydrate dissociation in the West Svalbard continental margin: Timing, rates, and geological controls. *Journal of Geophysical Research: Solid Earth*, *118*(1), 22–38. https://doi.org/10.1029/2012JB009605

Thomas, E. C. (1976). The Determination of Qv From Membrane Potential Measurements on Shaly Sands. *Journal of Petroleum Technology*, *28*(9), 1087–1096. https://doi.org/10.2118/5505-PA

Tisato, N., Quintal, B., Chapman, S., Podladchikov, Y., & Burg, J. (2015). Bubbles attenuate elastic waves at seismic frequencies: First experimental evidence. *Geophysical Research Letters*, *42*(10), 1–8. https://doi.org/10.1002/2015GL063538

Tishchenko, P., Hensen, C., Wallmann, K., & Wong, C. S. (2005). Calculation of the stability and solubility of methane hydrate in seawater. *Chemical Geology*, *219*(1–4), 37–52. https://doi.org/10.1016/j.chemgeo.2005.02.008

Tohidi, B., Agena, W. F., Clennell, M. Ben, Burgass, R. W., & Biderkab, A. B. (2001). Visual observation of gas-hydrate formation and dissociation in synthetic porous media by means of glass micromodels. *Geology*, *29*(9), 867–870. https://doi.org/10.1130/0091-7613(2001)029

Tohidi, B., Danesh, A., & Todd, A. C. (1995). Modelling single and mixed electrolyte solutions and its applications to gas hydrates. *Chemical Engineering Research and Design*, *73*(A4), 464–472. Retrieved from http://www.scopus.com/inward/record.url?eid=2-s2.0-0029301853&partnerID=tZOtx3y1

Toksöz, M. N., & Johnston, D. H. (1981). *Seismic wave attenuation*. Society of Exploration Geophysicists. Retrieved from https://www.abebooks.co.uk/9780931830167/Seismic-Wave-Attenuation-Geophysics-Reprint-0931830168/plp

Torres, M. E., Wallmann, K., Tréhu, A. M., Bohrmann, G., Borowski, W. S., & Tomaru, H. (2004). Gas hydrate growth, methane transport, and chloride enrichment at the southern summit of Hydrate Ridge, Cascadia margin off Oregon. *Earth and Planetary Science Letters*, *226*(1–2), 225–241. https://doi.org/10.1016/j.epsl.2004.07.029

Tulk, C. A. (1999). Storage and handling of natural gas hydrate. *Bulletin of the Geological Survey of Canada*, (544).

Uchida, T., Dallimore, S., & Mikami, J. (2000). Occurrences of Natural Gas Hydrates beneath the Permafrost Zone in Mackenzie Delta: Visual and X-ray CT Imagery. *Annals of the New York Academy of Sciences*, *912*(1), 1021–1033. https://doi.org/10.1111/j.1749-6632.2000.tb06857.x

Uchida, T., Takeya, S., Chuvilin, E. M., Ohmura, R., Nagao, J., Yakushev, V. S., … Narita, H. (2004). Decomposition of methane hydrates in sand, sandstone, clays and glass beads. *Journal of Geophysical Research: Solid Earth*, *109*(5), 1–12. https://doi.org/10.1029/2003JB002771

Vafaei, M. T., Kvamme, B., Chejara, A., & Jemai, K. (2014). A new reservoir simulator for studying hydrate dynamics in reservoir. *International Journal of Greenhouse Gas Control*, *23*, 12–21. https://doi.org/10.1016/j.ijggc.2014.02.001

van Genuchten, M. T. (1980), A closed-form equation for predicting the hydraulic conductivity of unsaturated soils, *Soil Science Society of America Journal*, *44*(5), 892-898,

doi:10.2136/sssaj1980.03615995004400050002x.

Vanneste, M., De Batist, M., Golmshtok, A., Kremlev, A., & Versteeg, W. (2001). Multi-frequency seismic study of gas hydrate-bearing sediments in Lake Baikal, Siberia. *Marine Geology*, *172*(1–2), 1–21. https://doi.org/10.1016/S0025-3227(00)00117-1

Waite, W. F., Winters, W. J., & Mason, D. H. (2004). Methane hydrate formation in partially water-satulated Ottawa sand. *American Mineralogist*, *89*(July), 1202–1207. https://doi.org/10.2138/am-2004-8-906

Waite, W. F., Bratton, P. M., & Mason, D. H. (2011). Laboratory Formation of Non-Cementing , Methane Hydrate-Bearing Sands. *7th International Conference on Gas Hydrates (ICGH)*.

Waite, W. F., Santamarina, J. C., Cortes, D. D., Dugan, B., Espinoza, D. N., Germaine, J., … Yun, T.-S. (2009). Physical properties of hydrate-bearing sediments. *Reviews of Geophysics*, *47*(4), RG4003. https://doi.org/10.1029/2008RG000279

Waxman, M. H., & Smits, L. J. M. (1968). Electrical Conductivities in Oil-Bearing Shaly Sands. *Society of Petroleum Engineers Journal*, *8*(2), 107–122. https://doi.org/10.2118/1863-A

Weitemeyer, K. A., Gao, G., Constable, S., & Alumbaugh, D. (2010). The practical application of 2D inversion to marine controlled-source electromagnetic data. *GEOPHYSICS*, *75*(6), F199–F211. https://doi.org/10.1190/1.3506004

Weitemeyer, K. A., Constable, S. C., Key, K. W., & Behrens, J. P. (2006). First results from a marine controlled-source electromagnetic survey to detect gas hydrates offshore Oregon. *Geophysical Research Letters*, *33*(3), 1–4. https://doi.org/10.1029/2005GL024896

Weitemeyer, K. A., Constable, S., & Tréhu, A. M. (2011). A marine electromagnetic survey to detect gas hydrate at Hydrate Ridge, Oregon. *Geophysical Journal International*, *187*(1), 45–62. https://doi.org/10.1111/j.1365-246X.2011.05105.x

Westbrook, G. K., Thatcher, K. E., Rohling, E. J., Piotrowski, A. M., Palike, H., Osborne, A. H., … Aquilina, A. (2009). Escape of methane gas from the seabed along the West Spitsbergen continental margin. *Geophysical Research Letters*, *36*(15), 1–5. https://doi.org/10.1029/2009GL039191

Westbrook, G. K., Chand, S., Rossi, G., Long, C., Bünz, S., Camerlenghi, A., … Zillmer, M. (2008). Estimation of gas hydrate concentration from multi-component seismic data at sites on the continental margins of NW Svalbard and the Storegga region of Norway. *Marine and Petroleum Geology*, *25*(8), 744–758. https://doi.org/10.1016/j.marpetgeo.2008.02.003

White, J. E. (1975). Computed Seismic Speeds and Attenuation in Rocks With Partial Gas Saturation. *Geophysics*, *40*(2), 224–232. https://doi.org/10.1190/1.1440520

White, R. S. (1977). Seismic bright spots in the Gulf of Oman. *Earth and Planetary Science Letters*, *37*(1), 29–37. https://doi.org/10.1016/0012-821X(77)90143-1

Winkler, K. W., & Murphy, W. F. (1995). Acoustic velocity and attenuation in porous rocks. In *AGU Reference Shelf* (Vol. 3, pp. 20–34). https://doi.org/10.1029/RF003p0020

Winkler, K. W., & Plona, T. J. (1982). Technique for measuring ultrasonic velocity and attenuation spectra in rocks under pressure. *Journal of Geophysical Research: Solid Earth*, *87*(B13), 10776–10780. https://doi.org/10.1029/JB087iB13p10776

Winters, W. J., Dillon, W. P., Pecher, I. A., & Mason, D. H. (2003). GHASTLI-determining physical properties of sediment containing natural and laboratory-formed gas hydrate: Chapter 24. In M. D. Max (Ed.), *Natural gas hydrate in oceanic and permafrost environments* (Vol. 5, pp. 311–322). Springer. https://doi.org/10.1007/978-94-011-4387-5_24

Winters, W., M. Walker, R. Hunter, T. Collett, R. Boswell, K. Rose, W. Waite, M. Torres, S. Patil, and A. Dandekar (2011), Physical properties of sediment from the Mount Elbert Gas Hydrate Stratigraphic Test Well, Alaska North Slope, *Marine and Petroleum Geology*, *28*(2), 361-380, doi:10.1016/j.marpetgeo.2010.01.008.

Wood, W. T., & Ruppel, C. (2000). Seismic and thermal investigations of the Blake Ridge gas hydrate area: a synthesis. In *Proceedings of the Ocean Drilling Program, 164 Scientific Results* (Vol. 164, pp. 253–264). Ocean Drilling Program. https://doi.org/10.2973/odp.proc.sr.164.203.2000

Wood, W. T., W. S. Holbrook, and H. Hoskins (2000), In situ measurements of P-wave attenuation in the methane hydrate and gas-bearing sediments of the Blake Ridge. In: Paull, C.K., Matsumoto, R., Wallace, P.J., and Dillon, W.P. (Eds.), *Proceedings of the Ocean Drilling Program*, *Scientific Results*, Vol. 164.

Xiong, L., Li, X., Wang, Y., & Xu, C. (2012). Experimental study on methane hydrate dissociation by depressurization in porous sediments. *Energies*, *5*(2), 518–530. https://doi.org/10.3390/en5020518

Yamamoto, A., Yamanaka, Y., Oka, A., & Abe-Ouchi, A. (2014). Ocean oxygen depletion due to decomposition of submarine methane hydrate. *Geophysical Research Letters*, *41*(14), 5075–5083. https://doi.org/10.1002/2014GL060483

Yamamoto, K., Terao, Y., Fujii, T., Ikawa, T., Seki, M., Matsuzawa, M., & Kanno, T. (2014).

Operational overview of the first offshore production test of methane hydrates in the Eastern Nankai Trough. In *Offshore Technology Conference*. Offshore Technology Conference. https://doi.org/10.4043/25243-MS

Yang, L., Falenty, A., Chaouachi, M., Haberthür, D., & Kuhs, W. F. (2016). Synchrotron X-ray computed microtomography study on gas hydrate decomposition in a sedimentary matrix. *Geochemistry, Geophysics, Geosystems*, *17*(9), 3717–3732. https://doi.org/10.1002/2016GC006521

Yefremova, A. G., & Zhizhchenko, B. P. (1974). Obnaruzheniye kristallgidradov gazov v osadkakh sovremennykh akvatoriy ["Occurrence of crystal hydrates of gases in the sediments of modern marine basins"]. *Doklady Akademii Nauk SSSR*, *214*, 1179– 1181.

You, K., Kneafsey, T. J., Flemings, P. B., Polito, P., & Bryant, S. L. (2015). Salinity-buffered methane hydrate formation and dissociation in gas-rich systems. *Journal of Geophysical Research: Solid Earth*, *120*(2), 643–661. https://doi.org/10.1002/2014JB011190

Yuan, J., & Edwards, R. N. (2000). The Assessment of Marine Gas Hydrates Through Electrical Remote Sounding: Hydrate Without a BSR? *Geophysical Research Letters*, *27*(16), 2397–2400. https://doi.org/10.1029/2000GL011585

Yun, T. S., Francisca, F. M., Santamarina, J. C., & Ruppel, C. (2005). Compressional and shear wave velocities in uncemented sediment containing gas hydrate. *Geophysical Research Letters*, *32*(10), 1–5. https://doi.org/10.1029/2005GL022607

Zhan, X., Schwartz, L. M., Toksöz, M. N., Smith, W. C., & Morgan, F. D. (2010). Pore-scale modeling of electrical and fluid transport in Berea sandstone. *Geophysics*, *75*(5), F135–F142. https://doi.org/10.1190/1.3463704

Zhang, X., Du, Z., Luan, Z., Wang, X., Xi, S., Wang, B., … Yan, J. (2017). In Situ Raman Detection of Gas Hydrates Exposed on the Seafloor of the South China Sea. *Geochemistry, Geophysics, Geosystems*, *18*(10), 3700–3713. https://doi.org/10.1002/2017GC006987

Zhao, J., L. Yang, Y. Liu, and Y. Song (2015), Microstructural characteristics of natural gas hydrates hosted in various sand sediments, *Physical Chemistry Chemical Physics*, *17*(35), 22632-22641, doi:10.1039/C5CP03698D.